CHARGE TRANSFER ACROSS LIQUID/LIQUID INTERFACES - THEORY AND APPLICATIONS

Paul Daniel Beattie

Degree of Doctor of Philosophy

University of Edinburgh

1995

To Paula and my parents

Acknowledgements

I would like to thank Professor Hubert Girault for all his help and encouragement during the course of this work. Thanks also to past and present members of the electrochemistry groups in Edinburgh and Lausanne, especially Cecile Belmont, Murray Osborne and Geoff Wellington.

I wish to acknowledge the financial support given to me by the Science and Engineering Research Council and Medisense (U.K.) for a C.A.S.E. award, and also the Ecole Polytechnique Federale de Lausanne (E.P.F.L.) for a visiting fellowship.

Thanks to Brian Senior of the I²M unit, E.P.F.L., for all his help with scanning electron microscopy, to Dr. Alain Delay, Laboratoire d'Electrochimie, E.P.F.L., for help and advice with a.c. impedance experiments, to Dr. Pierre Infelta, Institut de Chimie Physique (II), E.P.F.L., for help with modelling enzyme kinetics, and to Professor Horst Vogel, Institut de Chimie Physique, E.P.F.L., for the use of his pipette puller. Thanks also go to Gaynor Johnston for final year project work carried out on the inhibition of the enzyme butyrylcholinesterase by organophosphate compounds.

Abstract

This thesis is concerned with charge transfer processes at the interface between two immiscible electrolyte solutions (ITIES), from both a kinetic and an analytical viewpoint.

Microholes, formed by ultra-violet excimer laser photoablation of polyester films, and micropipettes, fabricated from borosilicate glass capillaries by means of a pipette puller, are both used to support the ITIES for the study of ion and assisted ion transfer reactions respectively. Using the techniques of steady-state voltammetry and a.c. impedance, both processes are found to be dependent on diffusion of the participating species to the interface only.

Electron transfer reactions at the ITIES are studied using cyclic voltammetry. Transfer between the hexacyanoferrate redox couple ($[Fe(CN)_6]^{3-/4-}$) in the aqueous phase, and ferrocene and 1,1'-dimethylferrocene, respectively, in the organic (1,2-DCE) phase, is investigated. Results obtained for transfer between copper (II) ions in the aqueous phase and ferrocene in 1,2-DCE are also presented.

An investigation is made into the inhibition of the enzyme butyrylcholinesterase by the organophosphate compound paraoxon (diethyl *p*-nitrophenyl phosphate), using butyrylcholine chloride as the substrate. Experimental measurement is based on the transfer of the butyrylcholine cation across the ITIES. By this method it is possible to determine the rate constants for both the inhibition of the enzyme and the hydrolysis of butyrylcholine.

List of Abbreviations

The symbols denoted below have been used throughout the thesis:

Roman Alphabet

a - activity

aq - aqueous (org - organic)

A - area, or amperes

ACh - acetylcholine

BChE - butyrylcholinesterase

BTPPA - bis(triphosphoranylidene)ammonium

ButCh - butyrylcholine

c (or conc.) - concentration

C - capacitance, or centigrade

D - diffusion coefficient

Db18C6 - dibenzo-18-crown-6

1,2-DCE - 1,2-dichloroethane

E - cell potential

f - frequency

F - farads, or the Faraday constant

Hz - hertz

i - current

i_{ss} - steady-state current

k - rate constant

K - association constant, or potassium

r - radius

R - resistance, or the universal gas constant

T - temperature in Kelvin (unless otherwise specified)

TBA - tetrabutylammonium

TIC/TID - transfer by interfacial complexation/dissociation

TMA -tetramethylammonium

TPAs - tetraphenylarsonium

TPB - tetraphenylborate

TPBCl - tetrakis(4-chlorophenyl)borate

U - enzyme units

z - charge number

Z - impedance

Greek Alphabet

α - phase denoted α

β - phase denoted β

$\mathring{A}$ - angstroms

$\tilde{\mu}$ - electrochemical potential

μ - chemical potential, or micro

ϕ^{α} - electrical potential of phase α

$\Delta_{\beta}^{\alpha}\phi$ - Galvani potential difference between phases α and β

η - viscosity

δ - diffusion layer thickness

θ - phase angle

υ - scan rate

ω - angular frequency

Ω - ohms

$\Delta G_{tr,i}^{\alpha\rightarrow\beta}$ - Gibbs free energy of transfer of an ion, i, from phase α to β

Table of Contents

Chapter One

INTRODUCTION

For almost a century, the study of the interface between two immiscible electrolyte solutions (ITIES) has stimulated researchers worldwide, and has led to a wealth of scientific literature. Key elements of research in this field include the pursuit of a clearer understanding of the mechanism of charge transfer processes, together with the search for practical applications of the ITIES.

1.1 Overview of the ITIES

The history of the ITIES effectively began in 1902, when Nernst and Riesenfield [1] observed the transfer of ions during the passage of current through a water/phenol/water system, using coloured inorganic electrolytes. This work was intended to establish a method for the determination of transport numbers of ions in non aqueous solvents. In 1906, however, Cremer [2] realised that these water/organic/water systems were analogous to the interface between cell membranes and their surrounding electrolytes. This resulted in an injection of interest from physiologists who wanted to use the ITIES as a simple model to help study the behaviour of more complex biological systems.

In 1939, Verwey and Niessen [3] postulated that the ITIES was composed of two back-to-back Gouy-Chapman diffuse layers. Subsequent to this theoretical work, Kahlweit and Strehlow showed in 1954 [4] that the

potential drop across the water/quinoline interface was spread mainly over the two diffuse layers. It was not until 1968, however, when Gavach *et al.* [5] showed that the ITIES could be polarised, like the metal electrode/electrolyte solution interface, that significant progress in this field was made. At this stage experimental studies were restricted to controlled current techniques [6-8] since the large ohmic (iR) drop across the organic phase precluded any attempt to use controlled potential methods.

The important technical breakthrough in ITIES research came in 1977, when Samec *et al.* [9] introduced the four electrode potentiostat and, using this in conjunction with a positive feedback loop in 1979 [10], demonstrated that it was possible to compensate for the effects of iR drop. This paved the way for controlled potential techniques to be applied to the study of charge transfer processes at the ITIES - cyclic voltammetry [10], chronoamperometry [11], current scan polarography [12,13], differential pulse stripping voltammetry [14], a.c. voltammetry [15], and a.c. impedance [16] are some of the techniques which have been used. Most work has involved the use of nitrobenzene, or 1,2-dichloroethane (1,2-DCE), as the organic phase solvent, due to their low miscibility with water and relatively high dielectric constants.

In 1986, Taylor and Girault [17] miniaturised the ITIES by supporting it at the tip of a micropipette. Another method of creating a micro-ITIES is to support it in a microhole, formed by UV (ultra-violet) excimer laser photoablation of a thin polyester film, as realised in 1989 by Campbell and Girault [18]. More recently, the ITIES has been the subject of detailed experimentation using the technique of laser induced surface second

harmonic generation (SSHG) [19,20], which can provide information on both the orientation of molecules at the interface, and the interfacial structure.

Other work in this field has included a theoretical evaluation of the free energy of reorganisation associated with electron transfer across an ITIES, by Marcus [21], as well as computer simulations of the dynamics of both ion and electron transfer by Benjamin [22,23].

1.2 Charge Transfer Phenomena at the ITIES

There are a number of charge transfer processes which can be studied at an ITIES. These include ion transfer [9], assisted ion transfer [24], electron transfer [25], and photo-induced charge transfer reactions [26].

1.2.1 Ion Transfer

In their preliminary investigations at the ITIES, Gavach *et al.* [6] studied the transfer of the tetrabutylammonium cation, TBA^+, from water to nitrobenzene, using chronopotentiometry (with sodium bromide and tetrabutylammonium tetraphenylborate (TBATPB) employed as the respective supporting electrolytes). The resulting voltage-time curves were identical to classical chronopotentiograms obtained for metal electrode/electrolyte solution systems, and they concluded that the current was carried through the interface only by the diffusion-controlled transfer of TBA^+. Later work by the same group [7,8] focused on the transfer of a series of tetraalkylammonium ions using the same technique.

Ion transfer currents observed at the ITIES are due to ionic flux across the interface and in no way correspond to oxidation or reduction of the components of the aqueous or organic phases.

As mentioned previously, the introduction of the four electrode potentiostat with iR drop compensation by Samec *et al.* [10] opened up the ITIES to study by a wide variety of potentiostatic techniques. These authors studied the reversible transfer of the caesium ion, Cs^+, from water to nitrobenzene using cyclic voltammetry (in this case the supporting electrolytes were lithium chloride (LiCl) and TBATPB respectively). This allowed evaluation of the standard Gibbs free energy of transfer for Cs^+, based on measurement of the half-wave potential for the transfer process. The diffusion coefficient of Cs^+ in water was also obtained, by means of a plot of the peak current versus the square root of the scan rate. Since then, many studies of reversible ion transfer reactions at the large (semi-infinite), or planar, ITIES have been performed. This has resulted in the accumulation of a large amount of thermodynamic data, which has been compiled in various reviews [27,28].

One of the main priorities of the work to date has been the determination of kinetic parameters such as the apparent standard rate constant, k^o, and the apparent charge transfer coefficient, α, for the ion transfer reaction. Samec *et al.* investigated the kinetics of transfer of caesium [29], acetylcholine and choline [30], and a series of tetraalkylammonium ions [31], from water to nitrobenzene, using convolution potential sweep voltammetry, and observed that the rate constants were of the order of 10^{-2} cms^{-1}. However, they realised that the main experimental error in these measurements was the uncompensated solution resistance, which cannot be distinguished from quasi-reversible kinetics. In a subsequent publication, they studied the

transfer of the picrate ion across the water/nitrobenzene interface [32] using the technique of a.c. impedance. They concluded that kinetic measurements at the ITIES which were based on the application of a small exciting signal to the system in thermodynamic equilibrium offered more reliable data than measurements involving large potential sweeps or variations, and that ionic rate constants measured under the conditions of direct current flow can be underestimated by a factor of two or three. Thus, most of the recent work on the kinetics of ion transfer by this group has involved the use of a.c. impedance [33,34].

Senda and co-workers have used a.c. polarography to study the transfer of a series of alkylammonium ions at the water/nitrobenzene interface [35,36]. Recently, however, they too have turned to a.c. impedance, in order to study the kinetics of transfer of various monovalent anions across the water/nitrobenzene interface [37]. In general, the values for the standard apparent ionic rate constants obtained by a.c. impedance, and a.c. polarography, tend to be of the order of 0.1 cms^{-1}.

In addition to the above work, Shao *et al.* [38,39] used the technique of chronocoulometry to study the transfer of acetylcholine across the water/1,2-DCE and water/nitrobenzene-tetrachloromethane interfaces. Despite the enormous volume of work on this subject, there is still considerable confusion over the ion transfer mechanism. This is a point which is discussed in detail in chapter two (2.1.5.1). The majority of kinetic studies, with few exceptions, have been undertaken using the large ITIES.

Other ion transfer systems which have been studied include hetero- and iso-polyanions [40,41] and a series of alkylcarboxylate/-sulphonate anions [42].

1.2.2 Assisted Ion Transfer

Assisted, or facilitated, ion transfer was first observed in 1979 by Koryta [24] who observed the assisted transfer of potassium and sodium ions in the aqueous phase by the synthetic polyether dibenzo-18-crown-6 (Db18C6) and the natural antibiotic valinomycin respectively which were dissolved in the organic phase. Complexation of the ion by the ionophore effected a decrease in the Gibbs free energy of transfer, causing a subsequent shift in ion transfer potential. This was a landmark in ITIES research because it meant that both potential window-limiting species and neutral ionophore molecules were now amenable to study.

As a result of this breakthrough, a great deal of time and attention was spent investigating assisted transfer of alkali and alkaline earth metal ions using different ionophores, both natural and synthetic, such as nonactin [43], calcium ionophore [44], valinomycin [24,45,46], monensin [47], nigericin [48] and Db18C6 [24,43,49,50,51].

Interest in this work spread rapidly to other groups [52,53,54,55] and in 1991, Shao *et al.* [56] proposed a new terminology to describe the possible mechanisms of assisted ion transfer. These are as follows:

TIC - Transfer by Interfacial Complexation
TID - Transfer by Interfacial Dissociation
ACT - Aqueous Complexation followed by Transfer
TOC - Transfer followed by Organic phase Complexation

There has been much speculation with regard to the assisted ion transfer mechanism. Sinru *et al.* [53] postulated that the reaction would proceed by the diffusion of the ionophore from the organic phase into the aqueous phase, followed by complexation and subsequent transfer (ACT). This would only be valid, however, if the ionophore was soluble in both phases, and for molecules such as Db18C6 this is clearly not the case. In consequence, Samec and Papoff [51], Kakutani *et al.* [52], and Shao *et al.* [56] all supported the idea of a TIC mechanism of transfer, which is analogous to electron transfer at a solid electrode (see figure 1.1).

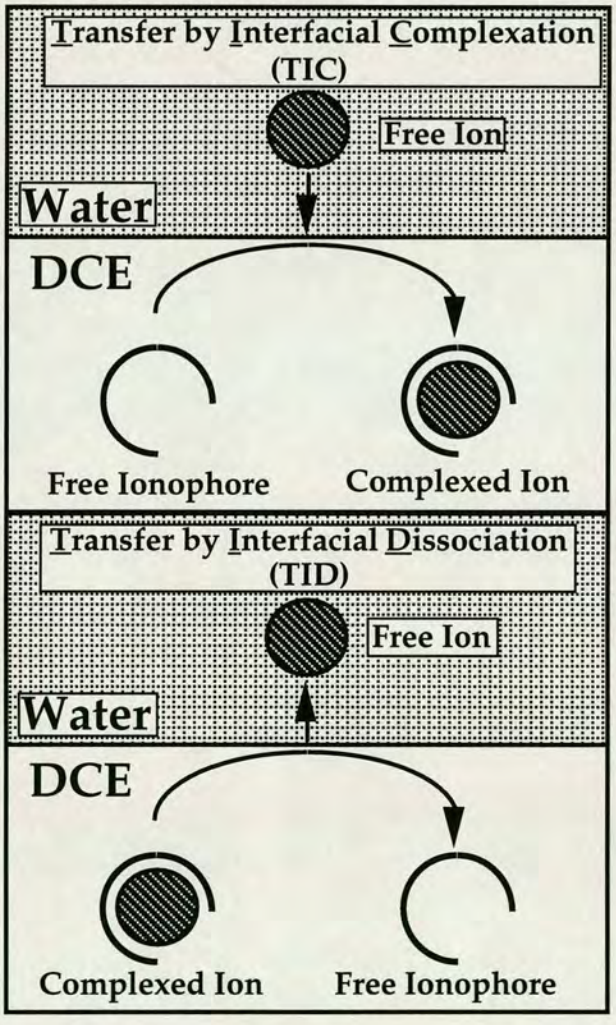

Figure 1.1 - Illustration of the TIC/TID mechanism for assisted ion transfer.

Essentially, there are two limiting cases in the TIC/TID mechanism, where the concentration of either the ion or the ionophore is in large excess of the other. In each case, the measured current is proportional to the diffusion to the interface of the species which is not in excess. In a recent paper by Matsuda *et al.* [57], general equations were derived for the above cases, which took into account the distribution coefficient of the ionophore between the two phases, and allowed the calculation of the complexation constant of the ionophore for a particular system. This methodology was utilised by Osborne and Girault [58] for the determination of association constants for complexation of potassium, sodium and ammonium ions with nonactin, valinomycin and Db18C6.

In spite of the large amount of work in this area, very little has emerged regarding the kinetics of the assisted ion transfer process. Campbell *et al.* [129] attempted to study the kinetics of the assisted transfer of the potassium ion (facilitated by Db18C6) from water to 1,2-DCE, using steady-state voltammetry - where the interface was suspended at the tip of a micropipette. Unfortunately, the authors neglected the effects of the magnesium ion, Mg^{2+} (present in the aqueous phase), which may have influenced their results. The apparent standard rate constant values quoted were of the order of 10^{-3} cms^{-1}. More recently, Sabela *et al.* [130] investigated the kinetics of assisted sodium ion transfer (facilitated by Db18C6), across the large water/nitrobenzene interface, by means of a.c. impedance. The measured rate constant values were between 0.01 and 1 cms^{-1}.

The ability to detect concentrations of ions using excess ionophore has been utilised in practical sensor schemes for the determination of ammonia and urea by Senda *et al.* [59,60]. This group used Db18C6 dissolved in a poly-

vinyl chloride (PVC) - nitrobenzene gel phase to facilitate the transfer of ammonium ions.

Many other assisted ion transfer reactions have been investigated. These include proton transfer by the α-hexylate anion [61], 1,10-phenanthroline [62], and drug molecules such as terramycin [63] - which is used as a multi-purpose antibiotic, and the anaesthetics Lidocaine and Dicaine [64]. Transfer of transition metal-terpyridine complexes [65], amino-complexed nickel (II) ions [66], and copper (II) chloride, $[Cu(II)Cl]^+$, transfer facilitated by a tetradentate phosphorus-nitrogen ligand [67], have also been studied.

1.2.3 Electron Transfer

Heterogeneous electron transfer is possibly the most significant type of reaction which may be studied at the ITIES, due to the analogy with electron transfer across biological cell membranes, and also its role in phase transfer catalysis [68]. In 1975, Guainazzi *et al.* [69] showed that aqueous copper (II) could be reduced to copper metal by passage of current across the water/1,2-DCE interface, using tetrabutylammonium hexacarbonylvanadate as the electron donor in the organic phase. It was in 1979, however, when Samec *et al.* [25,70] used their newly developed electrochemical methodology to investigate electron transfer between the hexacyanoferrate redox couple ($[Fe(CN)_6]^{3-/4-}$) in water and ferrocene in nitrobenzene, by cyclic voltammetry, that this area of research began to evolve significantly. These authors showed that the reversibility of the electron transfer depended on the concentrations of the reactants in both phases. Stewart *et al.* [71] later showed that the cyclic voltammetric response for electron transfer at an ITIES will only satisfy the normal criterion for reversibility (a

peak-to-peak separation, ΔE_p, of 59 mV) when one of the two redox species present in the adjacent phases is in excess with respect to the other. Furthermore, the excess species must be present in both of its oxidation forms. In light of the above, it was concluded that ΔE_p values greater than 60 mV may be observed purely as a consequence of diffusion, and not kinetic control.

In a later publication, Hanzlik *et al.* [72] showed that the product of the oxidation of ferrocene, the ferricenium ion, transferred at less positive potentials than that at which the electron transfer process took place - indicating that the electron transfer was not complicated by ion transfer. Subsequent to this, however, they stressed the importance of the choice of supporting electrolyte in these systems [73], showing that ferricenium could be reduced by the tetraphenylborate anion (TPB^-) and that ferrocene could be oxidised spontaneously in the presence of the tetraphenylarsonium cation ($TPAs^+$).

In 1988, Geblewicz and Schiffrin [74] studied electron transfer between $[Fe(CN)_6]^{3-/4-}$ in water and lutetium biphthalocyanine, ($Lu(PC)_2$), in 1,2-DCE, by cyclic voltammetry. The advantage of using $Lu(PC)_2$ as the organic phase redox system was that its hydrophobic nature precluded any possibility of partition to the aqueous phase, implying true heterogeneous electron transfer. These authors showed that the transfer process was quasi-reversible and evaluated a standard rate constant of 0.9×10^{-3} cms^{-1} - a value which is low compared with the expected electron transfer rate at metallic electrodes. They attributed this difference to a greater separation between redox centres at the ITIES compared with the metal electrode/electrolyte solution interface. Other organic phase redox systems studied have

included tin biphthalocyanine[75], and iron and ruthenium metalloporphyrin-pyridine complexes [76]. Recently, Cheng and Schiffrin [77] turned once more to the analysis of kinetics of electron transfer using a.c. impedance, as previously carried out by Chen *et al.* [78], and demonstrated that the apparent standard rate constant was between 10^{-2} and 10^{-3} cms^{-1}.

Other investigations have been performed by Kihara *et al.* [79], who studied a series of redox couples using current scan polarography. The Kyoto group has also studied ion transfer coupled with electron transfer at the ITIES [80]. In the latter case, they observed that electron transfer between $[Fe(CN)_6]^{3-/4-}$ in the aqueous phase and 7,7,8,8-tetracyanoquinodimethane (TCNQ) /$TCNQ^{\cdot -}$ in nitrobenzene, could effect the transfer of potassium in the aqueous phase by valinomycin in the organic phase. They also showed that this could be used as a method for separation of different ions in the aqueous phase.

1.2.4 Photo-Induced Charge Transfer

There are several types of photo-induced reactions which produce a current at the ITIES, some of which are classified as follows [81]:

IPET - Interfacial Photo-induced Electron Transfer
PE-IT - Photo-induced Electron transfer followed by Ion Transfer
PC-IT - Photo-Chemical reactions followed by Ion Transfer

There have been very few investigations of IPET due to the incumbent difficulties in finding systems in which the photoproducts do not cross the

interface, thereby affecting the measured photocurrent. Thomson *et al.* [82] reported photocurrent measurements for the system:

$$[Ru(bpy)_3]^{2+}_{(water)} + C_7V^{2+}_{(1,2\text{-DCE})} \rightleftharpoons [Ru(bpy)_3]^{3+}_{(water)} + C_7V^{+}_{(1,2\text{-DCE})}$$

where bpy = 2,2′-bipyridine, and C_7V = heptyl-4,4′-bipyridinium

In this process, the aqueous and organic phase photoproducts are more hydrophilic/-phobic than the initial reactants respectively, thereby ensuring that any observed photocurrent is due to electron transfer only. Most recently, Brown *et al.* [83] have investigated IPET between $[Ru(bpy)_3]^{2+}$ in water and TCNQ in 1,2-DCE. Marecek *et al.* [84,85] have also studied reactions of this type, involving the quenching of $[Ru(bpy)_3]^{2+}$ in the organic phase by methylviologen in the aqueous phase. In this case, however, the aqueous and organic phase photoproducts are more hydrophobic/-philic with respect to the reactants, which may result in complication of the observed currents due to ion transfer.

PE-IT reactions have been studied by Kuzmin *et al.* [86], who studied the photoinduced electron transfer between: (1) excited protoporphyrin and a quinone in 1,2-DCE, followed by transfer of the reduced radical quinone; and (2) excited quinone and the tetraphenylborate anion, followed by transfer of a related anion.

An example of a PC-IT reaction is the decomposition of a tetraaryl ion (such as tetraphenylborate, tetrakis(4-chlorophenyl)borate and tetraphenylarsonium) in 1,2-DCE by UV-light, followed by the transfer of a bridged phenyl intermediate, $[(Ph)_2B(biphenyl)]^-$, as realised by Samec *et al.* [26,87].

1.3 Adsorption

Another phenomenon which has been studied at the ITIES is that of adsorption. This was first reported by Guastalla in 1957 [88], who measured the change in interfacial tension between a solution of hexadecyltrimethylammonium bromide in nitrobenzene and an aqueous solution of potassium bromide, as a function of applied potential. He observed a decrease in the interfacial tension which was attributed to the adsorption of the hexadecyltrimethylammonium ion at the interface, and which was termed 'electro-adsorption'. This effect was subsequently studied by Blank [89] who concluded that electro-adsorption was a mass transfer phenomenon dominated by migration. Since then, there have been several investigations into the adsorption of long chain ionic, and non-ionic, surfactants at the ITIES and the effects which these have on charge transfer processes [90-92]. Most recently, Osborne and Girault [93] have studied the adsorption behaviour of the perfluorosulphonate ionomer Nafion at the polarised water/1,2-DCE interface.

Many studies of adsorbed monolayers of different types of phospholipid molecules have also been made at the ITIES, in an attempt to imitate one side of a biological membrane [94-96]. One further aspect of adsorption at the ITIES is that of ion pair formation, which occurs as a result of the high concentrations of supporting electrolytes present in the adjacent phases [97].

1.4 The Solidified Liquid/Liquid Interface

In an attempt to make the ITIES more practical with respect to sensor design, several investigations have been made into the possible solidification of

either the aqueous or the organic phase. Most of these studies have focused on the agar-water gel/nitrobenzene and the water/PVC-nitrobenzene gel interfaces [59,60,98-100]. Anion transfer across the membrane-stabilised ITIES has also been performed by Hundhammer *et al.* [101].

1.5 The Micro-ITIES

Ever since the late 1970's, when Fleischmann and co-workers popularised microelectrodes [102], the field has been continually developing and expanding. Major research applications include the study of reaction kinetics [103], characterisation and modification of surfaces [104], and in-vivo sensing [105]. The properties of micro and ultramicroelectrodes have been extensively reviewed elsewhere [106-108] but one of the main advantages, critical to so many applications, is the decreased effect of solution resistance. This criterion opened the way to studies in highly resistive media which were previously inaccessible by conventional means [109].

1.5.1 The Micropipette Tip-Supported ITIES

As previously mentioned (1.1), Taylor and Girault [17] miniaturised the ITIES by supporting it at the tip of a micropipette, in an effort to bypass the requirement of iR drop compensation (which is necessary for centimetre-scale interfaces). Indeed, initial results proved very promising, showing that it was relatively easy to study reversible ion transfer reactions at the micropipette tip-supported ITIES. Further work by Stewart *et al.* [110] focused on the use of the micropipette as a tool for the determination of the ionic species limiting the potential window.

Shao *et al.* [56] have investigated the assisted ion transfer of alkali metal cations from the aqueous to the organic phase using micropipettes. Assisted ion transfer from aqueous electrolyte solutions to low supporting electrolyte organic phase solutions has also been investigated [111]. Most of the above work suffered, however, from drawbacks associated with poor reproducibility of the tip geometry. Tips were produced on a trial and error basis by breaking the end of the pulled pipette, which meant that they were seldom regular in shape, and this led to a decrease in the mechanical stability of the interface.

In 1991, Senda *et al.* [112] investigated the analytical applicability of micropipettes, when they used a micropipette containing the organic phase to study the transfer of the acetylcholine cation, ACh^+, from water to nitrobenzene. Their studies showed that it was possible to carry out stripping voltammetry of ACh^+, at micromolar levels, by preconcentration of the ACh^+ in the nitrobenzene phase.

Ion transfer reactions at the micropipette are characterised by an asymmetric diffusion regime. The transfer of ions out of the pipette (egress) is controlled by linear diffusion, whereas transfer into the pipette (ingress) is controlled by diffusion of a spherical type. The two processes are easily distinguished during cyclic voltammetry, as the egress transfer leads to a peak shaped current response, and ingress transfer produces a steady-state wave [110]. Assisted ion transfer reactions on the other hand produce cyclic voltammograms which are steady-state during both the forward and reverse scans since the organic phase is normally outside the pipette (with the exception of [112]) and the current is controlled by spherical-type diffusion of the ionophore, or the ion-ionophore complex, to the tip.

1.5.2 The Microhole-Supported ITIES

As mentioned in 1.1, the other method of creating a micro-ITIES is to support the interface at a microhole - formed by UV excimer laser photoablation of a 12 micron (μm) thick polyester film [18]. Unlike the micropipette, the diffusion regime at a microhole-supported ITIES is approximately symmetrical. Thus, both ion transfer and assisted ion transfer reactions produce current responses of a steady-state type [18,113]. The exact position of the interface within the hole has not been fully established, although the observed currents are approximately the same as those for an inlaid microdisc electrode based on the laser entrance hole radius [113]. Osborne *et al.* [114,115] have used the microhole-supported ITIES as a transducer to follow enzyme reactions, such as the hydrolytic decomposition of urea by urease, and that of creatinine by creatinine deiminase.

1.6 Outline of the Present Work

This thesis is concerned with the fundamental nature of charge transfer processes at the ITIES and the practical applications which such phenomena may facilitate. Chapters two and three introduce the essential theory, electrochemical techniques and methodology, which are applicable to the experimental section.

Chapter four is devoted to the study of ion transfer kinetics. Using UV excimer laser photoablation of thin polyester films, microholes having radii ranging from approximately 25 to 3 μm in radius are produced and used to support the ITIES, thereby creating a micro-interface. By means of the technique of steady-state voltammetry, the kinetics of transfer of the ions

tetramethylammonium, TMA^+, tetraethylammonium, TEA^+, butyrylcholine, $ButCh^+$, and acetylcholine, ACh^+, across both the water/1,2-DCE and water/nitrobenzene interfaces are investigated. Furthermore, the method of a.c. impedance is applied to the analysis of the kinetics of TMA^+ transfer across the water/1,2-DCE interface.

Chapter five concentrates on the kinetics of assisted ion transfer reactions. Using the methodology applied in chapter four to ion transfer reactions, the assisted ion transfer of potassium, by the neutral ionophore Db18C6, across the water/1,2-DCE interface, is followed by steady-state voltammetry, chronoamperometry and a.c. impedance. In this case, the ITIES is suspended at the tip of micropipettes ranging from 15 to 0.6 μm in radius.

Chapter six is concerned with electron transfer reactions at the ITIES, studied by means of cyclic voltammetry. Transfer between the compounds ferrocene and 1,1'-dimethylferrocene respectively, present in the 1,2-DCE phase, and the hexacyanoferrate couple ($[Fe(CN)_6]^{3-/4-}$), in the aqueous phase is investigated. Experimental results associated with electron transfer between copper (II) ions in the aqueous phase and ferrocene in the 1,2-DCE phase are also presented.

In chapter seven, the hydrolysis of $ButCh^+$ by the enzyme butyryl-cholinesterase (BChE) is investigated using cyclic voltammetry. The effect of inhibition of the enzyme by the organophosphate compound paraoxon (1,1'-diethyl-*p*-nitrophenol phosphate) is also demonstrated.

Finally, chapter eight deals with the conclusions to the aforementioned work, as well as giving a brief outline of future work to be considered.

Chapter Two

THEORY AND EXPERIMENTAL TECHNIQUES

2.1 Theory

The following text is intended to outline the thermodynamics of equilibria taking place at an ITIES. This has already been treated in meticulous detail by Gavach and co-workers [6,7,8], and Koryta [24], and has been summarised in various reviews [27,28,81,116,117]. Effects due to ion-pairing processes are always neglected in the expressions which are derived below.

2.1.1 The Nernst Equation for the ITIES

If two immiscible electrolyte solutions, α and β, are brought into contact, the solutes partition themselves between the two phases until an equilibrium is reached. At equilibrium the electrochemical potential, $\tilde{\mu}$, of each phase is equal. Therefore, for a partitioning ion, i:

$$\tilde{\mu}_i^{\alpha} = \tilde{\mu}_i^{\beta} \qquad (2.1.1)$$

In order to consider an electrochemical system, it is convenient to divide the electrochemical potential of the ion into a chemical and an electrical part:

$$\tilde{\mu}_i^{\alpha} = \mu_i^{\alpha} + z_i F\phi^{\alpha} \qquad (2.1.2)$$

where z_i is the charge number of the ion, F is the Faraday constant, ϕ^α represents the bulk electrical potential of the α phase, and μ_i^α is the chemical potential defined as:

$$\mu_i^\alpha = \mu_i^{o,\alpha} + RT\ln a_i^\alpha \tag{2.1.3}$$

Here $\mu_i^{o,\alpha}$ represents the standard chemical potential and a_i^α is the activity. By substitution of equation 2.1.3 into 2.1.2, and by equating the electrochemical potentials, the standard Gibbs free energy of transfer of the ion, i, from the bulk of α to that of β, can be derived:

$$\Delta G_{tr,i}^{o,\alpha\rightarrow\beta} = \mu_i^{o,\beta} - \mu_i^{o,\alpha} = RT\ln\left(\frac{a_i^\alpha}{a_i^\beta}\right) + z_iF(\phi^\alpha - \phi^\beta) \tag{2.1.4}$$

This quantity is effectively the difference between the standard Gibbs free energies of solvation of the ion in the respective phases. The term $(\phi^\alpha - \phi^\beta)$ represents the Galvani potential difference between the two phases, written as $\Delta_\beta^\alpha\phi$. The Galvani potential difference is the driving force for the transfer process. Rewriting equation 2.1.4 yields:

$$\Delta_\beta^\alpha\phi = \frac{\Delta G_{tr,i}^{o,\alpha\rightarrow\beta}}{z_iF} + \left(\frac{RT}{z_iF}\right)\ln\left(\frac{a_i^\beta}{a_i^\alpha}\right) \tag{2.1.5}$$

Defining the standard potential of transfer for i as:

$$\Delta_\beta^\alpha\phi_i^o = \frac{\Delta G_{tr,i}^{o,\alpha\rightarrow\beta}}{z_iF} \tag{2.1.6}$$

the following relationship is obtained:

$$\Delta_{\beta}^{\alpha}\phi = \Delta_{\beta}^{\alpha}\phi_i^o + \left(\frac{RT}{z_i F}\right)\ln\left(\frac{a_i^{\beta}}{a_i^{\alpha}}\right) \qquad (2.1.7)$$

Equation 2.1.7 is analogous to the Nernst equation for the applied potential at a metal electrode/electrolyte solution boundary. Unfortunately, the standard Gibbs free energy of transfer for a single ion, $\Delta G_{tr,i}^{o,\alpha\rightarrow\beta}$, is not an experimentally accessible quantity. Therefore, to make its quantitative determination possible, an extra-thermodynamic assumption must be introduced.

Consider the following equilibrium for a salt MX:

$$M_{(\alpha)}^{+} + X_{(\alpha)}^{+} \rightleftarrows M_{(\beta)}^{+} + X_{(\beta)}^{+} \qquad (2.1.8)$$

where MX is completely dissociated (M^+ and X^- are solvated) in both phases. The standard Gibbs free energy of transfer of the salt MX from α to β is given by:

$$\Delta G_{tr,MX}^{o,\alpha\rightarrow\beta} = (\mu_{M^+}^{o,\beta} + \mu_{X^-}^{o,\beta}) - (\mu_{M^+}^{o,\alpha} + \mu_{X^-}^{o,\alpha}) \qquad (2.1.9)$$

In contrast with $\Delta G_{tr,i}^{o,\alpha\rightarrow\beta}$, $\Delta G_{tr,MX}^{o,\alpha\rightarrow\beta}$ is a measurable parameter (calculated from partition coefficient data), which can be expressed as the sum of the Gibbs free energies of transfer of the ions M^+ and X^-:

$$\Delta G_{tr,MX}^{o,\alpha\rightarrow\beta} = \Delta G_{tr,M^+}^{o,\alpha\rightarrow\beta} + \Delta G_{tr,X^-}^{o,\alpha\rightarrow\beta} \qquad (2.1.10)$$

Introducing the Grunwald assumption [118] - which states that the cation and anion of tetraphenylarsonium tetraphenylborate ($TPAs^+$ and TPB^-) have

equal standard Gibbs free energies of transfer for a given solvent pair - allows a scale for the standard Gibbs free energy of transfer of individual ions to be established.

$$\Delta G^{o,\alpha\rightarrow\beta}_{tr,TPAs^+} = \Delta G^{o,\alpha\rightarrow\beta}_{tr,TPB^-} = 1/2\Delta G^{o,\alpha\rightarrow\beta}_{tr,TPAsTPB} \qquad (2.1.11)$$

The principle of the assumption is that the size and structure of the cation and anion are very similar, therefore their solvation energies are likely to be very close in value.

Shao *et al.* [119] questioned the validity of the Grunwald or 'TPAsTPB' assumption on the grounds that it ignores the nature of the charge on the ions, and also that the As-C and B-C bond lengths are not equivalent (1.91 and 1.63 angstroms (Å) respectively [120,121]). The authors demonstrated that the difference in radii between the two ions should produce a difference in the Gibbs free energy of transfer of 14 $kJmol^{-1}$.

Girault and Schiffrin [122] proposed an alternative method of defining the absolute potential scale by using the potential of zero charge (pzc) as the absolute zero point. This quantity is normally measured by means of a streaming ITIES. The basis of this assumption is that the dipolar contribution to the Galvani potential difference at the pzc is negligible thus fixing an origin for the Galvani potential scale for the ITIES. Indeed, by measuring the pzc for their system, Shao *et al.* [119] showed that the Gibbs free energies of transfer of $TPAs^+$ and TPB^- do in fact differ by 14 $kJmol^{-1}$.

Clearly, based on the above considerations, the pzc assumption is a more accurate way of defining a scale for the standard Gibbs free energy of

transfer of a single ion. However, the necessity to determine the pzc for each and every system employed to study the ITIES is rather cumbersome and since the 'TPAsTPB' assumption is relatively good to a first approximation, it is this which is more commonly used.

2.1.2 The Polarisable ITIES

The ITIES may be classified into two different categories, namely ideally-polarisable and non-polarisable. In order to demonstrate the former case, consider a liquid/liquid system in which a very hydrophobic 1:1 electrolyte A_1B_1 is dissolved in the organic phase (org), and a very hydrophilic 1:1 electrolyte A_2B_2 is dissolved in the aqueous phase (aq). The convention for displaying an electrochemical cell such as this is as follows:

$$R1|A_1B_1(org)\|A_2B_2(aq)|R2 \qquad \textit{Cell 2.1.1}$$

where R1 and R2 represent the reference electrodes, which are reversible to either cation (A_1 or A_2) or anion (B_1 or B_2). The symbol $\|$ represents the liquid/liquid interface. The system may be represented by the following equations:

$$\Delta^{aq}_{org}\phi^{o}_{A_1} << 0, \text{ and } \Delta^{aq}_{org}\phi^{o}_{B_2} << 0 \qquad (2.1.12)$$

$$\Delta^{aq}_{org}\phi^{o}_{A_2} >> 0, \text{ and } \Delta^{aq}_{org}\phi^{o}_{B_1} >> 0 \qquad (2.1.13)$$

Under these conditions, there exists a potential range, or window, in which $\Delta^{aq}_{org}\phi$ is predominantly controlled by the electrical charge in the diffuse layers, rather than by the ion activities. This situation is analogous to that of

an ideally-polarisable metal electrode/electrolyte solution interface, and is termed the ideally-polarisable ITIES.

In contrast to the above situation, their can exist another type of interface - the non-polarisable ITIES. Consider the following system:

$$R1|A_3B_1(org)\|A_3B_2(aq)|R2 \qquad \textit{Cell 2.1.2}$$

where both phases have a common cation, A_3, which is transferable across the interface. The transfer of the anions B_1 and B_2 is negligible in the potential window, therefore the system may be described by the following equations:

$$\Delta^{aq}_{org}\phi^{o}_{B_1} >> 0, \text{ and } \Delta^{aq}_{org}\phi^{o}_{B_2} << 0 \qquad (2.1.14)$$

$$\Delta^{aq}_{org}\phi^{o}_{B_2} << \Delta^{aq}_{org}\phi^{o}_{A_3} << \Delta^{aq}_{org}\phi^{o}_{B_1} \qquad (2.1.15)$$

The electrical potential difference between the aqueous and organic phases is now determined by the activity of the ion A_3 in each phase according to equation 2.1.16 (provided that its concentration in each phase is comparable).

$$\Delta^{aq}_{org}\phi = \Delta^{aq}_{org}\phi^{o}_{A_3} + \left(\frac{RT}{z_{A_3}F}\right)\ln\left(\frac{a^{org}_{A_3}}{a^{aq}_{A_3}}\right) \qquad (2.1.16)$$

Normally, charge transfer reactions are studied at the polarisable ITIES, whilst the non-polarisable ITIES functions as a reference electrode which is reversible to the organic phase cation. The term 'ITIES' is normally used to describe the polarisable form.

2.1.3 The Structure of the ITIES

As mentioned in chapter one, the first model of interfacial structure was introduced by Verwey and Niessen [3]. They proposed that the ITIES is composed of two back-to-back Gouy-Chapman diffuse layers - one for each solvent. In 1977, Gavach *et al.* [123] put forward a modified version of the Verwey-Niessen model (the MVN model), again based on two back-to-back diffuse layers, but which are separated by an ion-free layer of orientated solvent molecules - the compact inner layer - which is characterised by a dipolar potential drop. The MVN model is, in effect, a direct analogy with the electrical double layer for a metal electrode/electrolyte solution interface, where the compact inner layer defines planes of closest approach (outer Helmholtz planes). The Galvani potential difference, $\Delta_{org}^{aq}\phi$, then splits into three components:

$$\Delta_{org}^{aq}\phi = (\phi^{aq} - \phi^{org}) = \Delta_{org}^{aq}\phi_{cl} + \phi_2^{org} - \phi_2^{aq} \qquad (2.1.17)$$

where $\Delta_{org}^{aq}\phi_{cl}$ is the dipolar potential drop across the compact inner layer, cl, and $\phi_2^{aq} = \phi_{OHP}^{aq} - \phi^{aq}$ and $\phi_2^{org} = \phi_{OHP}^{org} - \phi^{org}$ are the potential differences across the diffuse layers in the aqueous and organic phases respectively (OHP stands for outer Helmholtz plane).

The justification for this model is based on drop weight interfacial tension measurements at the water/nitrobenzene interface which showed that tetraethyl-, tetrapropyl- and tetrabutylammonium ions were not specifically adsorbed in the interfacial region. However, the authors conceded that this was not in fact the case for the tetrapentylammonium ion, thereby

suggesting that the compact inner layer model might not be completely valid.

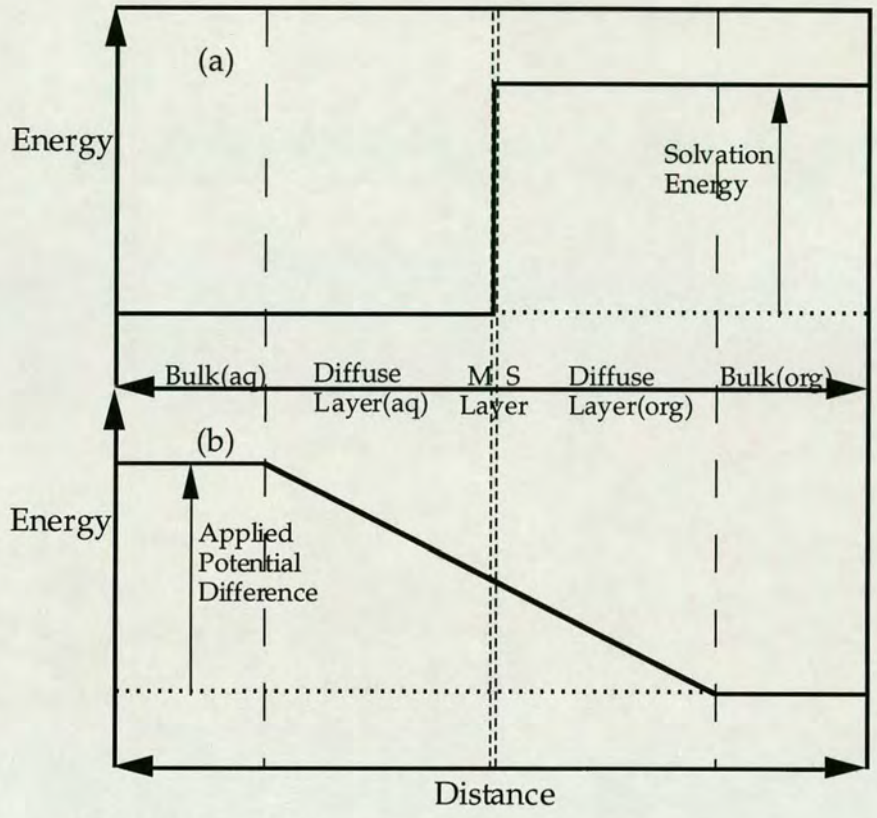

Figure 2.1 - Diagrams of the change in the Gibbs free energy of solvation (a), and the variation in the applied potential difference (b) across the interfacial region, expressed in energy terms (neglecting effects due to a Boltzmann distribution of ions) - for the mixed solvent layer model. The dashed vertical lines define different interfacial regions - MS represents 'mixed solvent'. Adapted from [39].

In 1985, Girault and Schiffrin [124] introduced the concept of the mixed solvent layer model to describe the ITIES. By measuring the potential of zero charge (pzc) for an electrolyte solution of water in contact with one of 1,2-DCE, they showed that the Galvani potential difference is not as large (in principle negligible) as would be expected for an interface composed of an orientated layer of solvent molecules. They proposed that the interface

could be considered to be a mixed solvent layer, a few molecular diameters in thickness (about 1 nm), separating the two diffuse layers. Essentially, the consequence of this model on the ion transfer mechanism is that all the difference in chemical potential is developed across the mixed solvent layer whilst the applied Galvani potential difference is effective across the whole interfacial region, including the two diffuse layers, with little variation across the mixed solvent region. This is illustrated in figure 2.1.

In a recent publication, Kharkats and Ulstrup [137] calculated analytically the electrostatic Gibbs free energy profile for transfer of an ion between two bulk phases separated by a sharp planar boundary. These authors demonstrated that the energy profile is more smoothed out than step-like. A similar result for the electrostatic Gibbs free energy profile was obtained by Benjamin [22], using a different approach. However, the majority of the change in the Gibbs free energy takes place over only three molecular diameters (most of which is distributed on the side of the interface which has the smaller dielectric constant). Therefore to a first approximation, when taking the interfacial region as a whole (including the two diffuse layers), the variation is like a step, in the same way that the applied potential difference is considered to be relatively small across the mixed solvent layer at the potential of zero charge [124].

Cheng *et al.* [97] have measured the capacitance of the ITIES for aqueous solutions of different alkali metal chloride salts in contact with a solution of 1,2-DCE containing tetrabutylammonium tetraphenylborate (TBATPB). The same experiments were also conducted for nitrobenzene containing TBATPB. Their results indicated that the alkali metal cations are specifically adsorbed in the order $Cs^+ > Rb^+ > K^+ > Na^+ > Li^+$ which corresponds to the

order of Gibbs free energies of ionic hydration. The authors proposed that the main origin of adsorption is interfacial ion-pairing between cations of one phase and anions of the other, and that the interface is most effectively represented by a mixed solvent layer - which is penetrated by different ions to varying extents depending on the Gibbs free energy of ionic hydration for a particular ion. Figure 2.2 shows a schematic illustration of the mixed solvent layer model.

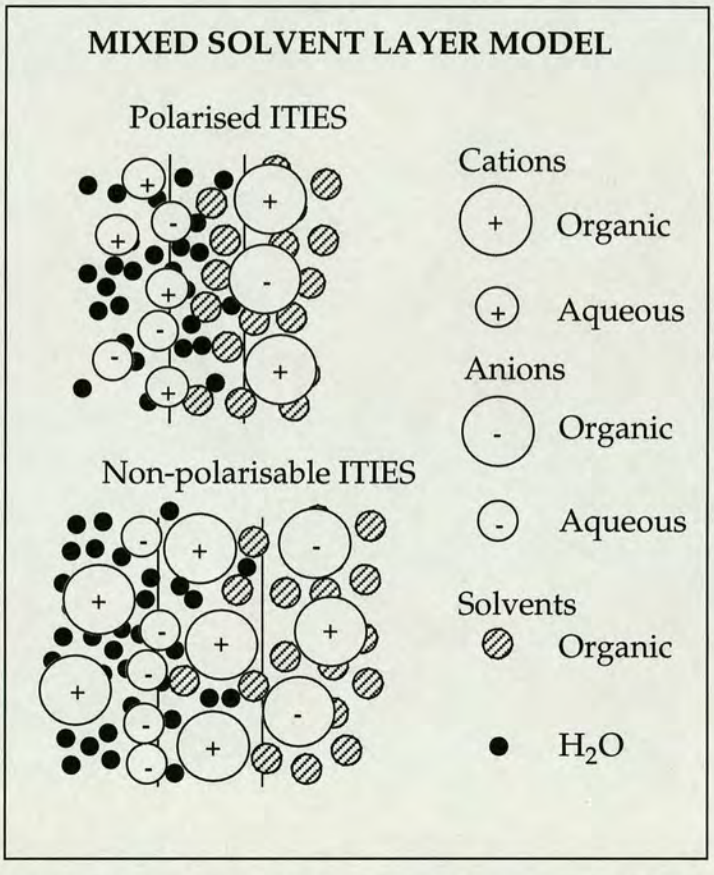

Figure 2.2 - Illustration of the mixed solvent layer model of the ITIES [124], showing the two general types of liquid/liquid interface.

2.1.4 Mass Transport to the ITIES

In a manner analogous to the metal electrode/electrolyte solution interface there are three methods by which mass transport to an ITIES can occur -

namely convection, migration and diffusion. This similarity has allowed the transposition to the ITIES of a great deal of the theory applicable to the metal electrode/electrolyte solution interface. In electrochemical experiments, the effects due to convection and migration are minimal provided that the solution is unstirred, the timescale of the experiment is short, and large concentrations of supporting electrolyte are used.

Charge transfer at the ITIES results in the formation of a concentration gradient in the vicinity of the interface. Movement of a species down such a concentration gradient may be described in terms of Fick's laws of diffusion. These describe the flux, J, of a substance, S and its concentration as a function of time, t, and position, x. The flux of S is the number of moles of S passing a given location x per unit time, per unit area. Fick's first law states that the flux is proportional to the concentration gradient, $\partial c_S / \partial x$:

$$-J_S(x,t) = D_S\left(\frac{\partial c_S(x,t)}{\partial x}\right) \qquad (2.1.18)$$

Using equation 2.1.18, Fick's second law of diffusion may be derived, which describes the rate of change in concentration of S, for a given value of x.

$$\frac{\partial c_S(x,t)}{\partial t} = D_S\left(\frac{\partial^2 c_S(x,t)}{\partial x^2}\right) \qquad (2.1.19)$$

2.1.5 Charge Transfer at the ITIES

As previously mentioned in chapter one, there are three general types of charge transfer which can occur at an ITIES - ion, assisted-ion, and electron transfer.

2.1.5.1 Ion Transfer

The theory of ion transfer kinetics at the ITIES is a very controversial subject. Much of the work to date has been interpreted only in terms of the compact inner layer (MVN) model of the ITIES proposed by Gavach *et al.* [123], and not the mixed solvent layer model as put forward by Girault and Schiffrin [124].

Proponents of the compact inner layer hypothesis hold that the ion transfer process can be described in terms of a three step mechanism as follows:

$$M^+(aq,b) \underset{\longleftarrow}{\overset{fast}{\longrightarrow}} M^+(aq,x_{OHP}) \underset{\longleftarrow}{\overset{rds}{\longrightarrow}} M^+(org,x_{OHP}) \underset{\longleftarrow}{\overset{fast}{\longrightarrow}} M^+(org,b) \qquad (2.1.20)$$

where b represents the bulk of the respective solvents and x_{OHP} is the plane of closest approach (outer Helmholtz plane). This mechanism was proposed by Buck [125].

Gurevich and Kharkats [131] used a stochastic approach to describe ion transfer across an ITIES, based on the Langevin equation of motion. The authors concluded that the ion transfer step required a certain activation energy and tried to illustrate the effect of the applied potential on the shape of the activation energy barrier.

In 1985, Girault and Schiffrin [126] proposed an alternative mechanism of ion transfer based on the mixed solvent layer model of the ITIES. The authors adopted the kinetic model of ionic mobility in liquids, put forward by Stearn and Eyring in 1940 [127], which is based on transition state theory. This model considers linear motion of an ion as a series of jumps between

successive equilibrium positions, and that passage from one to the next requires a corresponding activation energy. The rate determining step for transfer across the ITIES is assumed to take place in the mixed solvent layer. Girault and Schiffrin [126] state that this model is justified by virtue of the fact that the total difference of solvation energies between the two phases, given by the ionic standard Gibbs free energy of transfer, is rarely greater than that of the standard activation energy for diffusion for the systems for which ion transfer has been studied. Davies [128] studied the kinetics of diffusion of a salt across the water/nitrobenzene interface and showed that the 'Gibbs free activation energy of transfer' is very close to that of diffusion of the salt in both phases.

Despite the differences in opinion over the ion transfer mechanism, all of the protagonists agree that the rate determining step for the process occurs somewhere in the interfacial region, comprised of the two back-to-back diffuse layers separated by a narrow region of solvent molecules (mixed or otherwise). The transfer mechanism can be simplified to:

$$M^+(aq,b) \underset{k_b}{\overset{k_f}{\rightleftharpoons}} M^+(org,b) \qquad (2.1.21)$$

The kinetics of ion transfer is based on the first-order rate law

$$\frac{i}{zFA} = k_f c_{M^+}^{aq,s} - k_b c_{M^+}^{org,s} \qquad (2.1.22)$$

where the superscript s denotes surface concentration, i is the electrical current and A is the interfacial area. k_f and k_b are the apparent rate constants for ion

transfer from the aqueous to the organic phase and the reverse respectively, related to each other by the following equation [31]:

$$k_f = k_b \exp\left(\frac{zF\left(\Delta^{aq}_{org}\phi - \Delta^{aq}_{org}\phi^{o'}\right)}{RT}\right) \qquad (2.1.23)$$

where $\Delta^{aq}_{org}\phi^{o'}$, is the formal potential. The formal potential is related to the standard potential by the relation:

$$\Delta^{aq}_{org}\phi^{o'}_{M^+} = \Delta^{aq}_{org}\phi^{o}_{M^+} + \left(\frac{RT}{zF}\right)\ln\left(\frac{\gamma^{org}_{M^+}}{\gamma^{aq}_{M^+}}\right) \qquad (2.1.24)$$

where γ is the activity coefficient. Thus, the Galvani potential difference can be expressed in terms of the formal potential, as:

$$\Delta^{aq}_{org}\phi = \Delta^{aq}_{org}\phi^{o'}_{M^+} + \left(\frac{RT}{zF}\right)\ln\left(\frac{c^{org}_{M^+}}{c^{aq}_{M^+}}\right) \qquad (2.1.25)$$

The formal Gibbs free energy of transfer for the process, $\Delta G^{o',aq\rightarrow org}_{tr,M^+}$ is defined as:

$$\Delta^{aq}_{org}\phi^{o'}_{M^+} = \frac{\Delta G^{o',aq\rightarrow org}_{tr,M^+}}{zF} \qquad (2.1.26)$$

The apparent rate constant for ion transfer has been shown to be potential dependent [33,38,39] and to follow a Butler-Volmer relationship, therefore, in order to compare kinetic data obtained by different techniques it is usual to introduce the apparent standard rate constant, k^o, where:

$$k^o = k_f\left(\Delta^{aq}_{org}\phi = \Delta^{aq}_{org}\phi^{o'}_{M^+}\right) = k_b\left(\Delta^{aq}_{org}\phi = \Delta^{aq}_{org}\phi^{o'}_{M^+}\right) \qquad (2.1.27)$$

and the apparent charge transfer coefficient, α:

$$\alpha = \left(\frac{RT}{zF}\right)\left(\frac{\partial \ln k_f}{\partial \Delta_{org}^{aq}\phi}\right) \qquad (2.1.28)$$

This parameter has been shown to be relatively constant with applied potential [33,38,39]. Table 2.1 gives examples of reported values for the electrochemical parameters, k^o and α obtained by the method of a.c. impedance.

Most of the recent experimental investigations of the kinetics of ion transfer across the ITIES have involved the measurement of rate constants for a series of ions, such as the tetraalkylammonium and tetraalkylphosphonium ions [33,36]. These studies have usually been coupled with acquisition of the corresponding thermodynamic data by means of cyclic voltammetry.

Table 2.1 - Examples of kinetic parameters for ion transfer from water to nitrobenzene. Reference [37] T=25°C. Reference [33] T=20°C.

ion[33]	$10k^o(cms^{-1})$	α	ion[37]	$10k^o(cms^{-1})$	α
Me_4N^+	1.36	0.58	PF_6^-	1.63	0.50
Et_4N^+	0.90	0.64	ClO_4^-	1.08	0.53
Pr_4N^+	1.36	0.60	BF_4^-	1.73	0.44
Me_4P^+	1.48	0.55	SCN^-	0.91	0.45

Shao and Girault [38] carried out a series of investigations into the thermodynamics and kinetics of the transfer of acetylcholine, ACh^+, from the aqueous to the 1,2-DCE phase and the reverse, using the techniques of cyclic voltammetry (thermodynamics) and chronocoulometry (kinetics). In these

studies the viscosity of the aqueous phase was altered by the addition of sucrose to study the effect on the diffusion coefficient, the Gibbs free energy of transfer, and the apparent standard rate constant.

Their results showed that the apparent standard rate constant, k^o, is proportional to the fluidity, suggesting a direct proportionality between k^o and the diffusion coefficient of the transferring species. The diffusion coefficient of an ion is proportional to the fluidity (inverse of viscosity), obeying the limiting form of the Stokes-Einstein equation:

$$D^{aq}_{ACh^+} = kT / 6\pi r_s \eta \qquad (2.1.29)$$

where η is the viscosity, r_s is the Stokes radius, and k is the Boltzmann constant.

As with other direct current methods [31], they measured apparent rate constants of the order of 10^{-2} cms^{-1}, compared with the approximate figure of 0.1 cms^{-1}, for a.c. impedance measurements (table 2.1). In addition, the authors argued that the Gibbs free energy of hydration of acetylcholine decreases upon addition of sucrose, on the grounds that the slight variation in dielectric constant would only account for a small amount of the total potential shift observed.

Most recently, Wandlowski *et al.* [34] have studied the effect of temperature on the apparent standard rate constant for various ions and found that it increases with temperature, in step with the diffusion coefficient. These authors state that any ion transfer theory should account for the effects of viscous and dielectric friction, reorganisation of the ion-solvation shell, and

the long- and short-range forces which an ion experiences when crossing the interfacial region, including the electrical diffuse layers.

Kakiuchi [132], observed that the Nernst-Planck equation describing the variation in applied potential across an ITIES could be solved using a Goldman-type approximation - which has its origins in the realms of membrane science [133]. Furthermore, Kakiuchi *et al.* [134] showed that their experimental results - on the variation of the apparent standard rate constant with potential - could be best described in terms of this theory, and not Butler-Volmer kinetics. The authors conceded, however, that Butler-Volmer theory could be used to interpret their results to a first approximation.

Finally, in order to encompass the theory of ion transfer at the ITIES, it is necessary to broach the subject of 'electrical double-layer corrections'. One of the main areas of contention in mechanistic studies of ion transfer at the ITIES is the correction of the apparent rate constant for an 'electrical double-layer effect'. In the derivation of the Butler-Volmer equation the structure of the interfacial region is not considered. Thus, since this is based on the entire potential drop across the interfacial region being effective in driving the charge transfer process, it is important to correct for any inconsistencies. For metal electrode/electrolyte solution systems the grounds for the electrical double-layer correction are that: (1) the driving force for electron transfer is not the metal-solution Galvani potential difference but instead the potential difference between the metal and the outer Helmholtz plane; and (2) the concentration of the charged electroactive species at the outer Helmholtz plane is not the bulk value, but is given by the Boltzmann equation:

$$c^{OHP} = c^{b}\exp\left(-zF(\phi^{OHP} - \phi^{b}) / RT\right) \qquad (2.1.30)$$

This is the simplest approach to electrical double-layer correction and neglects effects due to specific adsorption of electroactive species at the electrode surface. This leads to the 'Frumkin' correction for electrode kinetics.

Implicit to the notion of double-layer corrections at the ITIES is the existence of a MVN type interface. Authors who believe in the MVN model support a Frumkin-type correction for kinetics across the ITIES [33], however, a Levich -type electrical double-layer correction has been proposed by Senda [135].

2.1.5.2 Assisted Ion Transfer

Assisted ion transfer reactions generally involve the transfer of an alkali, or alkaline earth, metal cation from the aqueous phase to the organic phase, by means of a neutral ionophore molecule, I:

$$M^{+}_{aq} + I \rightleftharpoons (MI)^{+}_{org} \qquad (2.1.31)$$

The homogeneous association constant for this reaction, K_a, is defined as:

$$K_a = \frac{a_{(MI)^+}}{a_{M^+} a_I} \qquad (2.1.32)$$

Consider the limiting case where the ion is in excess with respect to the ionophore. When the ionophore is insoluble in the aqueous phase, the mechanism of transfer is by interfacial complexation and dissociation (figure 1.1), and is analogous to electron transfer at a metal electrode/electrolyte solution interface. The Galvani potential difference is expressed by:

$$\Delta^{aq}_{org}\phi = \Delta^{aq}_{org}\phi^{o}_{(MI)^+} + \left(\frac{RT}{zF}\right)\ln\left(\frac{a^{org}_{MI^+}}{a^{org}_{I}}\right) = \Delta^{aq}_{org}\phi^{o}_{M^+} + \left(\frac{RT}{zF}\right)\ln\left(\frac{a^{org}_{M^+}}{a^{aq}_{M^+}}\right) \qquad (2.1.33)$$

which gives, by substitution of $\Delta^{aq}_{org}\phi^{o}_{(MI)^+}$:

$$\Delta^{aq}_{org}\phi = \Delta^{aq}_{org}\phi^{o}_{M^+} + \left(\frac{RT}{zF}\right)\ln\left(\frac{a^{org}_{MI^+}}{a^{org}_{I}}\right) - \left(\frac{RT}{zF}\right)\ln\left(\frac{a^{aq}_{M^+}a^{org}_{MI^+}}{a^{org}_{M^+}a^{org}_{I}}\right) \qquad (2.1.34)$$

Expressing equation 2.1.34 in terms of the formal potential yields:

$$\Delta^{aq}_{org}\phi = \Delta^{aq}_{org}\phi^{o'}_{M^+} + \left(\frac{RT}{zF}\right)\ln\left(\frac{c^{org}_{MI^+}}{c^{org}_{I}}\right) - \left(\frac{RT}{zF}\right)\ln\left(K^{org}_{c}c^{aq}_{M^+}\right) \qquad (2.1.35)$$

where K^{org}_{c} is the organic phase association constant expressed in terms of concentration.

2.1.5.3 Electron Transfer

Electron transfer across an ITIES may occur when there is an electron donor in one phase and an electron acceptor in the other (figure 2.3). Girault and Schiffrin [136] state that for electron transfer across an ITIES, the formation of an ion-pair type precursor is a prerequisite, which can be described by the following simplified mechanism:

$$O^{aq}_{1} + R^{org}_{2} \rightleftarrows O^{aq}_{1}\left|R^{org}_{2} \rightleftarrows R^{aq}_{1}\right|O^{org}_{2} \rightleftarrows R^{aq}_{1} + O^{org}_{2} \qquad (2.1.36)$$

Equation 2.1.36 omits the equilibria for relaxation of the precursor and successor complexes to a configuration appropriate for electron transfer.

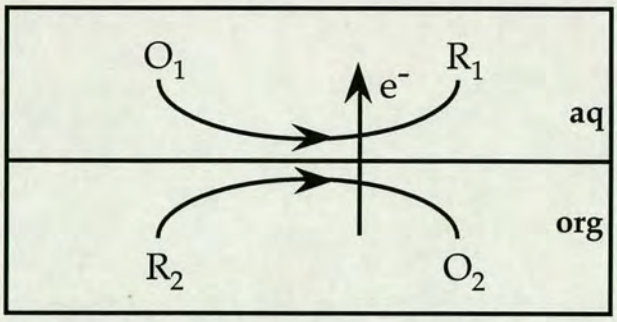

Figure 2.3 - Electron transfer at an ITIES.

In order to define the Galvani potential difference, a simplified form of equation 2.1.36 will be considered, where the equilibrium between precursor and successor complexes is ignored. The formal potential for electron transfer is defined in a manner analogous to that for ion transfer at an ITIES:

$$\Delta_{org}^{aq}\phi_{Redox}^{o'} = \frac{\Delta G_{Redox}^{o'(e^-,\, aq\rightarrow org)}}{zF} = -\frac{\Delta G_{Redox}^{o'(e^-,\, org\rightarrow aq)}}{zF} \qquad (2.1.37)$$

where $\Delta G_{Redox}^{o'(e^-,\, org\rightarrow aq)}$ is the formal Gibbs free energy of the reaction. This quantity is essentially the difference between the formal redox potentials of the two couples in the respective phases ($E_{O_2/R_2}^{o'} - E_{O_1/R_1}^{o'}$). The formal Gibbs free energy can be broken down to the following:

$$\Delta G_{Redox}^{o'} = (\mu_{O_2}^{o',org} - \mu_{R_2}^{o',org}) - (\mu_{O_1}^{o',aq} - \mu_{R_1}^{o',aq}) \qquad (2.1.38)$$

where $\mu^{o'}$ is the formal chemical potential.

The Galvani potential difference between the two phases is represented by:

$$\Delta_{org}^{aq}\phi = \Delta_{org}^{aq}\phi_{Redox}^{o'} - \left(\frac{RT}{zF}\right)\ln\left(\frac{c_{O_2}^{org}c_{R_1}^{aq}}{c_{O_1}^{aq}c_{R_2}^{org}}\right) \qquad (2.1.39)$$

The second term in equation 2.1.39 is unimportant when one of the two redox couples is present in excess.

As already mentioned in section 1.2.3, electron transfer reactions at the ITIES have been observed to be slower than ion transfer. This is thought to be related to (1) the distance between participating redox centres and (2) high reorganisation energies associated with electron transfer. As noted in section 1.1, Marcus [21] has recently derived expressions for the free energy of reorganisation associated with electron transfer at an ITIES.

2.2 Experimental Techniques

2.2.1 Cyclic Voltammetry

Cyclic voltammetry has become one of the most widely used techniques in electrochemistry, and is documented in all major electrochemical textbooks [138,139]. However, it was only when Samec *et al.* [10] successfully employed a four electrode potentiostat with iR drop compensation, to study reversible ion transfer, that it became one of the most powerful techniques for the study of charge transfer across the large, or planar, ITIES. Cyclic voltammetry is an example of a potential scan method, where the current is measured as a function of potential - which is ramped linearly, from an initial value to a switching potential, and then reversed to the initial value.

2.2.1.1 Polarisation Range

In section 2.1.2 it was explained that when very hydrophobic/-philic 1:1 electrolytes are dissolved in the organic and aqueous phases respectively, a

polarisation range or 'window' may be established within which no electrochemical processes occur. This window is limited by the transfer of specific 'supporting' or 'base' electrolyte ions. Much work has therefore been devoted to finding electrolytes which will allow the extension of the potential window of the ITIES, in order to increase the number of charge transfer reactions which may be observed.

There are two organic phase supporting electrolytes which are commonly used: tetrabutylammonium tetrakis(4-chlorophenyl)borate (TBA^+TPBCl^-), and bis(triphenylphosphoranylidene)ammonium, ($BTPPA^+$), $TPBCl^-$. These give potential windows of around 400 and 700 mV respectively when used with lithium chloride as the aqueous phase supporting electrolyte. Figure 2.4 illustrates a potential window for the latter case (cell 2.2.1), obtained by cyclic voltammetry, for the large (planar) ITIES.

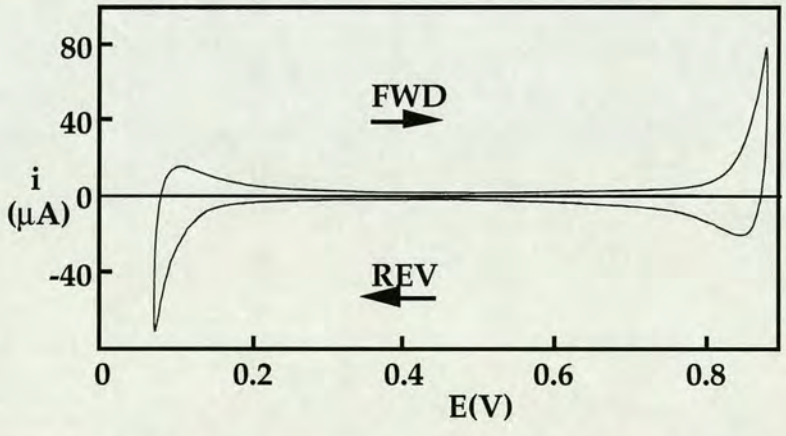

Figure 2.4 - Cyclic voltammogram for cell 2.2.1. Scan rate was 0.1 Vs^{-1}.

An increase in positive cell potential is associated with the potential of the aqueous phase becoming more positive with respect to the organic. Cell potential is arbitrary, and relates only to the system under study - this is

effective throughout the thesis. The convention for describing the system under study in figure 2.4 is analogous to cell 2.1.1, and is as follows:

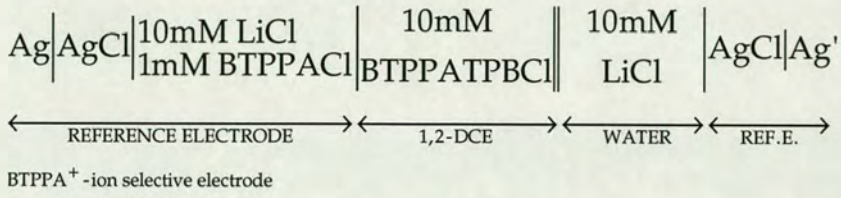

Cell 2.2.1

where REF.E. represents reference electrode. The potential window-limiting species for cell 2.2.1 are lithium, Li^+, on the forward scan and chloride, Cl^-, on the reverse scan (corresponding to transfer from the aqueous to the organic phase in each case).

2.2.1.2 Ion Transfer

In cyclic voltammetry, as an ion transfer potential is approached, the current is observed to rise corresponding to an increasing flux of ions across the interface. However, since the supply of ions from the bulk is governed by diffusion, the surface concentration at higher potentials begins to drop. Due to this depletion, the current begins to fall and the result is a peak-shaped current-potential characteristic. When the scan is reversed an inverted peak is obtained. Figure 2.5 shows such a response for cell 2.2.2.

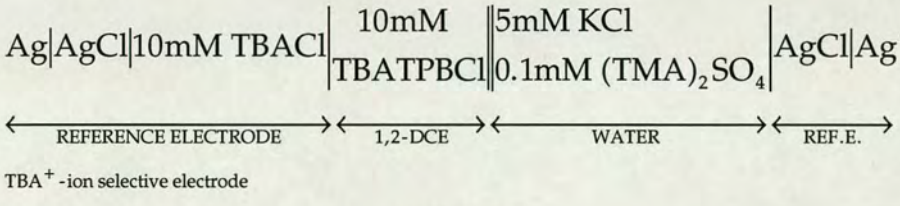

Cell 2.2.2

The forward peak current, i_{pf}, in figure 2.5 corresponds to the transfer of the tetramethylammonium ion, TMA^+, from the aqueous to the organic phase, and vice versa for the reverse peak current, i_{pr}.

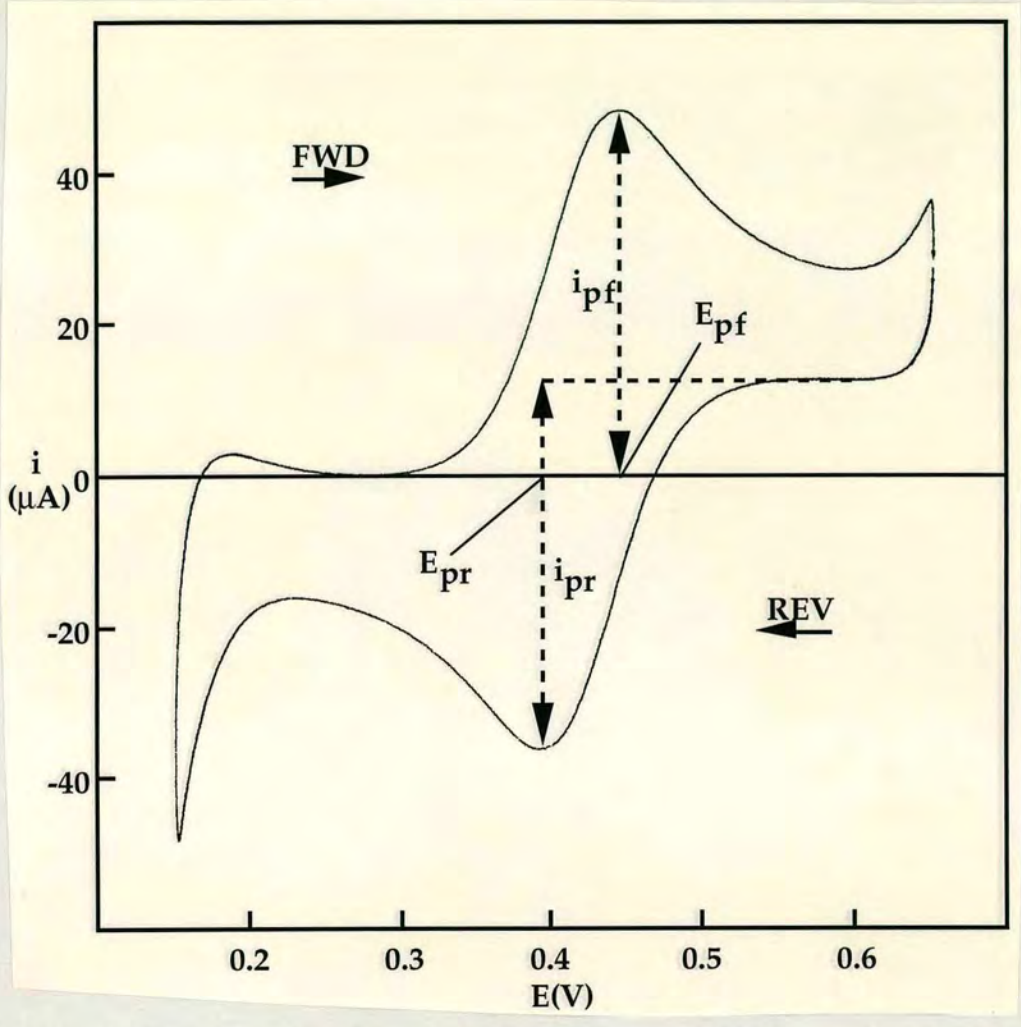

Figure 2.5 - Cyclic voltammogram for the transfer of TMA^+ across the water/1,2-DCE interface (cell 2.2.2). i_{pf} is the forward peak current, and E_{pf} and E_{pr} are the forward and reverse peak potentials respectively. The scan rate was 0.1 Vs^{-1}.

Here the forward scan is limited by the transfer of potassium ion, K^+, from the aqueous to the organic phase, and the reverse scan is limited by the transfer of TBA^+ from the organic to the aqueous phase.

The equations for mass transport to an ITIES are analogous to those for mass transport to a solid electrode. Therefore, for the large, or planar, ITIES, the Randles-Sevcik equation holds [139]:

$$i_p = 0.4463 z_S F A c_S^b \left(\frac{z_S F}{RT}\right)^{1/2} D_S^{1/2} \nu^{1/2} \qquad (2.2.1)$$

where A corresponds to the interfacial area in cm^2, ν is the scan rate in Vs^{-1}, c_S^b is the bulk concentration of the species of interest in $molcm^{-3}$, i_p is the peak current in amperes, and D_S is the diffusion coefficient of the species in units of cm^2s^{-1}. Thus, from a plot of peak current versus the square root of the scan rate it is possible to calculate the diffusion coefficient of the transferring ion.

For reversible, single charge transfer the following conditions apply:

(1) - the forward and reverse peak potentials, E_{pf} and E_{pr}, must be independent of scan rate

(2) - $E_{pf} - E_{pr}$ (ΔE_p) $\cong$ 59 mV.

(3) - plotting i_p versus $\nu^{1/2}$ yields a straight line which passes through the origin.

An important application of cyclic voltammetry is the determination of diffusion coefficients, and half-wave transfer potentials - from which the formal Gibbs energy of transfer for an ion can be evaluated. By direct transposition from the case for reversible one-electron transfer at a metal electrode/electrolyte solution interface, the half-wave potential for reversible, or diffusion-controlled, ion transfer may be expressed in terms of the formal potential as:

$$\Delta^{aq}_{org}\phi^{1/2}_{M^+} = \Delta^{aq}_{org}\phi^{o'}_{M^+} + \left(\frac{RT}{2zF}\right)\ln\left(\frac{D^{aq}_{M^+}}{D^{org}_{M^+}}\right) \qquad (2.2.2)$$

The ratio of the diffusion coefficients of the ion in the respective phases can be approximated to the inverse ratio of the solvent viscosities according to Walden's rule [139]:

$$\left(\frac{\eta^{org}}{\eta^{aq}}\right) = \left(\frac{D^{aq}_{M^+}}{D^{org}_{M^+}}\right) \qquad (2.2.3)$$

Therefore, the inverse ratio of the solvent viscosities must be taken into account when evaluating the formal potential from the measured half-wave potential.

From equation 2.1.35, the half-wave potential for a TIC/TID type, assisted ion transfer reaction can be written as:

$$\Delta^{aq}_{org}\phi^{1/2}_{MI^+} = \Delta^{aq}_{org}\phi^{o'}_{M^+} + \left(\frac{RT}{2zF}\right)\ln\left(\frac{D^{org}_{I}}{D^{org}_{MI^+}}\right) - \left(\frac{RT}{zF}\right)\ln\left(K_c^{org}c^{aq}_{M^+}\right) \qquad (2.2.4)$$

Thus, for a TIC/TID transfer mechanism the organic phase association constant may be evaluated by measurement of the reversible half-wave potential, assuming that the diffusion coefficient of the ionophore and the ion-ionophore complex are equivalent, and the formal potential for simple ion transfer is known.

In assisted ion transfer reactions the stoichiometry of the complexation process may influence the peak-to-peak separation, ΔE_p, as demonstrated by

Homolka *et al.* [140]. For 1:1 (cation to ligand) stoichiometry, ΔE_p is 59 mV. However, for the 1:2 and 1:3 cases, ΔE_p is 87 and 112 mV respectively.

2.2.2 Steady-State Techniques at the Micro-ITIES

The micro-ITIES has already been briefly introduced in section 1.5. In a similar fashion to solid microelectrodes, the attractions of using this type of interface as opposed to the large ITIES are the enhanced mass transport regime, and the benefits due to reduced diffuse layer capacitance and iR drop.

2.2.2.1 The Steady-State Condition

At a steady-state, the concentration profiles of both reactants and products of a given electrochemical reaction are unchanging in the vicinity of the electrode surface. This condition is approached as a limit and is never reached. Experimentally, however, it is possible to attain states which are indistinguishable from the steady-state. To facilitate a steady-state, the flux of reactants to the electrode surface must be maintained. Generally, this is achieved by either diffusive transport (microelectrodes) or forced convection (conventional sized electrodes - the rotating disc).

2.2.2.2 Chronoamperometry

In a chronoamperometric experiment, the electrochemical system of interest is subjected to a potential step, or pulse, from a potential where no electrochemical process occurs to one at which the rate of reaction is

controlled by diffusion of reactants to the interface. The current response of the system to the potential perturbation can be obtained by solving Fick's second law of diffusion, in spherical co-ordinates, with the necessary boundary conditions. For a microhemisphere embedded in an infinite insulating plane the current is given by [106]:

$$i = \left(\frac{zFAD_S^{1/2}c_S^b}{\pi^{1/2}t^{1/2}} \right) + 2\pi zFD_S c_S^b r_h \qquad (2.2.5)$$

where r_h is the radius of the hemisphere, and A is the interfacial area.

At short times (t), the first term in the equation dominates and Cottrell behaviour is observed, corresponding to linear diffusion (the first term is the Cottrell equation [139]). At longer times, however, the first term becomes negligible and the current approaches the steady-state value, given by the second term. The equation for the steady-state current at an inlaid microdisc was first established by Saito [141] in 1968, and is given by:

$$i_{ss} = 4zFD_S c_S^b r_d \qquad (2.2.6)$$

where r_d is the microdisc radius.

2.2.2.3 Steady-State Voltammetry

The derivative of the concentration with respect to time is zero under a steady-state, therefore, the concentration gradient may be approximated by the equation [106]:

$$\frac{i}{zFA} = \left(\frac{D_S[c_S^b - c_S^s]}{\delta}\right) \tag{2.2.7}$$

where c_S^s is the surface concentration of the reacting species, S. This is known as the Nernst approximation, where δ is the thickness of the diffusion layer - assumed to be constant. However, since the surface concentration of the reacting species is so small at the steady-state, equation 2.2.7 can be rearranged, for a microhemisphere, to:

$$\frac{i}{zFA} = \left(\frac{D_S c_S^b}{\delta}\right) = \left(\frac{D_S c_S^b}{r_h}\right) \tag{2.2.8}$$

Thus, the thickness of the diffusion layer can be approximated to $\delta = r_h$. For a microdisc, the diffusion layer thickness is equal to $(\pi/4)r_d$ [106].

Consider a simple, reversible ion transfer reaction at a hemispherical micro-ITIES. The ratio of the surface concentrations of the ion, M^+, is related to the Galvani potential difference (rearranging equation 2.1.25) by the equation:

$$\left(\frac{c_{M^+}^{org,s}}{c_{M^+}^{aq,s}}\right) = \exp\left[\left(\frac{zF}{RT}\right)\left(\Delta_{org}^{aq}\phi - \Delta_{org}^{aq}\phi_{M^+}^{o'}\right)\right] \tag{2.2.9}$$

Taking the case of ion transfer from the aqueous to the organic phase, the surface concentrations of M^+ may now be expressed in terms of equation 2.2.7, and the diffusion layer thickness:

$$c_{M^+}^{aq,s} = c_{M^+}^{aq,b} - \left(\frac{i}{2\pi zFD_{M^+}^{aq} r_h}\right) \tag{2.2.10}$$

and

$$c_{M^+}^{org,s} = \left(\frac{i}{2\pi z F D_{M^+}^{org} r_h} \right) + c_{M^+}^{org,b} \qquad (2.2.11)$$

However, the bulk concentration of the metal ion in the organic phase is normally zero, therefore it may be neglected in equation 2.2.11. Using the equation for the steady-state current at a microhemisphere (from equation 2.2.5), $c_{M^+}^{aq,b}$ can be written as

$$c_{M^+}^{aq,b} = \left(\frac{i_{ss}}{2\pi z F D_{M^+}^{aq} r_h} \right) \qquad (2.2.12)$$

Now equation 2.2.9 may be re-written as:

$$\left(\frac{i}{i_{ss} - i} \right) = \left(\frac{D_{M^+}^{org}}{D_{M^+}^{aq}} \right) \exp\left[\left(\frac{zF}{RT} \right) \left(\Delta_{org}^{aq}\phi - \Delta_{org}^{aq}\phi_{M^+}^{o'} \right) \right] \qquad (2.2.13)$$

This is a general expression applicable to any geometry of micro-ITIES which attains a steady-state, and is similar in form to the expression derived by Bond *et al.* [142] for an inlaid disc microelectrode. The half-wave potential is dependent on (D^{aq}/D^{org}), and not $(D^{aq}/D^{org})^{1/2}$ as in conventional cyclic voltammetry.

2.2.2.4 Kinetics from Steady-State Voltammograms

Oldham and co-workers [142,143] have been instrumental in promoting the use of steady-state voltammetry for the determination of kinetic parameters for electrochemical processes. Electrochemical systems may be classified according to whether the charge transfer step is (1) reversible (2) quasi-

reversible, or (3) irreversible. In steady-state experiments the characteristic length, λ, which is dependent on the dimensions of the electrode, and the quotient D_S/k^o are the parameters of interest:

$$D_S/k^o << \lambda: \quad \text{reversible} \tag{2.2.14}$$

$$D_S/k^o \cong \lambda: \quad \text{quasi-reversible} \tag{2.2.15}$$

$$D_S/k^o >> \lambda: \quad \text{irreversible} \tag{2.2.16}$$

Oldham *et al.* [143] observe that the characteristic length, λ, and the ratio of the diffusion coefficient to the apparent standard rate constant, k^o, can be related by the dimensionless quantity, κ^o:

$$\kappa^o = (\lambda k^o/D_S) \tag{2.2.17}$$

$$= (r_h k^o/D_S) \quad \text{- hemisphere} \tag{2.2.18}$$

$$= (\pi r_d k^o/(4D_S)) \quad \text{- disc} \tag{2.2.19}$$

These authors go on to define limits of confidence for κ^o:

$$\kappa^o > 40: \quad \text{effectively reversible} \tag{2.2.20}$$

$$0.2 \leq \kappa^o \leq 20: \quad \text{usefully quasi-reversible} \tag{2.2.21}$$

$$\kappa^o < 0.1: \quad \text{effectively irreversible} \tag{2.2.22}$$

on the grounds that full reversibility and total irreversibility are conditions which are approached as limits. Thus, for example, taking a D_S value of 1×10^{-5} cm^2s^{-1}, and a microdisc of radius 5 μm, a reversible system indicates that k^o must be greater than 1 cms^{-1}.

2.2.2.5 Quasi-Reversible Kinetics

Consider once more a simple ion transfer process. In the case where the reaction is quasi-reversible, the current density, I, (current/electrode area) depends on the rate of the forward and backward reactions:

$$I = zF(k_f c_{M^+}^{aq,s} - k_b c_{M^+}^{org,s}) \tag{2.2.23}$$

where I is the current density. The current density can also be expressed as:

$$I = \left(\frac{zFD_{M^+}^{aq}[c_{M^+}^{aq,b} - c_{M^+}^{aq,s}]}{r_h} \right) = \left(\frac{zFD_{M^+}^{org}[c_{M^+}^{org,s} - c_{M^+}^{org,b}]}{r_h} \right) \tag{2.2.24}$$

By equating the ionic fluxes at the interface, and substituting equations 2.2.10 and 2.2.11 into equation 2.2.23, the following relationship can be derived:

$$\frac{1}{I} = \frac{1}{zF(k_f c_{M^+}^{aq,b} - k_b c_{M^+}^{org,b})} + \frac{(k_f D_{M^+}^{org} + k_b D_{M^+}^{aq})r_h}{zF(k_f c_{M^+}^{aq,b} - k_b c_{M^+}^{org,b})D_{M^+}^{aq} D_{M^+}^{org}} \tag{2.2.25}$$

As before, the bulk concentration of the ion in the organic phase is usually zero and may be neglected, therefore equation 2.2.25 reduces to:

$$\frac{1}{I} = \frac{1}{zFk_f c_{M^+}^{aq,b}} + \frac{(k_f D_{M^+}^{org} + k_b D_{M^+}^{aq})r_h}{zFk_f c_{M^+}^{aq,b} D_{M^+}^{aq} D_{M^+}^{org}} \tag{2.2.26}$$

Thus, from a plot of the reciprocal of the current density at a given potential versus differing microhemisphere radii, it should be possible to evaluate the forward apparent rate constant, k_f, and to use this value to evaluate the

backward apparent rate constant, k_b, from the slope (assuming that one of the diffusion coefficients is known).

2.2.2.6 Irreversible Kinetics

In the case of irreversible ion transfer, the rate of the backward reaction is ignored and equation 2.2.26 becomes:

$$\frac{1}{I} = \frac{1}{zFk_f c_{M^+}^{aq,b}} + \frac{r_h}{zFc_{M^+}^{aq,b} D_{M^+}^{aq}} \qquad (2.2.27)$$

2.2.3 A.C. impedance of the ITIES

2.2.3.1 Introduction

In a typical a.c. impedance experiment, a d.c. equilibrium potential is applied to the electrochemical system of interest. Perturbation of the system by the superimposition of a low-amplitude sine wave voltage produces a corresponding low-amplitude sine wave current response. This response is then interpreted in terms of the physical and chemical nature of the electrochemical system [144].

The theory of a.c. impedance employs the use of phasors (rotating vectors) to describe the voltage drop, **E**, across an electrochemical cell and the resulting current, **i**. By virtue of Ohm's law:

$$\mathbf{E} = \mathbf{i}Z \qquad (2.2.28)$$

where Z is the electrochemical impedance. Z may be described using a complex plane, or Argand, diagram (figure 2.7) by the relationship:

$$Z = |Z|e^{j\theta} = Z' - jZ'' \qquad (2.2.29)$$

where Z' and Z'' are the 'real' and 'imaginary' parts of the impedance respectively, j is a complex number (equal to $(-1)^{1/2}$), and θ is the phase angle between the two phasors, **E** and **i** (which remains constant throughout the experiment). |Z| is the magnitude of the impedance, given by:

$$|Z| = \left[(Z')^2 + (Z'')^2\right]^{1/2} \qquad (2.2.30)$$

The relationship between the phase angle and the real and imaginary impedance is:

$$\tan\theta = \frac{Z''}{Z'} \qquad (2.2.31)$$

On a complex plane diagram, the real part of the impedance is simply the resistance, R, and the imaginary part is given by $1/\omega C$ - where C is the capacitance and ω is the angular frequency.

2.2.3.2 Equivalent Circuits

For the purpose of a.c. impedance analysis of ion transfer, the ITIES may be represented in terms of an electrical equivalent circuit, as shown in figure 2.6 [32]. This circuit is composed of three parameters in parallel - the interfacial capacitance, C_{int}, the faradaic impedance due to the transfer of base electrolyte ions, Z_b, and the faradaic impedance due to ion transfer Z_{IT}. This

is in series with the solution resistance, R_s. Thus, the total current through the interface is the sum of the contributions from the faradaic processes, i_f (equal to $i_{f(IT)} + i_{f(b)}$), and the charging of the interface, i_c.

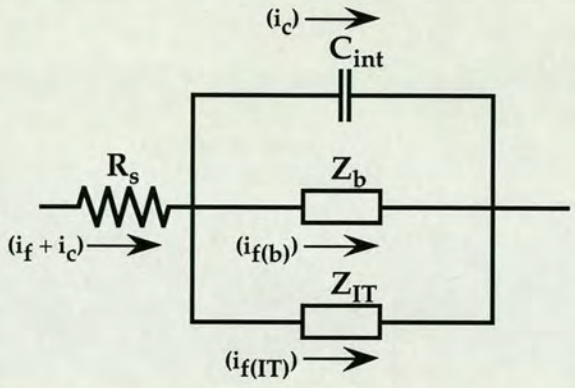

Figure 2.6 - Electrical equivalent circuit for the ITIES.

The assumptions are made that; (1) the transport of the ion, M^+, in solution is governed by linear, semi-infinite diffusion (only applicable to the large ITIES) and (2) the transfer of M^+, across the ITIES is controlled by a first-order rate law. The faradaic impedance Z_{IT} may then be written as the charge transfer resistance, R_{ct}, plus the Warburg impedance, Z_W:

$$Z_{IT} = (R_{ct} + Z_W) \tag{2.2.32}$$

The charge transfer resistance is given by:

$$R_{ct} = \frac{RT}{z^2F^2Ak^{o}c^{aq,b}_{M^+}} \tag{2.2.33}$$

since the bulk concentration of the metal ion in the organic phase is usually zero. The magnitude of the Warburg impedance, Z_W is:

$$|Z_W| = \sigma(2/\omega)^{1/2} \qquad (2.2.34)$$

and the parameter σ is defined as:

$$\sigma = \frac{RT}{z^2F^2A2^{1/2}(D^{aq}_{M^+})^{1/2}c^{aq,b}_{M^+}} \qquad (2.2.35)$$

for the case where the bulk concentration of the metal ion in the organic phase is zero.

The above equations are equally applicable to assisted ion transfer reactions of the TIC/TID type where the ionophore remains in the organic phase and the concentration of the metal ion in the aqueous phase is in great excess of the organic phase ionophore. In that case $c^{aq,b}_{M^+}$ in equation 2.2.33 is replaced by $c^{org,b}_I$, and $(D^{aq}_{M^+})^{1/2}c^{aq,b}_{M^+}$ in equation 2.2.35 is replaced by $(D^{org}_I)^{1/2}c^{org,b}_I$.

The faradaic admittance, Y_F, can be calculated from:

$$Y_F = Y_{IT} - Y_b \qquad (2.2.36)$$

where Y_{IT} and Y_b are the total admittances, corrected for the solution resistance R_s, in the presence and absence of the ion of interest, M^+. The real and imaginary components of the admittance terms are given by:

$$Y'_x = \frac{Z'_x - R_s}{(Z'_x - R_s)^2 + (Z''_x)^2} \qquad (2.2.37)$$

and

$$Y''_x = \frac{Z''_x}{(Z'_x - R_s)^2 + (Z''_x)^2} \qquad (2.2.38)$$

(x = IT, b).

Figure 2.7 shows an example of a complex plane diagram showing the two types of behaviour exhibited by the Randles equivalent circuit [145]. This can be obtained from figure 2.6 if the base electrolyte contribution to the faradaic impedance is ignored, and the faradaic impedance for ion transfer is separated into the charge transfer and Warburg parts.

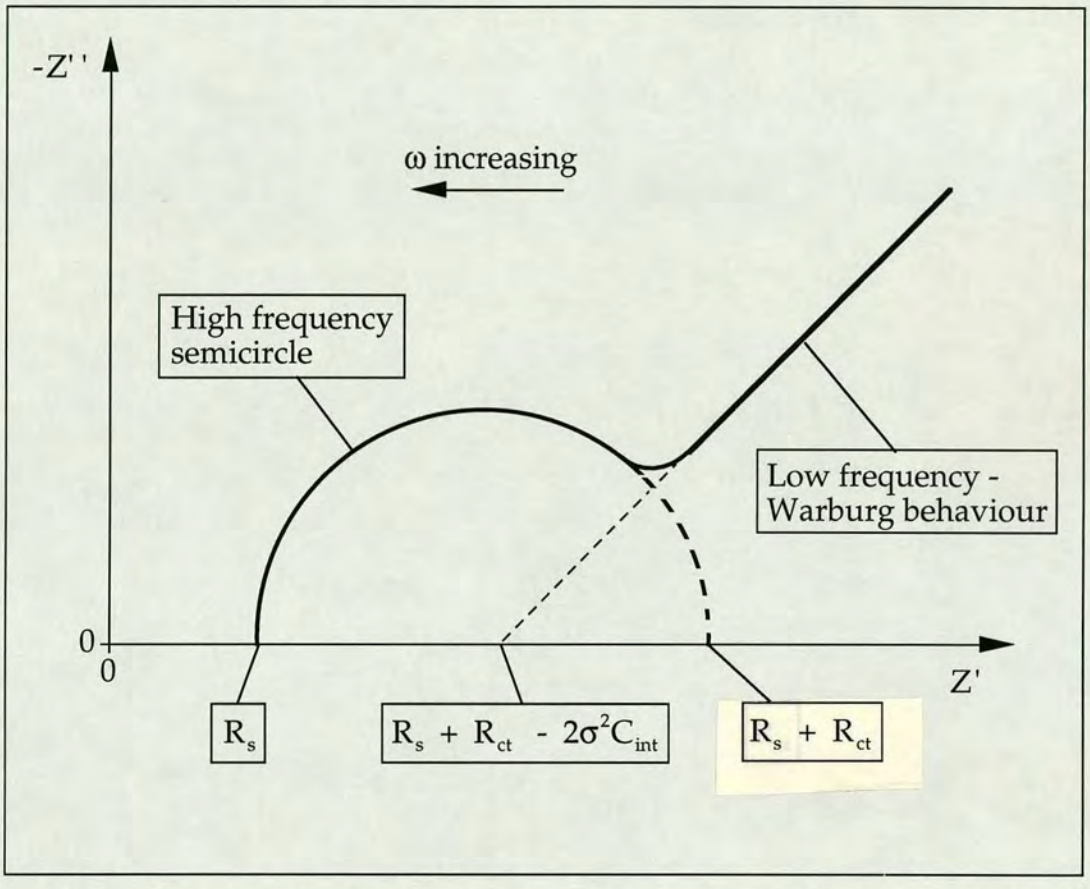

Figure 2.7 - Impedance behaviour expected for the Randles equivalent circuit.

2.2.3.3 Low-Frequency Limit

As the angular frequency, ω, tends to zero, the equations for the real and imaginary parts of the impedance, Z, approach the limiting forms [139]:

$$Z' = R_s + R_{ct} + \sigma\omega^{-1/2} \qquad (2.2.39)$$

and $$Z'' = \sigma\omega^{-1/2} + 2\sigma^2 C_{int} \quad (2.2.40)$$

Elimination of ω from equations 2.2.39 and 2.2.40 gives:

$$Z'' = Z' - R_s - R_{ct} + 2\sigma^2 C_{int} \quad (2.2.41)$$

Therefore, a plot of Z'' versus Z' should be linear with a slope of unity. The extrapolated plot intersects the real axis at $R_s + R_{ct} - 2\sigma^2 C_{int}$. The frequency dependence in equations 2.2.39 and 2.2.40 comes from Warburg impedance terms, therefore a linear relationship between Z'' and Z' is indicative of a linear diffusion controlled process. If the frequency is increased, the charge transfer resistance, R_{ct}, and the diffuse-layer capacitance, C_{int}, become significant and there is deviation from equation 2.2.41.

2.2.3.4 High-Frequency Limit

At very high frequencies the Warburg impedance becomes unimportant in relation to R_{ct}, and the components of the impedance are related by the equation [139]:

$$(Z' - R_s - (R_{ct} / 2))^2 + Z''^2 = (R_{ct} / 2)^2 \quad (2.2.42)$$

From equation 2.2.42, it is apparent that a plot of Z'' versus Z' takes the form of a semi-circle, centred at $Z' = R_s + (R_{ct} / 2)$ and $Z'' = 0$, with a radius of $(R_{ct} / 2)$. In this case the imaginary component of the impedance comes only from C_{int}. At high frequencies, Z'' falls to zero because it offers no impedance. All of the current passed is therefore charging current, and

the only impedance observed is the solution resistance, R_s. As the frequency is decreased, the finite impedance of C_{int} causes the value of Z'' to increase. At very low frequencies, C_{int} offers a high impedance, therefore the current is passed through R_s and R_{ct} - this causes Z'' to fall once more. In real electrochemical systems however, there is usually a departure from this behaviour at low frequencies due to the Warburg impedance and the result is a complex plane plot of mixed behaviour (figure 2.7).

2.2.3.5 Impedance Analysis of the Micro-ITIES

Recently, Bruce *et al.* [146] demonstrated that the use of ultramicroelectrodes, in conjunction with a.c. impedance, can be an important tool for the study of electron transfer kinetics. These authors state that it is possible to obtain apparent standard rate constant values in excess of 10 cms^{-1} despite encountering impedances approaching 100 MΩ.

The solution to the impedance problem at an ultramicrodisc electrode has been presented by Fleischmann and Pons [147]. This involves the replacement of the Warburg impedance by a generalised diffusional impedance in the equivalent circuit. This theory was experimentally verified by L.M.Abrantes *et al.* [148]. Bruce *et al.* [146] favoured an equivalent circuit in which the Warburg impedance is in parallel with a non-linear impedance, R_{nl}, which may be approximated to:

$$R_{nl} \cong \frac{0.54RT}{z^2F^2D_S r_d c_S^b} \qquad (2.2.43)$$

for a microdisc. These authors show that the two models are quite close to a first approximation. Figure 2.8 shows simulated complex plane impedance

plots for the cases where k^o is 0.1 and 0.01 cms^{-1}, D_S is 1 x $10^{-5}cm^2s^{-1}$, r_d is 5 x 10^{-4} cm, c_S^b is 0.5 x 10^{-6} $molcm^{-3}$, and R_s is negligible, using a model identical to that used by Bruce *et al.* [146]. These plots correspond to the frequency range 25 kHz to 3 Hz.

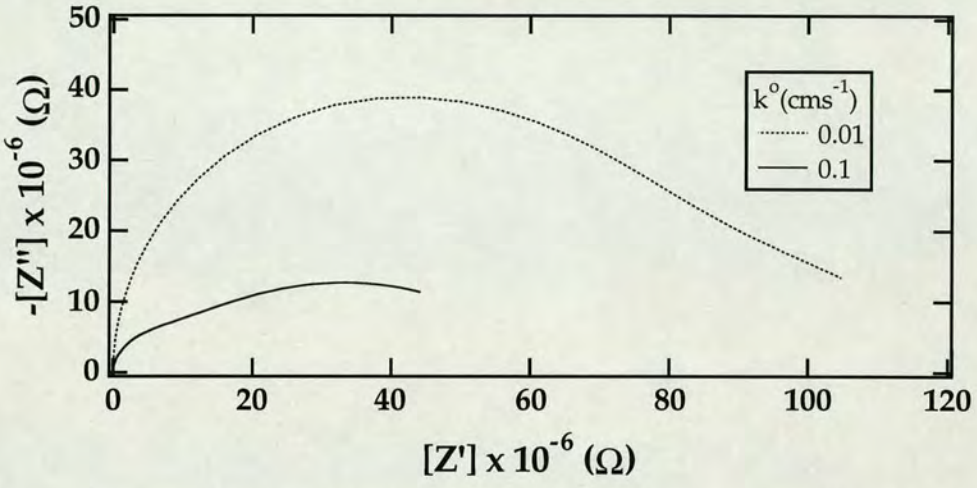

Figure 2.8 - Predicted impedance plots obtained using a model identical to that of Bruce et al. [146], for the frequency range 25 kHz to 3 Hz, corresponding to k^o values of 0.1 and 0.01 cms^{-1}. Conditions as stated in the text.

The complex plane behaviour for a microelectrode resembles classical RC behaviour at low frequencies as well as at high frequencies. When R_{ct} is high (k^o is small), the high-frequency semi-circle dominates the impedance plot. In contrast, if R_{ct} is low (k^o is large), the flattened semi-circle due to the diffusional impedance becomes more important.

Chapter Three

METHODOLOGY OF THE ITIES

3.1 The Large ITIES

The type of cell used to study the large ITIES was as shown in figure 3.1. This was a four-electrode system, where the interface was polarised by means of the two reference electrodes and the current was measured via the two counter electrodes. The centre section and side arms were cylindrical, and the surface area of the interface was about 1 cm^2 (see experimental chapters for precise values). The interface was positioned between the two luggin capillaries to facilitate minimisation of the iR drop. Due to surface tension effects, the interface was slightly curved.

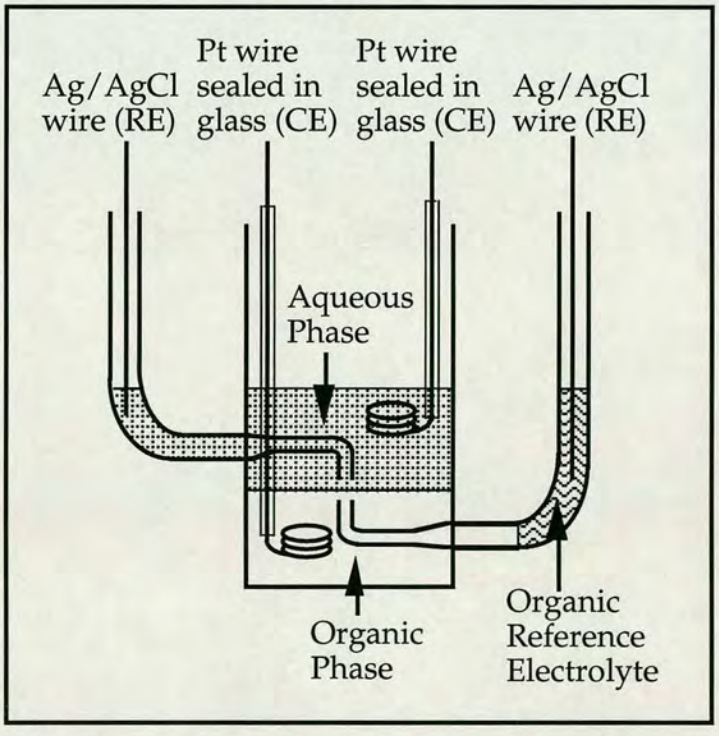

Figure 3.1 - Cell design for experiments at the large ITIES.

For the cyclic voltammetry experiments, the potential difference between the aqueous and organic phases was applied using a PPR1 waveform generator (Hi-Tek, U.K.), via a four-electrode potentiostat - consisting of a regular three-electrode potentiostat (Southampton University) and a 'home-made' zerostat. The potential and current output signals were measured on a X-Y recorder (Advanced Bryans Instruments, series 60000). The reference and counter electrodes associated with the organic and aqueous phases were connected to the potentiostat and zerostat respectively. The potential waveform was applied to the three electrode potentiostat, and the zerostat was used to compensate for the iR drop in the system, by feedback of a portion of the output signal back into the potentiostat.

In all of the experiments, the electrochemical cell and the four-electrode potentiostat were housed in an earthed Faraday cage to minimise background electrical noise.

3.2 The Micro-ITIES: Fabrication, Characterisation and Cell Design

3.2.1 Micropipette

Micropipettes were made from borosilicate glass capillaries (length 10 cm, outer diameter (o.d.) 1.5 mm, inner diameter (i.d) 1.17 mm (thin glass), and o.d. 1.5 mm, i.d. 0.86 mm (thick glass) from Science Products (Germany), and were pulled with a 'Flaming-Brown' type puller [149] (model P87, Sutter Instrument Co., U.S.A.). The pulling sequence was computer controlled, with the glass being clamped horizontally between two pulleys, and heated in the middle by means of a 3 mm cubic element open on two opposing sides (through which the glass was inserted). Once the melting glass reached a

certain velocity, monitored by the computer, the heating stopped and the glass was cooled automatically using an air pressure unit to prevent further melting. A series of such steps was required to form a micropipette, beginning with an element temperature equal to that at which the glass first melted (this was determined independently with a heat ramp test on a separate glass capillary). In each subsequent step the temperature was reduced by a fixed amount (20°C for thin glass, 10 or 20°C for thick glass). In this way it was possible to fabricate pipettes having internal tip diameters of between 5 and 38 μm (thin glass), and 2 μm or less (thick glass), which had very flat tips.

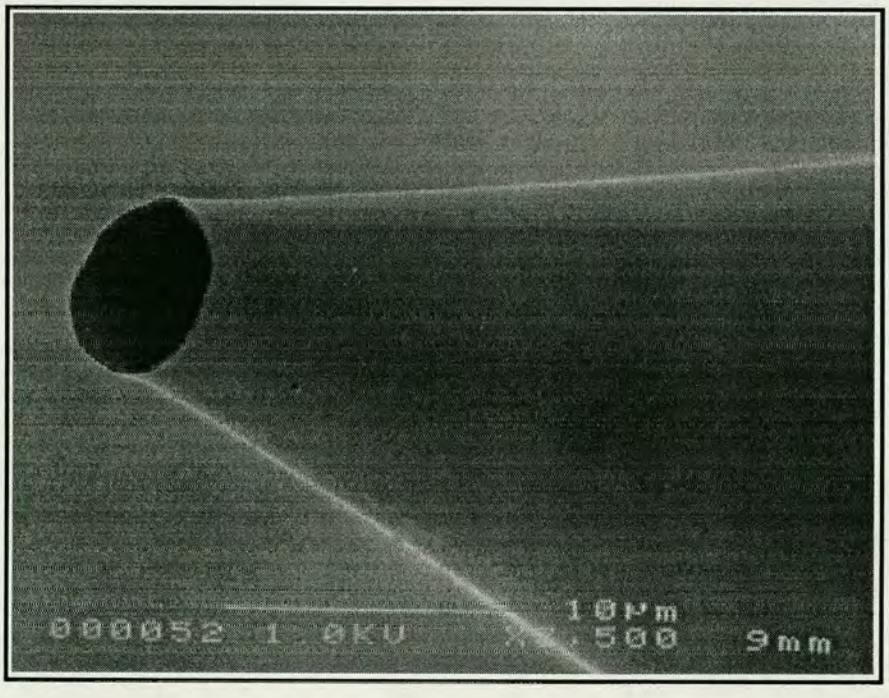

Figure 3.2 - S.E.M. picture of a 6 μm diameter (internal) pipette, magnified 3500 times using a JEOL JSM-6300F S.E.M. Visible on the upper inside right of the tip is the end of the fine capillary, which allowed back-filling of the pipette.

Figure 3.2 shows a scanning electron micrograph of a pipette tip (thin glass) with an internal diameter of 6 μm taken using a JEOL JSM-6300F scanning

electron microscope (S.E.M.). The advantage of this microscope was that it did not require gold coating of the pipette to be examined (unlike other materials - polyester films, for example). Tip diameters were first established using an Olympus IMT-2 microscope, fitted with a measuring graticle. The error on these measurements was estimated to be ± 0.5 μm (thin glass only), using scanning electron microscopy. Due to the large number of micropipettes being used it was not deemed practical, nor indeed was it possible, to analyse each one by S.E.M.

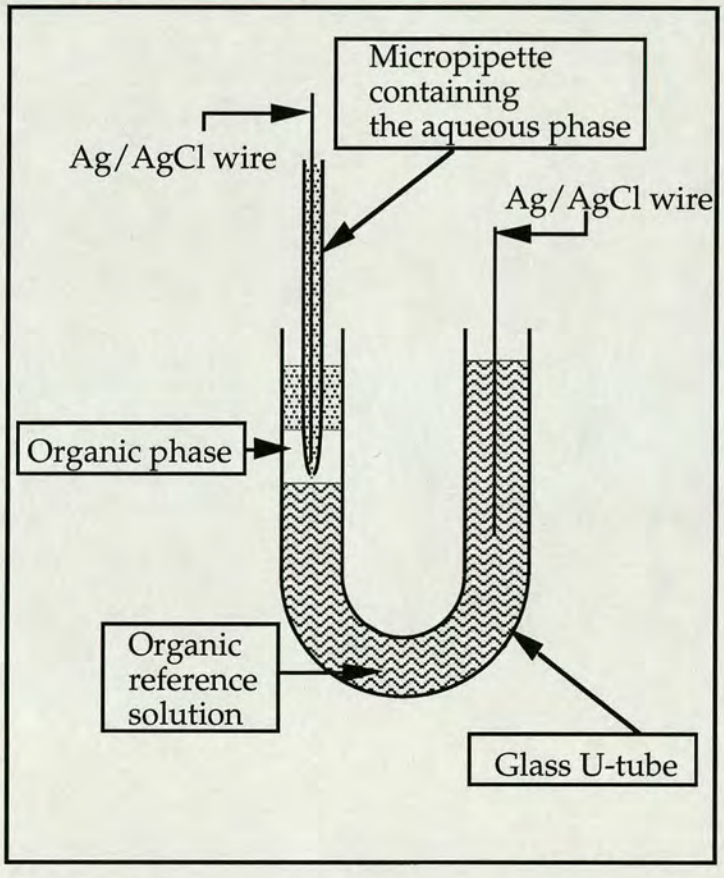

Figure 3.3 - Cell used for micropipette experiments.

The borosilicate capillaries had a very thin filament, running the entire length of the glass, on the inside. This meant that pipettes could be filled by

back-filling with a syringe and a very fine needle, the point of the pipette filling by capillary action.

The cell used for micropipette experiments was composed of a glass U-tube containing a small volume of the organic phase, supported by the organic reference solution. This was in turn covered with aqueous KCl to prevent release of harmful 1,2-DCE vapour. The micropipette, containing the same concentration of aqueous KCl, was immersed in the organic phase, and the distance between its tip and the organic reference solution was made as small as possible to minimise any effect due to iR drop. A two electrode electrochemical cell was configured by means of two silver/silver chloride wires acting as reference/counter electrodes (see figure 3.3).

3.2.2 Microhole

Machining of the microholes was performed by UV excimer laser photoablation of 12 μm thick Melinex (grade S) films (ICI, U.K.), based on a processing technique developed by Exitech Ltd. (Oxford, U.K.) [150]. An argon fluoride, ArF, laser beam (ArF laser - LPX 200, Lambda Physik, Germany) with a wavelength of 193 nm, and a maximum energy of approximately 500 mJ per pulse, was directed upon the film to be used, at a frequency of 10 Hz.

Polyester photoablation is the non-thermal destruction of polymer bonds, normally within a restricted volume, which causes a localised rise in pressure resulting in the ejection of organic material [151] - a mini-explosion in effect.

A schematic illustration of the apparatus used to drill the holes in the polyester films is shown in figure 3.4. The purpose of the attenuator in the assembly was to control the laser beam intensity. The beam was reflected through a field lens, and passed through a 100 μm hole in a metal surround - acting as the object to be imaged. The beam then passed through two adjustable circular diaphragms (with an aperture of about 1 mm), to minimise effects due to stray light, and was projected onto a backplate, via a series of lenses, where the film was positioned.

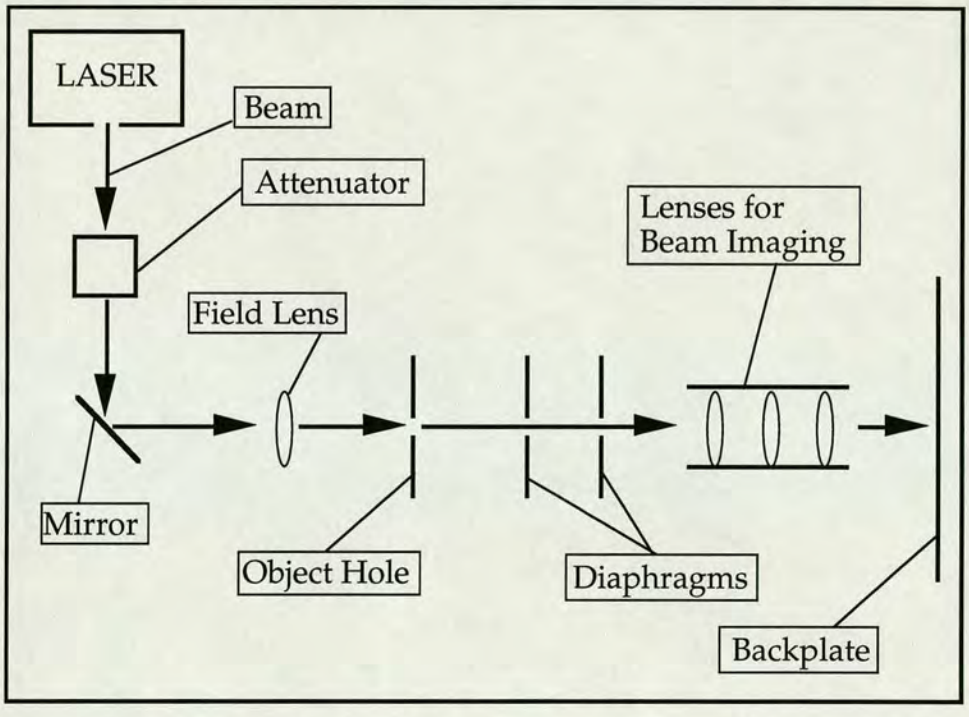

Figure 3.4 - Schematic diagram of the laser assembly used for hole fabrication.

The hole fabrication consisted of two steps:

(1) Hydrophilisation - the 100 μm object hole and all of the lenses were removed, and the diaphragms were set to an aperture radius of approximately 0.5 cm. The attenuator was set to deliver 60% of the full power from the laser, and the laser was fired for about 5 seconds This gave a circle of hydrophilised film, roughly 1 cm in diameter. Hydrophilisation had

the effect of roughening and charge activating the surface of the polyester film, thus allowing water to adhere more easily, and spread out over the surface. This was a prerequisite for experiments at the microhole-supported ITIES. The hydrophilised area was visible in the characteristics of the film, which appeared rough under a microscope - compared to the smooth appearance of the non-hydrophilised area. The hydrophilised area also had a 'milky' white appearance, compared with the transparent starting material.

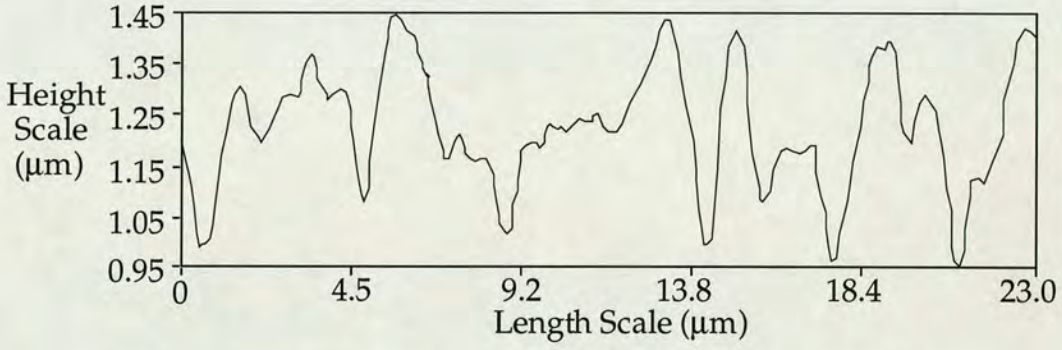

Figure 3.5 (a) - Surface cross-section profile of hydrophilised film, taken using an atomic force microscope.

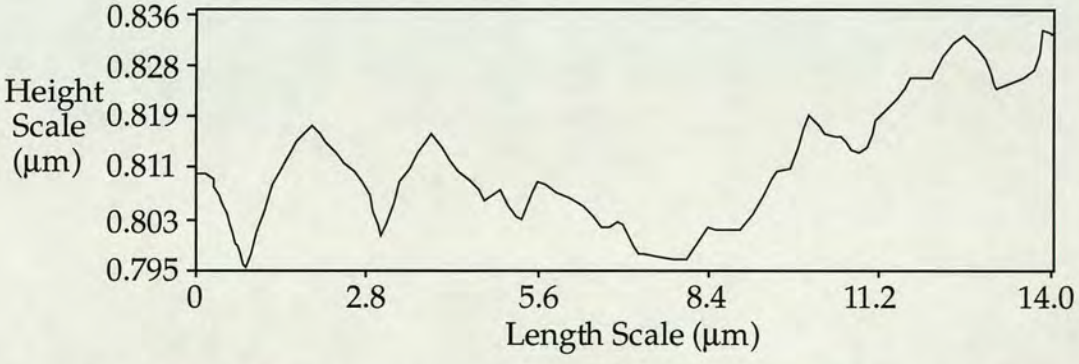

Figure 3.5 (b) - Surface cross-section profile of non-hydrophilised film, taken using an atomic force microscope.

Figure 3.5 shows surface cross-section profiles of hydrophilised and non-hydrophilised film taken using an atomic force microscope (ARIS-3300 Personal AFM, Burleigh Instruments) acquired by microcomputer and

interpreted using software from U.F.O. Systems, Inc. (U.S.A.). Figure 3.5 (a) shows the hydrophilised film, which had variation in depth of approximately 0.5 μm. In comparison, the non-hydrophilised film (figure 3.5 (b)) varied by only 0.04 μm.

(2) The film, now hydrophilised on one side, was drilled in the centre of the milky white area (either side of the film) by reassembling the apparatus, setting the diaphragms to a minimum and firing on full power for 10 - 15 seconds.

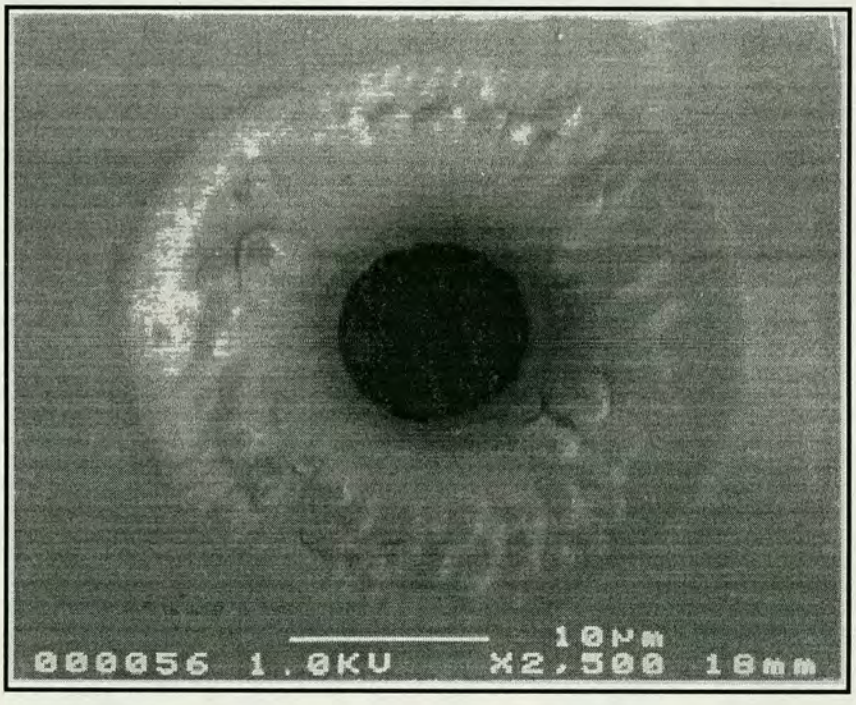

Figure 3.6 (a) - S.E.M. picture of the entrance side of a drilled polyester film (Melinex, 'S'-grade), magnified 2500 times.

Scanning electron micrographs of both sides of a finished hole, taken using the JEOL JSM-6300F scanning electron microscope (with gold-coating of the substrate) are shown on figure 3.6. Here the laser beam entrance hole was

on the non-hydrophilised side of the film (figure 3.6 (a)). The drilling process left the hole with a sloping wall characteristic - the extreme radius of the entrance side was about 30 μm whilst the exit side (figure 3.6 (b)) was roughly 10 μm. This sloping effect is termed anisotropic etching [150], and its extent depends on the optical arrangement.

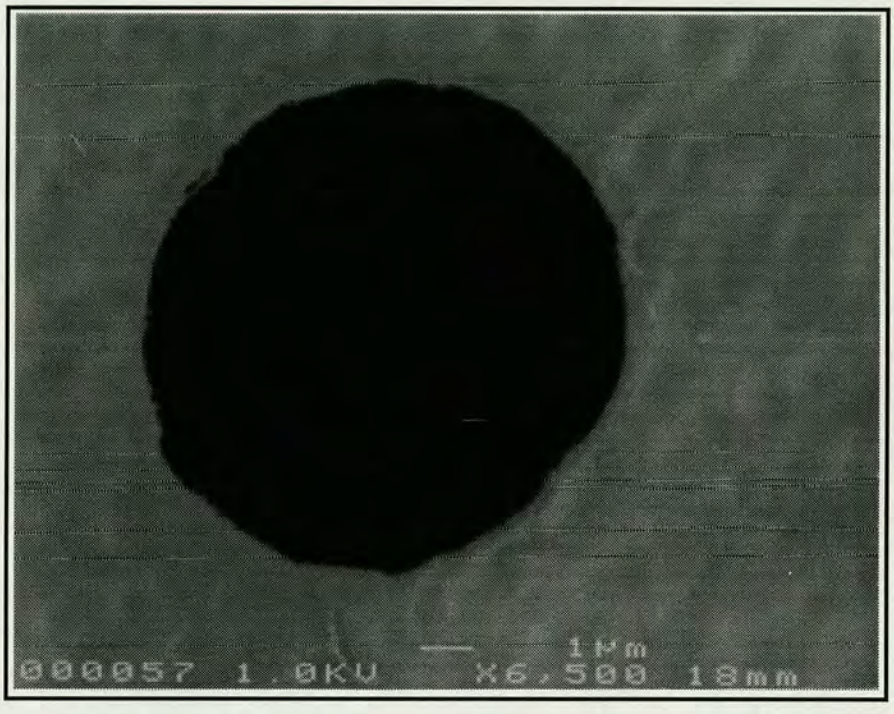

Figure 3.6 (b) - S.E.M. picture of the exit side of a drilled polyester film (Melinex, 'S'-grade), magnified 6500 times.

Figure 3.7 shows an atomic force microscope picture of a different hole (exit radius 10 μm), machined using approximately the same drilling characteristics as that of figure 3.6. Figure 3.8 (b) illustrates depth profiles of sections across the hole, which are shown in figure 3.8 (a). This shows that the sloping wall of the hole had a well defined edge. The limitations of the atomic force microscope were that depth profiles could only be made down to a maximum of 9 μm from the top of the film.

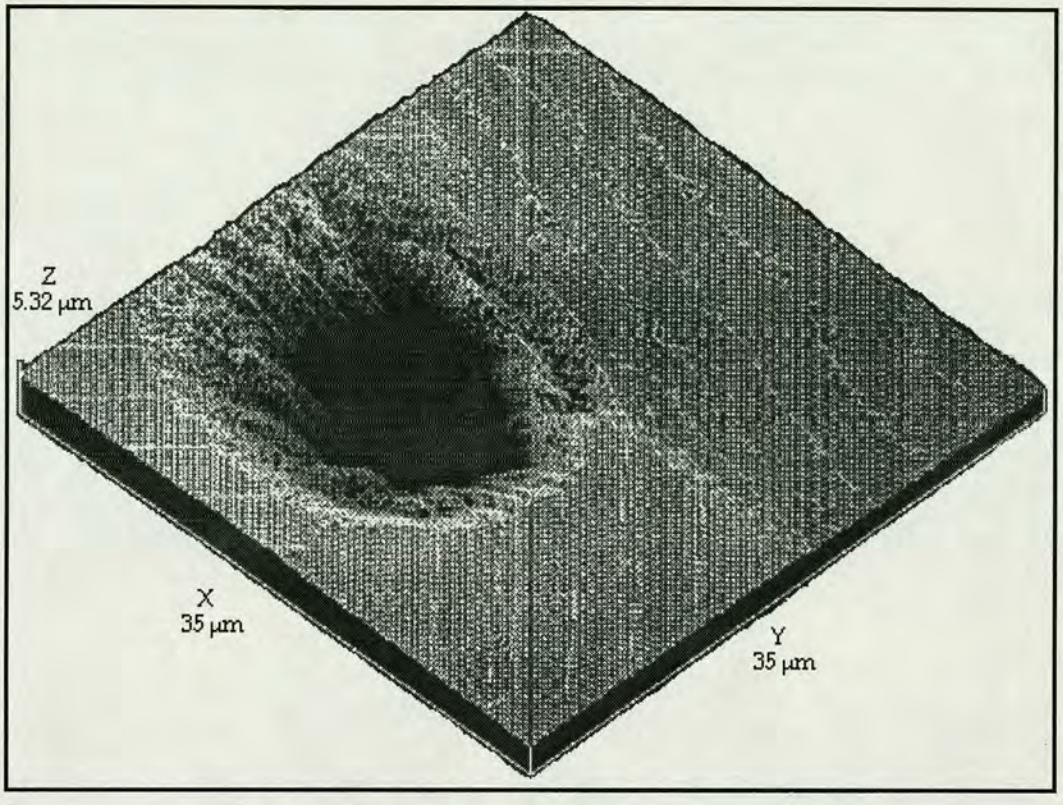

Figure 3.7 - A.F.M. picture of a drilled hole, different to that of figure 3.6, rotated 45º in the x and z planes.

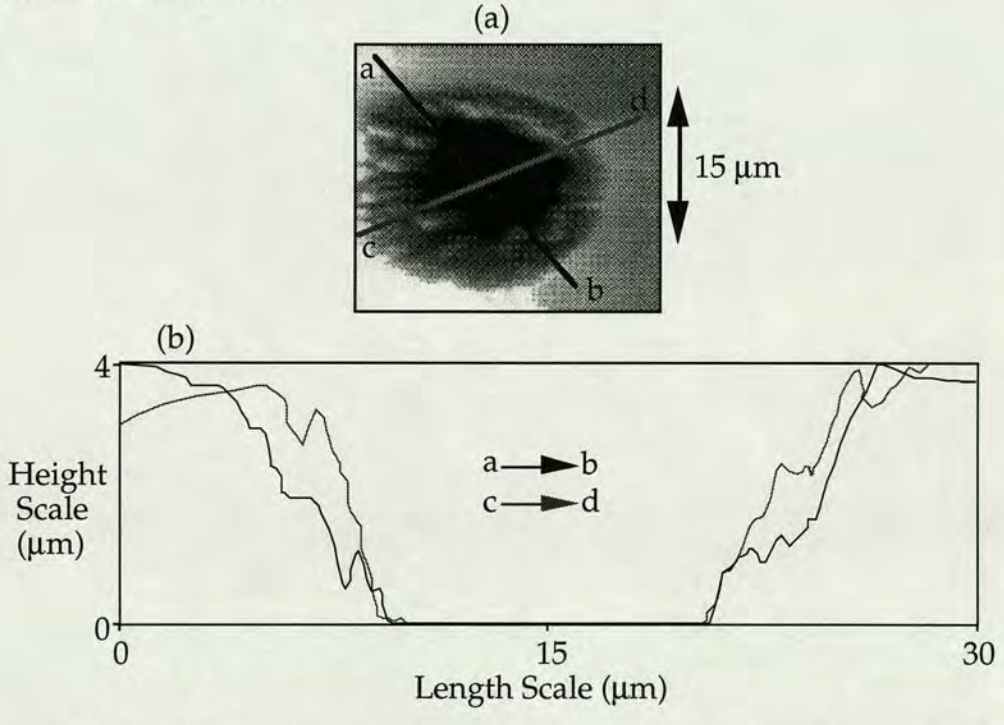

Figure 3.8 - (a) A.F.M. picture of hole in figure 3.7 (top view - no rotation in the X and Z planes) perpendicular to the film surface. (b) Depth profiles of sections on (a).

Looking at figure 3.8 (b) reveals that, after a depth of about 4 μm, the depth-profiles converge - corresponding to a diameter of roughly 10 μm. Thus, there was a depth of 8 μm where the hole walls must have deviated only very slightly from the vertical. In the case of smaller holes, tapering would be expected to be greater given that the drilling characteristics were approximately the same - the only difference being that the number of pulses required to form the hole was slightly less than that needed for a 10 μm diameter hole.

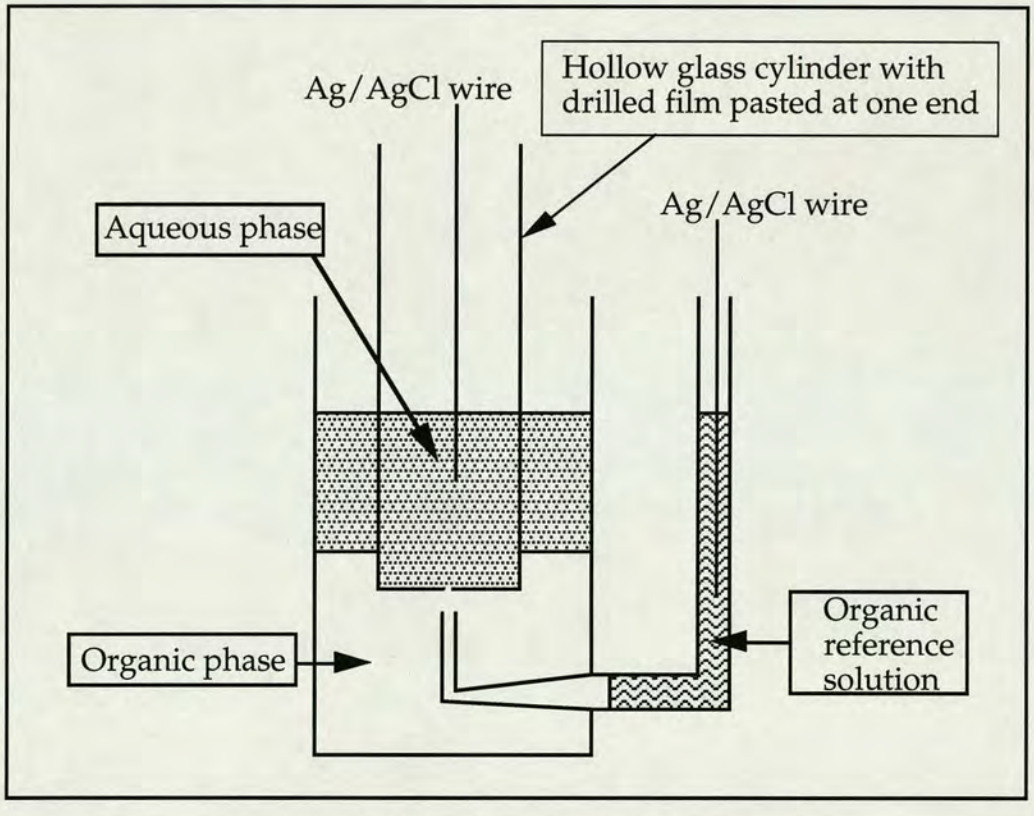

Figure 3.9 - Type of cell used for microhole experiments.

Figure 3.9 shows an illustration of the cell which was used for experiments on the microhole-supported ITIES. The machined film was pasted to one end of a hollow glass cylinder using silicone sealant.

3.2.3 Experimental Criteria for the Micro-ITIES

In the cyclic voltammetry and chronoamperometry micro-ITIES experiments, the voltage ramp and pulse respectively were supplied as for the large ITIES. The resulting current was measured with a current follower based on a high-input impedance FET operational amplifier (Burr Brown OAP 104). Voltammograms and chronoamperomograms were recorded as for the large ITIES. All of these experiments were carried out at a room temperature of 23 $\pm$ 1°C.

For the a.c. impedance micro-ITIES experiments, the d.c. potential was supplied by means of a Schlumberger Solartron 1286 Electrochemical Interface, while the a.c. signal was provided by a Schlumberger Solartron 1250 Frequency Response Analyser. The instruments were linked to a Hewlett Packard microcomputer which acquired the experimental data. Fitting programs for impedance data were written by Dr. A.Delay of the Institut Chimie Physique (III), E.P.F., Lausanne, Switzerland. These experiments were carried out at a room temperature of 25 $\pm$ 1°C.

All micro-ITIES experiments were conducted in an earthed Faraday cage and, as for the large ITIES, the cell potentials quoted refer to the potential difference of the aqueous phase with respect to the organic phase.

3.3 Reference Electrodes

The two types of reference electrodes used were Ag/AgCl and $Ag/Ag_2(SO_4)$. These were prepared by connecting the silver wire (purity 99.99%, Goodfellow, U.K.), and a counter electrode, to the positive and

negative terminals, respectively, of a 9V battery. Both wires were subsequently placed in an aqueous solution of the relevant sodium salt. The resultant current flow produced a layer of the insoluble silver salt on the silver wire.

3.4 Chemicals

3.4.1 Salts

All of the salts used were of purum grade (>98%) or better, unless otherwise specified.

Acetylcholine chloride - (Fluka)
Bis(triphenylphosphoranylidene) ammonium chloride (BTPPACl) - (Aldrich)
Butyrylcholine chloride - (Sigma)
Choline chloride - (Fluka, purum (>97%))
Copper (I) chloride - (Aldrich)
Copper (II) sulphate - (Merck)
Lithium chloride - (Fluka)
Lithium sulphate - (Fluka)
Potasssium hexacyanoferrate(III) - (Fluka)
Potassium hexacyanoferrate(II) trihydrate - (Fluka)
Potassium tetrakis(4-chlorophenyl)borate - (Lancaster Synthesis, U.K.)
Sodium chloride - (Fluka)
Sodium sulphate - (Fluka)
Tetrabutylammonium chloride - (Fluka)
Tetraethylammonium bromide - (Fluka)
Tetramethylammonium bromide - (Fluka)

Tetramethylammonium chloride - (Fluka)

Tetramethylammonium sulphate - (Fluka)

Tris(hydroxymethyl)aminomethane - (Fluka, Microselect)

Tris(hydroxymethyl)aminomethane hydrochloride - (Fluka, Microselect)

3.4.2 Solvents

All of the solvents were used as supplied.

Acetone - (Fluka, purum (>99%))

Methanol - (Fluka, purum (>99%))

1,2-dichloroethane - (Merck, puriss (>99%))

Nitrobenzene - (Fluka, puriss (>99.5%))

Water (Millipore, Milli-QSP Reagent water system)

3.4.3 Others

Butyrylcholinesterase, BChE (E.C. 3.1.1.8), from horse serum (500 units mg^{-1}) - (Sigma)

Buffer tablets (pH 4 and pH 7) - (Fluka)

Dibenzo-18-crown-6 - (Fluka, purum (>98%))

1,1'-diethyl-*p*-nitrophenyl phosphate, (paraoxon) - (Sigma (approx. 90%))

1,1'-dimethylferrocene - (Aldrich (97%))

Ferrocene - (Fluka, purum (>98%))

Nitrogen gas - (Carbagas, C.H.)

Silicone rubber sealant RTV 730 - (Dow Corning)

3.5 Preparation of Standard Solutions

Paraoxon was dissolved in acetone before being diluted with water to make standard solutions - these also contained butyrylcholine chloride. The enzyme BChE and lithium chloride (LiCl) were diluted with 0.1 M tris-HCl buffer to give a concentration of x units dm^{-3}, in a solution of 10 mM LiCl (where x is a value specified in the text) and a pH of 8 ± 0.05 at 37°C.

3.6 Preparation of Organic Phase Supporting Electrolytes

TBATPBCl (tetrabutylammonium tetrakis(4-chlorophenyl)borate), and BTPPATPBCl (bis(triphenylphosphoranylidene) ammonium tetrakis(4-chlorophenyl)borate), were prepared by metathesis of equimolar quantities of the corresponding salts - dissolved in a minimum amount of a 2:1 mixture of acetone:water or methanol:water. The resulting precipitate formed was recrystallised twice from the non-aqueous solvent used in the first step. Ordinary filtration after the first recrystallisation, and hot filtration after the second recrystallistaion, were carried out to facilitate removal of soluble and insoluble impurities respectively. The crystals obtained were then dried under vacuum before use.

Chapter Four

ION TRANSFER

4.1 Introduction

The main aim of this chapter was to assess the extent to which the micro-ITIES could be used to obtain kinetic data for ion transfer processes. The technology of microhole formation using UV excimer laser photoablation of thin polyester films, as outlined in chapter three (3.2.2), was exploited to achieve this. Both steady-state voltammetry and a.c. impedance of the microhole-supported ITIES were used to obtain estimates for the apparent standard rate constant, k^o, for ion transfer.

4.2 The Microhole-Supported ITIES

As stated in chapter one, Campbell and Girault [18] supported the ITIES at a microhole, formed by UV excimer laser photoablation of a thin polyester film. In this preliminary note, they studied the transfer of acetylcholine, ACh^+, from water to 1,2-DCE, with the interface supported at a 10 μm radius hole - drilled in 12 μm thick Melinex film. The authors made no comment on the reversibility of the steady-state waves obtained, however, they showed that at relatively high scan rates (100-200 mVs^{-1}) the steady-state response begins to peak, indicating deviation from spherical to linear type diffusion. This change in behaviour was attributed to linear diffusion of the transferring species within the hole itself, the effect of which becomes more significant at high scan rates.

A more rigorous study of the microhole-supported ITIES was undertaken by Osborne *et al.* [113] who carried out a steady-state current versus hole radius dependence for the transfer of the tetramethylammonium ion, TMA^+, from water to 1,2-DCE, using high quality holes drilled by Exitech Ltd. (Oxford, UK). Their results showed that the microhole produces steady-state currents of the same value as those expected for a solid inlaid microdisc electrode, according to equation 2.2.6. This result was based on a hole radius equivalent to that of the laser entrance side of the drilled polyester film. However, the relationship between entrance radius and steady-state current may only be used as an approximation, since the exact geometry of the interface at the single microhole has not been formally addressed to date.

For a 10 μm radius hole, the above authors [113] showed that the slope of the $\ln(i/i_{ss}-i)$ versus cell potential plot (equation 2.2.13), from the steady-state wave obtained for TMA^+ transfer, approaches the expected Nernstian response of 39.6 V^{-1} (for a temperature of 20°C), having an experimental value of 38.0 V^{-1}. In this experiment, the concentration of supporting electrolyte in the organic phase was only 1 mM. Interestingly enough, no comment on the reversibility of the waves used to construct the plot of the steady-state current versus hole radius was made. Had this aspect received more attention, a testing statement on the kinetics of ion transfer might have been made. Nevertheless, assuming that the result described above for the 10 μm radius hole can be taken to be effectively reversible, one can estimate a lower limit for the standard rate constant, k^o, for TMA^+ transfer across the polarised water/1,2-DCE interface. As mentioned in section 2.2.2.4, Oldham *et al.* [144] state that, for an effectively reversible steady-state voltammogram, the dimensionless parameter κ^o (which is equal to $\pi r_o k^o/(4D_S)$ for an inlaid microdisc - equation 2.2.19) should be greater than 40. Therefore, assuming

that the laser entrance side of the microhole is analogous to an inlaid solid microdisc electrode (ignoring effects due to linear diffusion within the hole), and taking an approximate value for the diffusion coefficient for TMA^+ of 9 x 10^{-6} cm^2s^{-1} [113], this creates a lower limit for k^o of 0.5 cms^{-1}. It should be stressed that this value is already 4 times faster than the value of 0.12 cms^{-1}, previously reported for TMA^+ transfer at the polarised water/nitrobenzene interface [34], at the same temperature. Here the rate constant evaluation was based on a.c. impedance data and involved the use of a much larger interface (19.2mm^2). Therefore, linear diffusion would have been the dominant form of mass transfer in this experiment.

4.3 Steady-State Voltammetry - Results and Discussion

4.3.1 Preliminary Investigations

In this work, microholes were fabricated, as described in 3.2.2, and were tested using the system:

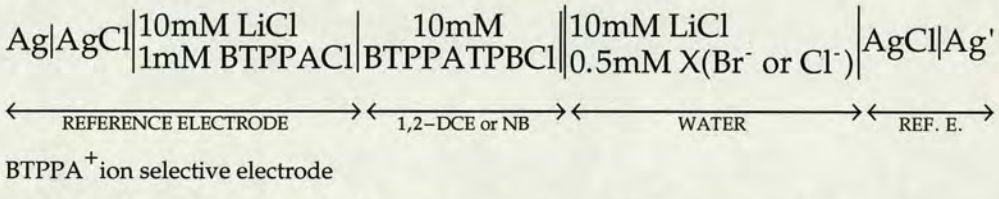

Cell 4.1 - where X represents the relevant cation of interest, and its counter ion is specified in the text. NB stands for nitrobenzene.

All hole sizes quoted, in this section and those which follow, correspond to the exit hole radius unless otherwise stated. In these preliminary studies, X was the TMA^+ ion, and its counter ion was chloride Cl^-. The Melinex polyester films were hydrophilised by UV excimer laser irradiation (see

section 3.2.2) on either the exit or entrance hole side, with respect to the drilling process. The hydrophilised side of the film was always that which was exposed to the aqueous phase of cell 4.1 (and figure 3.9).

Of those films which were hydrophilised on the exit hole side, only three of the microholes (two 4.5 μm holes, and one 2.3 μm hole) gave steady-state current responses which resembled those expected for an inlaid microdisc - based on the exit hole radius. The other holes (radii range ≅3.5 to 1 μm) produced current responses which were much bigger than expected. This suggests seepage of one of the two phases into the hole and could have been due to - (1) poor hydrophilisation of the exit hole side of the membrane resulting in the organic phase penetrating through to the other side, or (2) seepage of the aqueous phase into the hole, as a direct consequence of the crude mounting of the film for drilling purposes - if the film was not perfectly flat during drilling, then the hole could have been formed at an angle deviating from the perpendicular to the film. One other possibility for the increased current response could have been the presence of pinholes in the film, or the production of such holes during the drilling process. However, this was ruled out when a film, which initially seemed to have a hole of 1 μm radius, produced a purely capacitive response during a cyclic voltammetry experiment.

Figure 4.1 shows the steady-state current response for a 4.5 μm exit hole radius, at a scan rate of 20 mVs^{-1}. The organic phase solvent in this case was nitrobenzene. The forward scan of the experiment, corresponding to TMA^+ transfer from the aqueous to the organic phase, was found to be independent of the scan rate over the range 20 to 100 mVs^{-1}. This was based on measurement of the steady-state current and the slope of the $\ln(i/(i_{ss}-i))$

versus potential plot (these both remained constant). Using the forward wave in figure 4.1, the slope of the $\ln(i/(i_{ss}-i))$ versus potential plot yields a value of 38.6 V^{-1} and a Tomes' criterion ($E_{3/4} - E_{1/4}$) [139] of 60 ± 4 mV. For a fully reversible charge transfer process, the semi-logarithmic plot should yield a slope of 39.2 V^{-1}, and the Tomes' criterion should be equal to 55.5 mV, at 23°C. Thus, the TMA^+ transfer can be deemed to approach full reversibility at this hole size.

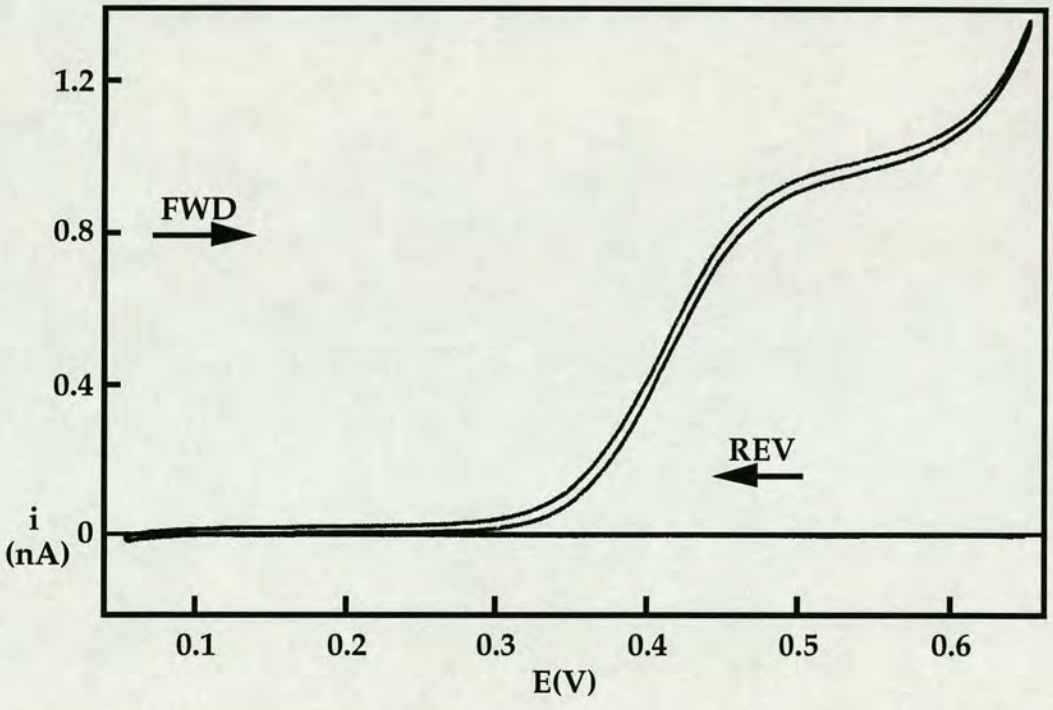

Figure 4.1 - Steady-state cyclic voltammogram for TMA^+ transfer across the interface between water and nitrobenzene, supported at a microhole of exit radius 4.5 μm - aqueous phase on exit hole side. Scan rate was 20 mVs^{-1}.

In the case of films which were hydrophilised on the entrance hole side, the steady-state current responses produced were for the most part much greater than that expected for a microdisc based on the entrance hole radius. Possible reasons for this have already been addressed. Figure 4.2 shows a

voltammogram obtained using an entrance hole radius of approximately 15 μm (exit hole radius 6 μm). The steady-state current produced corresponds to a microdisc having a radius of 25 μm. The organic phase solvent used in this case was 1,2-DCE. The slope of the $\ln(i/(i_{ss}-i))$ versus potential plot, for the forward wave, yields a value of 32.7 V^{-1}, and a Tomes' criterion of 70 ± 4 mV.

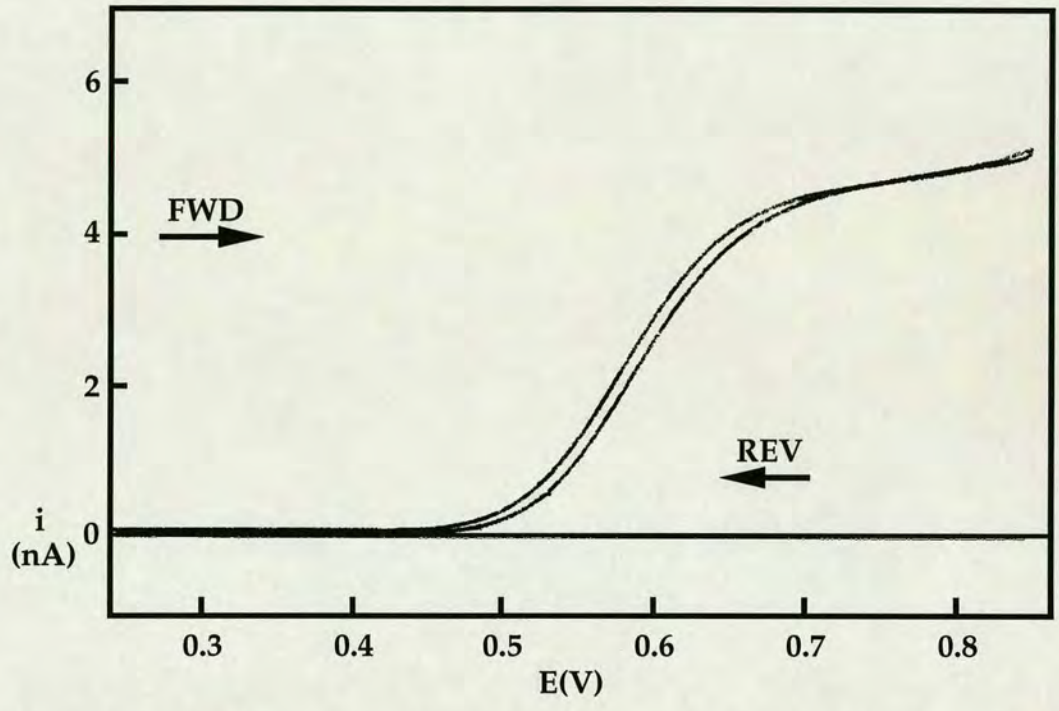

Figure 4.2 - Steady-state cyclic voltammogram for TMA^+ transfer across the interface between water and 1,2-DCE, supported at a microhole of exit radius 12 μm - aqueous phase on entrance hole side. Scan rate was 20 mVs^{-1}.

There are two possible explanations for this behaviour - (1) there may be some uncompensated resistance in the system, which could be due to a combination of factors: (a) the resistance of the electrolyte solution in the microhole; and (b) the resistance of the organic phase between the interface and the organic phase reference solution, including the luggin capillary and the side arm of the glass cell used (figure 3.9); or (2), given the size of the

steady-state current obtained it is feasible that the interface was bulging into the organic phase on the exit hole side of the film - this may have caused significant differences in the diffusion field symmetry leading to the observed slope.

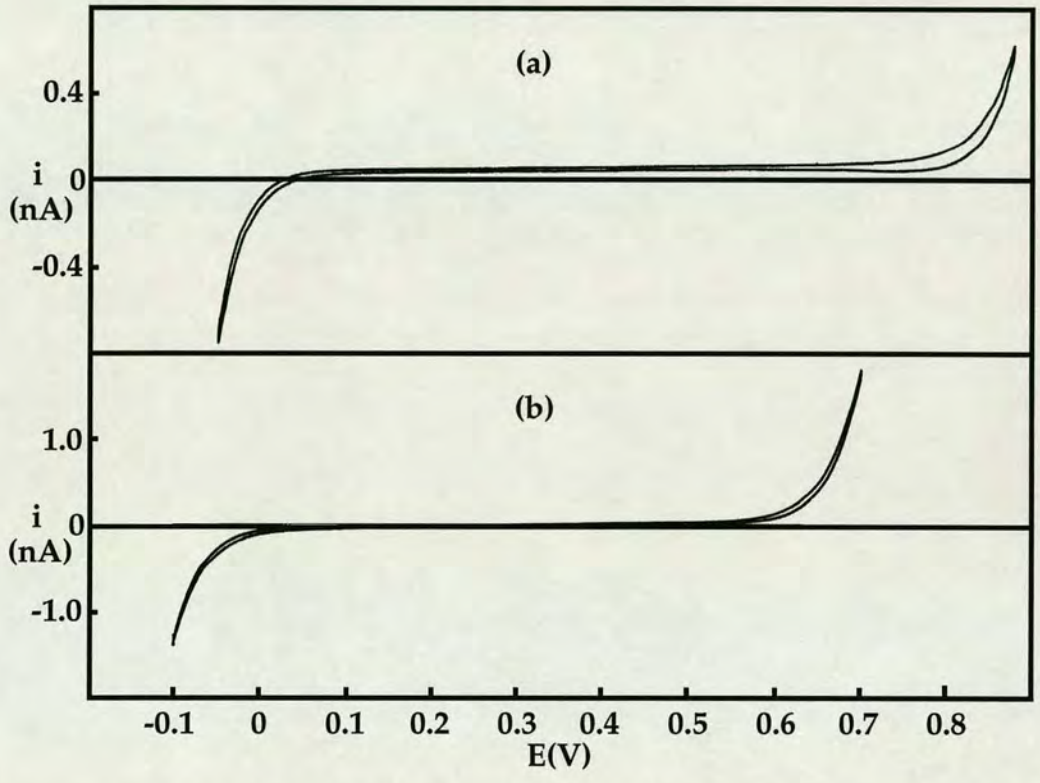

Figure 4.3 - Potential windows for cell 4.1 (no X present): (a) polarised water/1,2-DCE interface supported at a microhole of exit radius 2.3 μm; (b) polarised water/nitrobenzene interface supported at a microhole of exit radius 4.5 μm. Scan rate was 20 mVs^{-1} in each case.

Despite the discrepancies between the results obtained, it was decided that the holes which gave currents resembling those of an inlaid microdisc (where the hydrophilisation was on the exit side), should be used to carry out the bulk of the steady-state measurements described in the following section (4.3.2). Figure 4.3 shows the potential windows obtained for cell 4.1

(no X present) for the two different organic phase solvents employed, using a 2.3 μm ((a) - 1,2-DCE) and a 4.5 μm ((b) - nitrobenzene) exit hole radius respectively.

4.3.2 Ion Transfer Experiments

In this section, three microholes - two having exit hole radii of 4.5 ± 0.5 μm, and one of 2.3 ± 0.5 μm (error estimated by S.E.M. and optical microscope measurements) - were used to study the ion transfer across the polarised ITIES of four different ions: (1) TMA^+; (2) tetraethylammonium, TEA^+ (both of these ions were in bromide salt form); (3) acetylcholine, ACh^+; and (4) butyrylcholine, $ButCh^+$ (both of these ions were in chloride salt form). The system studied was that of cell 4.1 and both 1,2-DCE and NB were used for these experiments.

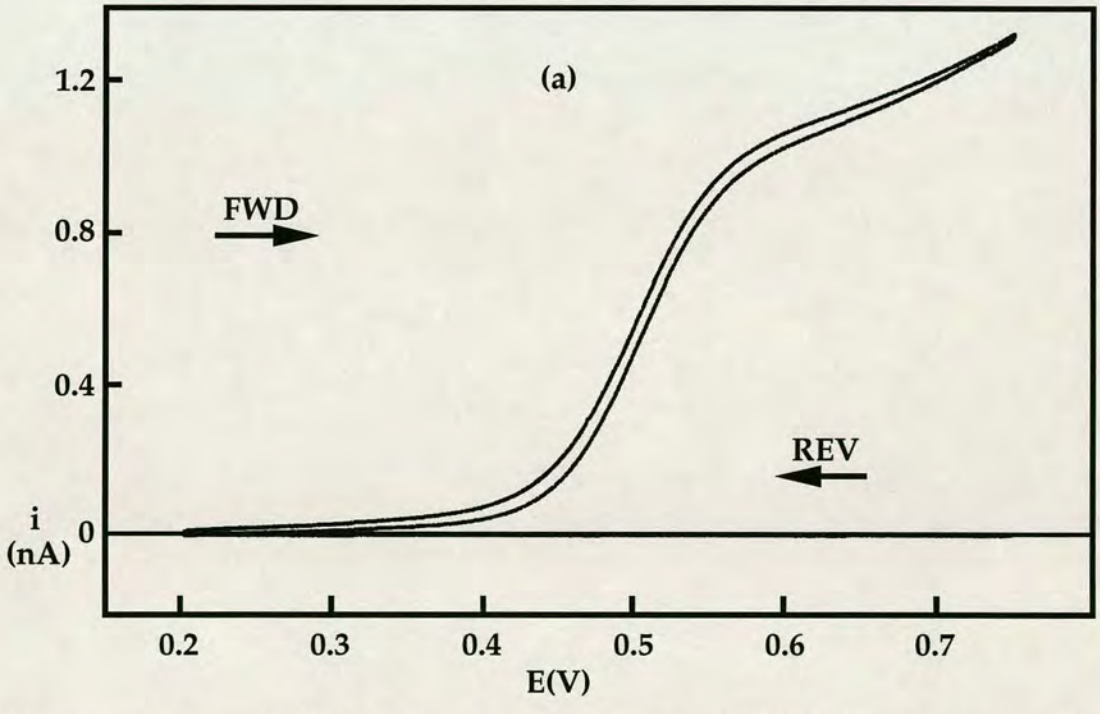

Figure 4.4 - Steady-state cyclic voltammogram for TMA^+ transfer across the interface between water and 1,2-DCE (microhole radius 4.5 μm).

Table 4.1 shows the information obtained from the forward waves of the observed steady-state responses (NB specifies nitrobenzene as opposed to 1,2-DCE). All experiments were conducted at a scan rate of 20 mVs^{-1}. Results in parentheses differentiate between the two 4.5 μm radii holes. Also shown is a result marked ((*) TMA^+)) where the concentration of supporting electrolyte in the organic phase, in this case 1,2-DCE, was increased to 0.1 M.

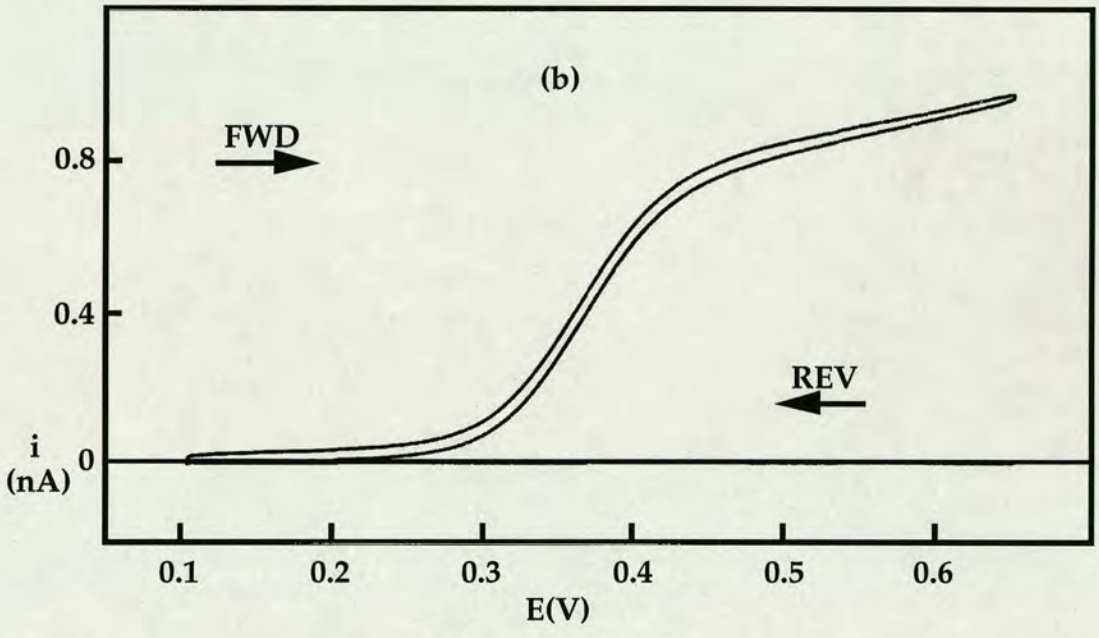

Figure 4.5 - Steady-state cyclic voltammogram for TEA^+ transfer across the interface between water and 1,2-DCE (microhole radius 4.5 μm).

Figures 4.4-4.7 give a selection of some of the steady-state voltammograms used to construct table 4.1. The main error in these measurements arises through the determination of the value for the steady-state current which had to be approximated due to the effect of sloping plateaus and baselines. The values obtained for the plots of $\ln(i/(i_{ss}-i))$ versus potential do not differ significantly on going from hole to hole, from ion to ion, or from one organic phase solvent to another. There is relatively good correlation between the

different half wave potentials, $E_{1/2}$, and the steady-state current values are also in good agreement (with the exception of the last result of the table).

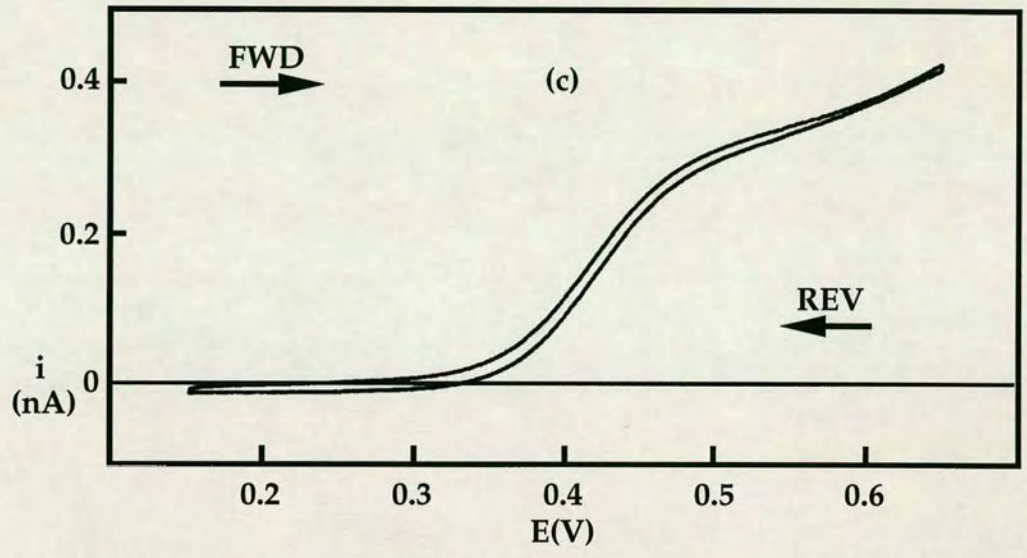

Figure 4.6 - Steady-state cyclic voltammogram for $ButCh^+$ transfer across the interface between water and 1,2-DCE (microhole radius 2.3 μm).

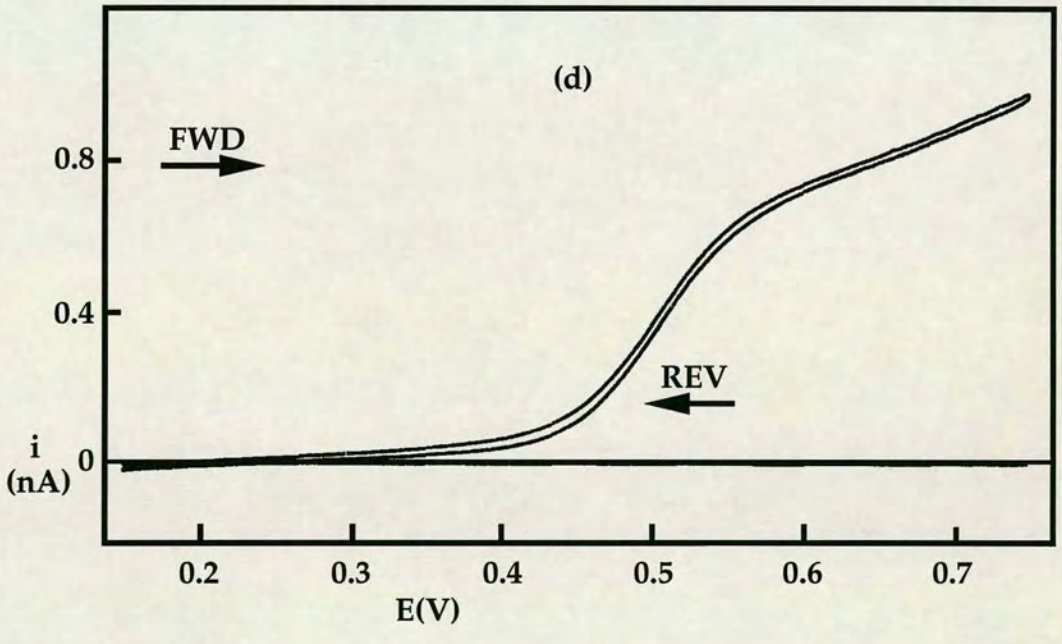

Figure 4.7 - Steady-state cyclic voltammogram for ACh^+ transfer across the interface between water and nitrobenzene (microhole radius 4.5 μm).

Table 4.1 - Experimental wave criteria from steady-state voltammograms.

Ion Type (X)	r_{Hole} ± 0.5 (μm)	$E_{3/4} - E_{1/4}$ ± 4 (mV)	Slope (V^{-1})	$E_{1/2}$ ± 2 (mV)	i_{ss} (nA)
TMA^+	2.3	61	37.2	499	0.52
TMA^+	4.5(4.5)	59(60)	37.6(37.7)	497(510)	1.00(1.00)
TEA^+	2.3	63	36.1	355	0.41
TEA^+	(4.5)	(63)	(36.1)	(362)	(0.78)
$ButCh^+$	2.3	61	36.9	418	0.30
$ButCh^+$	4.5	60	37.6	418	0.58
ACh^+	2.3	61	37.5	485	0.35
ACh^+	4.5	62	37.0	481	0.71
NB:TMA^+	2.3	60	37.2	405	0.46
NB:TMA^+	4.5	60(61)	38.6(37.2)	407(408)	0.92(0.94)
NB:TEA^+	2.3	62	37.0	303	0.37
NB:TEA^+	4.5	62	37.5	315	0.70
NB:$ButCh^+$	2.3	63	36.8	341	0.28
NB:$ButCh^+$	4.5	63	36.2	342	0.56
NB:ACh^+	(4.5)	(59)	(37.7)	(410)	(0.6)
(*) TMA^+	4.5	57	40.0	455	0.76

(r_{Hole} is the microhole radius (exit side))

Clearly, all the voltammograms exhibit behaviour which approaches Nernstian reversibility, however, it is only when the supporting electrolyte concentration in the organic phase is increased from 0.01 to 0.1 M that full reversibility is actually achieved. This result is depicted in figure 4.8 (a) and the corresponding plot of $\ln(i/(i_{ss}-i))$ versus potential is shown in figure 4.8(b). This suggests that there is uncompensated resistance arising as a

consequence of the cell design. This was confirmed in section 4.4 through a.c. impedance measurements.

It should be noted that the steady-state current value obtained using 0.1 M supporting electrolyte is rather lower than expected, compared with the previous values. Figures 4.9 (a) and (b) illustrate a possible reason for this, and also for hole failure in general. These figures show the entrance and exit hole sides of one of the 4.5 μm holes used in this section (for which the results in table 4.1 have been given in parentheses). It is clear that there has been a build up of impurities around the hole resulting in a sort of 'caking' effect around the rim of the hole. Similar pictures were also obtained for the other holes used. One might assume that dust from the air, particles present in the experimental solutions, or cleaning of the films with acetone, caused the observed effect.

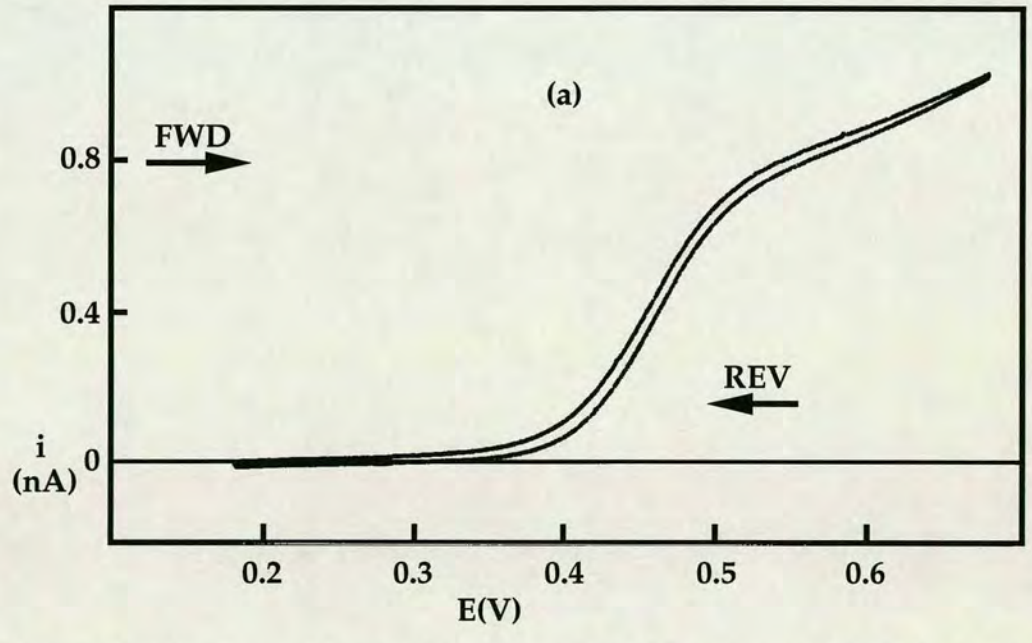

Figure 4.8 (a) - Reversible steady-state cyclic voltammogram for TMA^+ transfer across the interface between water and 1,2-DCE (hole radius 4.5 μm).

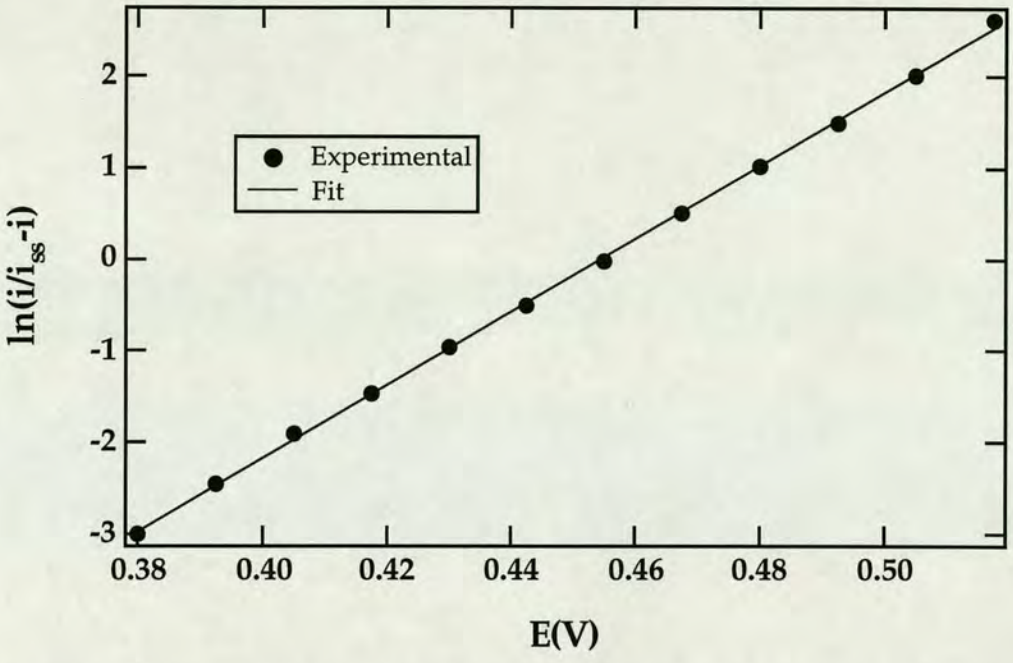

Figure 4.8 (b) - Plot of $ln(i/(i_{ss}-i))$ versus potential for the reversible steady-state voltammogram shown in figure 4.8 (a).

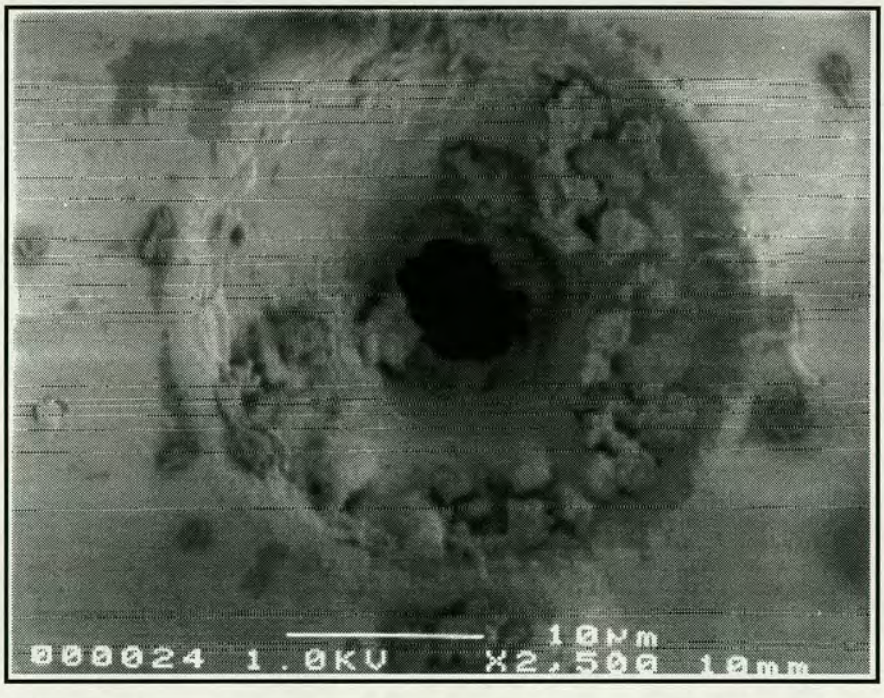

Figure 4.9 (a) - Laser entrance side of a used 4.5 µm radius hole, showing accumulation of debris.

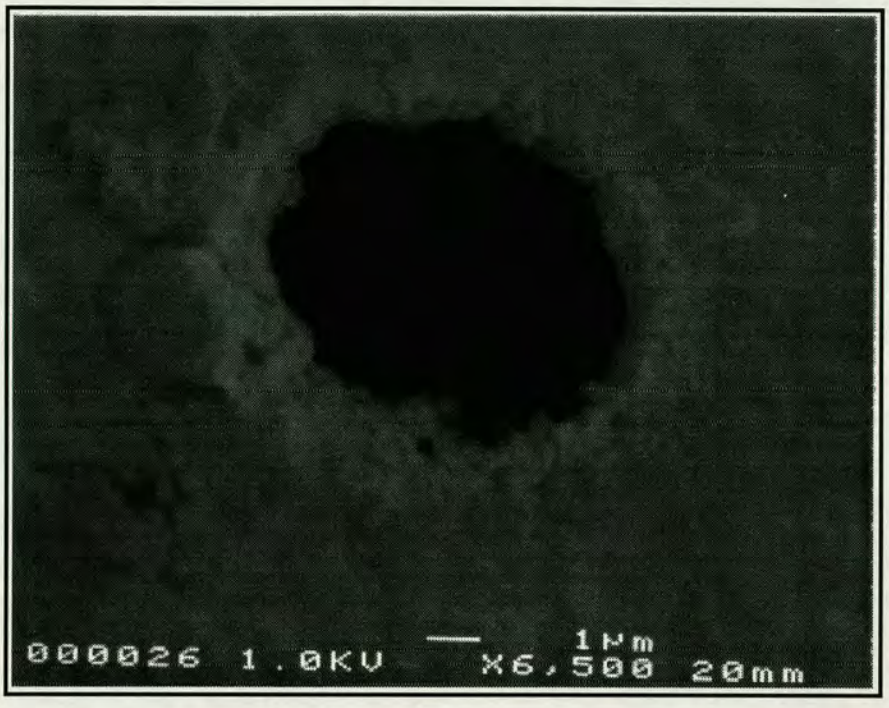

Figure 4.9 (b) - Laser exit side of a used 4.5 µm radius hole, showing accumulation of debris.

From the information given in table 4.1 it seems fair to conclude that all the ion transfer reactions would be expected to be effectively reversible under optimal conditions, namely increased organic phase supporting electrolyte concentration. If, as in the previous section, an approximate value for the diffusion coefficient of TMA^+ of 9×10^{-6} cm^2s^{-1} [113] is taken, the effective radii for the microholes, based on the approximation to a microdisc, can be evaluated using equation 2.2.6. Taking the steady-state current values for both solvents into account this gives effective disc radii of 2.8, 5.5 and (5.6) µm, for the 2.3, 4.5 and (4.5) µm holes respectively. The fact that no apparent kinetic shift is expected at an effective radius of 2.8 µm, means that the minimum apparent standard rate constant values for the different ions depend only on the respective diffusion coefficients. For TMA^+, the minimum value of k^o can be taken to be 1.6 cms^{-1}. This compares with the

previously stated value of Samec and co-workers [34] of 0.12 cms^{-1} for the large water/nitrobenzene interface (T = 20°C).

4.3.3 Conclusions to Steady-State Voltammetry

There are essentially two conclusions which may be drawn from the steady-state measurements discussed above, in conjunction with the results of Osborne *et al.* [113]: (1) there is a dependence of the 'minimum' standard rate constant, k^o, on the geometry of the interface - that is to say that, as the disc radius is decreased the value for the minimum can be set to a higher level - and (2) k^o for an ion transfer process is too high to be accessed using electrochemical methods, and its evaluation is dependent on the experimental technique employed. To establish whether this is in fact the case, an electrochemical method which can unambiguously separate the solution resistance from the charge transfer resistance needs to be employed. The method of a.c. impedance is ideally suited to this task.

4.4 A.C. Impedance - Results and Discussion

4.4.1 A.C. Impedance of Holes

In this section, the resistance corresponding to an aqueous solution of 1 M LiCl, present throughout the microhole cell design of figure 3.9 (in place of the solutions used for liquid/liquid studies) was evaluated by a.c. impedance. Impedance measurements on a 'blank' system, with no film present were also carried out. The impedance of the Ag/AgCl wires was assumed to be negligible.

The aim of this study was to assess the contribution of 'microhole' resistance, due to the volume of electrolyte solution in the microhole, to the data obtained for a.c. impedance of the microhole-supported ITIES (section 4.4.2).

The holes used were the 2.3 μm radius hole from the previous section, together with a newly drilled hole - exit radius approximately 5 μm. The amplitude of the potential perturbation was ± 10 mV, the d.c. potential was set to 0 V, and three acquisitions of experimental data were undertaken for each hole and the blank. The start frequency (f, not ω) was always 25 kHz, however, the end frequency was set to 1.57 kHz in the case of the 5 μm hole, and was varied for the 2.3 μm radius hole - here the end frequency was set to 970, 570 and 370 Hz respectively for the three different data acquisitions. In the latter case, the change in end frequency was used for comparison of fit data using model 4.1.

The results obtained are illustrated in averaged form in table 4.2. From this table, it is evident that a change in the end frequency for the 2.3 μm radius hole did not really affect the fit results.

Table 4.2 - Averaged data from experimental impedance of microholes - using model 4.1. Figures in brackets refer to the average of the percentage error on the individual fit results. Fitting was to all experimental points.

Hole size (μm)	$R_{Hole} \times 10^{-4}$ (Ω)	$C_{Film} \times 10^{10}$ (F)	$R_s \times 10^{-3}$ (Ω)
2.3	6.12 ± 0.06 (0.3)	2.34 ± 0.04 (0.6)	7.17 ± 0.31 (2.5)
5.0	2.14 ± 0.05 (1.1)	2.55 ± 0.09 (2.3)	9.14 ± 0.50 (2.9)

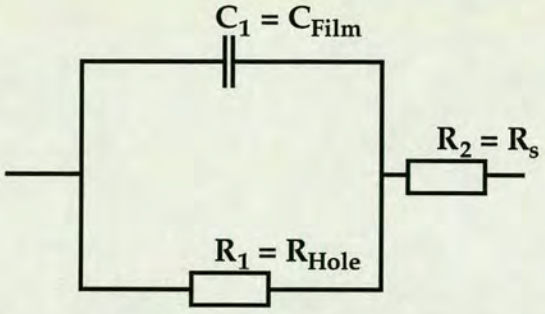

Model 4.1 - A resistance, R_2, in series with a parallel branch - composed of a capacitance, C_1, in parallel with another resistance, R_1.

The parameters C_1, R_1, and R_2, are denoted as follows:

(1) The measured capacitance, C_1, is assigned to the capacitance of the polyester film, C_{Film}. An order of magnitude calculation for C_1 was made using the equation for the capacitance of a parallel plate capacitor [139]:

$$C_1 = \frac{\varepsilon_r \varepsilon_o A}{d} \qquad (4.1)$$

where, in this case, d is the thickness of the film (this was 12×10^{-4} cm), ε_r is the dielectric constant of Melinex (S-grade) film (3.24 - [152]), ε_o is the permittivity of free space (8.854×10^{-14} $J^{-1}C^2cm^{-1}$), and A is the area of the film which was exposed to solution (0.785 cm^2). This yields a value for the capacitance of the film of 1.88×10^{-10} F. Thus, the results given in table 4.2 are of the correct order of magnitude to be attributed to the polyester film.

(2) The resistance corresponding to R_1 is associated with the resistance of the aqueous solution of LiCl in the microhole, and was termed R_{Hole}. Consider a case where the wall of the hole is vertical instead of sloping. In that instance the resistance is given by the equation [139]:

$$R_1 = \frac{\rho l}{A} \qquad (4.2)$$

where A, in this equation, corresponds to the cross-sectional area of the hole (cm^2), l is the length (depth) of the hole (12×10^{-4} cm), and ρ is the resistivity of the aqueous solution (ohmcm) - for a 1 M solution of LiCl, ρ is about 16 ohmcm [153]. Therefore, for holes of radii 5×10^{-4} cm and 2.3×10^{-4} cm, the resistance would be expected to be 2.4×10^4 Ω and 11.6×10^4 Ω respectively. The discrepancy in the values for the 2.3 μm hole may have been due to enhanced tapering of the hole walls relative to the 5 μm case (section 3.2.2).

(3) R_2 is assigned to the remaining solution resistance, R_s, of the cell, and varied slightly from experiment to experiment. The results indicate that a 10 mM solution of LiCl would be expected to give an R_s of approximately 8×10^5 Ω for the cell configuration used. The value of the impedance obtained for the blank cell without any polyester film was similar to the results obtained for R_s (table 4.2).

Figure 4.10 shows one of the complex plane impedance plots for the 2.3 μm radius hole, together with the fit to the data using model 4.1. Figure 4.11 shows the corresponding 'Bode' plot for the variation of the magnitude of the real part of the impedance, $|Z'|$, with frequency, f, plotted on natural logarithm scales. This demonstrates that the resistance of the hole, R_{Hole}, becomes less significant at higher frequencies.

The behaviour illustrated in figure 4.10 is analogous to the frequency dependence discussed in sections 2.2.3.3 and 2.2.3.4 for the Randles' equivalent circuit. However, in this case, there is no concentration gradient

and therefore no impedance corresponding to diffusion of ionic species. Thus, at lower frequencies, the plot retains a circular character.

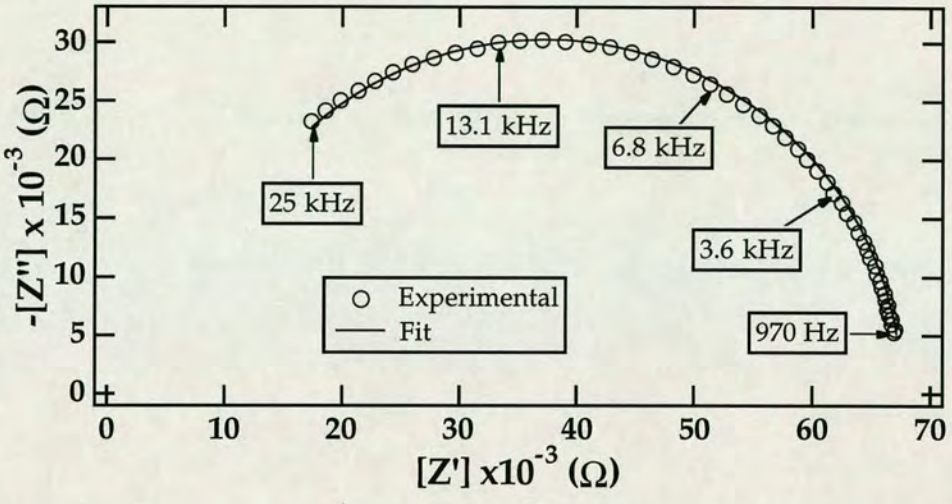

Figure 4.10 - Complex plane impedance plot for the case where there was only aqueous 1 M LiCl solution on both sides of the polyester film, and in the microhole (2.3 μm), in figure 3.9. Start, end, and some other frequencies are indicated.

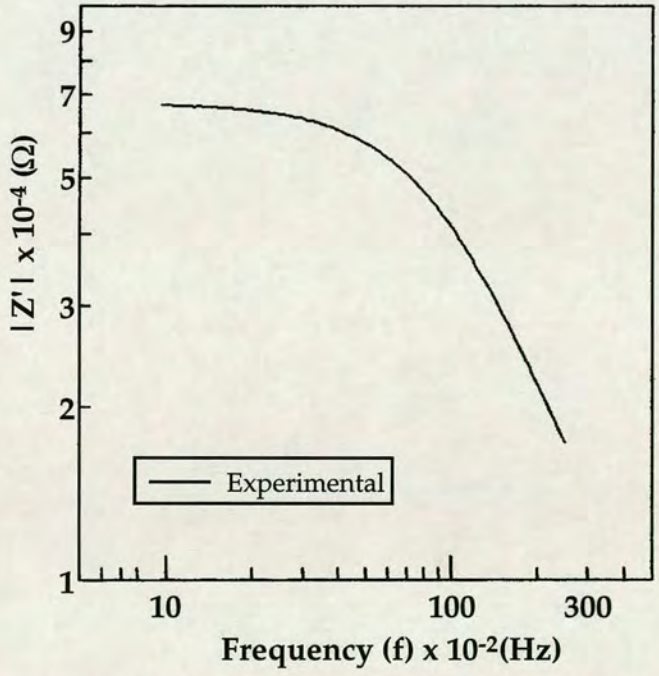

Figure 4.11 - 'Bode' plot of the magnitude of the real part of the impedance as a function of the frequency (2.3 μm hole). Scales are in natural logarithm form.

4.4.2 A.C. Impedance of the Microhole-Supported ITIES

In this section the impedance relating to cell 4.2 was determined. In these studies the impedance measurement was accepted when the difference between perturbation response cycles was 5%, as opposed to the previous section, which stipulated an accuracy of 1% between response cycles. For this work, new holes were machined and used.

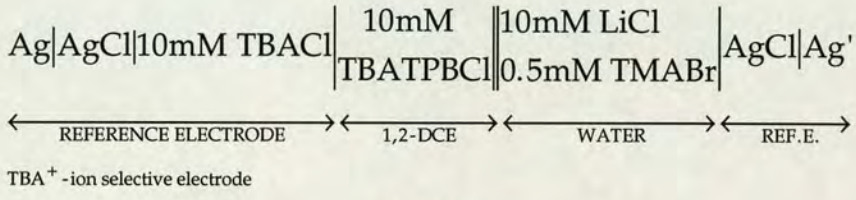

Cell 4.2

The cell design used initially for these studies was that of figure 3.9. The d.c. potential was set to the half-wave potential for TMA^+ transfer - determined by steady-state voltammetry. In this case, the exit hole radius was 5 μm and the steady-state current measured corresponded to a disc radius of 5.9 μm. Obviously, the fact that the voltammogram was in a pseudo quasi-reversible regime would mean that the equilibrium potential would have been slightly less positive than the measured half-wave potential. However, this factor was ignored in the a.c. impedance results presented in this chapter. The amplitude of the exciting signal was ± 20 mV, and again three measurements were made for a given hole. The start frequency was 25 kHz and the end frequency was 3 Hz in each case. Table 4.3 shows the fit results (averaged) obtained using model 4.2. Figure 4.12 shows one of the complex plane impedance plots for the system, together with the fit based on model 4.2.

Table 4.3 - Averaged data from experimental impedance of the microhole supported ITIES - using model 4.2. Figures in brackets refer to the average of the percentage error on the individual fit results. Fitting was to all experimental points.

Parameter	Value
$R_1 \times 10^{-7}$ (Ω)	9.40 ± 0.52 (8.0)
$S_1 \times 10^{-8}$ (Ωs^{A_1})	5.59 ± 1.40 (19.2)
$A_1 \times 10^{1}$	-5.00 ± 0.69 (8.2)
R_{ct} (Ω)	0.00 ± 0.00 (0.0)
$C_{Film} \times 10^{10}$ (F)	2.36 ± 0.11 (3.0)
$R_s \times 10^{-6}$ (Ω)	2.47 ± 0.06 (0.7)
$C_g \times 10^{11}$ (F)	1.18 ± 0.01 (0.6)

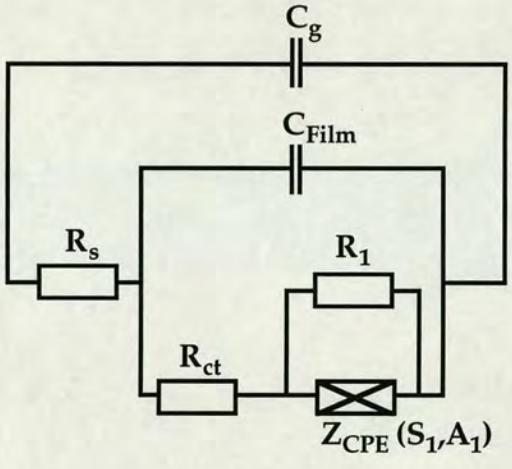

Model 4.2 - where C_g represents a geometrical capacitance, and Z_{CPE} is a constant phase element impedance (defined by S_1 and A_1, equation 4.3). Other symbols have their usual meaning.

The parameters comprising model 4.2 are discussed below:

(1) C_{Film} is represented in the diagram of model 4.2 instead of C_{int}, since the value obtained by data fitting for the capacitance is very similar to that

found in the previous section. This result is as expected, since the interfacial capacitance of the water/1,2-DCE interface has been established [97] as having a value of the order of 10^{-5} Fcm^{-2}. For a microhole-supported-ITIES, having an area of 7.85 x 10^{-7} cm^{-2} (5 μm radius hole), this translates to a capacitance of approximately 8 pF (picoFarads). Therefore, since the capacitance of the film and the interface are essentially in parallel the interfacial capacitance would be expected to be completely masked.

(2) The parallel branch composed of R_1 and Z_{CPE}, is a Z_{ARC} impedance - that is to say that it may produce an arc shape response in the complex plane. Z_{CPE} is a constant phase element impedance, represented by the equation [154]:

$$Z_{CPE} = S_1(j\omega)^{A_1} \qquad (4.3)$$

where S_1 is equal to σ (equation 2.2.35) and A_1 is $(2\theta/\pi)$. If A_1 has a value of -0.5, as is the case for the experimental results (table 4.3), then Z_{CPE} is a Warburg impedance, Z_W. In that event, model 4.2 is analogous to that used by Bruce *et al.* [146] (described in 2.2.3.5), except for the geometric capacitance, where R_1 is the resistance corresponding to non-linear diffusion, R_{nl} (equation 2.2.43). When A_1 has a value of -1 then Z_{CPE} acts as a capacitance.

(3) C_g represents the geometrical or 'stray' capacitance associated with the cell configuration.

(4) R_{ct} is a simplification, since there will be contributions from both the charge transfer resistance and the solution resistance associated with the microhole, R_{Hole}.

It should be stressed, that model 4.2 does not take the faradaic impedance associated with base electrolyte transfer into account. However, the effect of the base electrolyte was assumed to be negligible as far as the present impedance evaluations are concerned, since the d.c. potential applied was in the middle (approximately) of the potential window used. Furthermore it was demonstrated to be of no significance, in principle, for a hole of radius 25 μm (see later results, this section).

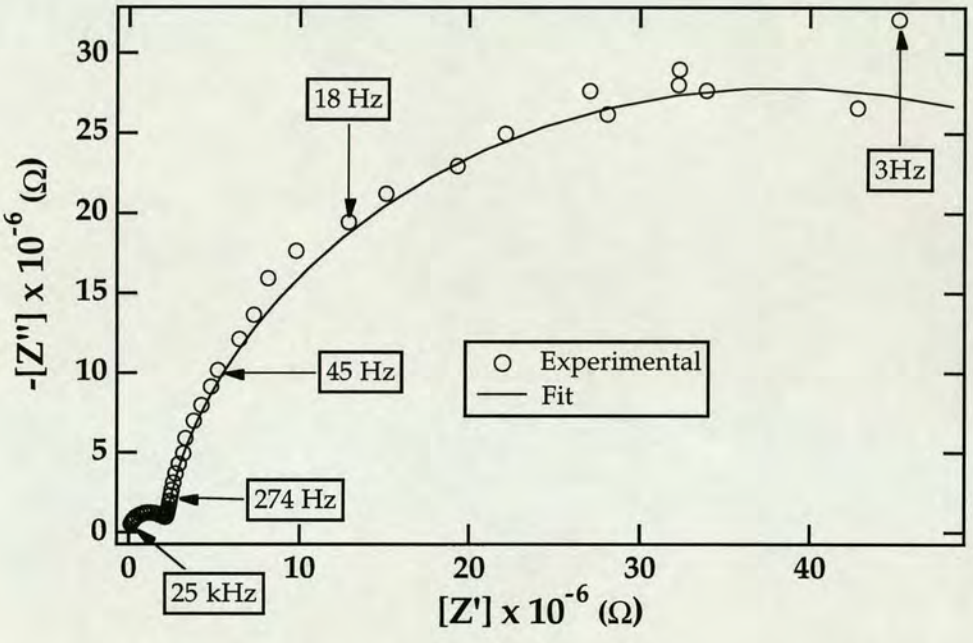

Figure 4.12 - Complex plane impedance plot for cell 4.2, at the half-wave transfer potential for TMA^+. Only half of the experimental points are shown for clarity. Start, end, and some other frequencies are indicated.

In figure 4.12, the small semi-circular phenomenon, present at high frequencies, is not due to the charge transfer resistance acting in parallel with the film capacitance, C_{Film}. Instead, as will be demonstrated in the following results, it is due to the geometric capacitance of the cell acting in parallel with the solution resistance, R_s (where other elements can be neglected, or

offer zero resistance in comparison (C_{Film})). A point to note here is the value for R_s of 2.47 x 10^6 Ω obtained from the fits, which is about three times the expected value for 10 mM LiCl. This can be easily explained by the higher resistance associated with the organic phase.

At lower frequencies, the impedance is dominated by spherical-type diffusion of ions to and from the interface, and in consequence part of a flattened semi-circle is evident in the complex plane. The results obtained from the fits for R_1, S_1 and A_1 are consistent with this: A_1 has a value of -0.5, therefore S_1 can be taken to be a Warburg impedance; S_1 is greater than R_1, so the impedance behaviour observed corresponds only to that of non-linear or spherical diffusion attributable to R_1. Using equation 2.2.43, R_1 should have a value of 5.4 x 10^7 Ω. Thus, to a first approximation, the fit corresponds closely to the experiment.

According to the fit, R_{ct} does not have an appreciable value. However, this does not necessarily mean that there was no R_{ct} - instead it is possible that the diffusional impedance was so large that any R_{ct} information was obscured. If correct though, it would mean that the kinetics of TMA^+ transfer across the interface are at least as fast as diffusion of the ion to the interface.

A problem with measurements made in the low frequency domain was the large degree of dispersion on the experimental data, which is thought to have arisen due to convection in the cell. This is not clearly illustrated on figure 4.12, but became obvious at about a frequency of 50 Hz. This factor may have affected the resulting fit data - highlighted by the average value for the errors (in brackets - table 4.3) on the fit data for R_1, S_1 and A_1.

From the above considerations, and in the interests of reproducing the rather astonishing possibility of infinite ion transfer kinetics, it was deemed sensible to repeat the experiment with a maximised cell configuration. Namely, one in which the solution resistance was minimised, thereby reducing the effects of geometric capacitance, and increasing the number of data points corresponding to the more relevant part of the impedance plot - that associated with the charge transfer resistance.

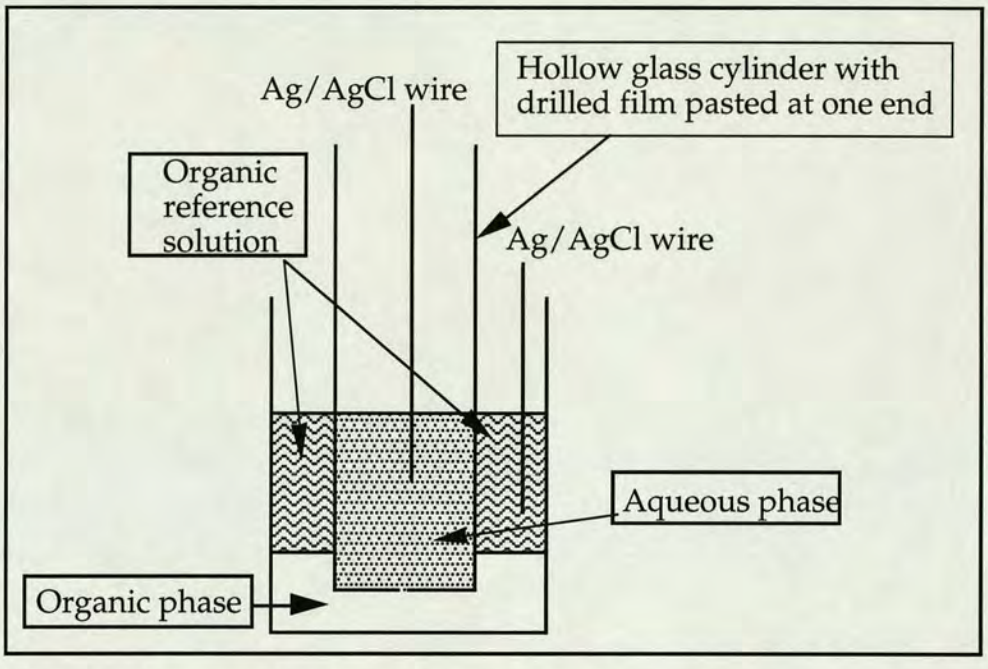

Figure 4.13 - Maximised cell configuration used for a.c. impedance experiments of the microhole-supported ITIES.

The cell configuration which gave the minimum amount of solution resistance, R_s, was determined by trial and error. The design finally used was very simple (figure 4.13), where the cylindrical tube with attached polyester film (containing the aqueous phase) was immersed in the organic phase (held in a beaker). The corresponding organic phase reference solution was administered to the top of the organic phase to complete cell 4.2. Thus, the resistance associated with the organic phase in the luggin

capillary of figure 3.9 was effectively removed. This gave a R_s of approximately 1×10^4 Ω.

*Table 4.4 - Averaged data from experimental impedance of the microhole supported ITIES - using model 4.2 - with the cell configuration maximised. Figures in brackets refer to the average of the percentage error on the individual fit results. * - Fitting corresponded to points in the frequency range 25 kHz to 122 Hz. * *- Fitting to all the points.*

Parameter	Value*	Value**
$R_1 \times 10^{-7}$ (Ω)	1.32 ± 0.18 (1.2)	1.47 ± 0.13 (1.0)
$S_1 \times 10^{-8}$ (Ωs^{A_1})	10.29 ± 3.42 (6.2)	4.67 ± 0.60 (11.2)
$A_1 \times 10^1$	-5.96 ± 0.41 (1.4)	-4.96 ± 0.18 (3.5)
R_{ct} (Ω)	0.00 ± 0.00 (0.0)	0.00 ± 0.00 (0.0)
$C_{Film} \times 10^{10}$ (F)	1.89 ± 0.07 (4.5)	1.46 ± 0.18 (22.8)
$R_s \times 10^{-4}$ (Ω)	1.06 ± 0.09 (9.2)	2.02 ± 0.50 (47.5)
$C_g \times 10^{11}$ (F)	3.42 ± 0.72 (27.3)	8.36 ± 1.98 (47.4)

The previous experiment, carried out for cell 4.2, was now repeated using a new 5 μm exit radius hole. Again the half-wave potential was determined by steady-state voltammetry - the value of 37.6 V^{-1} obtained for the plot of $\ln(i/(i_{ss}-i))$ versus potential was approximately the same as that recorded for holes used previously (table 4.1). The value for the steady-state current was as expected for an 8.2 μm exit radius hole (see 4.3.1 for possible reasons). The fit results (averages for the three determinations) are presented in table 4.4 - here the fits have been made to those data points corresponding to the frequency range 25 kHz to 122 Hz (60, out of 101 points), due to the existence of heavy dispersion in the low frequency domain. The same fits were made

using all the points with more or less similar results, however, the fitting precision was relatively poor (these are also shown in table 4.4).

From the average errors on the individual fit results (figures in brackets - table 4.4) it is evident that C_g does not carry the same significance as before and, by restricting the frequency range analysed, the precision on most of the parameters has been improved.

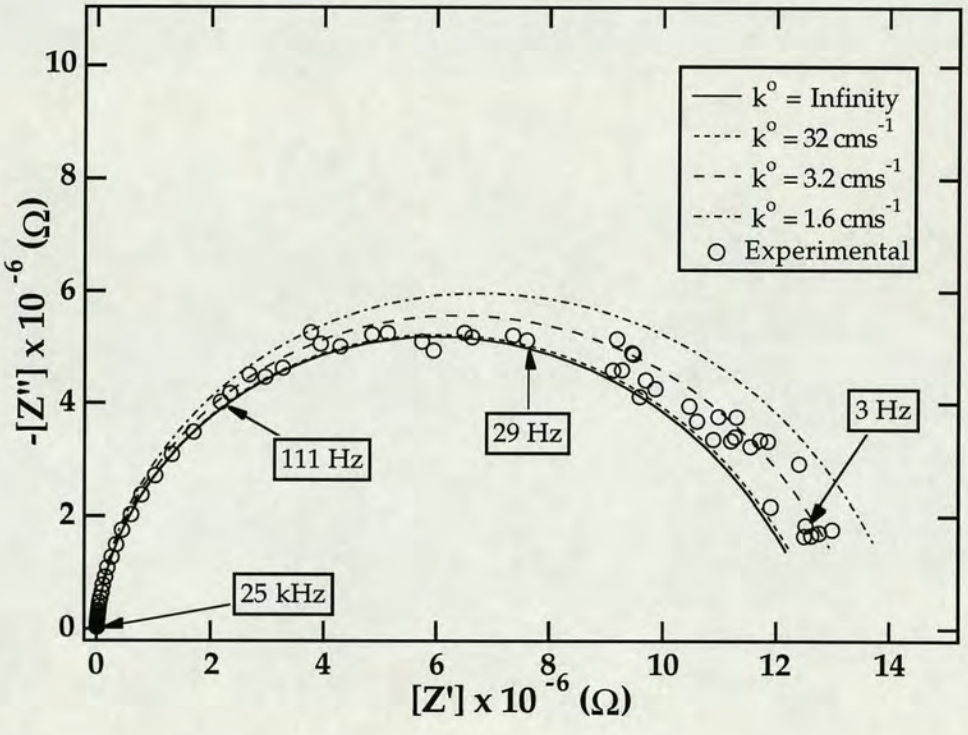

Figure 4.14 - Complex plane impedance plot for cell 4.2, using a maximised experimental cell configuration, at the half-wave transfer potential for TMA^+. Only half of the experimental points from a frequency of 25 kHz to 111 Hz are shown for clarity.

Figure 4.14 shows one of the complex plane impedance plots obtained, together with the fit to the data points in the frequency range 25 kHz to 122 Hz, using model 4.2. Also shown on figure 4.12 are predicted plots for

increasing values of R_{ct}, corresponding to different k^o values - based on an exit hole radius of 8.2 μm, and calculated using equation 2.2.33 - where all other fit parameters have been kept the same. It can be seen that there is little difference between an infinitely high k^o value and one of 32 cms^{-1}. Almost all of the points from the frequency range 25 kHz to 29 Hz lie on, or near, these two predicted fit lines.

Once again, the fitting procedure does not cope with an R_{ct} element in the system, suggesting a rate of ion transfer at least equal to the rate of diffusion. The resistance, R_{ct}, corresponding to a k^o value of 32 cms^{-1}. for an 8.2 μm radius hole is 7.83×10^4 Ω. All of the points are bounded by the line corresponding to an R_{ct} value of 1.57×10^6 Ω.

It was decided that, in order to corroborate the above findings, a much larger microhole should be employed. By replacing the 100 μm hole object used during the drilling procedure (figure 3.4) with one of 500 μm it was possible to fabricate holes having exit radii of approximately 25 μm (entrance hole radii 35 μm). One such hole was incorporated into the cell configuration, shown in figure 4.13, and the impedance of cell 4.2 was measured under the conditions previously employed. The difference, with respect to the previous experiment, was that the entrance hole side of the film was that which was hydrophilised and therefore in contact with the aqueous phase. The hole used produced a voltammogram which had a steady-state current value equal to that expected for a disc radius of 35 μm - this is just outwith the range which most experimentalists would consider to be micro. From the forward wave of the voltammogram the $\ln(i/(i_{ss}-i))$ versus potential plot yielded a slope of 33.5 V^{-1} and a Tomes' criterion of 66 ± 4 mV.

In addition to the above experiment (experiment 1, table 4.5), the impedance of a cell containing no TMA^+ was measured under exactly the same conditions (experiment 2, table 4.5). An aliquot of solution, corresponding to a cell concentration of 0.16 mM TMA^+, was then added to the aqueous phase and the impedance re-measured. Results from both sets of experiments are listed in table 4.5. Fitting was to all the experimental points, since the degree of dispersion on the data points at lower frequencies was small compared with previous experiments.

Table 4.5 - Averaged data from experimental impedance of the microhole supported ITIES, using model 4.2, and with the interface supported at a 25 μm exit/35 μm entrance radius hole. Figures in brackets refer to the average of the percentage error on the individual fit results. Fitting was to all the points. (INF = infinity).

Parameter	Experiment 2	Experiment 2	Experiment 1
TMA^+ (mM)	0	0.16	0.50
$R_1 \times 10^{-7}$ (Ω)	25.80 ± 5.50 (6.3)	INF	INF
$S_1 \times 10^{-7}$ (Ωs^{A_1})	97.90 ± 2.30 (2.6)	2.94 ± 0.34 (0.8)	1.68 ± 0.03 (0.6)
$A_1 \times 10^1$	-8.52 ± 0.01 (4.6)	-5.07 ± 0.03 (0.4)	-4.86 ± 0.03 (0.3)
$R_{ct} \times 10^{-5}$ (Ω)	6.24 ± 0.16 (2.9)	6.33 ± 0.07 (1.0)	6.91 ± 0.02 (0.6)
$C_{Film} \times 10^{10}$ (F)	2.24 ± 0.10 (36.5)	1.90 ± 0.08 (7.3)	1.82 ± 0.16 (4.1)
$R_s \times 10^{-4}$ (Ω)	1.04 ± 0.09 (77.6)	1.52 ± 0.15 (16.1)	1.86 ± 0.20 (9.4)
$C_g \times 10^{11}$ (F)	3.86 ± 0.94 (227)	7.55 ± 0.82 (20.1)	7.38 ± 2.04 (11.9)

Figure 4.15 shows complex plane impedance plots for each of the three different cases in table 4.5, together with the relevant fits obtained using model 4.2.

Base electrolyte results: Only part of the impedance plot for the base electrolyte system is shown, since the remainder - which forms part of a large arc - would have dwarfed the other two responses. The large value obtained for R_1, signifies that the base electrolyte contribution to the impedance values for those cases where TMA^+ was present would have been effectively negligible. Since A_1 has a value which approaches -1, the Z_{CPE} of model 4.2 acts more like a capacitance than an impedance.

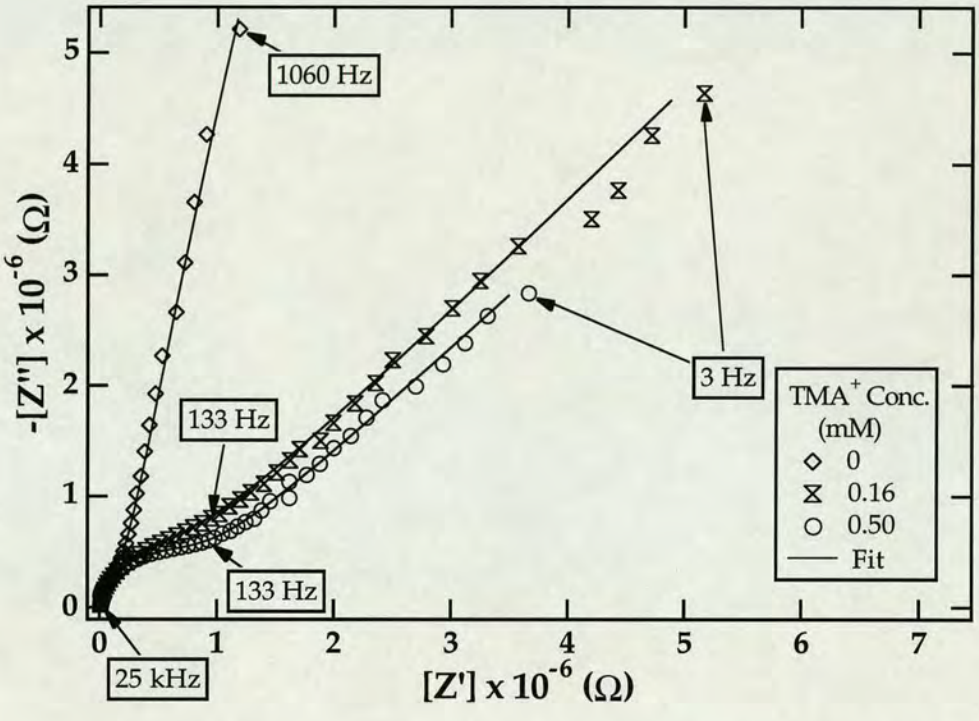

Figure 4.15 - Complex plane impedance plots for cell 4.2, using different concentrations of TMA^+, where the interface was supported at a 25 μm hole. Only half of the experimental points are shown in each case.

TMA^+ results: Clearly, from the fit results of R_1, S_1 and A_1, the change in hole size has resulted in a deviation in the nature of the mass transport, from spherical towards linear diffusion, over the frequency range considered.

Most importantly, it was found that by adding a small amount of TMA^+, to a system where none was initially present, no effect on the value for the charge transfer resistance, R_{ct}, was observed within experimental error. The value of the 'microhole' resistance, R_{Hole}, for a 25 μm hole, using equation 4.2, is estimated to be roughly 1×10^5 Ω for a solution of 10 mM LiCl. For a 10 mM solution of organic phase supporting electrolyte this can be of the order of 3×10^5 Ω, based on previous results. Thus, the values for R_{ct}, in table 4.5 are of a similar order of magnitude to R_{Hole}.

There is basically only one conclusion which may be drawn from the above information, namely that R_{ct} cannot be observed for ion transfer across the ITIES, and any faradaic impedance observed is entirely due to diffusion. This means that the ITIES cannot be represented in terms of a Randles' equivalent circuit, and instead, may only be discussed in terms of figure 2.6 where the faradaic impedance due to ion transfer depends only on diffusion of species to and from the interface.

4.5 Conclusions

Taking both the data from steady-state voltammetry and a.c. impedance into account, the only possible interpretation is that the rate of ion transfer across the interface between two immiscible electrolyte solutions is a quantity which is inaccessible to electrochemical techniques. This is a far cry from the early days of ion transfer kinetics investigations [9], in 1977, where the apparent standard rate constant, k^o, for TMA^+, was thought to be of the order of 10^{-4} cms^{-1}, using cyclic voltammetry - this value was discarded with the advent of iR drop compensation in 1979 [10] - compared with the present study, which sets the k^o value at 32 cms^{-1} or greater. The most recent

evaluation of k^o for TMA^+ transfer was carried out at the large water/nitrobenzene interface (T=20°C), using the technique of a.c. impedance, and yielded a value of 0.12 cms^{-1} [34].

Thus, it has been conclusively shown, by two independent electrochemical techniques, that ion transfer across the ITIES is controlled by diffusion only. All of the forces which are said to influence an ion when it crosses the interface can be assumed to be negligible in comparison with the standard potential for ion transfer.

This conclusion has grave repercussions for those involved in the field of ion transfer kinetics research, whose various standpoints were discussed in chapter two (2.1.5.1). In essence, the a.c. impedance experiments of Samec and colleagues [32], on the transfer of the picrate ion across the large water/nitrobenzene interface, marked a turning point in the pursuit of kinetic data for ion transfer reactions. It has been widely held since then that the standard apparent ionic rate constant, k^o, and the apparent charge transfer coefficient, α, for an ion transfer reaction, are quantities which are easily accessible to accurate measurement. This viewpoint has been enhanced by the work of Senda and co-workers [37] who achieved similar rate constant values for ion transfer, using a.c. impedance. All of the associated theories concerning electrical double layer corrections, energy barriers to the ion transfer reaction, dielectric friction to ion transfer, and so on, are dependent on the fact that kinetic parameters are amenable to measurement. Ongoing work in the field associated with variation of physical parameters of either of the two phases, in relation to kinetics of the ion transfer reaction is necessarily dependent.

The current investigation has shed significant doubt on all of the work that has been carried out previously in the field, and essentially dismisses all of the kinetic theories previously established. In essence, there is no kinetic information which may be achieved through electrochemical analysis of the ITIES - only thermodynamic data may be obtained.

Chapter Five

ASSISTED ION TRANSFER

5.1 Introduction

In a similar fashion to chapter four, the main aim of the experimental work presented in this chapter was to test the ability to which the micro-ITIES could be used to provide kinetic information concerning, in this instance, assisted ion transfer reactions. To that end, the 1:1 assisted ion transfer of potassium across the micropipette tip-supported interface between water and 1,2-dichloroethane (1,2-DCE), by the neutral ionophore dibenzo-18-crown-6 (Db18C6) was investigated using the techniques of steady-state voltammetry and a.c. impedance.

5.1.1 Dibenzo-18-Crown-6

Dibenzo-18-crown-6 was discovered, through serendipity, by Pedersen [155,156] who, at the time, was investigating the effects of bi- and multidentate ligands on the catalytic properties of the vanadyl group, VO, in oxidation and polymerisation reactions. During an attempt to synthesise the multidentate ligand bis[2-(*o*-hydroxyphenoxy)ethyl]ether he observed the formation of a small quantity of white crystals which, as it turned out, were those of Db18C6 (figure 5.1(a)). These crystals were only sparingly soluble in methanol. However, the solubility in methanol increased dramatically when the solvent contained any soluble sodium salt.

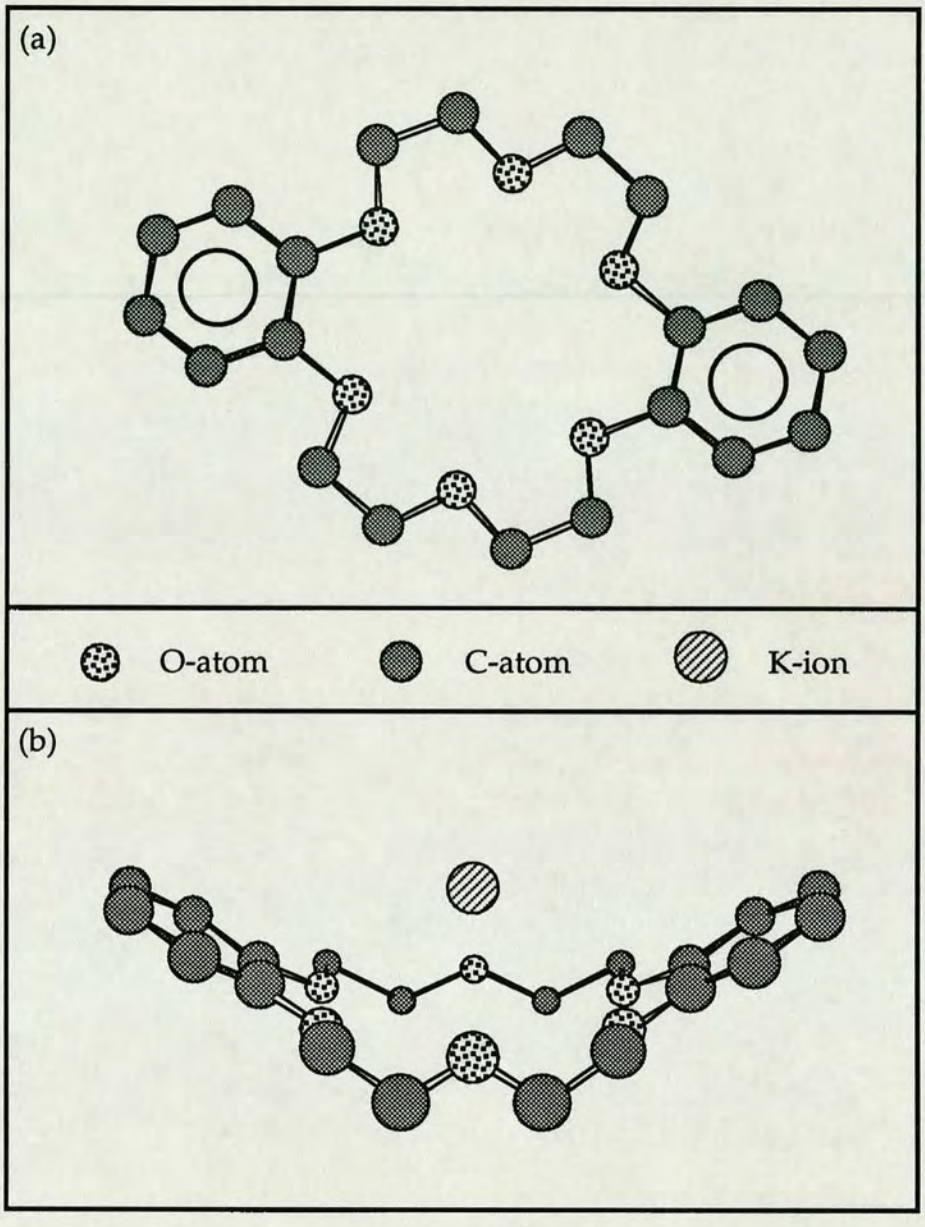

Figure 5.1 - (a) Planar model of Db18C6. (b) Crown-like conformation of Db18C6 in the presence of a potassium ion.

Pedersen concluded that the sodium ion was held in the centre of the Db18C6 molecule by electrostatic attraction between its positive charge and the negative dipolar charge on the six oxygen atoms, arranged symmetrically around it on the polyether ring. Further tests showed that other alkali metal ions and the ammonium ion behaved similarly. The significance of this

discovery was that no one had previously found a synthetic compound which formed stable complexes with sodium and potassium. Pedersen then went on to create many more synthetic macrocyclic polyether compounds which he distinguished with the term 'crown', since the molecular model of Db18C6 reminded him of this shape [155]. Figure 5.1(b) shows a model of the crown-like conformation of the Db18C6 molecule in the presence of a potassium ion.

5.2 Results and Discussion

The reaction under study was:

$$K^+(aq) + Db18C6(org) \underset{k_b}{\overset{k_f}{\rightleftharpoons}} K^+Db18C6(org) \qquad (5.1)$$

where k_f and k_b have their usual meaning, and the cell used for this study was the following:

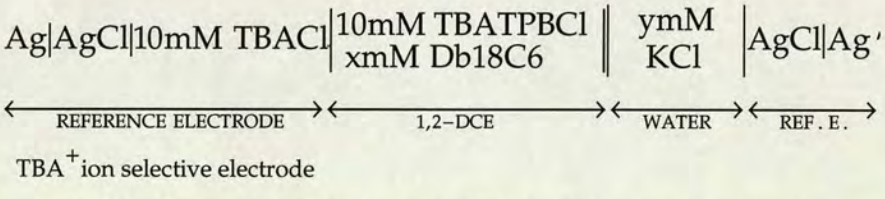

Cell 5.1 - where x and y correspond to a value given in the text.

5.2.1 Determination of the Diffusion Coefficient of Db18C6

The diffusion coefficient of the Db18C6 in the organic phase, D^{org}_{Db18C6}, was calculated from cyclic voltammetry experiments conducted at the large ITIES (at a room temperature of 23 ± 1°C), using cell 5.1, where x and y were 0.6 (mM Db18C6) and 10 (mM KCl) respectively.

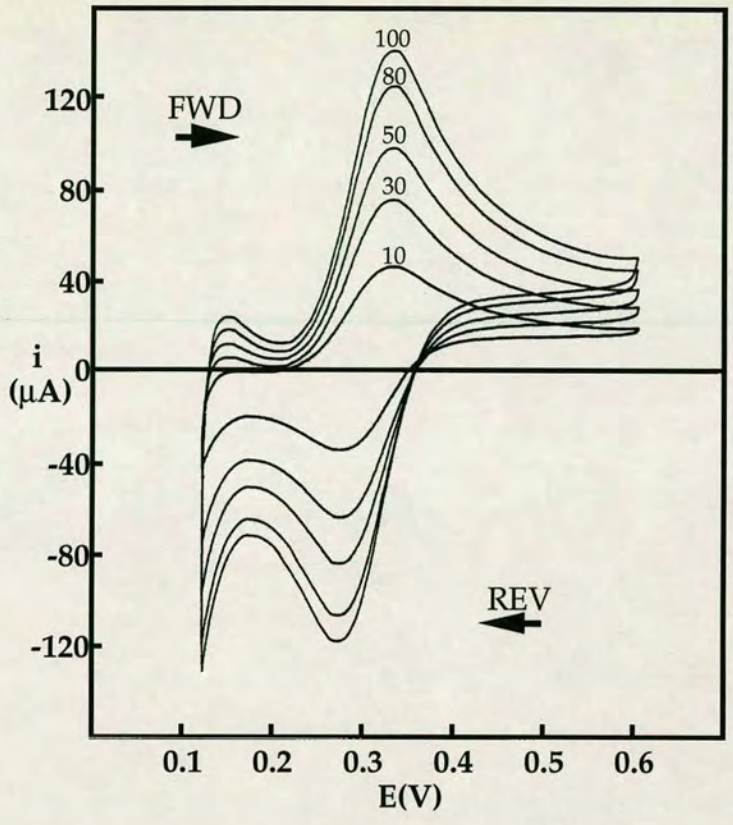

Figure 5.2 - Cyclic voltammograms for potassium ion transfer, facilitated by Db18C6, at the large interface between water and 1,2-DCE - using different scan rates (10, 30, 50, 80, and 100 mVs^{-1}). x = 0.6, y = 10, cell 5.1.

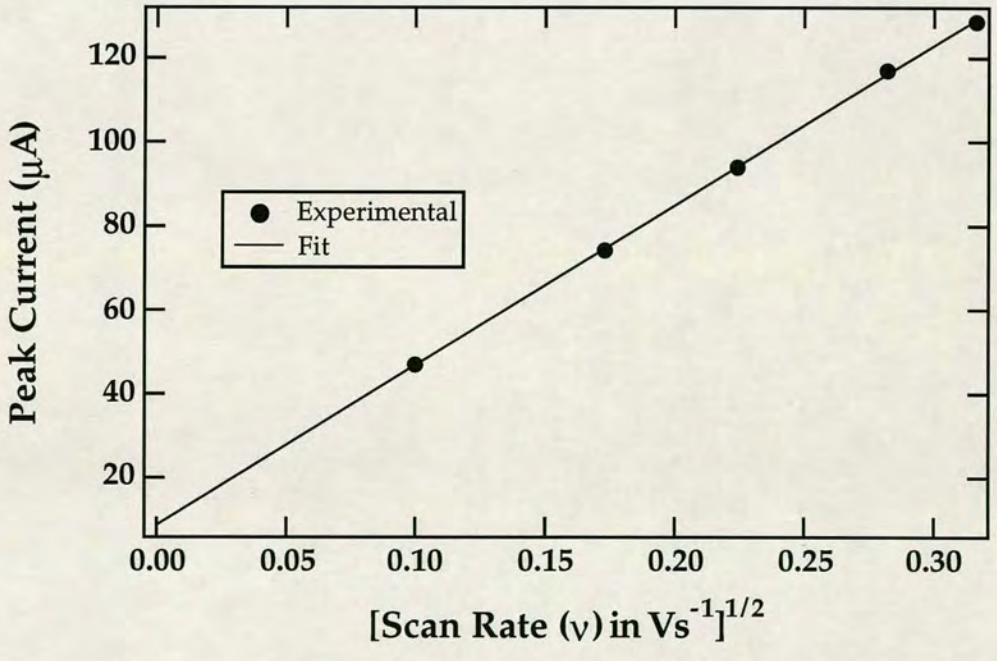

Figure 5.3 - Graph of peak current versus the square root of the scan rate for the voltammograms shown in figure 5.2.

The slope of the plot of peak current versus the square root of the scan rate gives a value for D^{org}_{Db18C6} of 4.55 (± 0.25) x 10^{-6} cm^2s^{-1} (average of two results) using the Randles-Sevcik equation (equation 2.2.1). The area of the interface was taken to be 1.13 cm^2. Figure 5.2 shows a series of cyclic voltammograms, recorded at different scan rates, for the transfer process at the large ITIES, and figure 5.3 shows the graph of peak current versus the square root of the scan rate for figure 5.2. The value obtained for D^{org}_{Db18C6} is in good agreement with that reported by Osborne *et al.* [58] of 4.8 x 10^{-6} cm^2s^{-1}, for the assisted transfer of ammonium across the water/1,2-DCE interface.

5.2.2 Internal Tip Radius Dependence Study

5.2.2.1 Steady-State Voltammetry

Micropipettes were fabricated as described in 3.2.1, and figure 5.4 shows the potential window obtained for a micropipette which had an internal tip radius of 4.5 μm. Tip radii quoted hereafter always refer to internal tip radii.

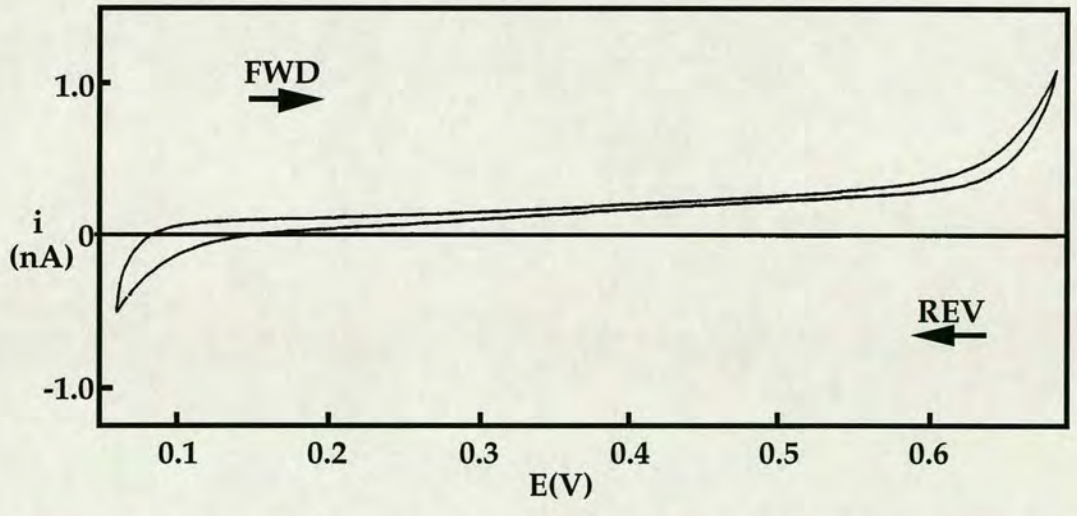

Figure 5.4 - Cyclic voltammogram for cell 5.1 (x = 0, y = 10). The scan rate was 0.1 Vs^{-1}. Tip radius = 4.5 μm.

In the first set of experiments, the steady-state current with respect to the internal tip radius was investigated. Thin-walled micropipettes (denoted (a) in table 5.1), having internal tip radii of 16, 8, 6, 5, 3.5, and 2.5 μm, and thick-walled micropipettes (denoted (b) in table 5.1) having internal tip radii of 0.84 and 0.6 μm, were used to support the micro-interface between the aqueous KCl phase inside the pipette (y = 10, cell 5.1) and the organic (1,2-DCE) phase outside it, containing the Db18C6 (x = 0.6, cell 5.1). The scan rate in all of the cyclic voltammetry experiments was 0.1 Vs^{-1}. This might be considered excessive when attempting steady-state voltammetry, however, the response was shown to be independent of the scan rate between 0.1 and 0.02 Vs^{-1}. Thus, since the micropipette can suffer adversely from vibrations, leading to somewhat erratic responses over lengthy sweeps, a scan rate of 0.1 Vs^{-1} was considered optimal.

Figure 5.5 shows the steady-state cyclic voltammogram recorded for the 16 μm radius tip, and figure 5.6 is the semi-logarithmic plot of $\ln(i/(i_{ss}-i))$ versus potential for the forward wave, which yields a straight line, with a slope of 39.9 V^{-1}. The Tomes' criterion for the forward wave ($E_{3/4}-E_{1/4}$) was found to be 55 ± 4 mV . As mentioned in chapter four, for a fully reversible charge transfer process, the semi-logarithmic plot should yield a slope of 39.2 V^{-1}, and the Tomes' criterion should be equal to 55.5 mV, at 23°C. Thus, the assisted ion transfer of potassium by Db18C6 can be said to be effectively reversible under the experimental conditions. Therefore, the effect of iR drop in the micropipette tip and in the organic phase seems to have been eliminated at this tip size.

Figures 5.7(a) and 5.7(b) show the steady-state cyclic voltammetric responses obtained for internal tip radii of 8, 6, 5, 3.5, and 2.5 μm. These waves were

analysed in the same way as the 16 μm radius tip, and the results are presented in table 5.1, together with values for the half-wave potential.

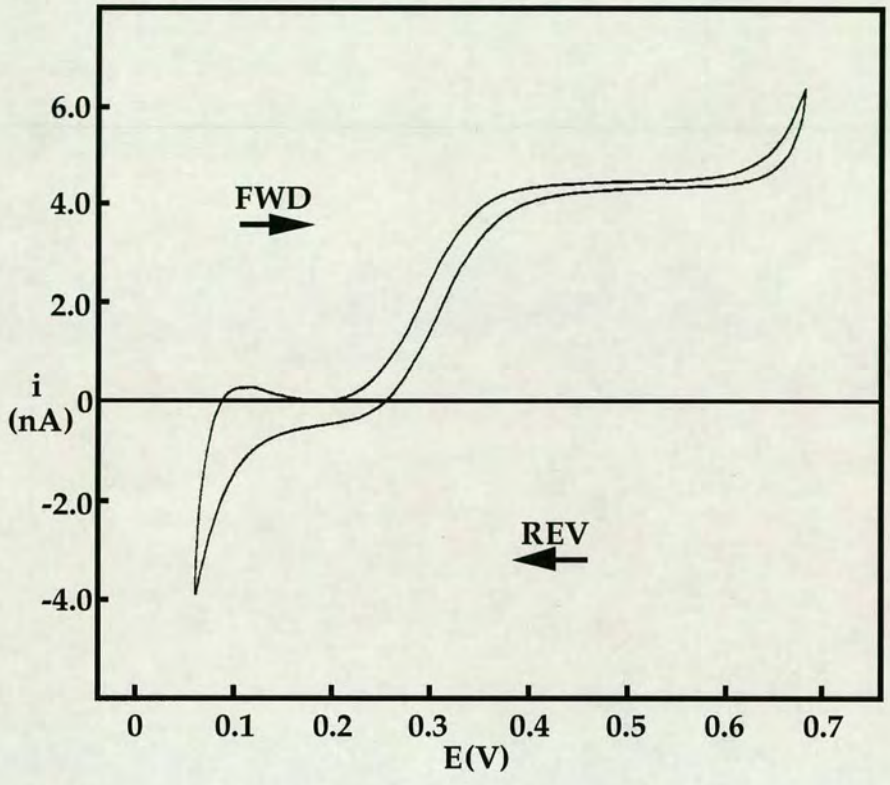

Figure 5.5 - Steady-state cyclic voltammogram for an internal tip radius of 16 μm (thin-walled glass). x = 0.6 (mM Db18C6), y = 10 (mM KCl), cell 5.1.

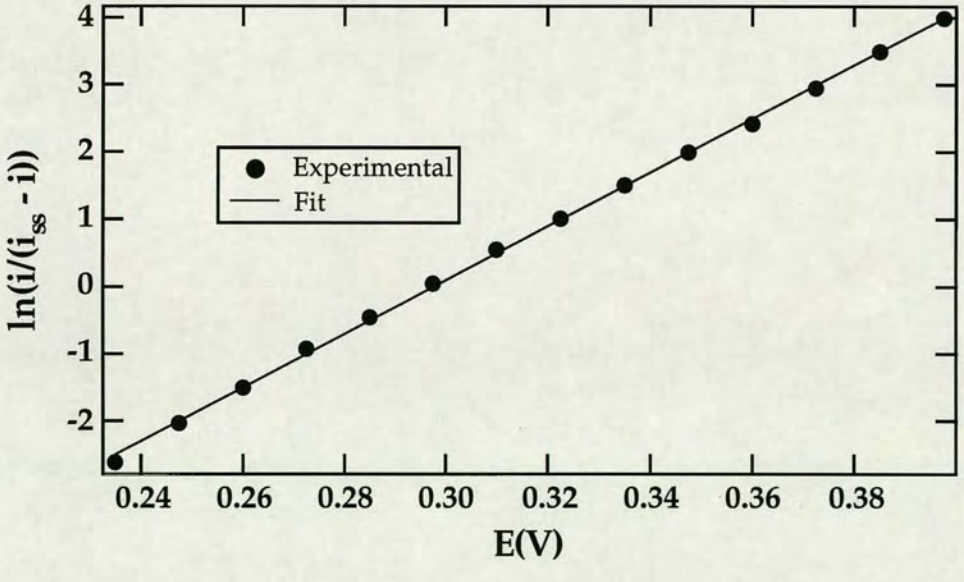

Figure 5.6 - Plot of $ln(i/i_{ss} - i)$ versus potential for the 16 μm radius tip.

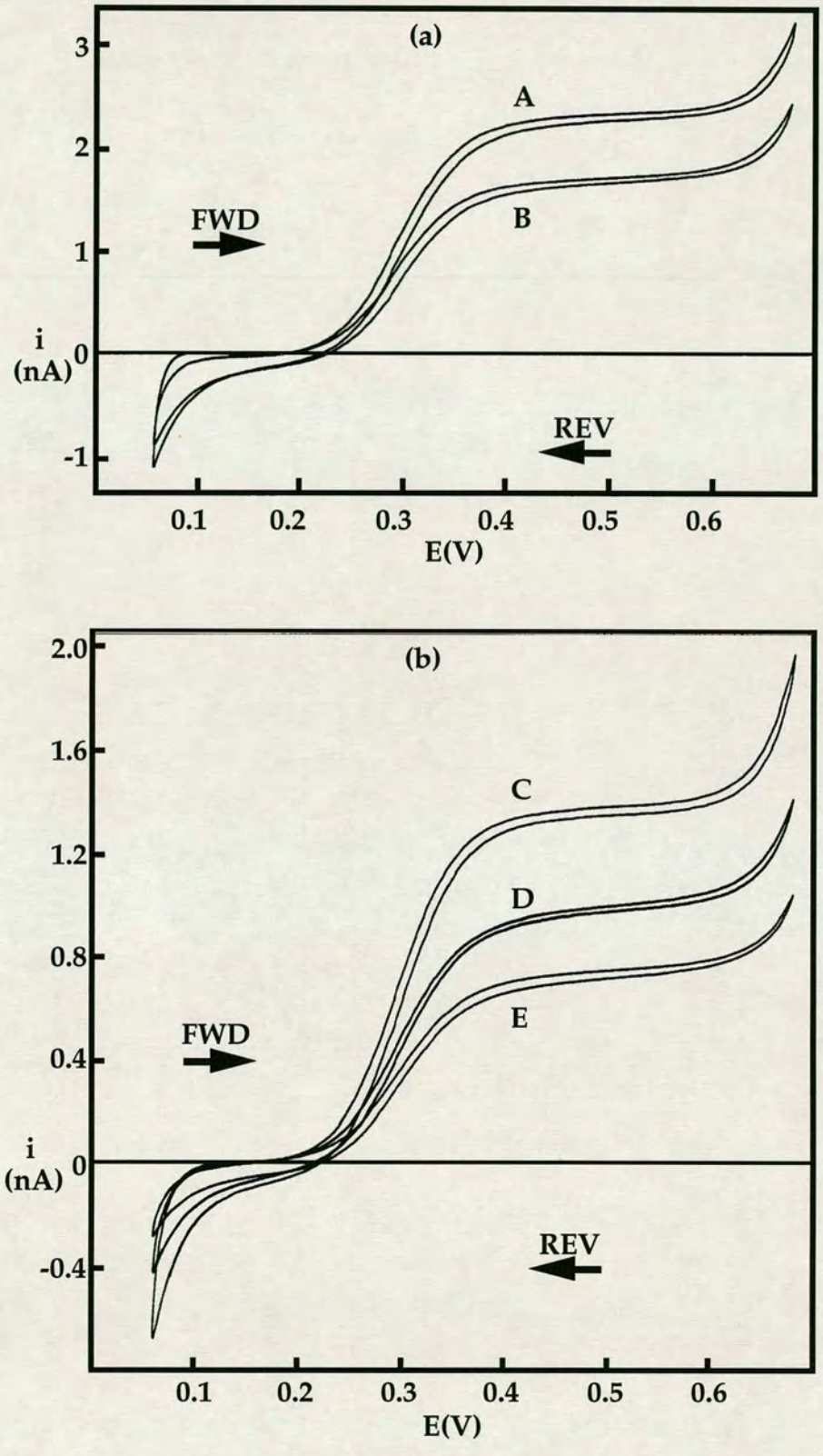

Figure 5.7 - Steady-state cyclic voltammograms for internal tip radii of (A) 8, (B) 6, (C) 5, (D) 3.5 and (E) 2.5 μm (thin-walled glass). x = 0.6 (mM Db18C6), y = 10 (mM KCl), cell 5.1.

Table 5.1 - Data from tip radius dependence study (potassium ion concentration = 10 mM; Db18C6 concentration = 0.6 mM (cell 5.1))

Tip Radius (μm)	i_{ss} (nA) ± 12%	Slope (V^{-1})	$E_{3/4}$-$E_{1/4}$ ± 4(mV)	$E_{1/2}$ ± 2 (mV)
(a) 16 ± 0.25	4.40	39.9	55	295
8 ± 0.25	2.30	34.6	62	296
6 ± 0.25	1.65	35.7	63	297
5 ± 0.25	1.35	35.6	64	301
3.5 ± 0.25	0.96	33.4	65	302
2.5 ± 0.25	0.70	34.7	63	304
(b)0.84*± 0.05	0.16	34.1	65	300
0.6**± 0.05	0.10	35.0	64	302

(- thick-walled glass, pulling protocol with -10°C between heating steps)*

*(** - thick-walled glass, pulling protocol as for thin-walled glass)*

There was a significant change in behaviour between a tip radius of 16 μm and that of 8 μm. The transfer process appears to be reversible at 16 μm, whereas for tip radii of 8 μm or less the transfer process deviates from this to become quasi-reversible in nature. At the same time, however, the slope of the $\ln(i/(i_{ss}-i))$ versus potential plots and the Tomes' criteria remain relatively constant over the range of tip radii 8 - 0.6 μm, suggesting that the change in behaviour must occur below a certain size of tip. Initially, it was thought that this phenomenon was a consequence of increased tip resistance when working with smaller micropipettes. However, this notion was ruled out when, as will be shown later (section 5.2.3), experimental evidence was obtained which showed that if the tip resistance was the controlling factor, then the expected iR drop for the 16 μm radius tip would be greater than that

for the rest. Clearly, this is in conflict with the result in figure 5.5 which demonstrates the transfer process to be reversible.

Another aspect of the experimental results seems to be a change in the half-wave potential for the transfer process with decreasing tip size. However, this is misleading since results obtained using thick-walled glass pipettes, listed in table 5.1(b), illustrate that the half-wave potential is effectively constant over the radii range 8 to 0.6 μm. This then rules out the possibility that the reaction is controlled by charge transfer kinetics over the range of tip sizes studied, having already ruled out iR drop. Figure 5.8 shows the steady-state response obtained for the 0.6 μm radius, thick-walled, micropipette, and figure 5.9 shows the scanning electron micrograph of the tip. This picture illustrates one of the disadvantages of the micropipette technique - namely, the accumulation of debris in the tip. This debris usually takes the form of glass or AgCl fragments, and contributes to the non-reusability of the micropipette.

The steady-state current versus tip radius for the 8, 6, 5, 3.5 and 2.5 μm radii tips (table 5.1(a)) was plotted as shown in figure 5.10. Additional lines on this figure, showing the theoretical response for a shrouded hemisphere in an infinite insulating plane, and for an isolated sphere, were calculated using the diffusion coefficient value previously stated.

The results demonstrate that for thin-walled glass the micropipette tip-supported ITIES exhibits behaviour between that of a hemisphere and a sphere:

Microhemisphere: $$i_{ss} = 2\pi zFD^{org}_{Db18C6}\, c^{org,b}_{Db18C6}\, r_h \qquad (5.2)$$

Micropipette: $$i_{ss} = 3.35\pi zFD^{org}_{Db18C6} c^{org,b}_{Db18C6} r_p \quad (5.3)$$

Microsphere: $$i_{ss} = 4\pi zFD^{org}_{Db18C6} c^{org,b}_{Db18C6} r_s \quad (5.4)$$

where $c^{org,b}_{Db18C6}$ = bulk concentration of Db18C6 in the organic phase, and r=radius (the subscripts p and s represent pipette and sphere respectively).

The reasons for this behaviour are not explicitly clear, yet there are two possibilities:

(i) The interface is a partial sphere, with the aqueous phase bulging out of the pipette, thereby leading to an increased steady-state current by virtue of the greater interfacial area.

(ii) The interface is hemispherical in shape and the difference in current arises through Db18C6 diffusing to the tip from above the imaginary insulating plane. The interface is, of course, not in an infinite insulating plane, and the glass wall at the tip of the micropipette was very thin (see figure 3.2). Shoup and Szabo [157], showed that for a microdisc embedded in the top of a cylinder, the radius of the surrounding insulating material should be at least twice the radius of the disc for the behaviour of the electrode to be similar to that of a microdisc in an infinite insulating plane. In the case where the insulating material is of negligible thickness, they predicted an increased current of 40%. Obviously, for a hemisphere the increase would be somewhat different.

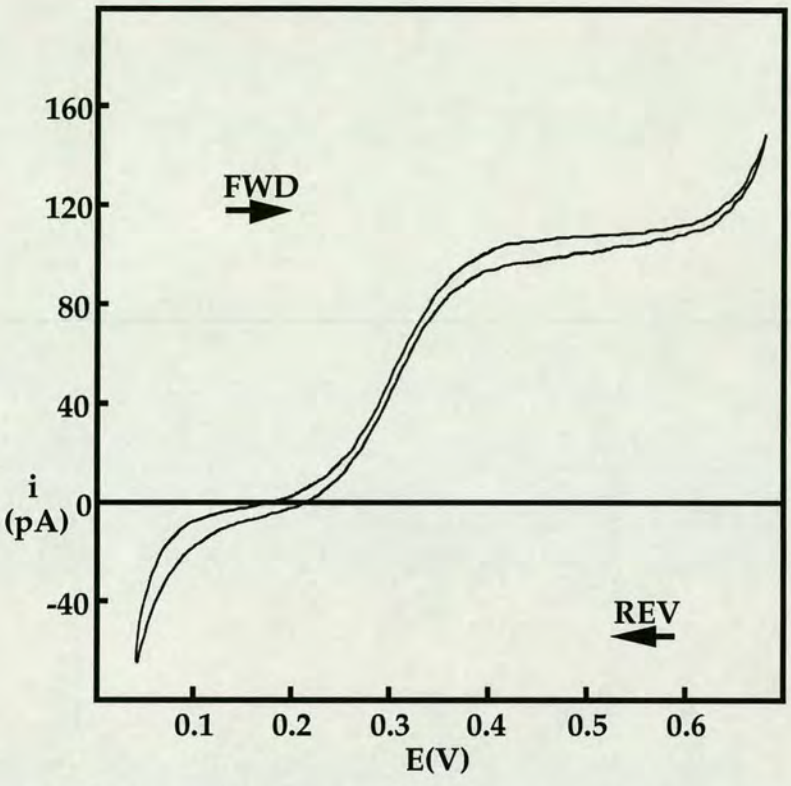

Figure 5.8 - Steady-state cyclic voltammogram for an internal tip radius of 0.6 μm (thick-walled glass). x = 0.6 (mM Db18C6), y = 10 (mM KCl), cell 5.1.

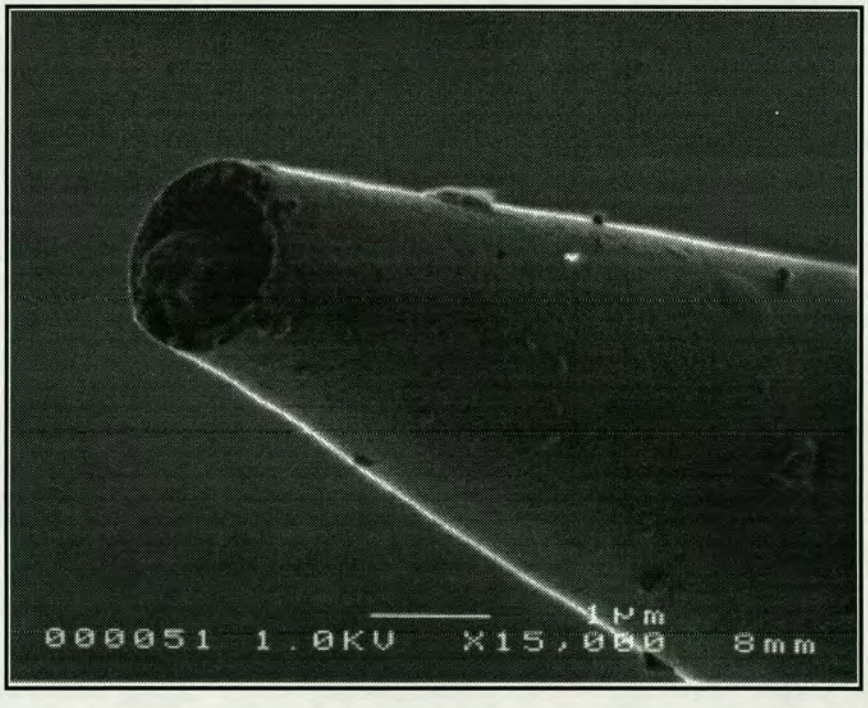

Figure 5.9 - S.E.M. picture of a 0.6 μm radius pipette, magnified 15000 times.

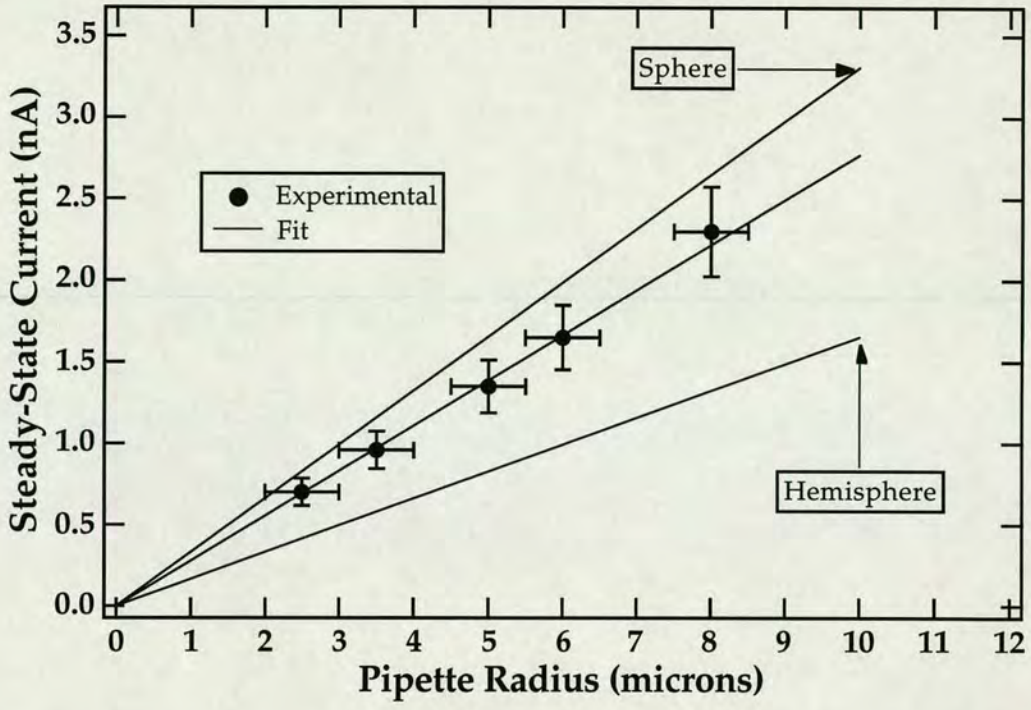

Figure 5.10 - Plot of the steady-state current versus tip radius for the voltammograms in figure 5.7.

Stewart *et al.* [158] showed the behaviour of their thick-walled micropipettes to be between that of a microdisc and a microhemisphere, in an infinite insulating plane, for ingress transfer of the tetraethylammonium ion. As explained in chapter one (1.5.1), however, the crudity of their pipette manufacture may have influenced this result. Another factor, however, may be the fact that the micropipette profiles are very different for thick- and thin-walled glass. In general, the profile for the thick glass is much more cylindrical than that of the thin glass, for the same pulling protocol. This might have an effect on the shape of the interface from pressure related considerations. The results obtained using thick-walled glass in this case, (table 5.1(b)) showed behaviour which was close to that of a hemisphere in an infinite insulating plane.

5.2.2.2 Chronoamperometry

The current-time response, under the same experimental conditions as in 5.2.2.1, was followed by means of chronoamperometry, for micropipettes having tip radii of 2.5 and 5 μm. The potential was pulsed from a point where there is effectively zero assisted ion transfer (0.160 V on figure 5.7) to a point on the limiting current plateau (0.460 V on figure 5.7) thereby producing the observed current-time responses shown in figure 5.11.

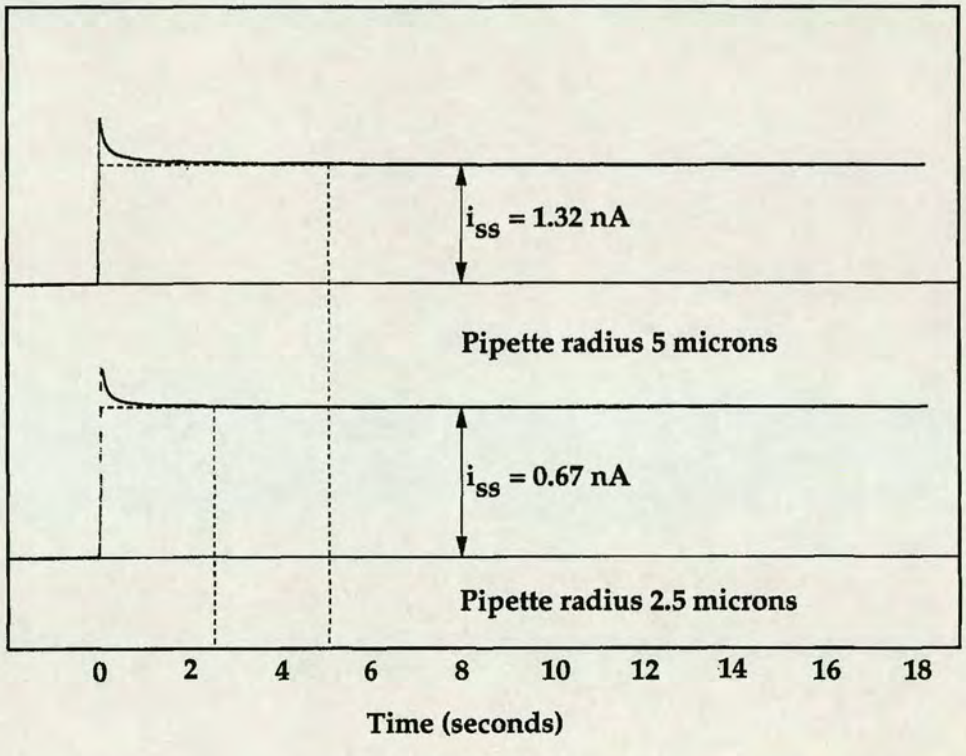

Figure 5.11 - Chronoamperograms for internal tip radii of 5 and 2.5 μm.

These experiments were carried out in order to have independent steady-state current values for comparison with those obtained using cyclic voltammetry. The data shown in figure 5.11 and table 5.1(a) demonstrate that the two techniques are in good agreement. The times taken to reach a steady-state (the point at which there is no further decrease in current with

respect to the baseline) were 2.5 and 5 seconds (approximately) for the 2.5 and 5 μm radius pipettes respectively.

5.2.3 Variation of the Potassium Ion Concentration

In this investigation, the concentration of aqueous KCl (y in cell 5.1) was varied, and a series of 3.5 μm radius pipettes were used to conduct the experiments. Potassium ion concentrations of 5, 50 and 100 mM were studied, with x = 0.6 (mM Db18C6).

The cyclic voltammograms obtained are shown in figure 5.12, together with the result obtained for y = 10 (cell 5.1) from section 5.2.2.1. The relevant wave information is presented in table 5.2. From the results it is evident that there is good correlation between the different micropipettes and the steady-state current values. The results also illustrate that the observed current is proportional to the Db18C6 concentration when x << y (cell 5.1).

Table 5.2 - Data from potassium ion concentration variation study. (Radius of micropipette tips = 3.5 μm; Db18C6 concentration = 0.6 mM (cell 5.1)).

K^+ conc. (mM)	i_{ss} (nA) ± 12%	Slope (V^{-1})	$E_{3/4}$-$E_{1/4}$ ± 4 (mV)	$E_{1/2}$ ± 2 (mV)
100	1.00	38.9	57.5	186
50	0.98	35.9	60	210
10	0.96	33.4	65	302
5	0.96	31.1	70	340

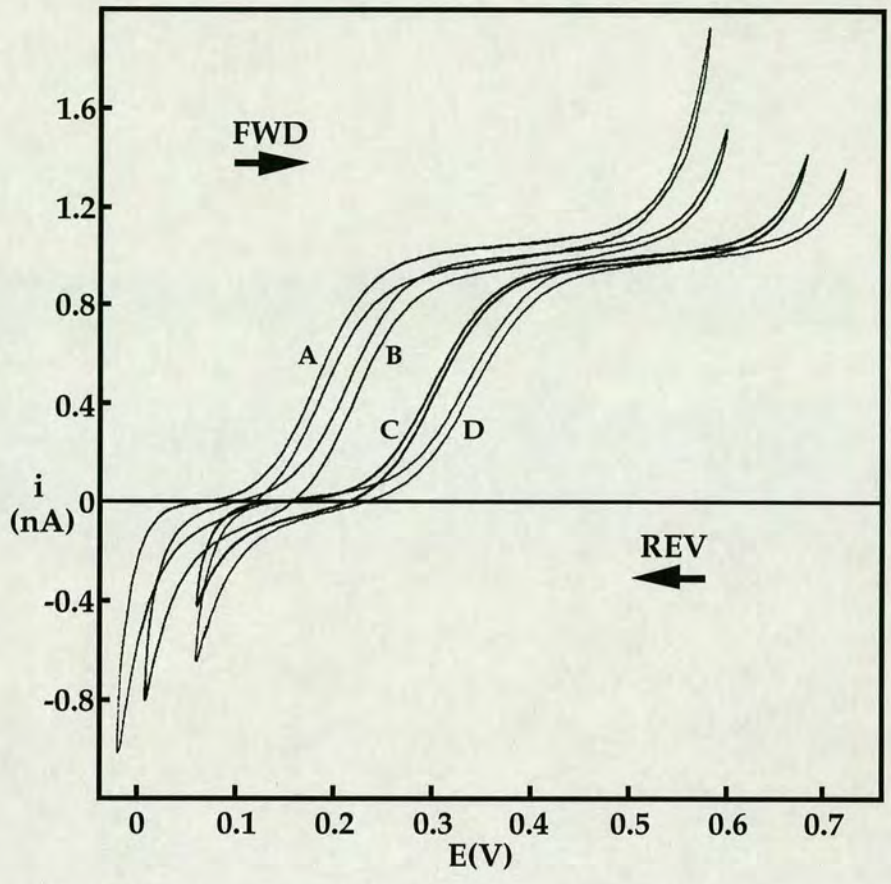

Figure 5.12 - Steady-state cyclic voltammograms for potassium ion concentrations of (A) 100, (B) 50, (C) 10, and (D) 5 mM. Db18C6 concentration = 0.6 mM; radius of micropipette tips = 3.5 μm (cell 5.1).

In chapter two, it was explained that the half-wave potential of the assisted ion transfer reaction could be expressed in terms of the following equation (equation 2.2.4), for the case where x<<y (cell 5.1):

$$\Delta_{org}^{aq}\phi_{MI^+}^{1/2} = \Delta_{org}^{aq}\phi_{M^+}^{o'} + \left(\frac{RT}{2zF}\right)\ln\left(\frac{D_I^{org}}{D_{MI^+}^{org}}\right) - \left(\frac{RT}{zF}\right)\ln\left(K_c^{org}c_{M^+}^{aq}\right) \qquad (5.5)$$

Thus, for each decade increase in potassium ion concentration the half-wave potential should shift to less positive potentials by approximately 60 mV. This is only valid, however, when the half-wave potential value is referenced

against the half-wave transfer potential of TMA^+ (an exercise which is relatively impossible to carry out for the micropipette) and when a fully reversible reaction is under consideration. Clearly the micropipette is only in the reversible case for 100 mM KCl. The half-wave potential values quoted in table 5.2 show shifts of 118 and 130 mV. This result is not unexpected since these values are not referenced on the 'TPAsTPB' scale, and the cell potential is affected by the addition of both potassium and chloride ions.

Values for $\ln K_c^{org}$ of 9.9 and 10.4 for the K^+Db18C6 system have been reported by Campbell [158] and Sabela [159] respectively. Normally, the assumption is made that the diffusion coefficient of the ionophore and the ion-ionophore complex are equal. Indeed, Osborne [114] demonstrated that for the assisted transfer of the ammonium ion by Db18C6, at the large ITIES, the diffusion coefficients are effectively equivalent.

Shao *et al.* [56], in their micropipette experiments, showed that the diffusion coefficient of the free ionophore, D^{org}_{Db18C6}, is approximately 1.6 times faster than that of the ion-ionophore complex, however, the drawbacks of previous pipette experiments have already been described, and it has been noted that micropipette experiments can suffer from a 'floating' baseline, which was not taken into account in their paper.

The data in table 5.2 demonstrate that as the potassium ion concentration is increased the effect of migration on the wave shape is minimised.
This then shows the change from full reversibility for the 10 mM K^+ case to be an artifact created by the asymmetry of the diffusion regime at the micropipette. Essentially, on the rising portion of the wave, the assisted ion

transfer reaction is dependent on both the diffusion of the potassium ion (linear) and Db18C6 (spherical). At high rates of mass transfer, however, the reaction becomes limited only by the diffusion of Db18C6 to the interface.

Osborne [114], using a 10 μm radius hole drilled in a polyester film, showed that the assisted ion transfer of potassium by Db18C6 at the microhole-supported ITIES is fully reversible - even when the potassium ion concentration is 1 mM and that of the Db18C6 is 0.5 mM. This result confirms the conclusion for the micropipette, that the change in reversibility is an artifact of the diffusion regime, and not of the reaction itself.

5.2.4 Variation of the Db18C6 Concentration

In these experiments, the steady-state current as a function of Db18C6 concentration was studied, using values of x = 0.25, 0.5, 0.6 and 1 (mM, cell 5.1), and a series of 3 μm radius pipettes. The concentration of the potassium ion was 10 mM (y, cell 5.1). The observed current responses are illustrated in figure 5.13. The waves were analysed as before and the data is displayed in table 5.3.

Table 5.3 - Data from Db18C6 concentration variation study. (Radius of micropipette tips = 3 μm; Potassium ion concentration = 10 mM)

Db18C6 conc. ± 0.06 (mM)	i_{ss} (nA) ± 12%	Slope (V^{-1})	$E_{3/4}$-$E_{1/4}$ ± 4 (mV)	$E_{1/2}$ ± 2 (mV)
1.0	1.40	31.0	71	310
0.6	0.81	34.6	65.5	301
0.5	0.67	36.0	63.5	303
0.25	0.38	36.3	61	304

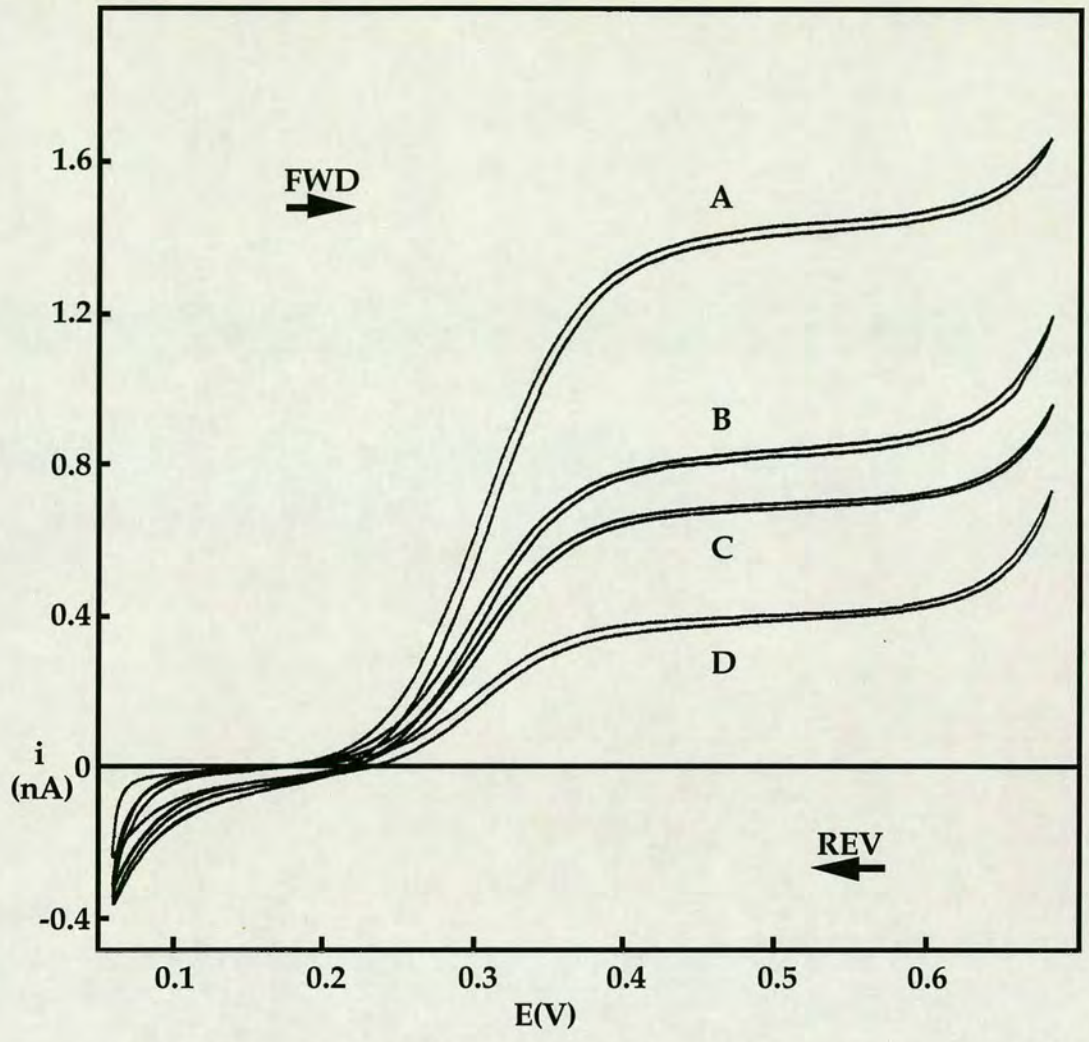

Figure 5.13 - Steady-state voltammograms for Db18C6 concentrations of x = (A) 1, (B) 0.6, (C) 0.5 and (D) 0.25 (mM), y = 10 (mM KCl), cell 5.1. Radius of micropipette tips = 3 μm.

In this case, the effect of migration on the wave shape is minimised by a decrease in the Db18C6 concentration. Figure 5.14 shows a plot of the steady-state current versus Db18C6 concentration. On the same plot is the line calculated using equation 5.3, showing good agreement between the experimental and the expected steady-state current.

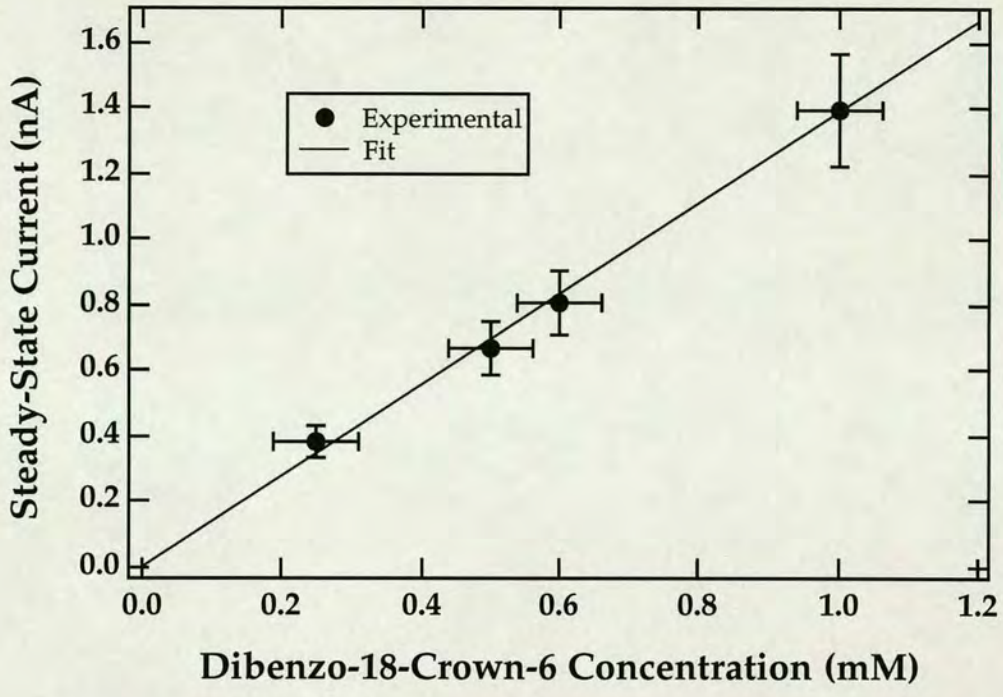

Figure 5.14 - Plot of steady-state current versus Db18C6 concentration.

5.2.5 Steady-State Response for Sodium and Rubidium Ions

In this study the potassium ion, in cell 5.1, was substituted by sodium and rubidium (both known to form stable 1:1 complexes with Db18C6) in successive experiments. The concentration of Db18C6 (x in cell 5.1) was 0.6 mM, and the concentration of the alkali metal ion was 10 mM. Here the radius of the micropipette tips used was 2.5 μm. These experiments were performed to check whether the change in reversibility of the transfer reaction applied for different ions. The wave criteria are listed in table 5.4, and those of the result for the potassium ion (from table 5.1(a)) are also included for comparison. The steady-state response obtained for rubidium is shown in figure 5.15.

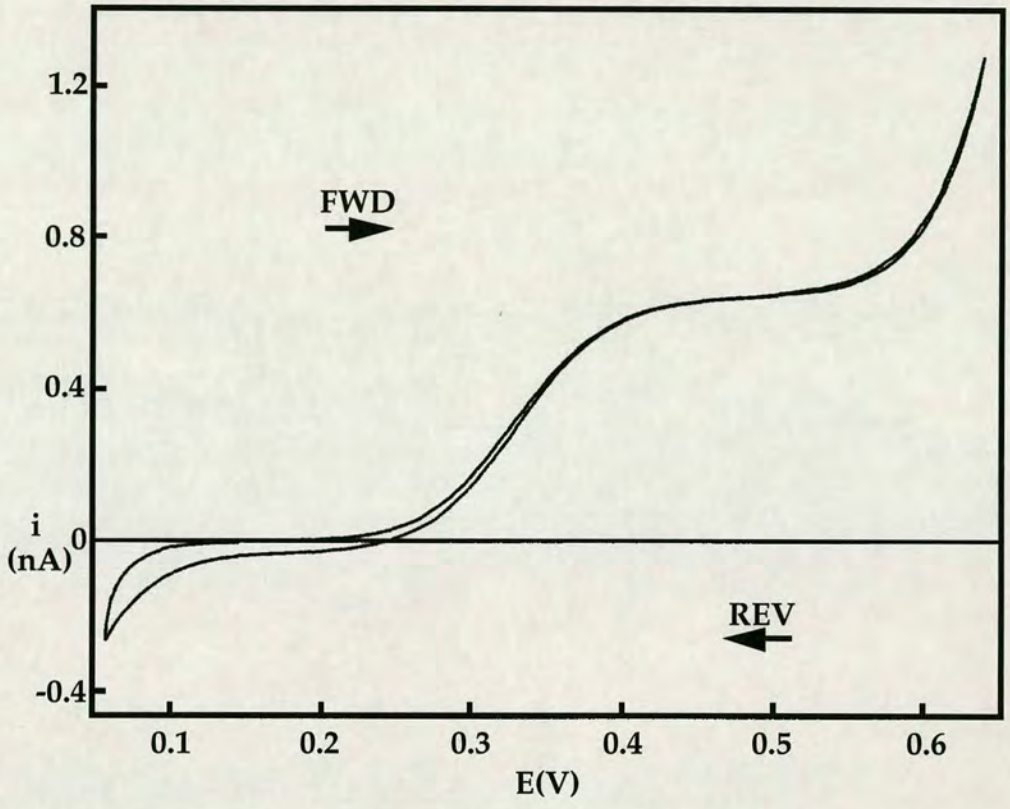

Figure 5.15 - Steady-state voltammogram for rubidium ion transfer across the water/1,2-DCE interface, assisted by Db18C6. RbCl concentration = 10 mM; Db18C6 concentration = 0.6 mM (cell 5.1 - no KCl). Tip radius = 2.5 μm.

Table 5.4 - Experimental wave criteria for assisted transfer of different ions, by Db18C6. Metal ion concentration = 10 mM; Db18C6 concentration = 0.6mM; radius of micropipette tips = 2.5 μm.

Ion	i_{ss} (nA) ± 12%	Slope (V^{-1})	$E_{3/4}$-$E_{1/4}$ ± 4 (mV)
Sodium	0.71	35.4	65
Rubidium	0.62	36.7	63
Potassium	0.70	34.7	63

The results in table 5.4 indicate that the change in reversibility at a certain size of micropipette tip is not exclusive to potassium, and further

demonstrate the reproducibility of the steady-state current with respect to tip radius. The data also show that the ionic radius is relatively unimportant in terms of the reversibility of the transfer process.

5.2.6 A.C. Impedance

5.2.6.1 Evaluation of the Micropipette Tip Resistance

In this investigation, the impedance of a solution of KCl present throughout the cell design of figure 3.3, in place of those solutions used previously for the steady-state voltammetry measurements, was evaluated. The impedance of the system was measured under different conditions - the KCl concentration and tip radius were varied independently. These experiments were carried out for two purposes - (1) to evaluate the possibility of the tip resistance affecting the steady-state voltammetric responses observed in the previous sections and (2) to assess the effect of tip resistance on a.c. impedance measurements of the micropipette tip-supported ITIES. Impedance measurements on a 'blank' system, with the micropipette tip broken off were also carried out.

The total resistance was approximated to be the sum of the resistance of: (1) the KCl solution between the end of the Ag/AgCl wire placed in the micropipette and the micropipette tip cone; (2) the solution in the micropipette tip cone; and (3) the solution of KCl between the end of the tip and the other Ag/AgCl wire. The finite impedance of the Ag/AgCl wires was deemed to be negligible, as in chapter four.

In the first part of this study, a series of 3.5 μm radius pipettes (and the remainder of the glass cell) were filled with varying concentrations of KCl (0.01, 0.1, and 1 M) and the impedance was evaluated. The amplitude of the exciting signal was ± 30 mV for 0.01 M KCl, ± 25 mV for 0.1 M KCl, and was varied between ± 25 and ± 15 mV for 1 M KCl (these values were chosen arbitrarily). The frequency range in these experiments was 5 kHz to 53 Hz for 0.01 M KCl, and 5.09 kHz to 73 Hz for 0.1 and 1 M KCl. The accuracy between response cycles was stipulated to be 1%. Table 5.5 lists the data obtained for all the experiments. Each result was based on an average of the last ten Z' results in the low frequency domain, for a given experiment, and was furthermore an average of at least two such determinations using the same pipette. Figures 5.16-5.18, showing the 'Bode' plots of Z' versus the frequency (f) for the three different concentrations, demonstrate the efficacy of this approach.

As the concentration of KCl is increased by a factor of 10, the total impedance decreases by a factor of 10, approximately. From the 'Bode' plots it was observed that Z' diminishes as the frequency is increased, and that the amount of diminution depends on the concentration of KCl employed - a large decrease for 0.01 M KCl, and effectively no decrease for 1 M KCl.

Table 5.5 - Data from a.c. impedance analysis of pipettes - (K^+ concentration dependence using 3.5 μm radius pipettes).

Potassium ion concentration (M)	Total resistance (Ω) x 10^{-4}
1	4.74 ± 0.07
0.1	46.3 ± 1.3
0.01	498 ± 10

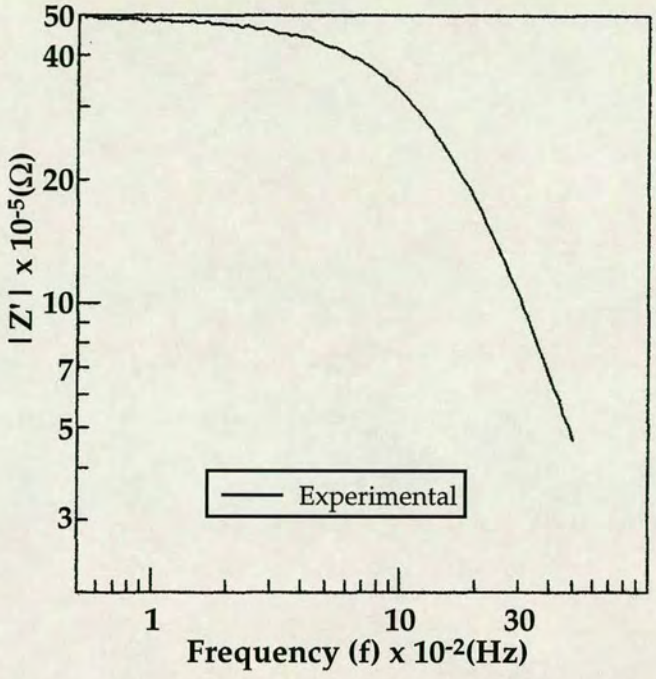

Figure 5.16 - 'Bode' plot of the magnitude of the real part of the impedance as a function of the frequency for 0.01 M KCl. Scales are in natural logarithm form.

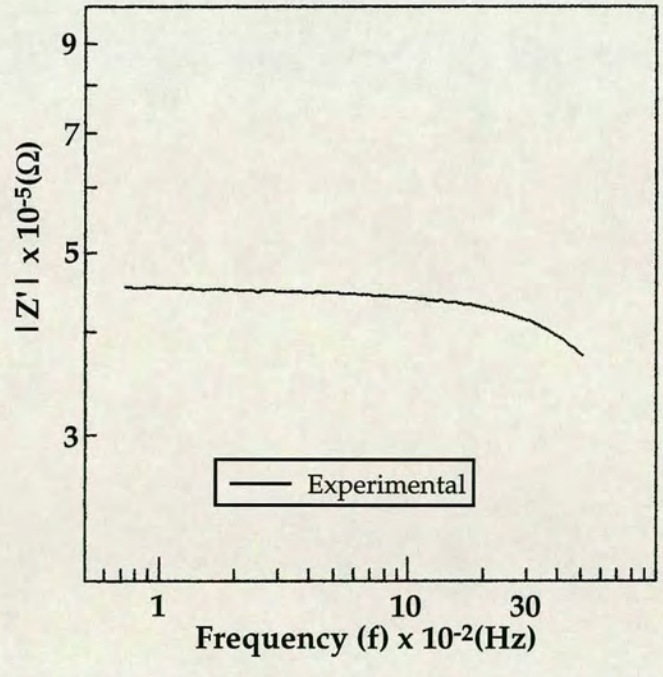

Figure 5.17 - 'Bode' plot of the magnitude of the real part of the impedance as a function of the frequency for 0.1 M KCl. Scales are in natural logarithm form.

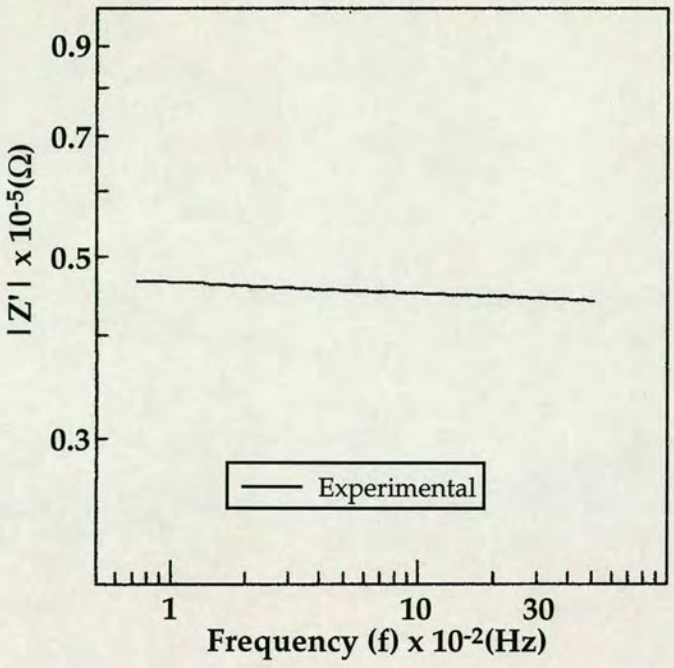

Figure 5.18 - 'Bode' plot of the magnitude of the real part of the impedance as a function of the frequency for 1 M KCl. Scales are in natural logarithm form.

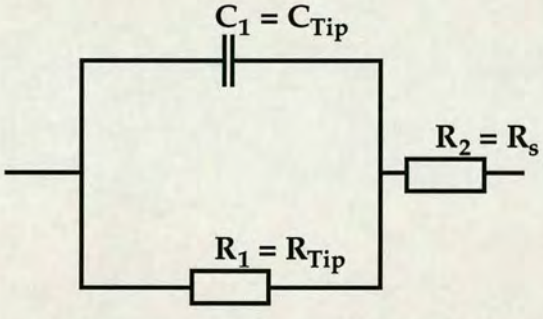

Model 5.1 - Analogous to model 4.1 (chapter four).

In light of the high frequency behaviour observed for the 0.01 and 0.1 M KCl experiments, it was decided to try to model the impedance results obtained using model 5.1 (analogous to model 4.1, where C_1 is now assumed to be equivalent to the capacitance of the tip, C_{Tip}, and R_1 is assigned to the resistance of the electrolyte solution in the volume of the tip, R_{Tip}). For fitting purposes, only the first 70 points out of 101 were considered in each case, corresponding to the frequency ranges 5 kHz to 217 Hz (0.01 M KCl)

and 5.09 kHz to 272 Hz (0.1M KCl). The reason for this was simply that the quality of the impedance data, especially in the case of the results for 0.1 M KCl, was relatively poor at lower frequencies. The average of the fit results (two determinations) are given in table 5.6.

Table 5.6 - Averaged data from experimental impedance of micropipettes - using model 5.1. Figures in brackets refer to the average of the percentage error on the individual fit results. Fitting was to points in the frequency range 5 kHz to 217 Hz (0.01 M KCl) and 5.09 kHz to 272 Hz (0.1 M KCl).

KCl (M)	0.01	0.1
$R_{Tip} \times 10^{-5}$ (Ω)	47.73 ± 0.69 (0.4)	3.36 ± 0.10 (1.8)
$C_{Tip} \times 10^{11}$ (F)	2.34 ± 0.01 (0.7)	5.18 ± 0.14 (3.7)
$R_s \times 10^{-5}$ (Ω)	1.29 ± 0.05 (7.3)	1.18 ± 0.07 (5.2)

Figures 5.19 and 5.20 illustrate the complex plane behaviour exhibited by the micropipette for the two different concentrations of KCl, together with the fits obtained using model 5.1. Although the fits are not of the same precision as those shown in chapter four, they are still good enough to allow the capacitance of the tip, C_{Tip}, to be assigned an order of magnitude value. The importance of this will be demonstrated in section 5.2.6.2.

In the second part of the investigation, the effect of pipette radius on the total resistance was evaluated using a KCl concentration of 1 M. These results were then used to predict an iR drop value for the 10 mM KCl case, based on the expected steady-state current for the respective pipettes (calculated using equation 5.3), and an expected increase in R_{Tip} by a factor of 100. In this way the error on the resistance evaluation was minimised. These results are

shown in table 5.7, and were calculated in the same way as for the KCl concentration variation study.

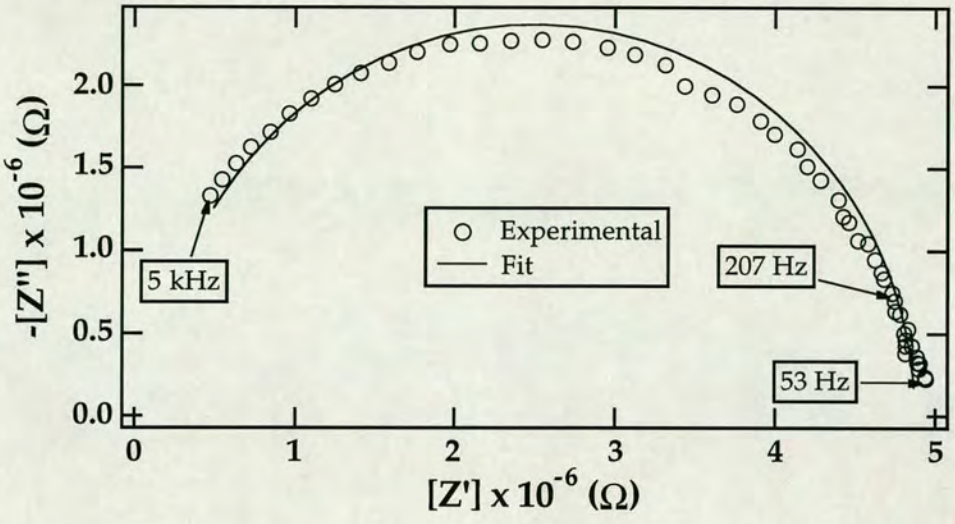

Figure 5.19 - Complex plane impedance plot for 0.01 M KCl, together with the fit to the data using model 5.1. Only half of the experimental points are shown for clarity.

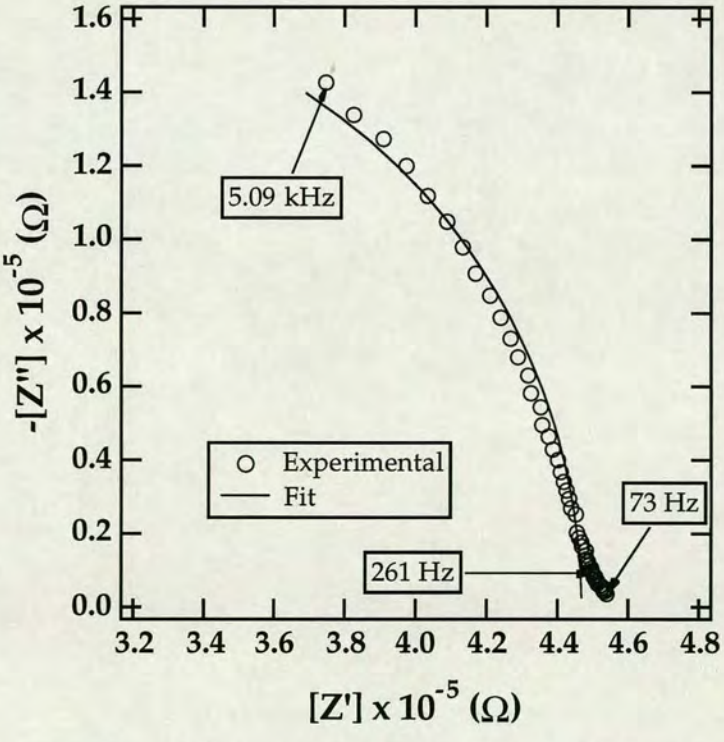

Figure 5.20 - Complex plane impedance plot for 0.1 M KCl, together with the fit to the data using model 5.1. Only half of the experimental points are shown for clarity.

In one of these experiments the end of the pipette was broken off and the resistance of the system re-evaluated. The value obtained, for the cell minus the micropipette tip, was of the order of 0.5 kΩ, and was therefore judged to be relatively insignificant with respect to the total resistance.

*Table 5.7 - Data from a.c. impedance analysis of micropipettes - internal tip radius dependence (concentration of potassium (c_{K+}) = 1 M). * specifies thick-walled glass.*

Tip Radius (μm)	Total Resistance (Ω) x 10^{-4}	iR drop (mV) for [(c_{K+})=10 mM]
19	1.50 ± 0.01	7.9
13	1.92 ± 0.03	6.9
10	2.24 ± 0.12	6.2
6.5	3.02 ± 0.15	5.4
3.5	4.74 ± 0.07	4.5
2.5	7.19 ± 0.09	5
0.6*	76.71 ± 0.17	8

The calculated iR drop value for the 13 and 19 μm radii pipettes is higher than those of the other pipettes. Thus, as mentioned in section 5.2.2, the change in wave behaviour from reversible to quasi-reversible, in going from a tip size of 16 μm to one of 8 μm, cannot be attributed to tip resistance, since the iR drop for a 16 μm tip would be expected to be larger than that of tips with sizes between 8 and 2.5 μm. It must, therefore, be a characteristic of micropipettes which are below a certain size or critical dimension. The absolute value of the critical dimension is difficult to assess without further experiments in the tip size range 16-30 μm.

Figure 5.21 shows the plot of total resistance versus the reciprocal of the micropipette tip radius, for the thin-walled glass (first six results of table 5.7). This illustrates that the total resistance is proportional to the inverse of the tip radius. This result is as expected since the tip resistance, R_{Tip}, is given by the equation [160]:

$$R_{Tip} = 1 / \pi\theta\sigma r_p \qquad (5.6)$$

where $\pi\theta$ is related to $\pi\theta^2$ (in radians), which is the angle subtended by the micropipette tip (see [160]), and σ is the conductivity of the electrolyte solution.

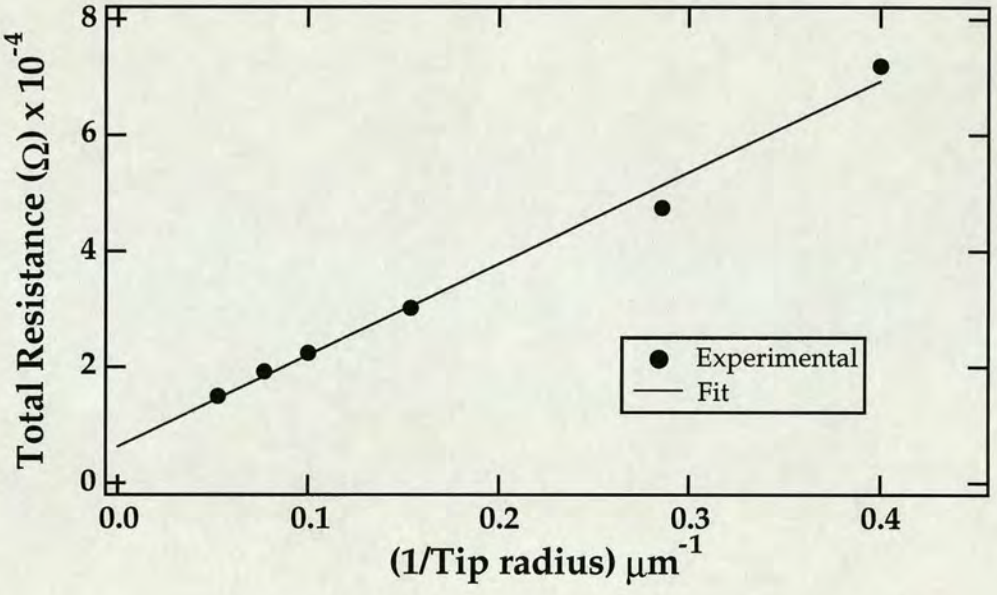

Figure 5.21 - Plot of total resistance versus the reciprocal of the micropipette tip radius for the thin-walled glass results in table 5.7.

The plot did not pass exactly through zero, presumably due to contributions from the resistance of the KCl solution between the end of the Ag/AgCl wire in the micropipette and the micropipette tip cone, and the resistance of the solution in the glass U-tube.

In conclusion, it is clear that, below a certain tip size, the asymmetry of the diffusion regime at the micropipette, and the fact that the interface is not in an insulating plane, begins to affect the assisted ion transfer reaction by leading to a shortage of potassium ions near the interface. This idea is strengthened by the results from section 5.2.3 and 5.2.4 which establish the trends in reversibility as being related to the potassium ion and Db18C6 concentrations respectively. Indeed, in section 5.2.3, the reaction was found to be fully reversible for a potassium ion concentration of 100 mM.

The results shown in tables 5.1 and 5.2 indicate that a 0.6 μm pipette is not small enough to create a kinetic shift when the potassium ion concentration is in excess with respect to the Db18C6. Equation 2.2.18 states that $\kappa^o = (r_h k^o/D_S)$ for a hemisphere, and equation 2.2.20 states that for an effectively reversible transfer process, $\kappa^o > 40$. Thus, a lower limit for k^o of 3 cms^{-1} can be set for the charge transfer step of the assisted transfer of the potassium ion from the aqueous phase to the organic phase. For this evaluation the assumption was made that the micropipette tip-supported ITIES takes the form of a hemisphere, with an increased current contribution due to the fact that it does not lie in an infinite insulating plane.

To fully corroborate the findings that once more the kinetics of an ion transfer process may not be accessed using electrochemical methods - as demonstrated in chapter four - it was decided to undertake a further investigation of the reaction given in equation 5.1, using the technique of a.c. impedance of the micropipette tip-supported ITIES.

5.2.6.2 A.C. Impedance of the Micropipette Tip-Supported ITIES

5.2.6.2.1 Tip Radius Dependence

For these studies it was deemed sensible to work in an experimental regime which was fully reversible. Therefore, a KCl concentration of 0.1 M and a Db18C6 concentration of 0.5 mM (cell 5.1) were utilised. The frequency range studied was 25 kHz to 207 Hz and the amplitude of the exciting signal was ± 20 mV. The frequency range could not be extended to lower frequencies - this was presumably due to effects from the vibration of the tip. Thin-walled micropipettes were used for all these experiments. Experiments using thick-walled glass were attempted, however, it was very difficult to resolve any information because the measured impedances were very high and the dispersion on the points was quite significant. Steady-state voltammograms were not recorded for these experiments, since the lifetime of the micropipettes could be rather short. The accuracy between response cycles was stipulated to be 5%.

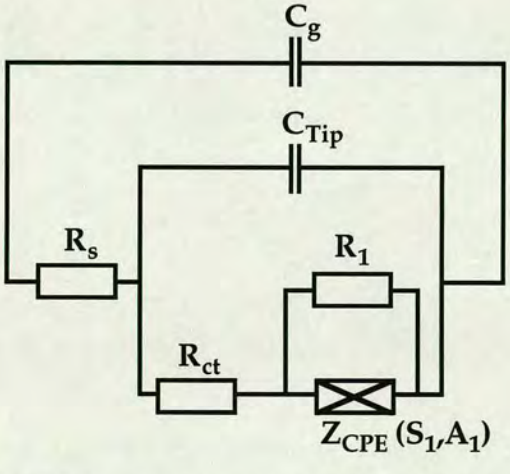

Model 5.2 - Analogous to model 4.2 (chapter four).

Micropipettes having internal tip radii of 9, 5 and 3 μm were employed in the first instance and the impedance of cell 5.1 was evaluated. The experimental results obtained were analysed using model 5.2 - this is analogous to model 4.2, where the film capacitance C_{Film} is replaced by the micropipette tip capacitance, C_{Tip}. The average fit values obtained for three determinations using the same micropipette are given in table 5.8. Figure 5.22 shows complex plane impedance plots for each of the three tip sizes together with the fit to the data using model 5.2. The geometric capacitance of model 5.2 was found to be negligible in all experiments conducted at the micropipette tip-supported ITIES.

Table 5.8 - Averaged data from experimental impedance of the micropipette tip-supported ITIES - using model 5.2. Figures in brackets refer to the average of the percentage error on the individual fit results. Fitting was to all the points.

Tip Radius (μm)	9	5	3
$R_1 \times 10^{-7}$ (Ω)	1.57 ± 0.18 (3.2)	3.60 ± 0.63 (3.3)	4.12 ± 0.12 (2.9)
$S_1 \times 10^{-8}$ (Ωs^{A_1})	3.05 ± 0.79 (3.3)	9.77 ± 1.70 (3.7)	11.97 ± 3.16 (4.5)
$A_1 \times 10^{1}$	-6.40 ± 0.21 (0.7)	-6.42 ± 0.23 (0.7)	-5.89 ± 0.28 (1.0)
$R_{ct} \times 10^{-5}$ (Ω)	7.55 ± 0.31 (1.1)	11.14 ± 0.96 (3.1)	0.00 ± 0.00 (0.0)
$C_{Tip} \times 10^{11}$ (F)	4.09 ± 0.04 (0.4)	4.11 ± 0.04 (0.4)	3.52 ± 0.04 (0.5)
$R_s \times 10^{-4}$ (Ω)	1.87 ± 0.09 (2.8)	1.56 ± 0.21 (2.8)	1.48 ± 0.04 (2.1)

The results obtained for C_{Tip} are consistent with the order of magnitude determined previously in section 5.2.6.1, and once more preclude any possible resolution of the interfacial capacitance, C_{int}. The fit values for R_1 (the non-linear resistance) and $S_1(\sigma)$ indicate that spherical diffusion is the dominant form of mass transport. The value obtained for A_1 is a little higher

than expected. However, given that the interface has already been deemed to have a hemispherical geometry, this may have influenced the results. Another possible explanation is discussed in section 5.2.6.2.2.

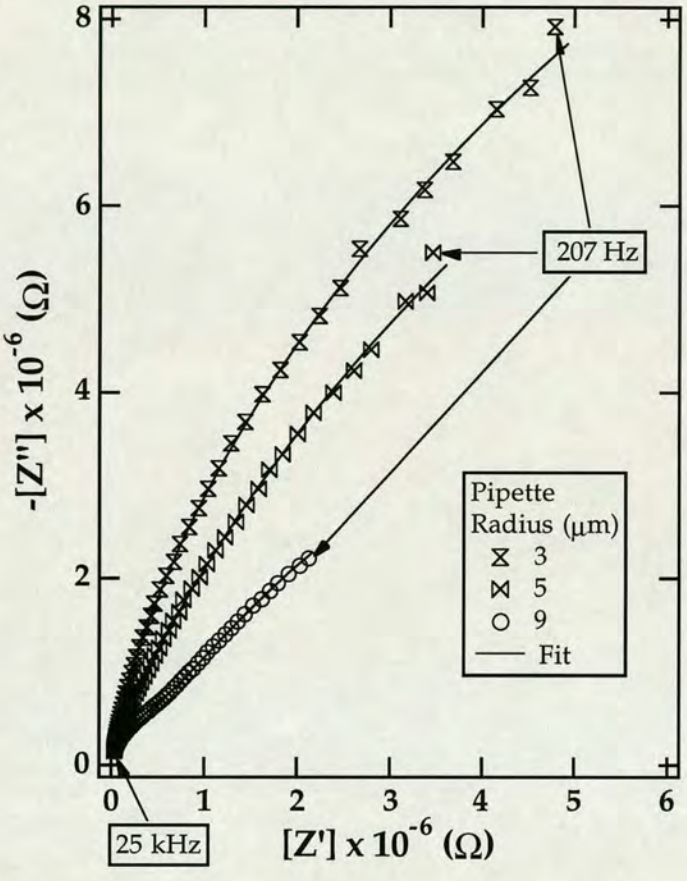

Figure 5.22 - Complex plane impedance plots for cell 5.1, together with the fits to the data using model 5.1, at the half-wave potential for assisted potassium ion transfer by Db18C6 - tip radius dependence study. Only half of the experimental points are shown for clarity. Start and end frequencies are indicated.

As Bruce *et al.* [146] pointed out, the diffusion to a microdisc approximates closely to diffusion to a microhemisphere at high and low frequencies. Therefore, equation 2.2.43 may be used to establish an order of magnitude value for the non-linear resistance, R_1, of model 5.2. This yields values for the 9, 5, and 3 μm tips of 7.0, 12.6, and 21.1 (x $10^7(\Omega)$) respectively.

Obviously, these estimated values correspond to an interface in an infinite insulating plane, and as already noted the micropipette does not fall into this category. It is no surprise, therefore, that the R_1 values obtained from the fits are lower than the predicted values.

In a manner analogous to the a.c. impedance experiments of the microhole supported ITIES in chapter four, the value obtained for R_{ct} in model 5.2 - which in this case would have been comprised of the charge transfer resistance and the resistance of the micropipette tip, R_{Tip} - is found to disappear at a tip size of 3 μm (as shown in table 5.8). That is to say, the model does not cope with an R_{ct} element in the system at this tip size - obviously due to the magnitude of the diffusional impedance.

5.2.6.2.2 Db18C6 Concentration Variation

Using a 6 μm tip and a value of x = 0 (mM Db18C6), the impedance of cell 5.1 was evaluated - under the same experimental conditions used in 5.2.6.2.1. To the cell were added successive aliquots of a solution of 5 mM Db18C6/10mM TBATPBCl in 1,2-DCE, to give cell concentrations of x = 0.24, 0.45 and 0.65. In each case the impedance of the system was determined.

The fit results for these experiments using model 5.2 are presented in table 5.9 and correspond to an average of 4, 3, 2, and 2 determinations for x = 0, 0.24, 0.45 and 0.6 respectively. Figure 5.23 shows complex plane impedance plots for each of the cases listed in table 5.9, together with the fits to the experimental data using model 5.2.

Once again, the mode of mass transport is spherical diffusion, given that the value for S_1 is much greater than that of R_1. The value of R_1 obtained for the system with x = 0 suggests that there may be a significant contribution to the faradaic impedance from the tetrabutylammonium ion, TBA^+, of the 1,2-DCE phase supporting electrolyte - this is reasonable, given the proximity of the assisted potassium transfer wave to the end of the potential window, for the 0.1 M KCl case (figure 5.12). This would also help explain the low values obtained for R_1 in the previous section (relative to the values calculated using equation 2.2.43).

Table 5.9 - Averaged data from experimental impedance of the micropipette tip-supported ITIES - using model 5.2 - for Db18C6 concentration variation (x, cell 5.1). Figures in brackets refer to the average of the percentage error on the individual fit results. Fitting was to all the points.

Db18C6(mM)	0	0.24	0.45	0.65
$R_1 \times 10^{-7}$ (Ω)	9.55 ± 0.11 (3.5)	4.65 ± 0.38 (1.8)	4.46 ± 0.50 (2.7)	3.74 ± 0.31 (3.9)
$S_1 \times 10^{-9}$ (Ωs^{A_1})	15.8 ± 0.20 (3.6)	6.48 ± 0.44 (3.0)	1.60 ± 0.10 (3.0)	0.71 ± 0.02 (4.7)
$A_1 \times 10^{1}$	-8.89 ± 0.21 (0.4)	-7.80 ± 0.08 (0.4)	-6.37 ± 0.08 (0.5)	-5.56 ± 0.01 (1.1)
$R_{ct} \times 10^{-6}$ (Ω)	1.61 ± 0.13 (2.6)	1.35 ± 0.03 (3.6)	0.77 ± 0.04 (10.3)	0.78 ± 0.04 (11.6)
$C_{Tip} \times 10^{11}$ (F)	2.74 ± 0.02 (0.7)	2.72 ± 0.01 (0.7)	2.60 ± 0.01 (1.3)	2.66 ± 0.01 (1.0)
$R_s \times 10^{-4}$ (Ω)	2.23 ± 0.19 (6.0)	2.19 ± 0.03 (5.0)	1.81 ± 0.05 (7.9)	2.10 ± 0.07 (4.9)

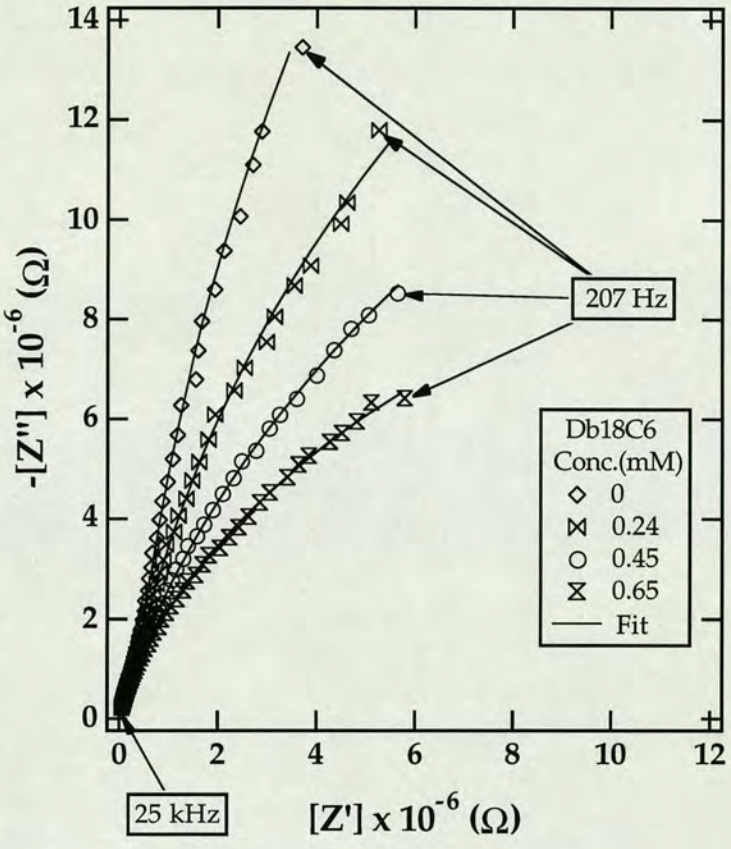

Figure 5.23 - Complex plane impedance plots for cell 5.1, at the half-wave potential for assisted potassium ion transfer by Db18C6 - Db18C6 concentration dependence study. Only half of the experimental points are shown for clarity. Start and end frequencies are indicated.

An interesting feature of the results obtained is the rapid decrease in the value of S_1 upon successive additions of Db18C6, and the progressive change in A_1 from -0.889 to -0.556. This suggests a move from capacitive-type behaviour to a Warburg impedance (indicative of linear diffusion). It is possible, that this may have been associated with increasing demand for potassium ions in the micropipette tip, by the Db18C6 in the organic phase outside it. The fact that A_1 and S_1 seem to be quite strongly linked to the concentration of the Db18C6 in the cell makes the results obtained for A_1 in

the previous set of experiments easier to explain - rather than simply saying that A_1 is only linked to the geometry of the interface.

A possible explanation of the behaviour is as follows. As the concentration of Db18C6 in the organic phase is increased the potassium ions are able to transfer across the interface by the method of transfer by interfacial complexation. The Z_{CPE} element begins to behave less like a capacitance and more like a Warburg impedance: initially, after the addition of Db18C6, and since the concentration of potassium ions is in vast excess of the Db18C6 concentration, the value for A_1 is affected only slightly; as the demand for ions is increased, the value for A_1 tends towards -0.5. This scenario is rationalised by the values obtained for R_1 which, although less than the value of S_1, remained relatively constant after the first addition of Db18C6. Obviously, the S_1 and A_1 values must reflect to some extent the contribution of linear diffusion to the interface of both Db18C6 and the TBA^+ of the organic phase supporting electrolyte, therefore, the hypothesis discussed is not quantifiable. To a first approximation, however, it seems quite reasonable.

Most important of all, were the results obtained for R_{ct} upon successive additions of Db18C6. Initially, there was a slight change in the R_{ct} value observed but this quickly fell to a reproducible value for the 0.45 and 0.65 mM Db18C6 cases. This suggests that a real physical barrier to the assisted ion transfer process is lifted, and that the remaining R_{ct} in the system is due to the resistance of the tip, R_{Tip}, and the contribution from the supporting electrolyte. This is a fairly realistic standpoint given that the values of R_{ct} listed in table 5.8, for x = 0.5 show that a 6 μm tip should have a R_{ct} value of between 7.55 and 11.14 (x 10^5 (Ω)). The values for x = 0.45 and 0.65 were 7.7

and 7.8 (x 10^5 (Ω)) respectively. The value expected for the resistance of a 6 μm tip containing a 0.1 M KCl solution, using figure 5.21, is 3.25 x 10^5 (Ω). However, given that the solution resistance of the hemispherical solution outside the tip also needs to be taken into account the difference in the two values would not be expected to be very great.

Thus, since the charge transfer resistance for ion transfer has already been shown to be unmeasurable, it was assumed that the variation in the R_{ct} value for model 5.2 was only due to the increase in Db18C6 concentration. $R_{ct(K^+Db18C6)}$ can only be assigned an order of magnitude value, due to the difference in the fit results observed. Taking the value of $R_{ct(K^+Db18C6)}$ as the difference between the starting value of 1.61 x 10^6 Ω and the value at x = 0.45 of 0.77 x 10^6 Ω, yields a value of 0.84 x 10^6 Ω. This in turn yields a value for k^o of 0.31 cms^{-1}. However, it is more than likely that this value would be dependent on the radius of the micropipette used, based on the results obtained using steady-state voltammetry. Using equation 2.2.20 the expected value for k^o, for a fully reversible, diffusion controlled system is 0.30 cms^{-1} (using a value for r_h of 6 μm). Thus, it seems fair to conclude, that the kinetics of the assisted ion transfer process are at least as fast as the rate of diffusion of the Db18C6 to the interface.

5.3 Conclusions

Once again, in a manner analogous to ion transfer (chapter four), the rate of the assisted ion transfer of potassium by Db18C6 across the interface between water and 1,2-DCE has been shown to be an effectively unmeasurable quantity using electrochemical methodology. This conclusion was first of all based on the fact that the apparent standard rate constant, k^o,

was shown to be geometry dependent - using the technique of steady-state voltammetry. Furthermore, the reaction was demonstrated to be completely diffusion-controlled under the conditions of 100:0.6 potassium ion:Db18C6 concentration. Using the technique of a.c. impedance, it was qualitatively shown that the resistance to charge transfer gave a result for k^o, which was approximately equivalent to that expected for a fully reversible process, based on the radius of the micropipette tip employed.

As indicated in section 1.2.2, Sabela *et al.* [130] used a.c. impedance to study the Na^+/Db18C6 system at the large water/nitrobenzene interface, obtaining k^o values of between 0.01 and 1 cms^{-1}. Based solely on the steady-state voltammetry results presented in this chapter, the value of k^o for both the Na^+/Db18C6 and the K^+/Db18C6 systems would be expected to be greater than 3 cms^{-1}.

Chapter Six

ELECTRON TRANSFER

6.1 Introduction

The aim of this chapter was to study electron transfer reactions at the ITIES using cyclic voltammetry. In the first part, transfer between the hexacyanoferrate redox couple ($[Fe(CN)_6]^{3-/4-}$) in the aqueous phase, and ferrocene and 1,1'-dimethylferrocene, respectively, in the organic (1,2-DCE) phase, was investigated. In the second part, experimental results which were obtained for transfer between copper (II) ions in the aqueous phase and ferrocene in 1,2-DCE are presented.

6.2 The Ferrocene and 1,1'-Dimethylferrocene/Hexacyanoferrate Systems

6.2.1 Summary of Work to Date

As already mentioned in chapter one (1.2.3), Samec and co-workers [25,70,72, 73] have studied electron transfer between $[Fe(CN)_6]^{3-/4-}$ in the aqueous phase, and ferrocene (Fec) in nitrobenzene. In the last of these publications, it was shown that the product of the oxidation of Fec, the ferricenium ion (Fec^+), transferred at less positive potentials than that at which the electron transfer process took place. This illustrated that the electron transfer was not complicated by ion transfer.

Subsequently, Brown [161] studied the same electron transfer reaction, also using cyclic voltammetry, for the system:

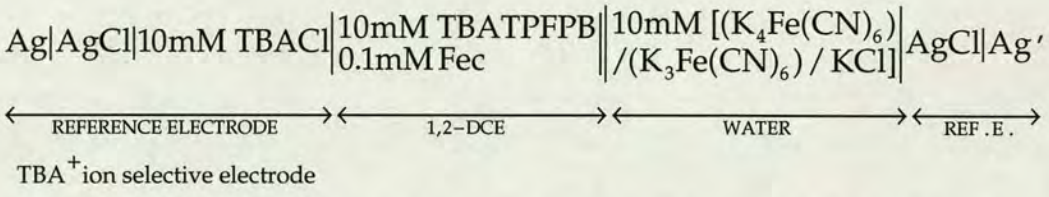

Cell 6.1 - where TPFPB stands for the tetrapentafluorophenylborate anion.

By the author's own admission, however, the wave obtained was not well formed, and was also partially obscured by the end of the potential window. Nevertheless, an approximate value of the electron transfer half-wave potential, relative to the half-wave transfer potential of TMA^+, of -5 mV was reported. The author chose to use TBATPFPB as the organic phase supporting electrolyte, citing the non-redox activity of TPFPB over a wide potential range as the main advantage over the tetraarylborate salts normally employed. It was also noted that the electron transfer wave illustrated in the paper by Hanzlik *et al.* [72] for the same redox system, but with a different supporting electrolyte, had a shape similar to that observed by Brown [161].

Campbell [158] studied electron transfer at the micropipette tip-supported ITIES between water and 1,2-DCE for the Fec (org) ‖ $[Fe(CN)_6]^{3-/4-}$ (aq) system. The author showed that under the conditions of (1) excess Fec, and (2) a ratio of Fe(III)/Fe(II) of 5 in the aqueous phase, the solution in the micropipette tip turned blue, which was attributed to Fec^+. Thus, it was postulated that (1) Fec partitions from the 1,2-DCE to the aqueous phase, and (2) the aqueous Fec is readily oxidised to Fec^+ by the Fe(III) - present in a concentration five times greater than the Fe(II). Although the partition of Fec to water from 1,2-DCE would be expected to be only slight, it was argued

that the oxidation of Fec in the aqueous phase would drive the Fec partition process allowing more Fec(aq) to be oxidised.

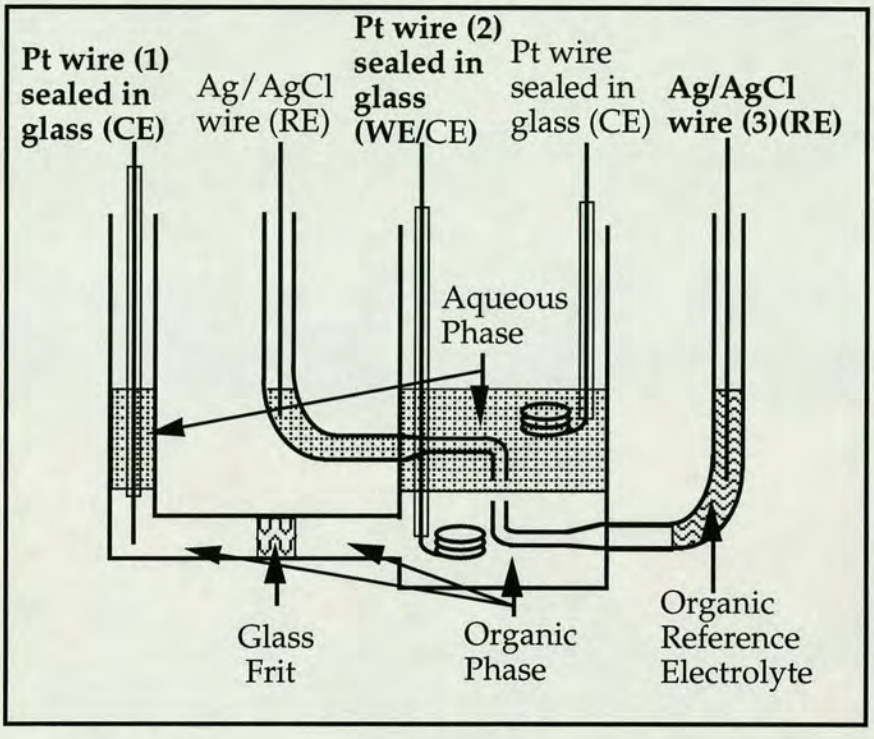

Figure 6.1 - Cell used for electro-oxidation of ferrocene and 1,1'-dimethylferrocene in 1,2-DCE. Writing in bold refers to three electrode mode used for electro-oxidation: (1) counter electrode; (2) working electrode; (3) reference electrode. For four electrode mode, wire (1) was disconnected and wire (2) was used as a counter electrode.

Brown [161] has also investigated the electro-oxidation of both ferrocene and 1,1'-di-n-butylferrocene (DbFec) in 1,2-DCE, using a cell design very similar to that shown in figure 6.1. This configuration allows the subsequent study of the transfer across the ITIES of the cationic species produced, by operating the cell in four-electrode mode. This is only possible through the judicious inclusion of the glass frit in the cell design of figure 6.1, preventing the products of the reaction at the counter electrode (Pt wire (1) - figure 6.1) from interfering with the ion transfer analysis. In this way, Brown was able to

obtain values for the formal potentials, $\Delta^{aq}_{1,2\text{-DCE}}\phi^{o'}$, for Fec^+ transfer (40 mV) and $DbFec^+$ transfer, (-255 mV). In addition, a large reproducible pre-peak to the transfer of $DbFec^+$ from 1,2-DCE to the aqueous phase was observed. This was postulated to be the transfer of adsorbed $DbFec^+$. The conclusion was made that adsorbed product molecules formed in heterogeneous electron transfer reactions may well lower the effective area of the interface, and thus the observed current densities.

Campbell [158] has studied the oxidation of both Fec and DbFec at a 25 μm diameter platinum disc, observing both reactions to be fully reversible.

6.2.2 Results and Discussion

6.2.2.1 Electron Transfer at the ITIES

The first system studied was the following:

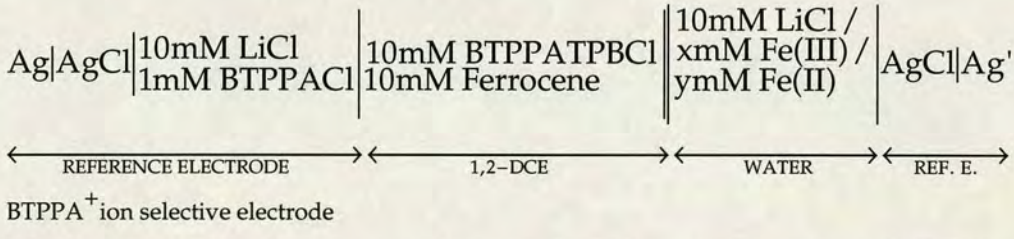

Cell 6.2 - where x and y correspond to a value given in the text, and Fe(III) and Fe(II) are $K_3Fe(CN)_6$ and $K_4Fe(CN)_6$ respectively.

The scan rate in all experiments was 0.1 Vs^{-1} unless otherwise stated, and maximum iR drop compensation was also employed. In the first experiment, the initial concentrations of Fe(III) and Fe(II) (x and y, cell 6.2) were zero and a concentration of 10 mM Fec was shown to exhibit no effect

within the potential window (an analogous result was obtained for the case where x = y = 10 (mM), and the concentration of ferrocene was zero). An aliquot of Fe(III)/Fe(II)/10 mM LiCl was then added to give a cell concentration of x = y = 0.1 (cell 6.2). The reason for choosing such a low concentration of the Fe(III)/Fe(II) couple in the aqueous phase and a high concentration of Fec in the 1,2-DCE phase was to try to resolve the electron transfer wave from the end of the potential window with respect to previous work [161], which was affected by the high concentration of potassium - present as the counter ion of the Fe(III)/Fe(II) couple. The cyclic voltammetric response obtained is shown in figure 6.2.

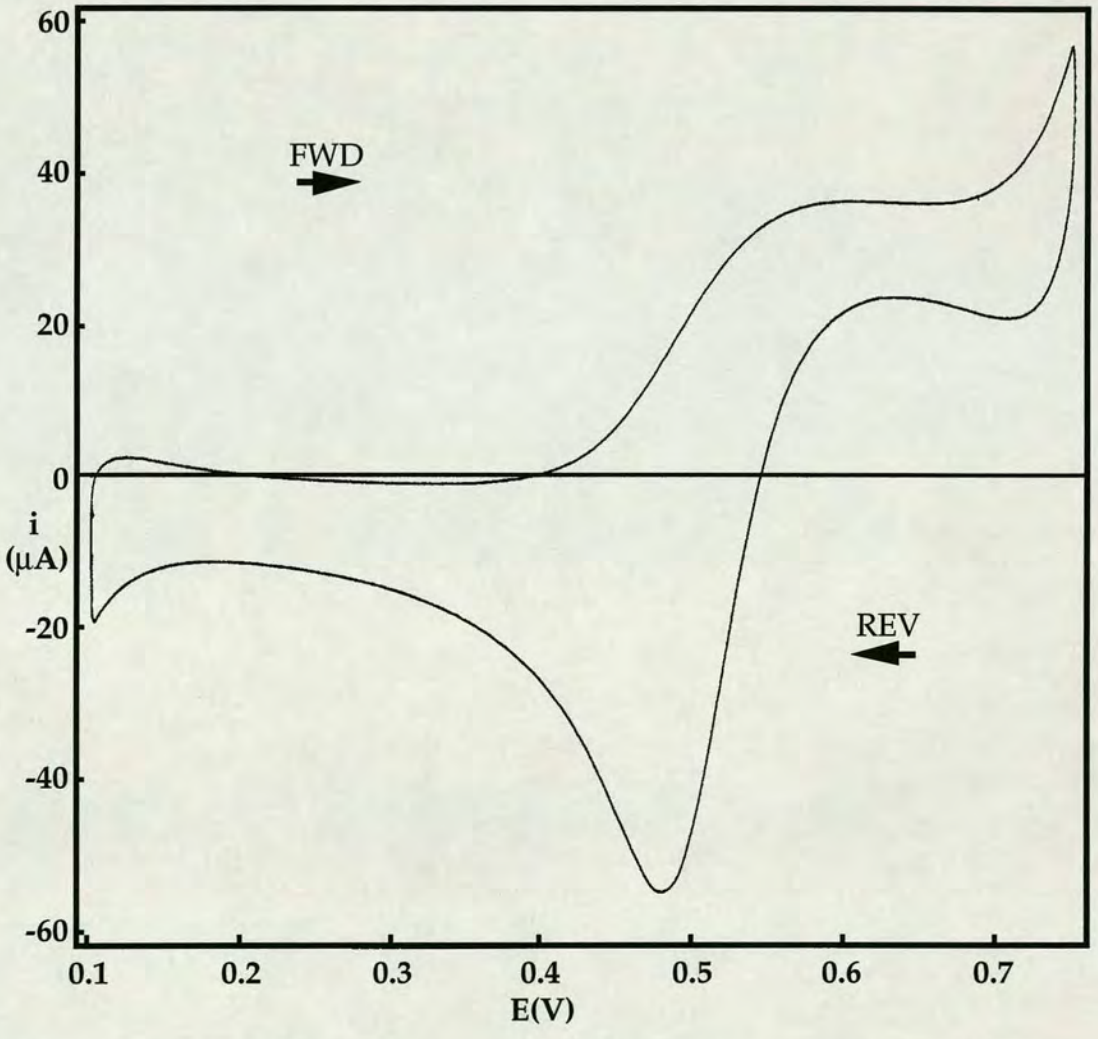

Figure 6.2 - Cyclic voltammogram for cell 6.2, where x = y = 0.1 (mM).

In light of the work of Brown [161], it is clear that the odd shape of the forward wave has little to do with interference from the supporting electrolyte (BTPPATPBCl). The shape of the transfer wave can be deemed to be analogous to electron transfer at a solid electrode where weak adsorption of the product occurs. Since both aqueous phase and organic phase reactants were individually demonstrated not to exhibit either adsorption or transfer behaviour within the potential window, it is possible that the wave shape might be a result of some form of interaction between Fec^+ and Fe(II).

One possible mechanism is as follows: (1) the Fec and Fe(III) come together to form the electron transfer precursor complex; (2) electron transfer occurs; (3) the successor complex of Fec^+ and Fe(II) is formed; and (4) the successor complex remains at the interface in ion pair form, rather than separating to allow diffusion of the products into the respective phases. This could account for the difference in the forward and reverse peak currents.

While attempting a scan rate dependence for the system, a post-peak (B - figure 6.3) began to become resolved from the electron transfer forward wave (A - figure 6.3) during continuous cyclic scanning, and the return peak of the electron transfer wave diminished slightly. The post-peak continued to become clearer and the voltammogram stabilised after a time of approximately thirty minutes. Figure 6.3 shows the scan rate dependence subsequently obtained. The experiment was also repeated for the case where both aqueous and 1,2-DCE phase solutions had been sparged individually for fifteen minutes prior to use (to remove any dissolved oxygen), and a very similar result was obtained. In an adsorption process the post-peak should be dependent in the scan rate, and not its square root.

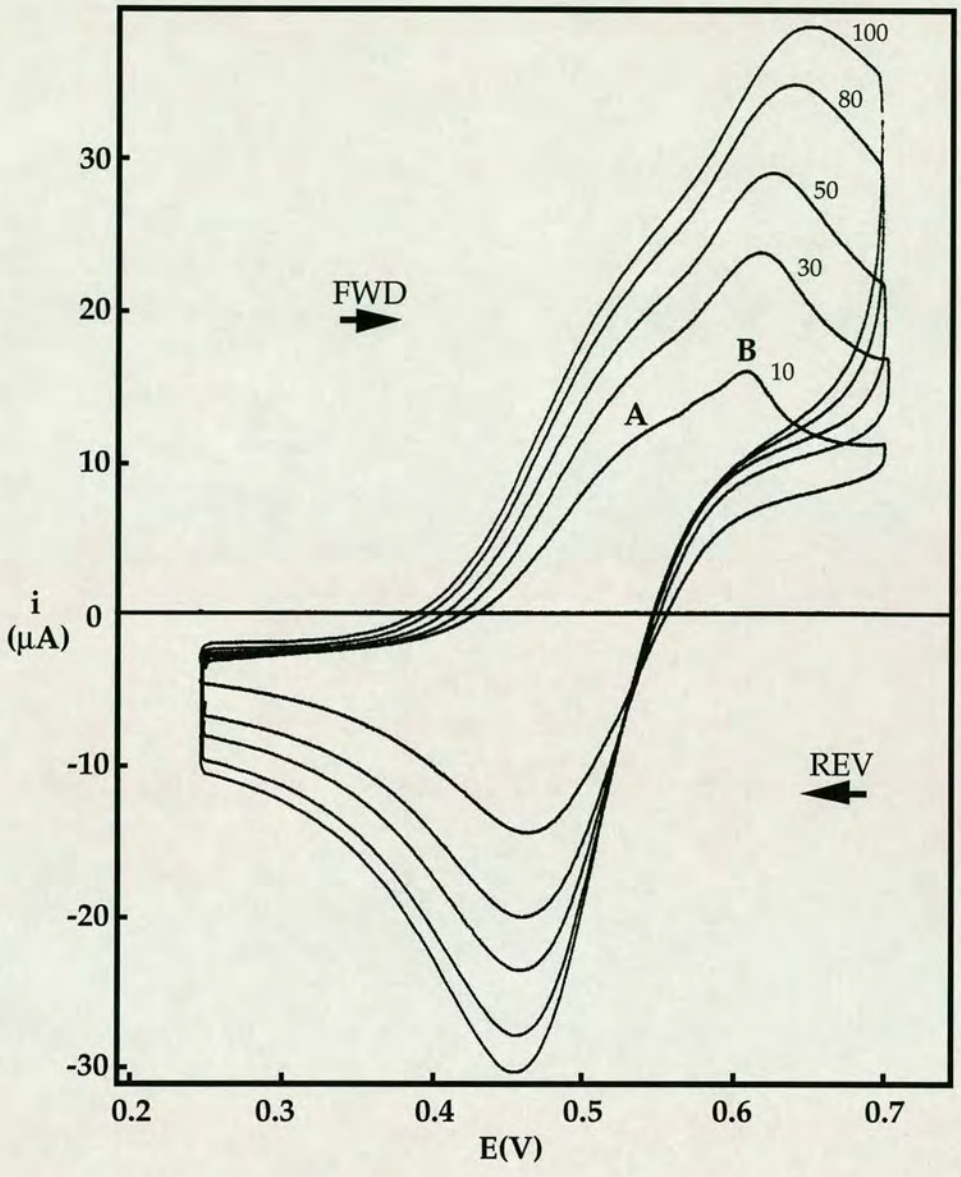

Figure 6.3 - Cyclic voltammograms for cell 6.2, x = y = 0.1 (mM), after thirty minutes continuous scanning - at scan rates of 10, 30, 50, 80 and 100 mVs^{-1}. A - electron transfer peak; B - post-peak to electron transfer.

The notion that the observed phenomenon is adsorption must be understood as being purely speculative on the part of this author since no quantitative analysis of the forward waves was realistically possible. One aspect of these results is the absence of a corresponding pre-peak to the reverse electron transfer process, which would normally be expected to be aligned with the

post-peak on the forward scan (by analogy with the metal electrode/electrolyte solution interface). To eliminate the possibility that the absence was due to masking by the end of the potential window, it was decided to repeat the experiment in the absence of Fe(II) (y = 0, cell 6.2).

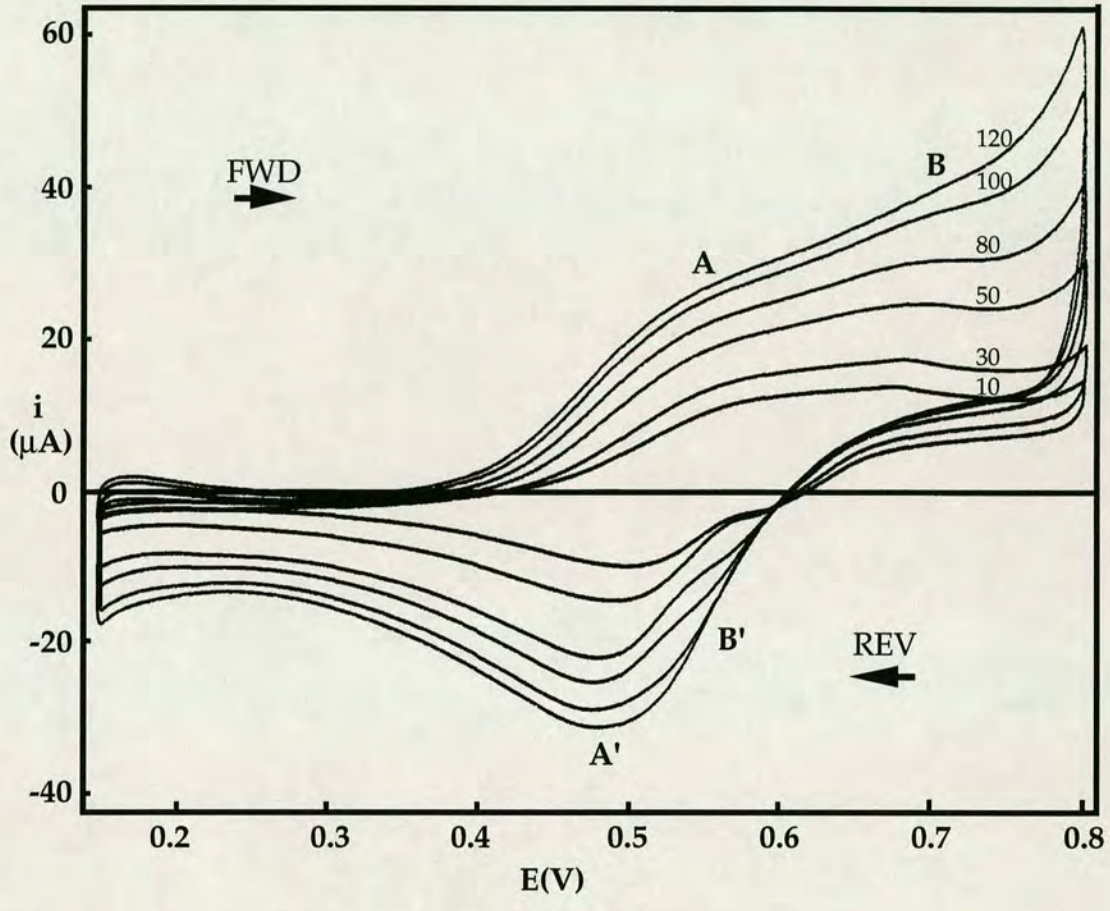

Figure 6.4 - Cyclic voltammograms for cell 6.2 (x = 0.1, y = 0 (mM)), recorded at scan rates of 10, 30, 50, 80, 100 and 120 mVs^{-1}.

Initially, the voltammogram looked very similar to that shown in figure 6.2, but the shape changed with time, in a similar manner to previous experiments. Figure 6.4 shows a scan rate dependence for the system after stabilisation. Here the pre-peak to the reverse electron transfer process is observed (B' - figure 6.4), and is especially clear at low scan rates (note that the post- and pre-peaks are not aligned). This type of adsorption

phenomenon can been described as adsorption/transfer and has been demonstrated by Osborne and Girault [93] for the adsorption of Nafion at the water/1,2-DCE interface. The use of the term 'adsorption/transfer' is justified by the fact that current at the ITIES arises through flux of charge through the interface (or through direct electron transfer).

One final point of interest here is the separation between the electron transfer wave and the post-peak (figure 6.4) which has increased relative to figure 6.3, suggesting that the adsorption/transfer behaviour is favoured by an increase in the Fe(II) concentration. It also means that in the case of the voltammograms shown in figure 6.3, the proximity of the end of the potential window to the reverse wave might not be the reason for the reverse adsorption/transfer process being masked.

The Fec (org) ‖ $[Fe(CN)_6]^{3-/4-}$ (aq) system seems to be complicated by the effects of adsorption, which means that it would be very difficult to glean accurate thermodynamic information of any kind. Thus, in the quest for an uncomplicated electron transfer system, it was decided to test the 1,1'-dimethylferrocene, DmFec, (org) ‖ $[Fe(CN)_6]^{3-/4-}$ (aq) system.

Cell 6.3 - where x, y and z correspond to a value given in the text, and Fe(III) and Fe(II) are $K_3Fe(CN)_6$ and $K_4Fe(CN)_6$ respectively. DmFec represents 1,1'-dimethylferrocene.

In the first instance, a concentration of z = 2.5 (mM DmFec) was employed, together with x = y = 0.1 (mM Fe(III)/Fe(II)), for cell 6.3. The cyclic voltammetric responses obtained for a scan rate dependence are illustrated in figure 6.5. Clearly, the adsorption behaviour exhibited by the Fec (org) ‖ $[Fe(CN)_6]^{3-/4-}$ (aq) system is not specific to Fec. However, with time the electron transfer wave was not observed to change at all, suggesting that the addition of methyl groups to the cyclopentadienyl rings of the Fec molecule prevents the irreversible behaviour which was previously observed, perhaps through steric hindrance.

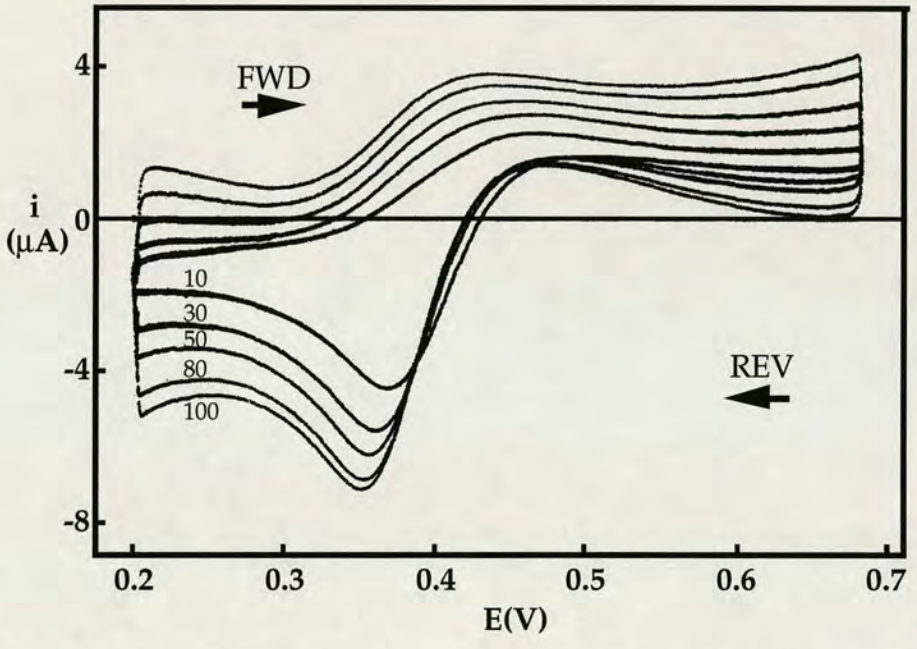

Figure 6.5 - Cyclic voltammograms for cell 6.3: x = y = 0.1 (mM), z = 2.5 (mM DmFec). Recorded at sweep rates of 10, 30, 50, 80, and 100 mVs^{-1}.

There is little or no variation in the height of the forward wave between different scan rates (figure 6.5), however, the height of the reverse peak is found to vary with the square root of the scan rate, as indeed were the previous reverse peaks for Fec (figures 6.3 and 6.4). The forward and reverse peaks shift in the direction of more positive potentials with decreasing scan

rate, which is analogous to weak adsorption of the product of an electron transfer reaction at the metal electrode/electrolyte solution interface [139].

The reverse peak of the electron transfer wave was referenced against the reverse peak for TMA^+ transfer by adding a few drops of tetramethyl-ammonium sulphate, $(TMA)_2SO_4$ to cell 6.3 as an internal reference. The peaks were found to have a separation of 145 ± 4 mV, using a scan rate of 0.1 Vs^{-1}. This value is to be compared with the separation of the experimental half-wave potentials for $DmFec^+$ and TMA^+ transfer (section 6.2.3) which is 223 ± 4 mV, indicating that the electron transfer is not complicated by ion transfer.

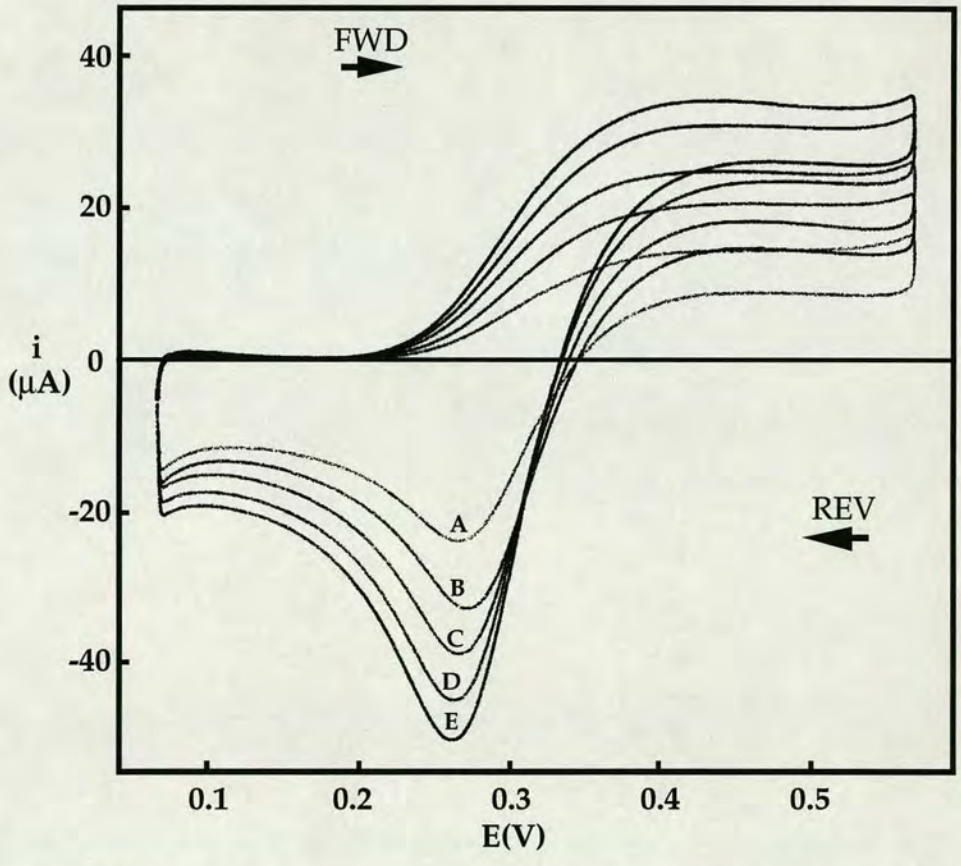

Figure 6.6 - Cyclic voltammograms corresponding to the variation of the DmFec concentration. z = (A) 0.6, (B) 0.8, (C) 1.0, (D) 1.2, (E) 1.4 (mM); x = y = 10 (mM Fe(III)/Fe(II)); cell 6.3.

The electron transfer wave for the DmFec (org) ‖ $[Fe(CN)_6]^{3-/4-}$ (aq) system seems to occur at lower cell potentials than that of the Fec case, suggesting that DmFec is more easily oxidised by $[Fe(CN)_6]^{3-}$ than Fec. It was decided therefore to take advantage of this fact and perform an experiment under conditions of excess Fe(III)/Fe(II). Here the concentrations used were x = y = 10 (mM Fe(III)/Fe(II)), and a z concentration of 0.6-1.4 (mM DmFec) - cell 6.3. The cell concentration of DmFec in the organic phase was increased in steps of 0.2 mM (cell 6.3). Figure 6.6 shows the cyclic voltammograms obtained. Both forward and reverse waves were observed to increase in height with increasing DmFec concentration.

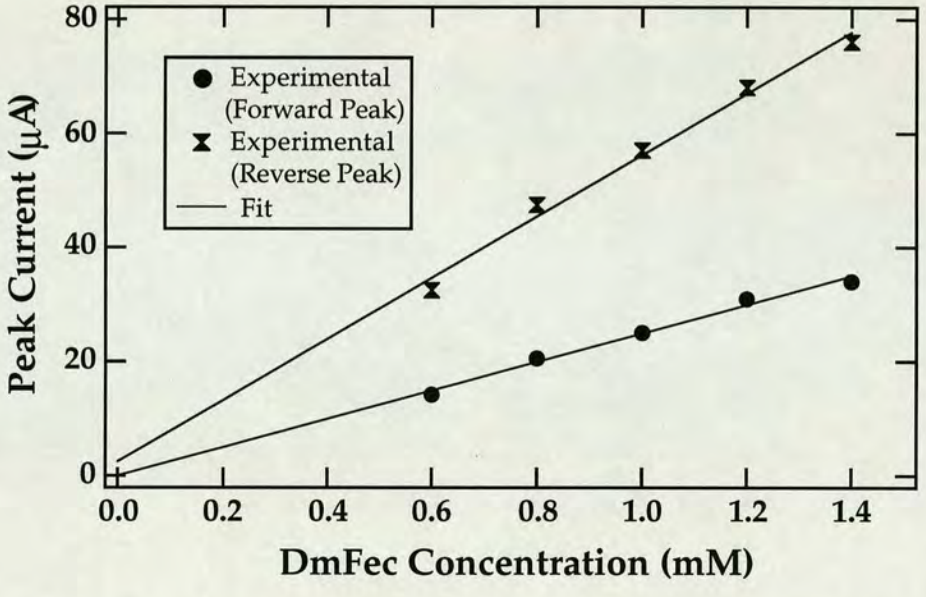

Figure 6.7 - Plots of peak current versus DmFec concentration for the forward and reverse waves of the voltammograms shown in figure 6.6.

Figure 6.7 shows the plots of forward and reverse peak current (obviously the forward wave is not strictly peak-shaped) versus the DmFec concentration, together with the best fit lines. These demonstrate that the

forward and reverse peak currents are directly proportional to the DmFec concentration in the organic phase.

A study was also made, where the DmFec concentration in the organic phase was 10 mM (z - cell 6.3), and the concentration of the Fe(III)/Fe(II) couple in the aqueous phase (x, y - cell 6.3) was varied between 0.1 and 0.7 mM. The cyclic voltammograms for this experiment are shown in figure 6.8. In this case, however, a linear dependence in the concentration of Fe(III)/Fe(II) was not observed for either the forward or the reverse waves.

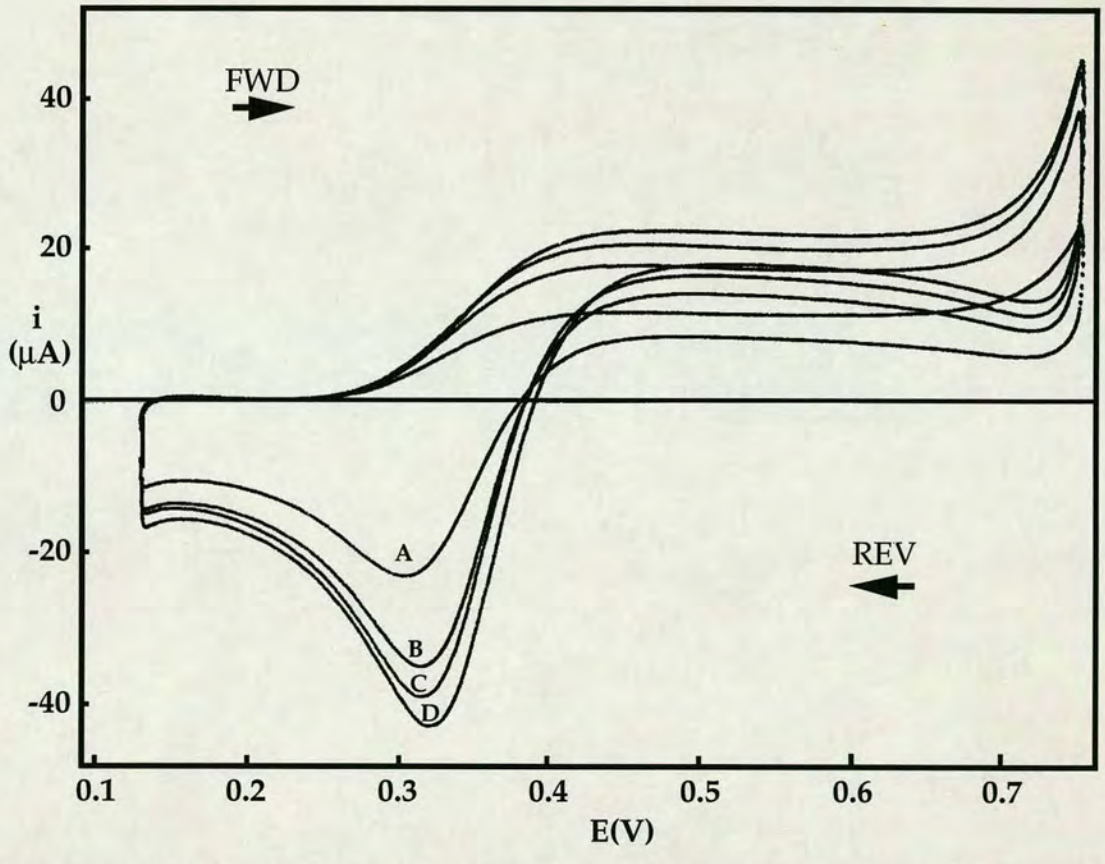

Figure 6.8 - Cyclic voltammograms for the variation of the Fe(III)/Fe(II) concentration, x = y = (A) 0.1, (B) 0.3, (C) 0.5, (D) 0.7 (mM); z = 10 (mM DmFec); cell 6.3.

A point to note at this stage is the value for the separation of the reverse peaks due to the reduction of Fec^+ (figure 6.2) and $DmFec^+$ (wave A, figure 6.8). Essentially, both these waves have been recorded under identical conditions - namely a scan rate of 0.1 Vs^{-1}, a concentration of x = y = 0.1 (mM Fe(III)/Fe(II), cells 6.2 and 6.3) and a Fec (or DmFec) concentration of 10 mM. The reverse peak corresponding to the reduction of $DmFec^+$ is about 175 mV less than that for the reduction of Fec^+. This then indicates that DmFec is more easily oxidised than Fec.

A test experiment involving nitrobenzene as the organic phase was also carried out using concentrations of 10 mM Fe(III)/Fe(II) and 0.5 mM DmFec. This gave exactly the same wave shape as for 1,2-DCE.

6.2.3 Electro-Oxidation

In this study the electro-oxidations of Fec and DmFec to Fec^+ and $DmFec^+$ respectively were carried out using the following cell:

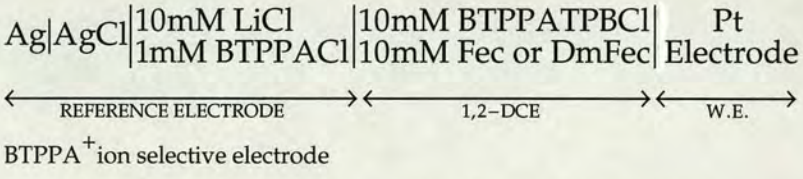

Cell 6.4 - where W.E. represents working electrode.

The cell design shown in figure 6.1 was used for this work. The cell potential was set to a value slightly greater than that required for oxidation of the Fec or DmFec, and the cell was left for approximately 20 minutes. Cyclic voltammograms for the Fec^+ and $DmFec^+$ transfer were then recorded, after which the cell was left scanning continuously for a further 30 minutes.

Cyclic voltammograms were then re-recorded to check the stability of the cationic species produced. Scan rate dependences and internal references to TMA^+ transfer were also carried out.

In each case the cationic species produced were found to be stable with time, and no other waves were observed in the potential window, suggesting no interaction with the supporting electrolyte. Table 6.1 lists the half-wave potentials obtained for the transferring species together with the half wave-potential for the transfer of TMA^+. On the same table are the formal potential values for Fec^+ and $DmFec^+$ which were calculated using the following relationship:

$$\Delta^{aq}_{org}\phi^{o'}_{Fec^+(DmFec^+)} = \Delta^{aq}_{org}\phi^{1/2}_{Fec^+(DmFec^+)} - \left[\Delta^{aq}_{org}\phi^{1/2}_{TMA^+} - \Delta^{aq}_{org}\phi^{o'}_{TMA^+}\right] \qquad (6.1)$$

where $\Delta^{aq}_{org}\phi^{o'}_{TMA^+}$, the formal potential for TMA^+ transfer, is taken to be 160 mV on the tetraphenylarsonium tetraphenylborate (TPAsTPB) scale [183]. To allow calculation of the formal potentials of Fec^+ and $DmFec^+$, it is necessary to assume that Walden's rule (equation 2.2.3) applies for the transfer of the electro-generated species across the water/1,2-DCE interface.

Table 6.1 - Half-wave and formal potentials for Fec^+ and $DmFec^+$ transfer across the water/1,2-DCE interface. Exptal. stands for experimental.

Ion	$\Delta^{aq}_{1,2\text{-DCE}}\phi^{1/2}_{Exptal.}$ (mV)	$\Delta^{aq}_{1,2\text{-DCE}}\phi^{1/2}_{TMA^+(Exptal.)}$ (mV)	$\Delta^{aq}_{1,2\text{-DCE}}\phi^{o'}$ (mV)
Fec^+	360 ± 2	513 ± 2	7 ± 4
$DmFec^+$	292 ± 2	515 ± 2	-63 ± 4

Figure 6.9 shows the cyclic voltammograms obtained for the transfer of $DmFec^+$ across the water/1,2-DCE interface, demonstrating the process to be fully reversible (characterised by a peak-to-peak separation of approximately 60 mV). Figure 6.10 shows the plot of the peak current versus the square root of the scan rate, which yields a straight line.

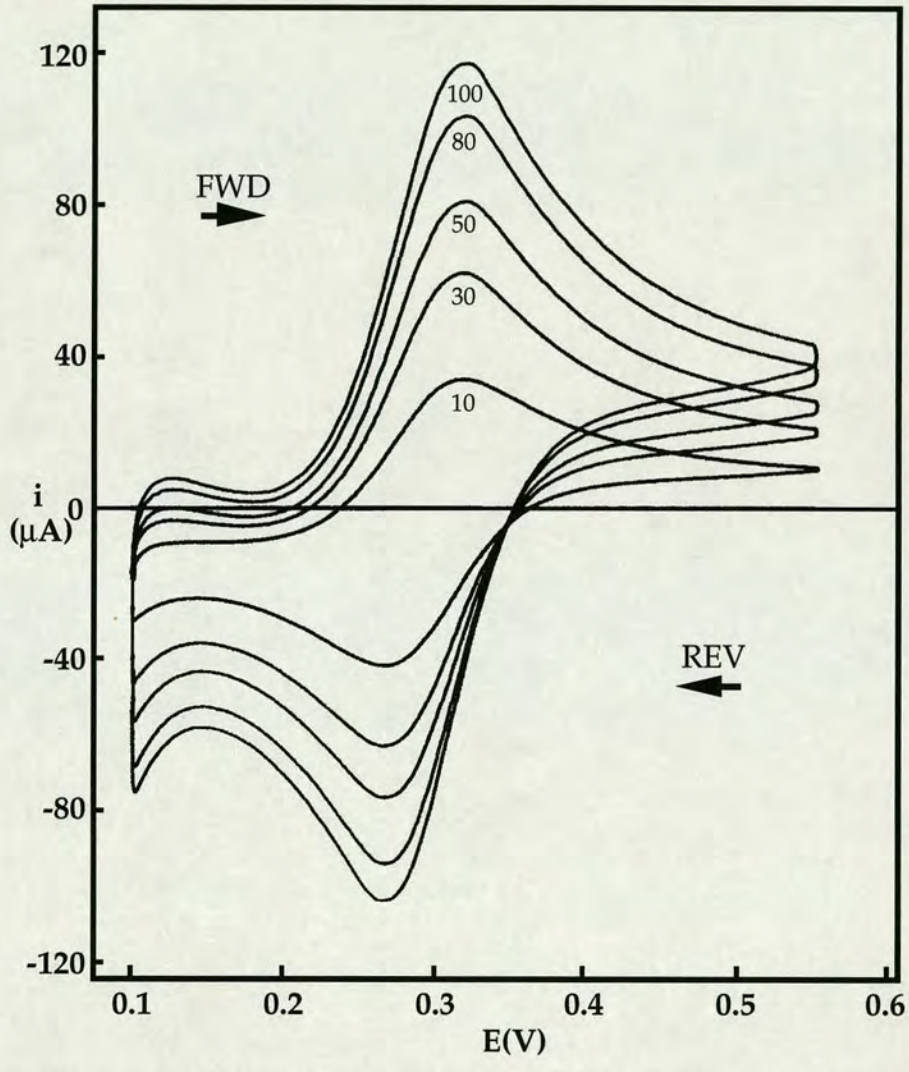

Figure 6.9 - Cyclic voltammograms recorded at different scan rates (10, 30, 50, 80, and 100 mVs^{-1}) for cell 6.4, 30 minutes after electro-oxidation of DmFec.

The value obtained for Fec^+ transfer (7 ± 4 mV) is lower than the value of 40 mV previously reported by Brown. To this author's knowledge, no value

has previously been reported for the transfer of $DmFec^+$. As already stated in section 6.2.2, the difference between the experimental half-wave potential values obtained indicates that the electron transfer process involving DmFec is uncomplicated by ion transfer. This has already been established for Fec [72].

The oxidation of DmFec and Fec was also carried out for cell 6.4, where the platinum working electrode was replaced with a 25 μm diameter platinum disc. The concentration of DmFec (and Fec) utilised was of the order of 1 mM. Figure 6.11 shows the steady-state voltammograms obtained. The separation between the half-wave electron transfer potentials is 130 mV, with DmFec being more easily oxidised than Fec. This is in step with the results acquired for the ITIES, and furthermore underlines the fact that interfacial electron transfer across the ITIES does indeed occur.

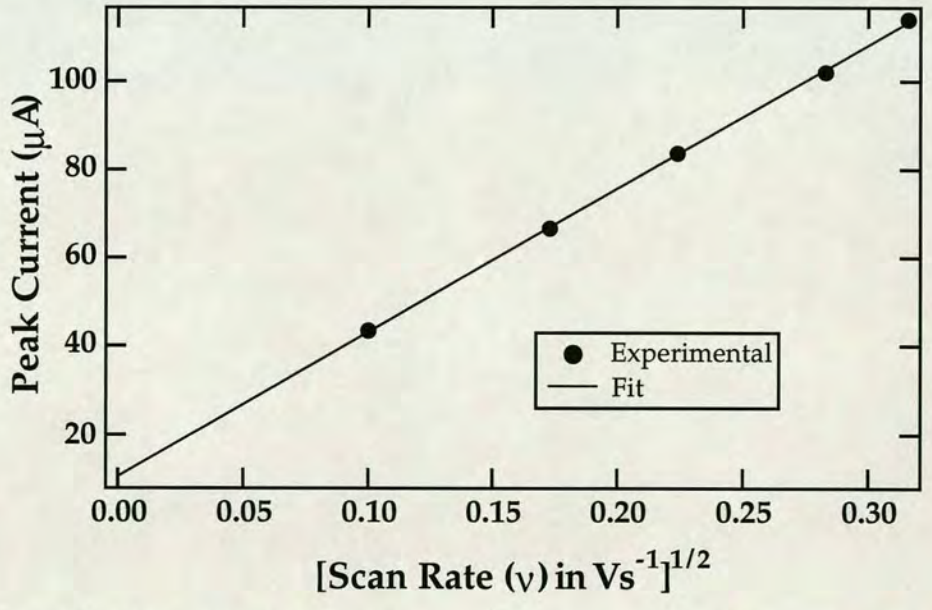

Figure 6.10 - Plot of peak current versus the square root of the scan rate for the voltammograms shown in figure 6.9.

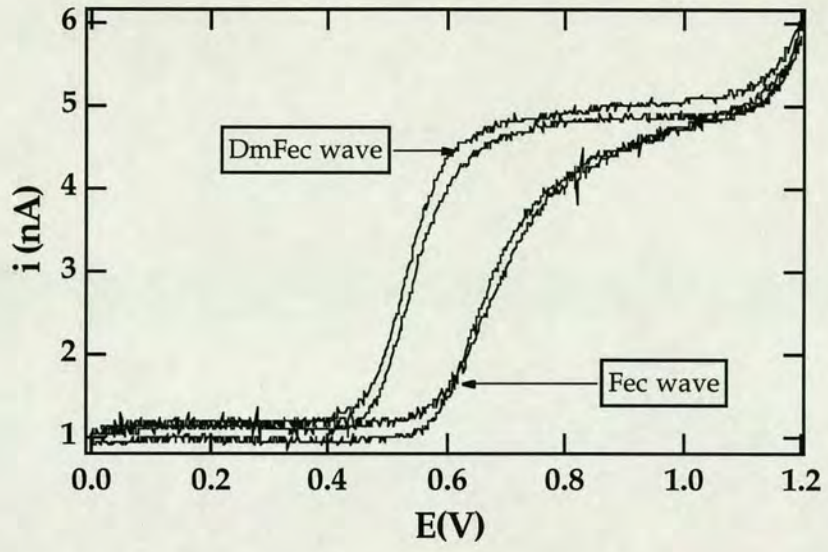

Figure 6.11 - Steady-state voltammograms obtained for the oxidation of Fec and DmFec at a 25 μm radius platinum disc electrode. Waves recorded using a Tacussel Pol 150 T (Polaro Analyser) and acquired using Windows-driven software. The scan rate in each case was 2 mVs^{-1} and the apparatus was unshielded.

6.2.3 Conclusions

It has been shown that the ferrocene and 1,1'-dimethylferrocene /hexacyano-ferrate electron transfer systems are far from simple under the conditions employed. It has also been shown that dissolved oxygen is not a factor in experiments of this nature. One possibility is that the Fe(II) produced in the forward scan of the experiment is unstable and gives rise to a species which will complex with the Fec^+ or $DmFec^+$. It may be, for instance, that there is only a certain pH at which Fe(II) is stable. Indeed, in reference [139] the standard electrode potential for the reduction of $[Fe(CN)_6]^{3-}$ is quoted for the condition of molar H_2SO_4. This value is 690 mV, whereas in neutral conditions the value is 358 mV [153].

The oxidation of DmFec has been observed to be easier than that of Fec. The separation of the peaks of the reverse electron transfer processes correlates with the half-wave potentials obtained for the oxidation of Fec and DmFec in 1,2-DCE at a solid platinum microdisc electrode. An unresolved issue is the non-dependency of the DmFec/$[Fe(CN)_6]^{3-/4-}$ system in the concentration of the aqueous redox couple. The reason for this behaviour is unclear but may be related to the stability of the $[Fe(CN)_6]^{3-/4-}$ couple.

The electron transfer from DmFec to $[Fe(CN)_6]^{3-}$ was found to be uncomplicated by the effects of ion transfer as previously established for Fec [73]. A formal potential value for the $DmFec^+$ ion of -63 ± 4 mV was also reported, as well as a new value for Fec^+ of 7 ± 4 mV.

6.3 The Ferrocene/Copper (II) System

The initial purpose of this work was to use copper (II) in the aqueous phase as a substitute for the hexacyanoferrate redox couple used previously, in order to ascertain whether a reversible electron transfer reaction involving Fec could be observed.

6.3.1 Results and Discussion

The cell used for these studies was as shown:

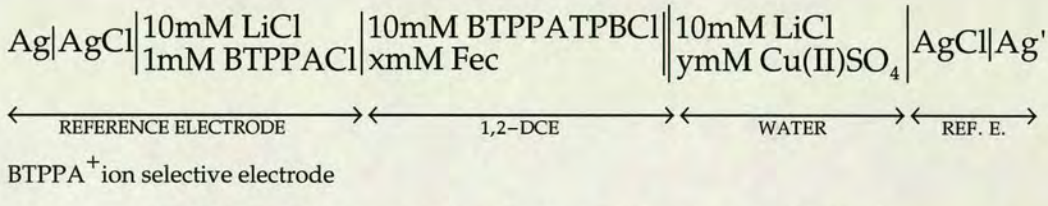

Cell 6.5 - where x and y refer to a value given in the text.

It should be stated that Cu(II) was not observed to transfer within the potential window utilised. For the first experiment, values of x = 10 (mM Fec) and y = 0.1-0.9 (mM Cu(II)SO_4) were employed in cell 6.5. A wave was observed to develop in the middle of the window, the height of which was found to exhibit a non-linear dependence in the concentration of Cu(II) used, as was the case for Fe(III)/Fe(II).

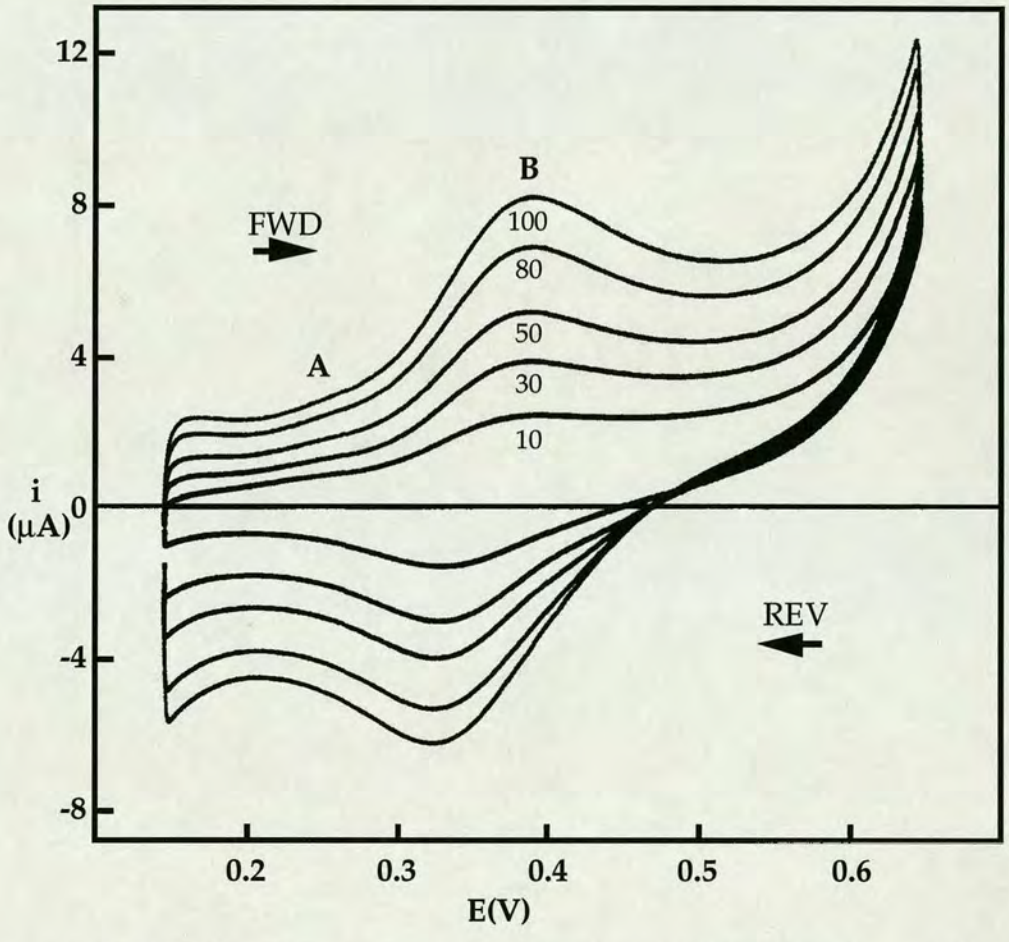

Figure 6.12 - Cyclic voltammograms for cell 6.5: x = 10 (mM Fec); y = 0.9 (mM Cu(II)); scan rates = 10, 30, 50, 80, 100 mVs^{-1}.

Figure 6.12 illustrates cyclic voltammograms recorded at various scan rates for y = 0.9. There are three distinguishing features associated with the voltammograms obtained: (1) the wave in the centre (B - figure 6.12) exhibits

behaviour expected for reversible single charge transfer, namely a linear dependence of the forward peak current in the square root of the scan rate, and a peak to peak separation of about 60 mV; (2) an odd shape to the right hand side of the potential window is observed, which would seem to indicate no charge transfer on the reverse scan; and (3) an obvious 'bump' (A - figure 6.12) preceding the main wave on the forward scan.

Wave B in figure 6.12 was assigned a formal potential value of 7 ± 4 mV by internal reference to TMA^+ transfer using the method described in section 6.2. This value is the same as the formal potential ascribed to Fec^+ transfer, listed in table 6.1. Therefore, wave B is assumed to be transfer of Fec^+.

The odd shape of the right hand side of the potential window, noted above, may be explained as follows: The potential is ramped linearly on the forward scan to the electron transfer potential, at which point a positive current is observed due to electron transfer from Fec to Cu(II). At this stage there are three possibilities (1) Cu^+ forms $[CuCl_2]^-$; (2) Cu^+ is automatically transferred to the organic phase upon formation; or (3) Cu^+ spontaneously disproportionates in water according to the reaction:

$$2Cu^+ \rightleftharpoons Cu^{2+} + Cu(s) \qquad (6.2)$$

In the case of (2), Cu^+ would be expected to be spontaneously re-oxidised to Cu^{2+} in the organic phase since the standard reduction potentials in water, for the reactions:

$$Cu^{2+} + e^- \rightleftharpoons Cu^+ \qquad (6.3)$$

and $Fec^+ + e^- \rightleftharpoons Fec$ (6.4)

are 153 and 400 mV respectively [153]. However, if this is in fact the case, the reaction must be relatively slow since Fec^+ clearly persists in the organic phase. Any of the processes described above would result in an apparent absence of charge transfer on the reverse scan.

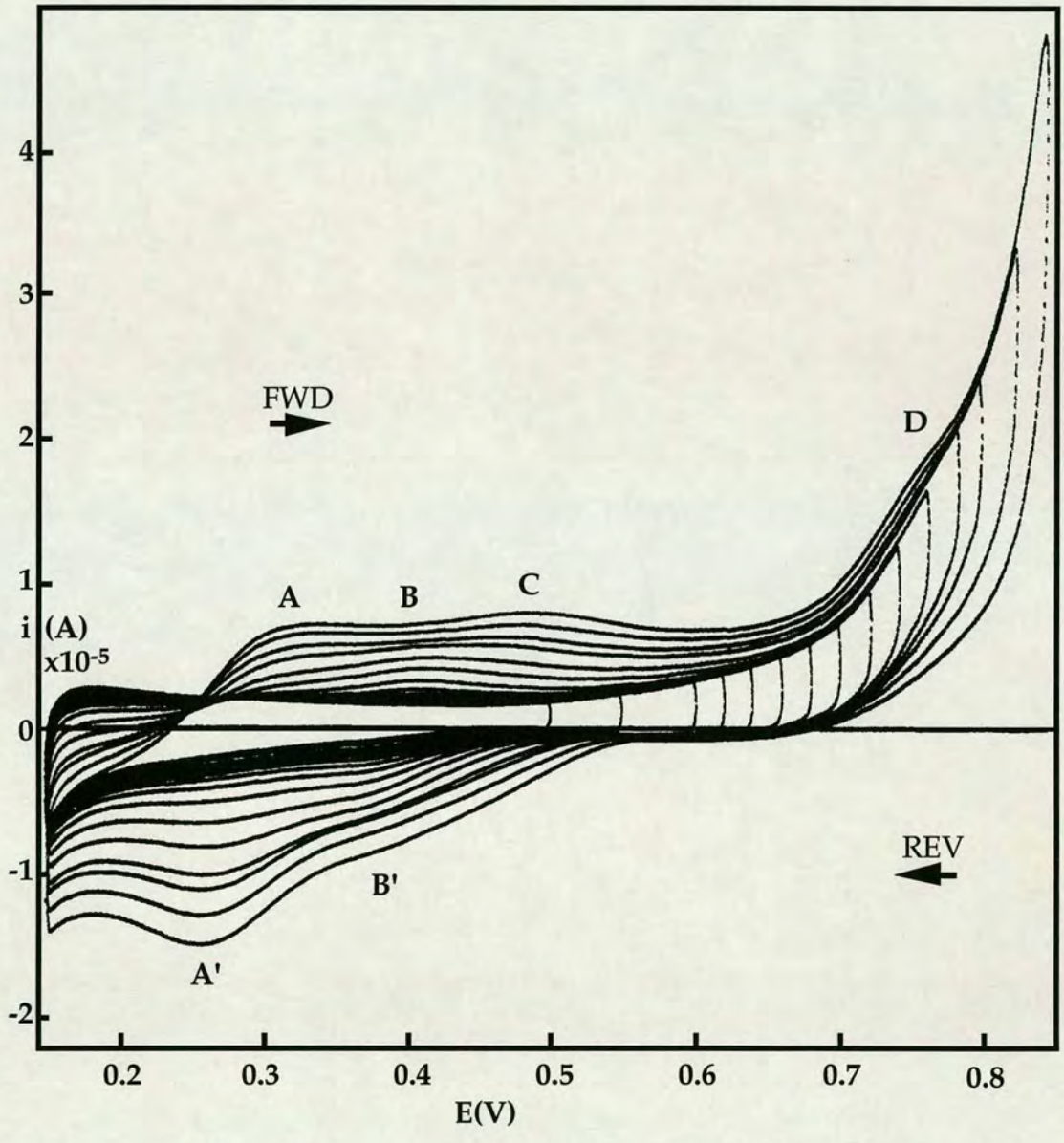

Figure 6.13 - Cyclic voltammograms for cell 6.5: an outward potential sequence for x = 0.5 (mM Fec)/y = 10 (mM Cu(II)).

In the interests of characterising the system more fully, it was decided to carry out potential dependence studies for cell 6.5, using values of x = 0.5 (mM Fec) and y = 10 (mM Cu(II)), and x = 10 mM Fec and y = 0.5 mM Cu(II) respectively.

In these experiments, the left-hand side of the potential window was always a constant cell potential value and the right hand side was expanded from a value at which no electrochemical processes were observed to occur, to one at which several reactions seemed to be taking place. Potential progressions of 50 mV, and subsequently 20 mV, were used. Each voltammogram was recorded after two minutes of continuous cyclic scanning. The same procedure was also carried out, but in reverse, after the outward potential sequence.

Figure 6.13 illustrates voltammograms of the outward potential sequence for the x = 0.5 (mM Fec)/y = 10 (mM Cu(II)) case - cell 6.5. Four waves (A, B, C, and D - figure 6.13) are apparent. Wave B is thought to be Fec^+ and wave D is clearly the electron transfer wave (Fec to Cu(II)). When the inward potential sequence was carried out, the voltammograms retraced the outward potential sequence almost exactly - back to a point where no electrochemical reactions were observed. This indicates that all the transfer reactions are reversible, or that the species produced are unstable. Fec^+ has already been demonstrated to be stable and to exhibit reversible transfer, therefore the identity and stability of waves A and C is of interest. The separation between waves A and C is approximately 160 mV.

The potential window limits were set to 100 and 830 mV and a scan rate dependence was performed (not shown). Wave A was found to exhibit a

linear dependence in the square root of the scan rate, and to possess a peak-to-peak separation of approximately 60 mV, indicating reversible single charge transfer. By reference to TMA^+ transfer, wave A was assigned a formal potential value of -105 ± 4 mV, and wave B was confirmed to be Fec^+ transfer. Wave C, on the other hand was more difficult to analyse in terms of its dependence on the scan rate, the data obtained being relatively poor. When an experiment involving 10 mM Cu(II) and 10 mM Fec was performed, however, wave C was demonstrated to have a linear dependence in the scan rate with the best fit line passing close to the origin. This suggests that wave C is due to adsorption/transfer of some species.

The formal potential value obtained for wave A allows a formal potential value for the electron transfer between Fec and Cu^{2+} of 360 mV to be assigned. A value for the formal potential for electron transfer for the $[Fe(CN)_6]^{3-/4-}$/Fec system may be calculated using Brown's data [161] and equation 6.1 - this yields a value of 155 mV. Clearly, the reduction of Cu^{2+} is more difficult than that of $[Fe(CN)_6]^{3-}$. This observation is in line with the standard reduction potentials for $[Fe(CN)_6]^{3-/4-}$ (358 mV) and $Cu^{2+/+}$ (153 mV) [153]. The difference between each set of values is identical, and reflects the analogy between the metal electrode/electrolyte solution interface and the ITIES.

Figure 6.14 demonstrates the results obtained for x = 10 (mM Fec)/y = 0.5 (mM Cu(II)). As before, the same behaviour on the inward as on the outward potential progression was observed. Waves A, B and C are again evident, however, wave D is not clearly resolved. The relative positions of waves A and B are unchanged with respect to each other, but the difference between waves A and C has increased quite dramatically (separated by

about 250 mV). This suggests that a decrease in the Cu(II) concentration leads to less favourable adsorption/transfer behaviour. The above experiment was also carried out using degassed solutions with very similar results, indicating that dissolved oxygen played no part in the processes.

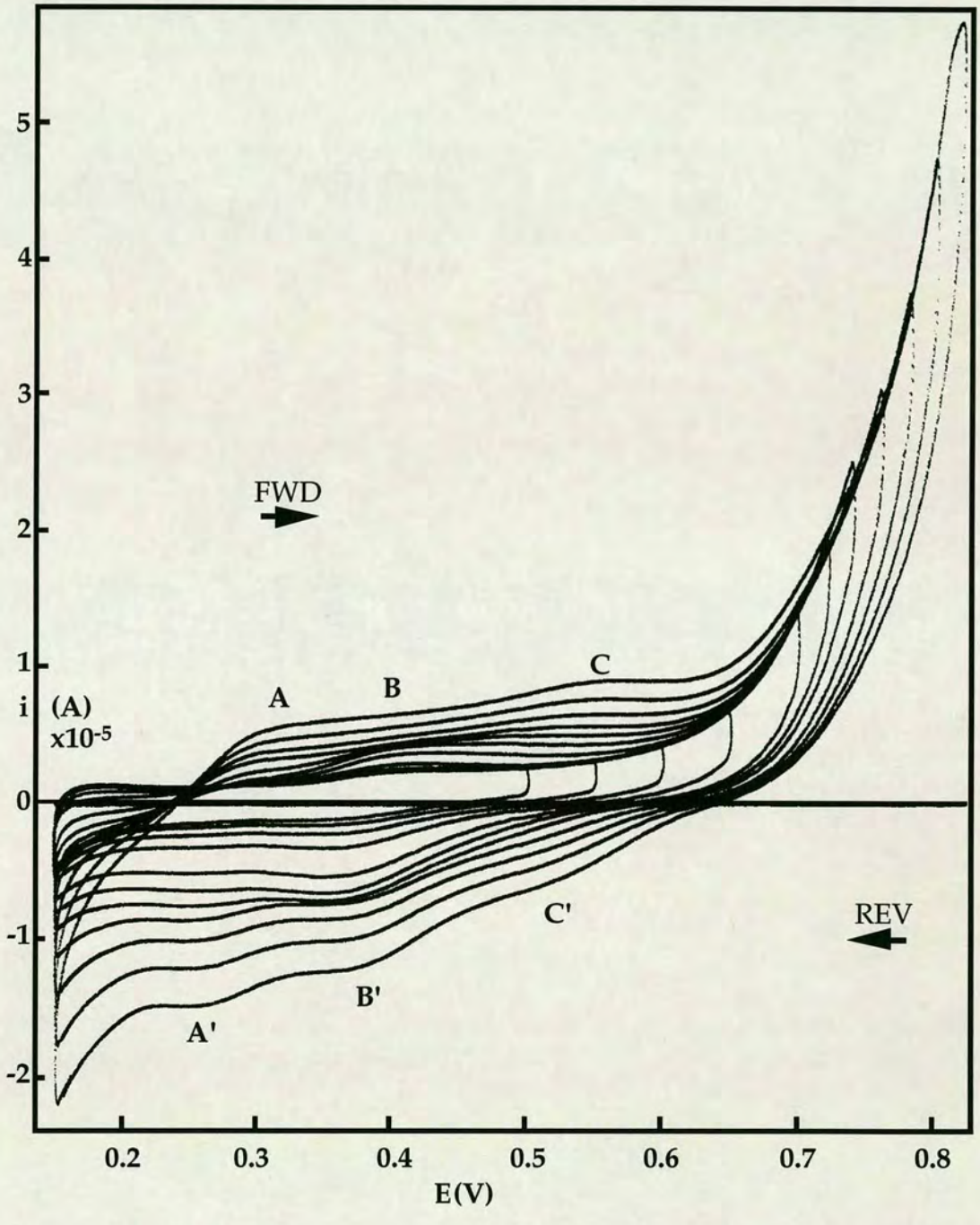

Figure 6.14 - Cyclic voltammograms for cell 6.5: an outward potential sequence for x = 10 (mM Fec)/y = 0.5 (mM Cu(II)).

In a recent publication by Schiffrin and co-workers [67] it was demonstrated that the ion transfer of $[Cu(II)Cl]^+$, between water and 1,2-DCE could be facilitated by a tetradentate phosphorus-nitrogen ligand. The importance of this work was that the starting system utilised 0.1 mM $Cu(II)SO_4$/2 mM ligand/50 mM Li_2SO_4 as the aqueous phase. Under these conditions, no wave for Cu(II) transfer was observed. However, by the addition of a cell concentration equivalent of 2 mM LiCl a wave corresponding to reversible single charge transfer was evident. This indicates that Cl^- can co-ordinate to the Cu(II) ion.

The above result is of great interest to the present investigations, and also for the identity of wave A. It was decided, therefore, to perform an experiment in the absence of LiCl in the aqueous phase, using cell 6.6.

$$\begin{array}{l} Ag|AgCl\left|\begin{array}{l}10mM\ LiCl\\1mM\ BTPPACl\end{array}\right|\begin{array}{l}10mM\ BTPPATPBCl\\10mM\ Fec\end{array}\left\|\begin{array}{l}10mM\ Li_2SO_4\\0.5mM\ Cu(II)SO_4\end{array}\right|Ag_2SO_4|Ag' \\ \longleftarrow\ \text{REFERENCE ELECTRODE}\ \longrightarrow\longleftarrow\ \text{1,2-DCE}\ \longrightarrow\longleftarrow\ \text{WATER}\ \longrightarrow\longleftarrow\ \text{REF. E.}\ \longrightarrow \\ BTPPA^+\text{ion selective electrode} \end{array}$$

Cell 6.6

The voltammograms obtained are shown in figure 6.15. Clearly, there has been a dramatic change in the behaviour of the system. There is no evidence of wave A, although waves B and C are still present. When the right hand side of the window was extended to more positive potentials however, wave A did appear. These results suggest that formation of A is heavily dependent on stabilisation by chloride ions in the aqueous phase.

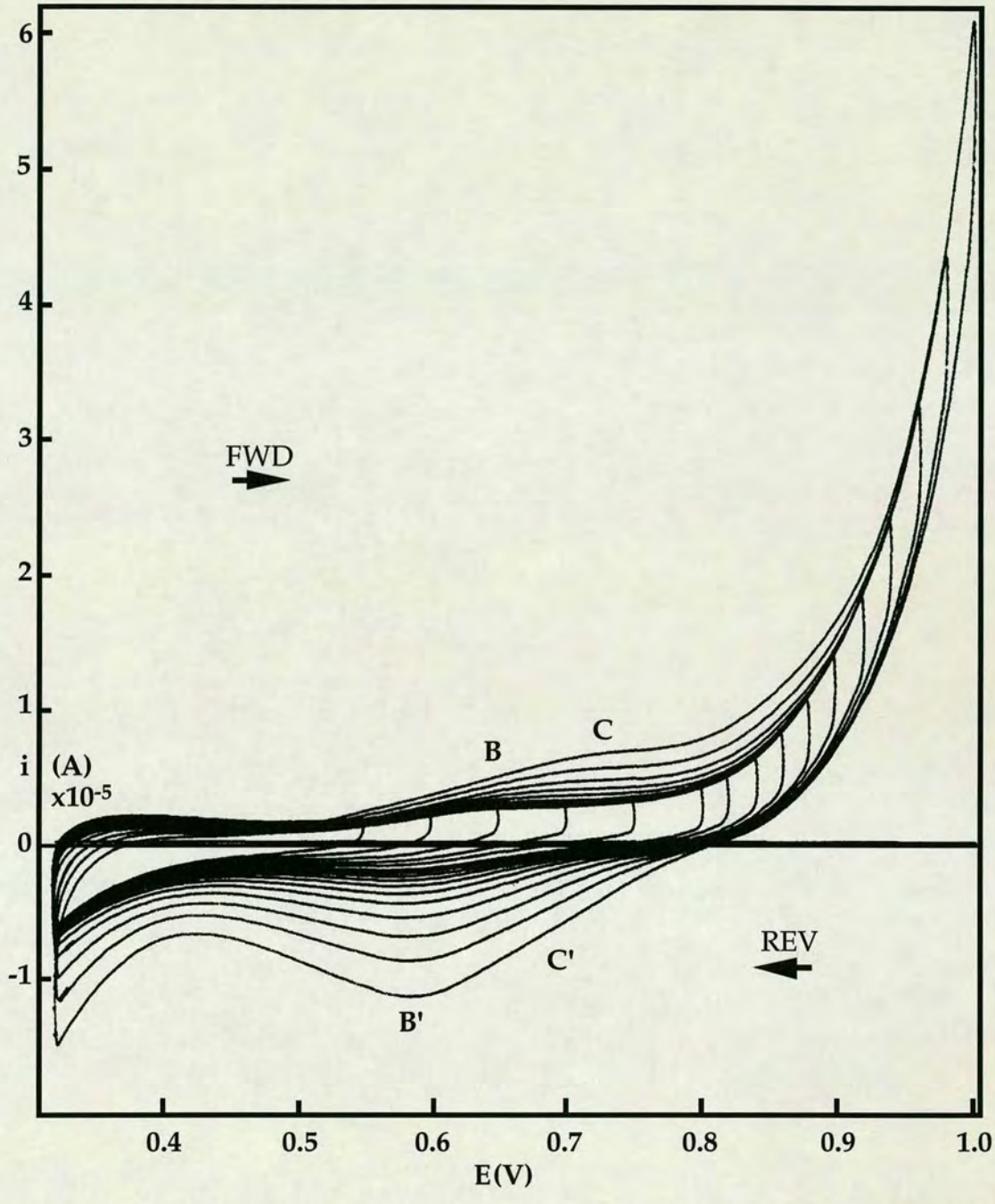

Figure 6.15 - Cyclic voltammograms obtained for cell 6.6: outward potential sequence.

In a single scan study, starting at time zero, no waves were visible on the forward scan other than that observed for electron transfer on the right hand side of the potential window. On the reverse scan however, waves B′ and C′ were clearly seen. This indicates that there is little electron transfer on the

reverse scan due to transfer of Cu^+ from the aqueous phase to the organic phase leading to a subsequent build up of Fec^+.

6.3.2 Copper (I) Chloride

An additional experiment, utilising cell 6.7, where Cu(I)Cl was present in the aqueous phase, and no Fec was present in the organic phase, yielded significant results. Cu(I)Cl is only sparingly soluble in water, therefore the concentration of solvated Cu(I) is difficult to ascertain. Despite this fact, a cell concentration equivalent of 1 mM Cu(I)Cl was used in the aqueous phase.

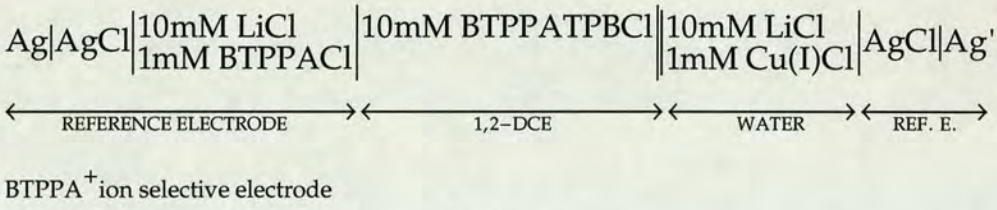

Cell 6.7

The voltammograms obtained for an outward potential sequence are illustrated in figure 6.16. Three waves (X, Y, and Z) were observed. Wave X was found to be relatively independent of the change in potential, however, wave Y only began to appear after scanning above 600 mV. When the inward potential sequence was carried out wave Y disappeared in an analogous manner to wave C in previous experiments. Wave Z must therefore be an electron transfer process. Wave X is probably $[CuCl_2]^-$.

Wave X was referenced to TMA^+ transfer and found to have a formal potential of -125 mV, which is relatively close to the value obtained for wave

A in previous experiments. Both A and X may therefore be attributed to $[CuCl_2]^-$ transfer.

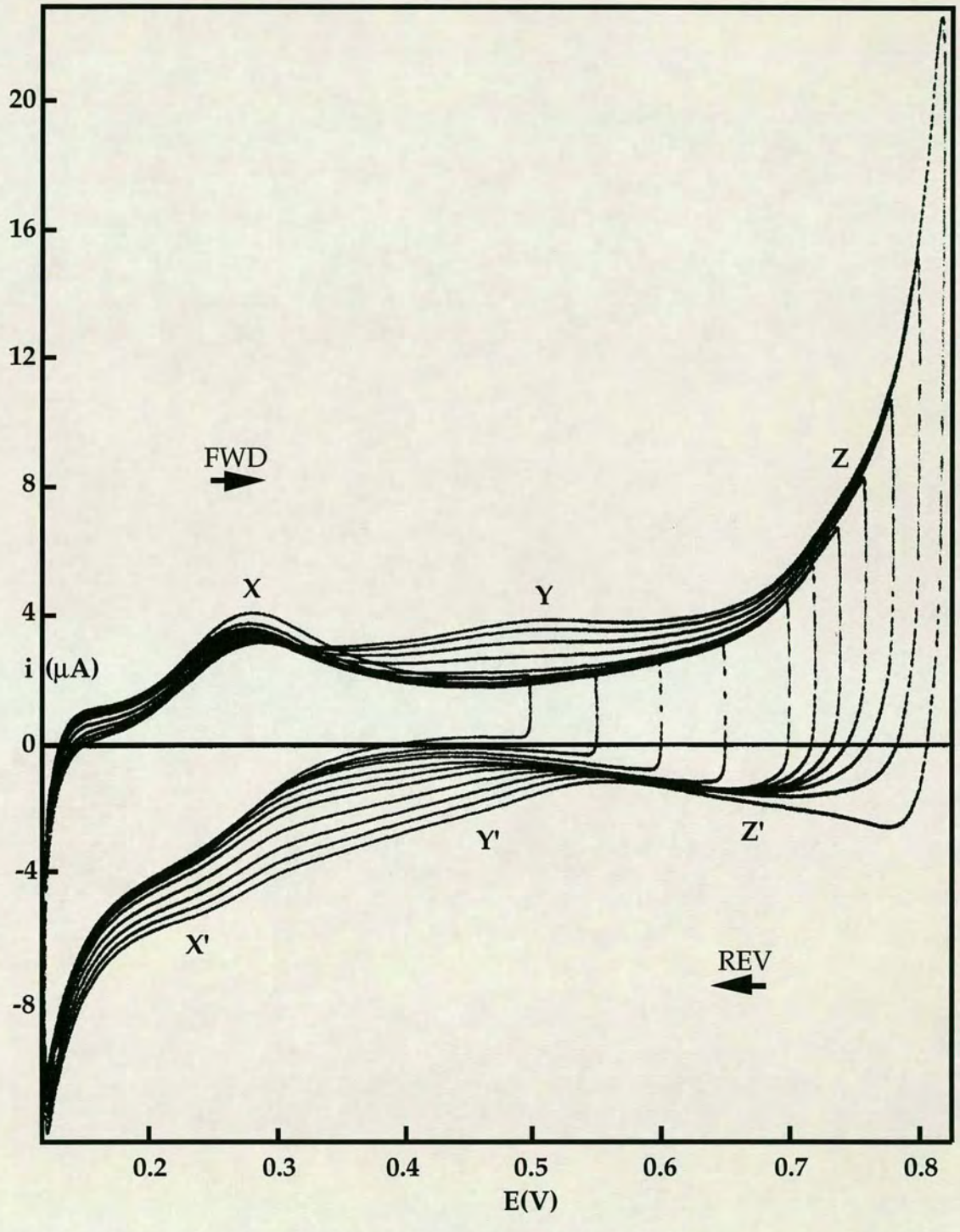

Figure 6.16 - Cyclic voltammograms obtained for cell 6.7: outward potential sequence.

It is difficult to ascertain whether waves Y and Z are due to contamination of the glassware from the high concentrations of Fec previously employed. The only other possibility is that heterogeneous electron transfer takes place between Cu(I) and the organic phase supporting electrolyte at a certain potential. It was impossible to confirm whether this was the case or not due to the lack of a pure source of BTPPATPFPB - this would have been immune to any form of redox species [161] and would have demonstrated unequivocally the true nature of the observed phenomenon.

6.3.3 Conclusions

The Cu(II)/Fec system has been demonstrated to be essentially reversible in terms of the potential dependence of the electron transfer reaction and the species produced. The electron transfer itself has been assigned an approximate formal potential value of 360 mV. The reduction of Cu^{2+} to Cu^{+} was demonstrated to be more difficult than the corresponding reduction of $[Fe(CN)_6]^{3-}$ to $[Fe(CN)_6]^{4-}$. This is expected from the standard reduction potentials quoted in the literature.

Most of the features associated with the electron transfer reaction have been resolved with the exception of wave C which is thought to be adsorption/transfer of some species. The identity of this species is difficult to ascertain without using a redox inactive supporting electrolyte.

Copper (I) has been illustrated to form and transfer on the forward scan of the experiment (positive potential of the aqueous phase increasing) leading to an odd shape to the reverse scan of the experiment. Furthermore, the $[CuCl_2]^-$ ion has been shown to have a formal potential value of approximately -105 ±

4 mV, indicating that it is relatively hydrophobic in character. Cu^+ formation was also demonstrated to be favoured by the presence of chloride ions in the aqueous phase.

6.4 Conclusions to Chapter Six

Heterogeneous electron transfer at the ITIES has been successfully demonstrated for both the Cu(II)/Fec system, and the $Fe(CN)_6^{3-/4-}$/Fec and $Fe(CN)_6^{3-/4-}$/DmFec systems. The potentials at which these reactions occur relate to the general scheme of standard reduction potentials observed at the metal electrode/electrolyte solution interface.

Footnote: Work performed in a subsequent study by F.Dubois and Dr. R.G.Wellington of the Institut d'Electrochimie, E.P.F.Lausanne, Switzerland [184] has indicated that the $Fe(CN)_6^{3-/4-}$/Fec electron transfer reaction is a fully reversible, single charge transfer process, uncomplicated by adsorption effects. This was achieved by using a pre-acidified (1M HCl) aqueous phase of 10 mM Fe(III)/Fe(II). This illustrates that the adsorption behaviour previously observed is associated with the stability of the Fe(II) species in the aqueous phase. This then opens the door to future studies, involving the use of the microhole-supported ITIES to investigate the kinetics of the electron transfer process.

Chapter Seven

ENZYMATIC ANALYSIS AT THE ITIES

7.1 Introduction

In this chapter, the hydrolysis of the butyrylcholine cation ($ButCh^+$) by the enzyme butyrylcholinesterase (BChE) was studied using ion transfer across the polarised water/1,2-DCE interface, and the inhibition of the enzyme by the organophosphate compound paraoxon was demonstrated.

Organophosphate compounds, and related substances, are the most widely used insecticides in the world having replaced the older, and more persistent organochlorine compounds. The target of these substances is the central nervous system (CNS) of insects but because the CNS of both vertebrates and invertebrates operate by cholinergic transmission, accidental poisonings due to crop spraying or other uses may severely harm humans [162].

Nerve transmission ends when the enzyme acetylcholinesterase (AChE) hydrolyses the neurotransmitter acetylcholine (ACh^+) to choline (Ch^+) and acetic acid in order to re-establish the initial state of the post-synaptic membrane [162]. Organophosphate compounds imitate the overall molecular shape of ACh^+ and can bind irreversibly to the esteratic active site of the enzyme rendering it non-functional [163].

Due to the health threat posed by the build up of pesticide residues in the environment, legislation has made the detection of these compounds at the

parts per billion (ppb) and sub-ppb domains a necessity. At the moment the best detection techniques are gas chromatography (GC), high performance liquid chromatography (HPLC), or GC coupled with mass spectrometry (GC/MS) [164]. Although such techniques are the best available they are costly, and require skilled personnel to operate them efficiently. In the search for cheaper alternatives, much effort has been devoted to the development of relatively inexpensive electrochemical techniques, such as enzyme or antibody-based biosensors, to try and effect the same performance as the conventional methods. Some examples of enzymatic methods developed specifically for the detection of organophosphate compounds are described below. These methods generally fall into two broad categories: (1) - amperometric, where the rate of the enzyme reaction is monitored by directly recording the current that arises at the electrode interface; and (2) - potentiometric, where a membrane (for instance glass) selectively extracts a charged species into the membrane phase, creating a potential difference between the internal filling solution and the sample solution, which can be subsequently measured.

Potentiometric methods:

A commercial, field-based instrument utilising replaceable pads with gel-entrapped BChE as the sensor was developed by Goodson *et al.* [165] in the 1970's. Pesticide detection was based on the production of electroactive thiocholine from the hydrolysis of butyrylthiocholine . The inhibition of the enzyme produced a change in the measured voltage of the cell.

Durand *et al.* [166], and Kumaran and Tran-Minh [167] used pH electrodes modified with an enzymic layer to investigate AChE [166] and BChE [167] inhibition, using ACh^+ and butyrylcholine ($ButCh^+$) as the respective

substrates. The method of detection was based on the fact that one proton is produced per hydrolysed substrate molecule.

Amperometric methods:

Razumas *et al.* [168] studied inhibition of BChE in solution using indoxyl acetate as the substrate, producing indoxyl, which could be measured amperometrically.

Campanella *et al.* [169] investigated AChE and BChE inhibition using a method based on an oxygen electrode covered with a dialysis membrane, on which choline oxidase was immobilised. AChE or BChE was either free in solution or immobilised with the choline oxidase. The substrates used were ACh^+ and $ButCh^+$. Inhibition of the enzyme led to an increase in the oxygen concentration being measured. Their results showed that BChE is more sensitive to organophosphate inhibition than AChE, for a given inhibitor.

Bernabei *et al.* [170] studied AChE inhibition using the same principles but replaced the oxygen electrode with a hydrogen peroxide sensor and sandwiched the enzyme loaded nylon net membrane between two other membranes: a cellulose acetate membrane to protect the electrode from electrochemical interferences; and a dialysis membrane to protect the enzyme from large molecules and bacteria. Their results showed that experiments with the AChE free in solution are more sensitive than for the immobilised case.

Kulys and D'Costa [171] and Skladal [172] studied BChE inhibition using printed-strip amperometric sensors containing the immobilised enzyme and a redox mediator. The substrate used in each case was butyrylthiocholine.

From the various investigations cited above [165-172], the general conclusions are that the inhibition of the enzyme is favoured by incubation with the pesticide for a certain amount of time, and that the longer the incubation time, the greater the observed inhibition. It is clear, however, that in general, amperometric techniques tend to give much greater sensitivity than the potentiometric methods.

Vanysek and Behrendt [173] investigated the hydrolysis of ACh^+ by AChE at the polarised water/NB interface, in an attempt to demonstrate an alternative assay for enzyme activity. The problem with this method, however, is that the ACh^+ and Ch^+ peaks are poorly resolved making it difficult to allow unambiguous determination of enzyme activity. As will be demonstrated, the resolution of $ButCh^+$ and Ch^+ is much clearer.

7.1.1 BChE and AChE

BChE and AChE are type B carboxylesterases [174] which have similar catalytic properties [175]. Each enzyme can hydrolyse ACh^+ to acetic acid and Ch^+, but AChE is subject to marked substrate inhibition, whereas BChE is capable of interacting with a wider range of choline esters [175]. As previously mentioned (7.1), the main function of AChE in the body is the termination of the action of ACh^+ in the CNS. BChE, on the other hand, has no known physiological function, although it has been postulated that the enzyme acts in place of acetylcholinesterase during foetal development [176]. BChE is of interest to pharmacologists, since it is responsible for the hydrolysis of succinylcholine - a drug used in surgery as a short-acting blocker of the ACh^+ receptor [176].

7.1.2 Paraoxon

Paraoxon (diethyl *p*-nitrophenyl phosphate, figure 7.1(b)) belongs to a group of compounds called oxons, and it is produced when the phosphorothionate molecule parathion (figure 7.1(a)) undergoes desulphuration by cytochrome P-450 monooxygenases (present in bacteria, fungi, plants and animals) [177]. Oxons are very powerful inhibitors of AChE, and for this reason phosphorothionate compounds (being relatively poor AChE inhibitors themselves) are often employed as commercial pesticides [177]. Figure 7.2 shows the $ButCh^+$ ion for comparison.

(a)

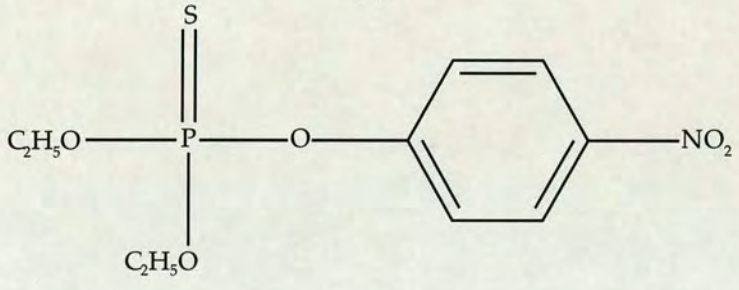

(b)

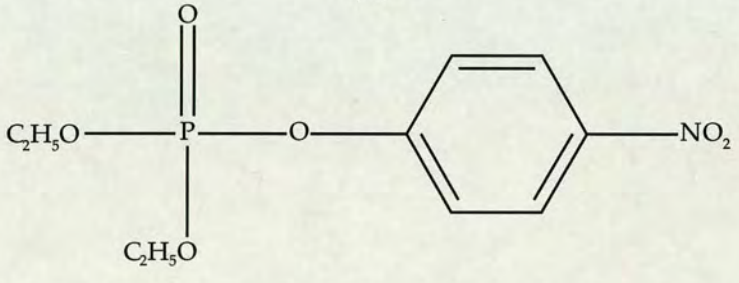

Figure 7.1 - (a) Parathion, and its metabolite (b) Paraoxon [178].

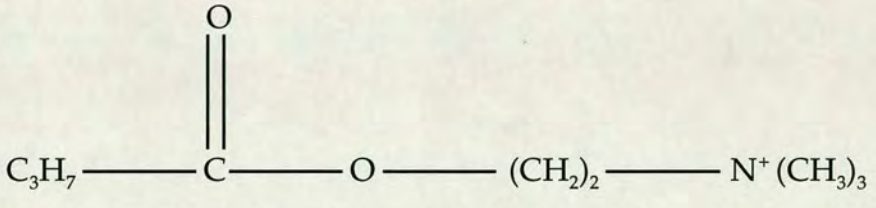

Figure 7.2 - Butyrylcholine ion ($ButCh^+$).

7.2 Results and Discussion

The basic reaction studied was the following:

$$\text{ButCh}^+ \xrightarrow{\text{BChE}} \text{Ch}^+ + \text{Butyric Acid} \qquad (7.1)$$

and the system used for the experiments was as described below:

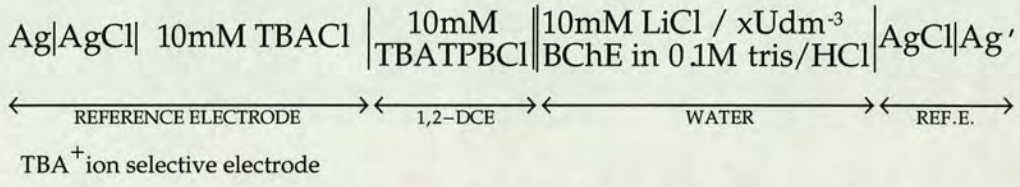

Cell 7.1 - where x is specified in the text, and U represents enzyme units.

During cyclic voltammetry, the scan rate was 0.1 Vs^{-1} (unless otherwise stated), the aqueous phase was unstirred, and iR drop compensation was not used (unless specified in the text).

The equations for enzyme kinetics were first developed by Michaelis and Menten [179] and are based on the mechanism:

$$E + S \underset{b}{\overset{a}{\rightleftharpoons}} ES \xrightarrow{c} E + \text{Prod} \qquad (7.2)$$

where the substrate, S, combines with the enzyme, E, to form an enzyme-substrate complex, ES, which proceeds to form the product, Prod, and the free enzyme (a, b, and c, are rate constants for the processes described above). The reaction involving BChE and ButCh^+ is similar to this. The enzyme contains two active sites: one is an esteratic site, the function of which is to cleave the ester linkage; and the other is an anionic site which

orientates the substrate molecule into position, by interaction with the nitrogen group, while cleavage of the ester linkage occurs.

A simplified equation for the reaction is as follows:

$$E + ButCh^{+} \underset{b}{\overset{a}{\rightleftharpoons}} EComp \xrightarrow{c} EBut + Ch^{+} \xrightarrow{d} E + ButA \quad (7.3)$$

where the last step is recovery of the enzyme (EComp = enzyme-substrate complex, ButA = butyric acid). It is the last step which the inhibiting molecule interferes with. In the case of the butyrylated enzyme (EBut) the last step is very fast (to illustrate, - for acetylated AChE, the half-life of the equivalent step is 42 microseconds [180]), but for a phosphorylated enzyme this step is very slow. Although the phosphorylation is not completely irreversible, the dephosphorylation is slow enough to render the enzyme effectively non-functional, the half-life of the phosphorylated enzyme varying from hours to months depending on the nature of the alkyl substituents on the inhibiting molecule.

In the case of reversible inhibition, where the inhibitor is in equilibrium with the enzyme or enzyme-substrate complex, Michaelis-Menten principles may be applied for analysis of the results. Irreversible inhibition, however, cannot be treated in a similar manner [181]. An equation based on a simplified approach to the enzyme kinetics for irreversible inhibition (see appendix 2) was therefore used to treat the experimental results obtained.

Figure 7.3 shows the potential window obtained for cell 7.1 with a value of x=1000 (Udm^{-3}). This indicates that the enzyme does not give rise to any noticeable adsorption phenomena over the potential range utilised. The

window limiting species, which are normally Li^+ (w →,1,2-DCE forward scan) and TBA^+ (1,2-DCE→ w, reverse scan) in the absence of buffer, could not be rigidly assigned since the buffer concentration was so high.

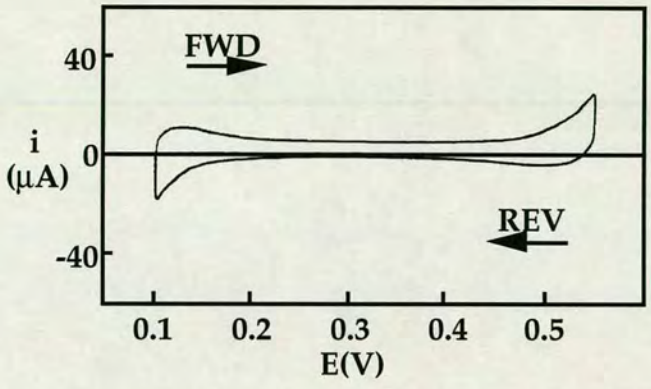

Figure 7.3 - Cyclic voltammogram showing the potential window for cell 7.1, where x = 1000 (Udm^{-3}).

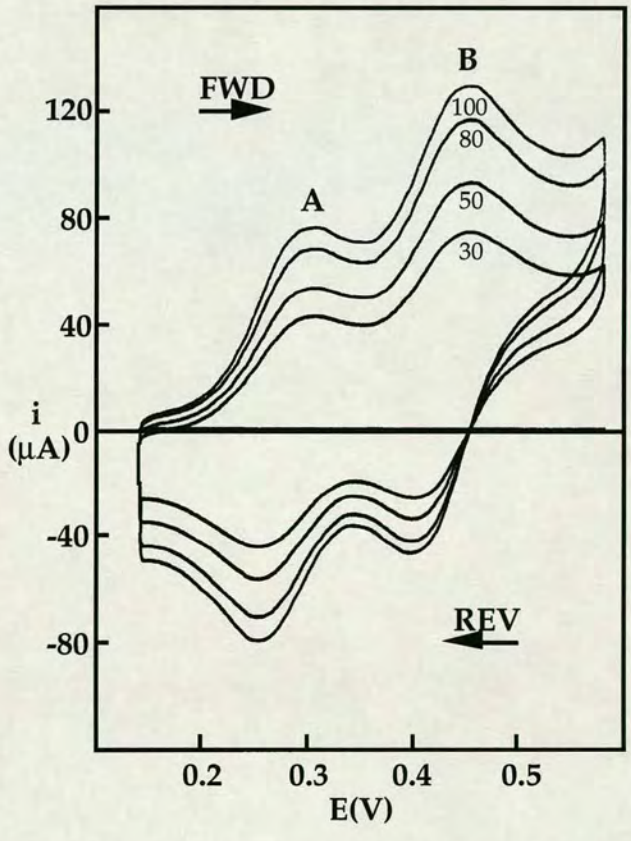

Figure 7.4 - Cyclic voltammograms for cell 7.1 with x = 0 (Udm^{-3}), and $ButCh^+$ and Ch^+ added. (A) = $ButCh^+$ (B) = Ch^+. Scan rates = 30, 50, 80, and 100 mVs^{-1}.

The effect of a small quantity of *p*-nitrophenol, present as an impurity in the paraoxon standards, was also shown to be inconsequential using x = 0 (cell 7.1). Figure 7.4 shows the responses obtained at different scan rates when a few drops of 10 mM $ButCh^+$ and Ch^+ chloride were added to the aqueous phase of cell 7.1 (x = 0). The separation of the $ButCh^+$ (A) and Ch^+ (B) waves, under full iR drop compensation, is approximately 150 mV. The transfer of both species is fully reversible, characterised by a peak-to-peak separation of approximately 60 mV, and a linear dependence of the peak current versus the square root of the scan rate.

7.2.1 Sample Addition Experiments

These experiments were carried out chiefly to investigate the feasibility of a rapid test for enzyme inhibition based on the liquid/liquid interface acting as a transducer for the enzymatic process, and which does not involve incubation with the sample under study. 100 µl of the standard of paraoxon containing $ButCh^+$ (see Preparation of Standard Solutions - chapter three, 3.6) was injected into the thermostated cell, and the decrease in the $ButCh^+$ peak height with time (1 minute intervals) was followed. The emergence of a peak due to the production of Ch^+ was also observed.

Experiments were carried out for an aqueous phase concentration of 50 µM $ButCh^+$, with 0, 20, 35, 50, 70, 100 and 120 ppb of paraoxon. A concentration of $ButCh^+$ of 50 µM was chosen because it offered a good compromise between the time scale of the experiment and the limit of detectability for the cyclic voltammetry experiments. A concentration of x = 350 (Udm^{-3}, cell 7.1) was utilised for all these experiments.

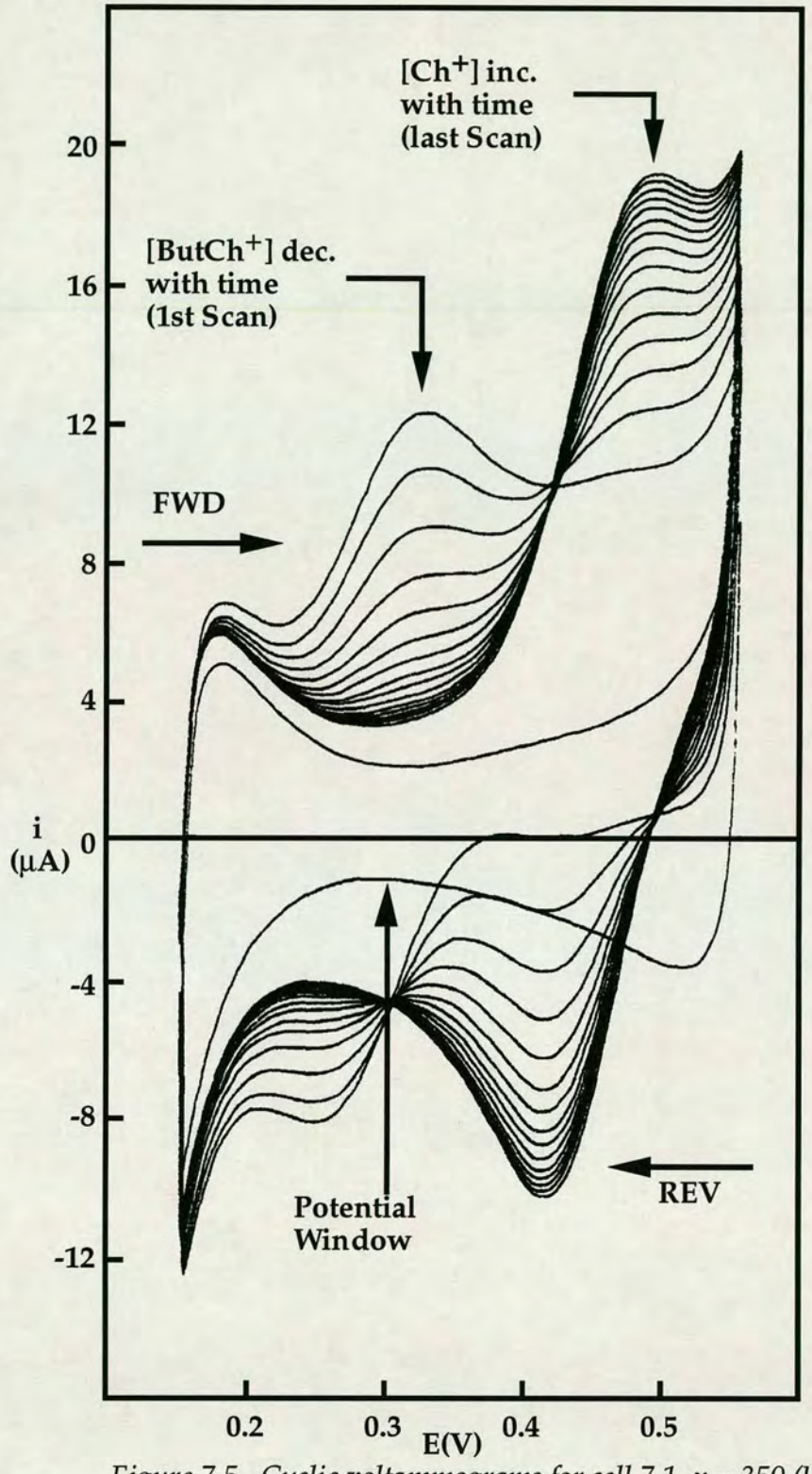

Figure 7.5 - Cyclic voltammograms for cell 7.1, x = 350 (Udm^{-3}).
Initial $ButCh^+$ concentration = 50 μM; paraoxon concentration = 0.
Time range = 1-15 mins after addition of $ButCh^+$.

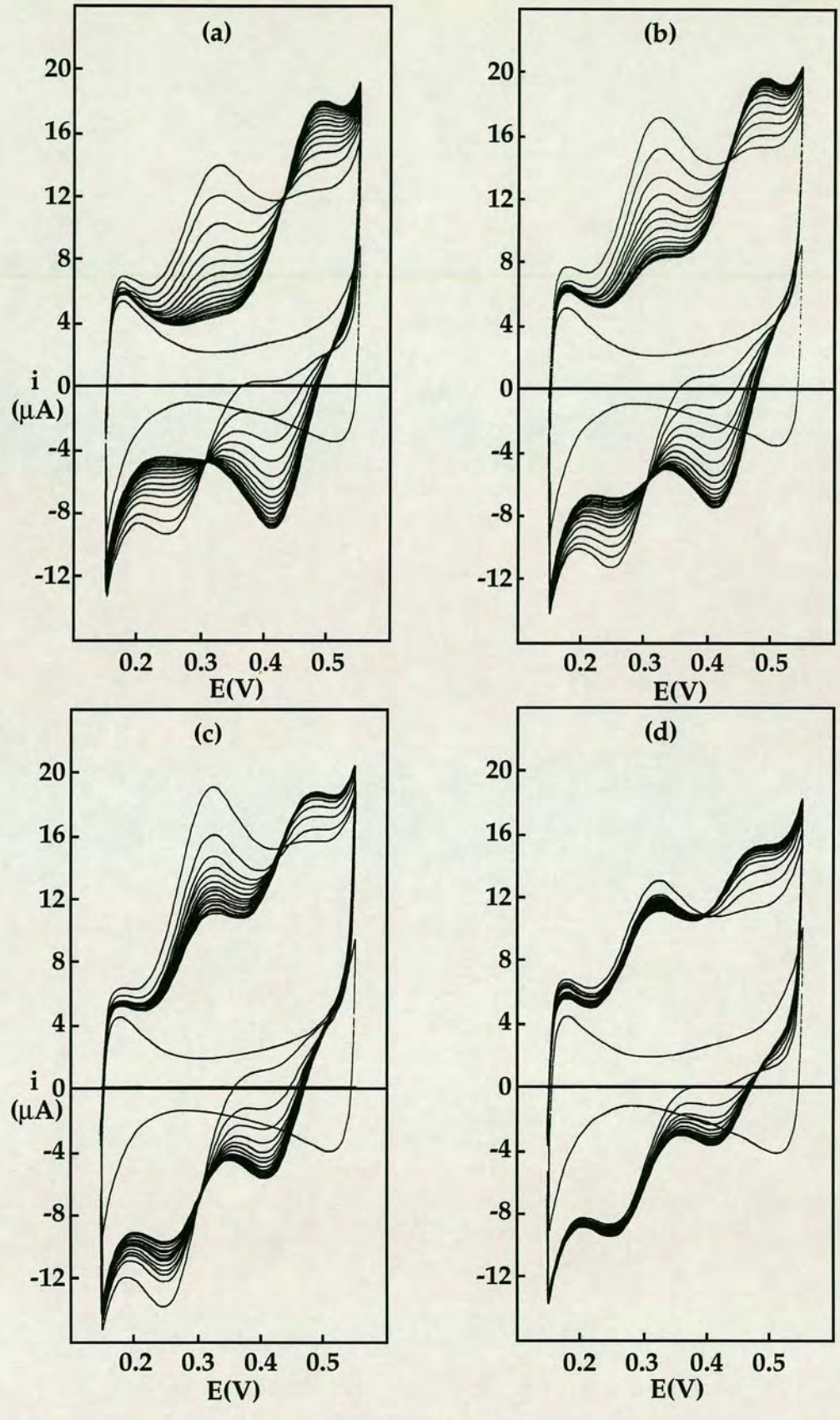

Figure 7.6 - As 7.5 but paraoxon conc. (ppb) = 20 (a), 50 (b), 70 (c), 120 (d).

Figure 7.5 shows the cyclic voltammetric responses for the enzyme reaction with the blank sample, containing only $ButCh^+$ (cell 7.1). The peak of interest here is that of (A), corresponding to $ButCh^+$, at approximately 0.32V on the forward scan. Scans were performed at one minute intervals after the addition of the substrate. On the same figure is the scan prior to addition, showing the potential window. The $ButCh^+$ peak was observed to decrease with time, and the emergence of peak (B), corresponding to Ch^+, at about 0.49 V (forward scan), produced by the enzyme reaction, was observed. In subsequent experiments with the paraoxon standards, the separation between successive scans was observed to decrease, as illustrated in figure 7.6.

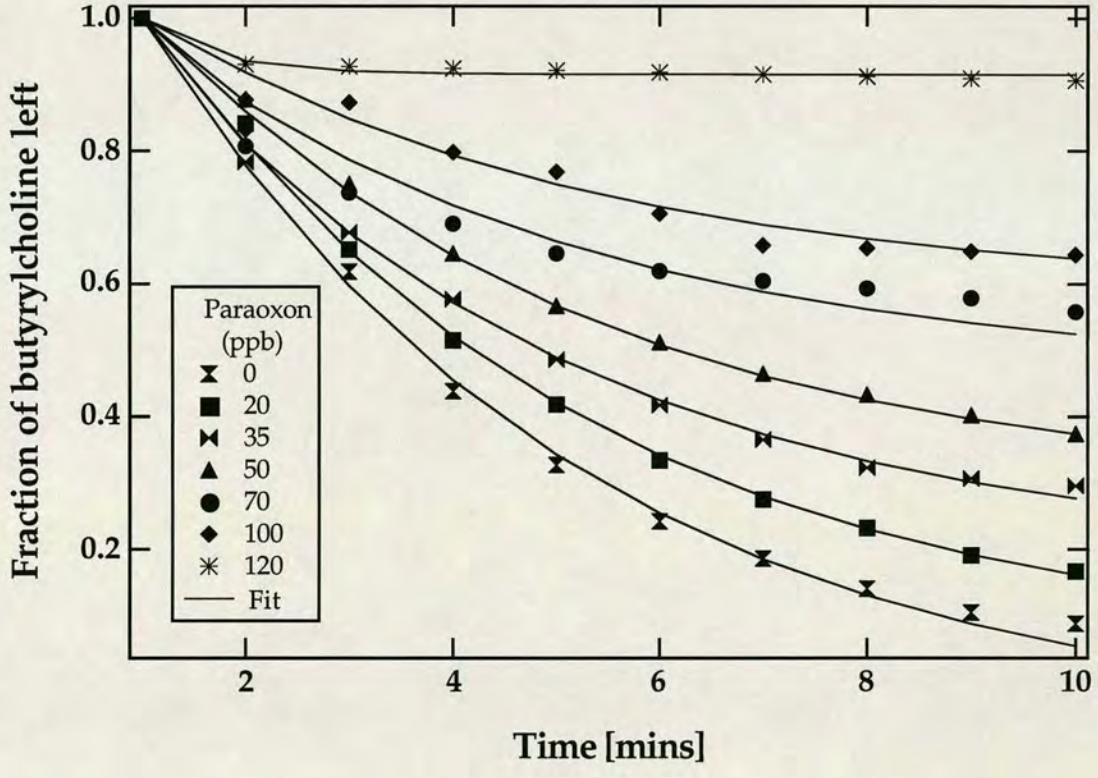

Figure 7.7 - Plots of fraction of substrate left versus time, for the sample addition experiments, with best fit lines. mins = minutes.

The results obtained for all the reactions were analysed according to the height of the $ButCh^+$ peak at one minute after the addition of the sample. The peaks corresponding to the range 1-10 minutes were measured and expressed as a fraction of the one minute peak. The reason for this approach was to mitigate against the intrinsic difficulty of reproducibility at the concentration of $ButCh^+$ being used (50 μM). The main reasons for peak height inconsistency in the different experiments were (1) the simplicity of sample injection into the aqueous phase, and (2) the fact that the aqueous phase was unstirred. Other factors such as bubble formation at the interface during the course of the experiment, due to the elevated cell temperature, may also have contributed. The results obtained are shown in figure 7.7.

The following equation (see appendix two) was used to fit the data:

$$\ln\frac{[S]}{[S_1]} = \frac{k_2K}{k_3}\ln\left\{e^{-k_3([E_0]-[P_0])(t-1)}\,\frac{([E_0]-[P_0])e^{-k_3([E_0]-[P_0])}}{[E_0]-[P_0]e^{-k_3([E_0]-[P_0])t}}\right\} \qquad (7.4)$$

where $[S_1]$ represents the substrate concentration at time (t) = 1 minute, [S] represents the substrate concentration at a given time during the experiment, and E_o and P_o are the concentrations of enzyme and paraoxon respectively at time (t) = 0, according to the reaction schemes 7.5 and 7.6. k_3 is the forward rate constant for scheme 7.6, and k_2K that of scheme 7.5, where $K = k_1/k_{-1}$ (K is assumed to be very small). Scheme 7.5 is exactly the same as that of 7.2.

$$E + S \underset{k_{-1}}{\overset{k_1}{\rightleftharpoons}} ES \xrightarrow{k_2} E + Prod \qquad (7.5)$$

$$E + P \xrightarrow{k_3} EP \text{ (enzyme consumed)} \qquad (7.6)$$

(a)

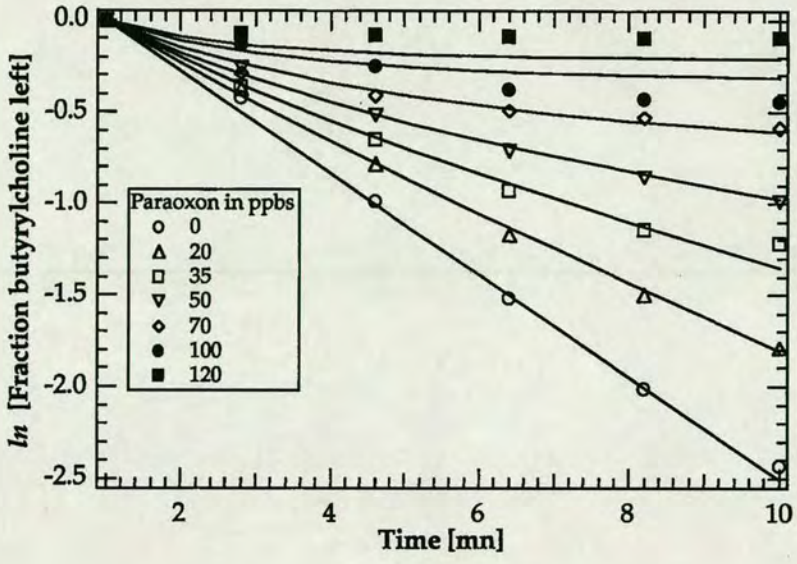

(b)

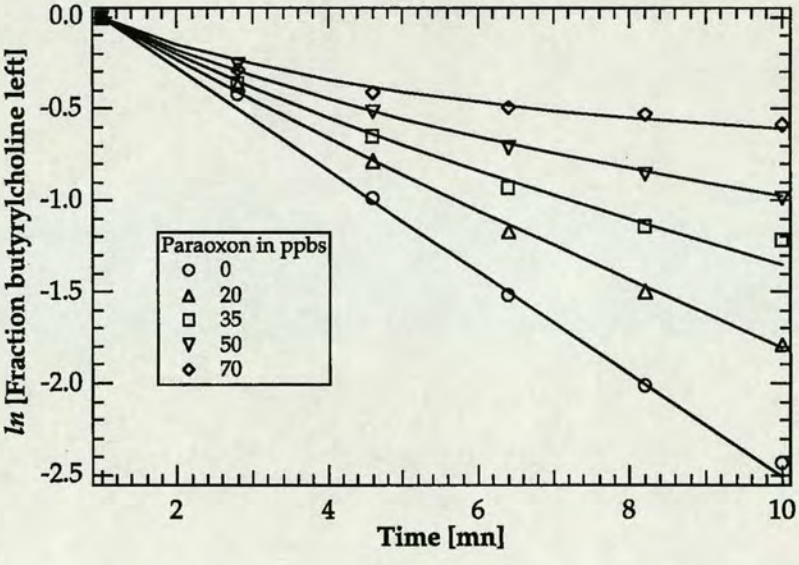

Figure 7.8 - Plots of ln(fraction of substrate left) versus time. Fits to sample addition results using equation 7.3 are shown. (a) = 7, (b) = 5 data sets. mn = minutes.

The fit to the above relation together with the experimental data is shown in figure 7.8. At higher concentrations of paraoxon the data do not fit the model as well as expected (figure 7.8 (a)). This could possibly be attributed to a change in the factors affecting the rate of hydrolysis as the activity of the

enzyme tends to zero, or could perhaps be a manifestation of the experimental conditions, given that individual experimental results are under consideration. Figure 7.8 (b) shows the results where the best five data sets are used.

In chapter three (3.2.6), it was explained that the paraoxon was dissolved in a small amount of acetone before being diluted with water to make the necessary experimental standards. The effect of acetone on the enzyme, at a concentration equivalent to that present in the 100 ppb paraoxon standard, was found to be negligible using x = 250 (Udm^{-3}, cell 7.1).

The fit to the data is very good in each case and the values obtained for the parameters are very similar on going from seven to five data sets. The three parameters each have an error of approximately 10%, and are shown in table 7.1.

Table 7.1 - Fit data obtained by using equation 7.3 in conjunction with the experimental results obtained for the sample addition experiments.

Seven data sets	Five data sets
$k_2K = (1.34 \pm 0.11) \times 10^6$ mol^{-1} min^{-1}	$k_2K = (1.51 \pm 0.13) \times 10^6$ mol^{-1} min^{-1}
$k_3 = (2.21 \pm 0.15) \times 10^6$ mol^{-1} min^{-1}	$k_3 = (2.00 \pm 0.14) \times 10^6$ mol^{-1} min^{-1}
$\boldsymbol{a} = (5.93 \pm 0.47) \times 10^{-10}$ $molU^{-1}$	$\boldsymbol{a} = (5.29 \pm 0.45) \times 10^{-10}$ $molU^{-1}$

*(where **a** is the predicted value for the initial concentration of the enzyme).*

The value obtained for ***a*** using a molecular weight for the protein of about 440,000 and a value of 500 units per mg of protein was 4.5×10^{-12} $molU^{-1}$. Therefore, there would seem to be a discrepancy, in that the value obtained

for *a* from the fit predicts either a smaller molecular weight for the protein, or a much smaller activity.

According to the supplier's specifications the activity should have been hydrolysis of 1 micromole of $ButCh^+$ by 1 unit of enzyme during one minute, at 37°C and at pH 8.0. Therefore, under ideal conditions it should have taken just over 8 seconds for the enzyme to hydrolyse the 0.1 micromoles of $ButCh^+$ in the cell. The stated value is presumably for the case where the substrate is in large excess compared with the available active sites of the enzyme. Therefore, the reaction would be expected to be limited by the efficiency of the enzyme only.

It is clear that, under the experimental conditions employed, the activity is roughly 1% of the stated value. An important point to remember, is that the cell was unstirred during the course of the experiment. Another contributing factor could have been the choice of buffer for the experiments. Tris/HCl was chosen primarily for its ability to buffer in the pH range 7.1-8.9 [182]. Other groups [166-172] have tried using phosphate, glycine, and phosphate/glycine buffers in varying concentrations, but always in the stated pH range. Goodson *et al.* [165] however, used tris buffer in their commercial system.

The high ionic strength of the aqueous phase might also have had an effect on the enzyme, especially considering that one of the active sites plays an electrostatic role. A combination of the above factors probably accounts for the low activity observed, however, an independent test of enzyme activity would be required to bear this out.

Another experiment, which was carried out at room temperature (23 ± 1°C), showed that the $ButCh^+$ was hydrolysed just as quickly as at 37°C. Thus, the effect of temperature on the rate of the hydrolysis, under the experimental conditions, is clearly minimised - possibly due to the fact that the solution was unstirred.

7.2.2 Sample Incubation Experiments

This work was conducted to assess the effect of incubation of the enzyme with the sample under study over different lengths of time. 10 ppb of paraoxon (aqueous phase concentration) was incubated with the enzyme for times of 0, 5, 10, and 15 minutes prior to addition of the $ButCh^+$. $ButCh^+$ and enzyme concentrations were the same as in section 7.2.1.

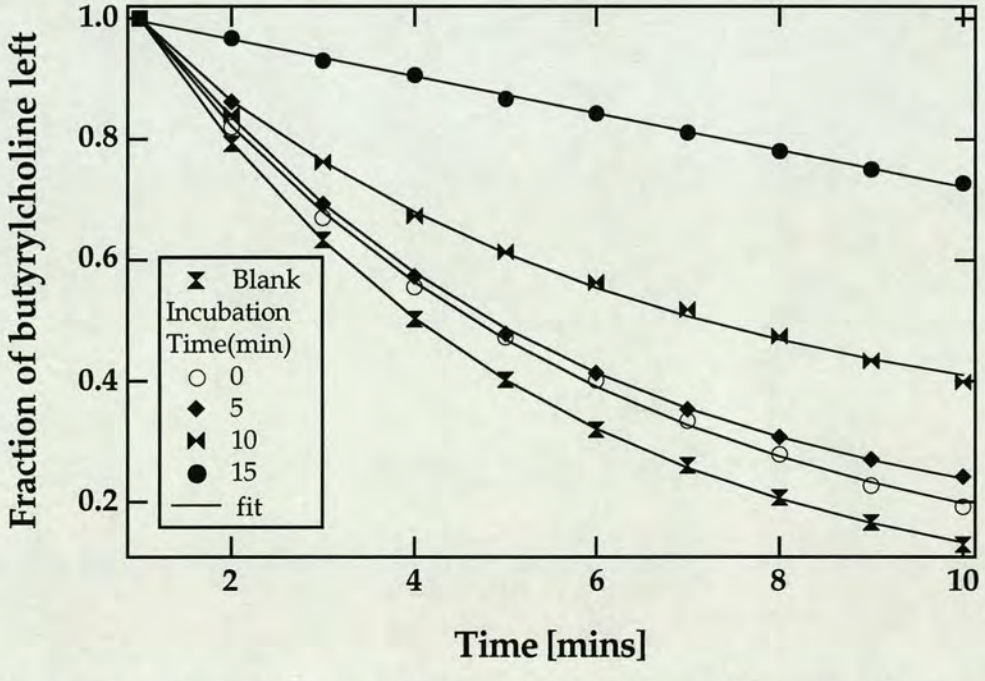

Figure 7.9 - Plots of fraction of substrate left versus time. Results for sample incubation experiments - 10 ppb of paraoxon, incubated for different times with x = 350 (Udm^{-3}, cell 7.1).

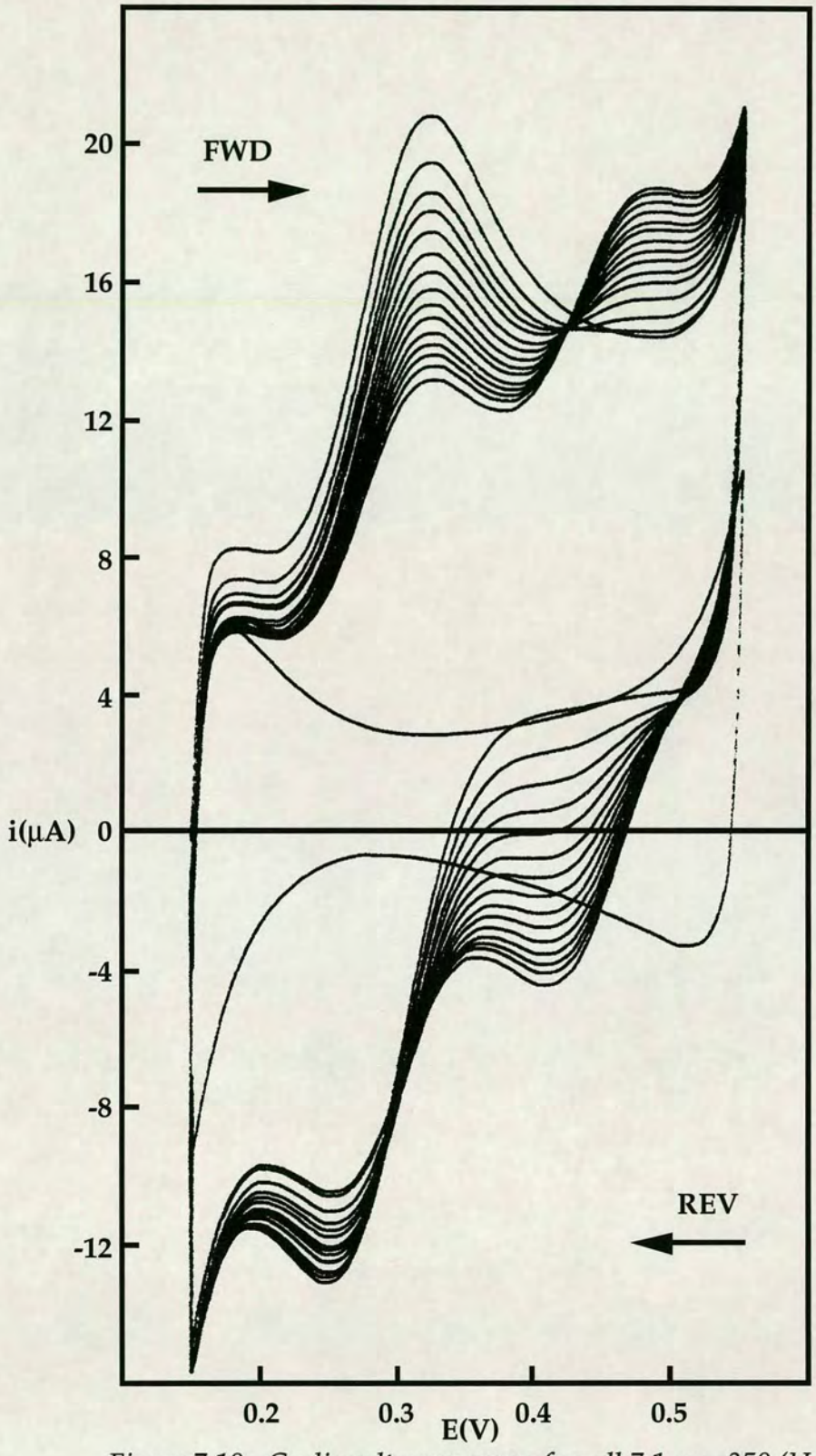

Figure 7.10 - Cyclic voltammograms for cell 7.1, x = 350 (Udm^{-3}).
10 ppb of paraoxon incubated for 15 minutes.
Time range = 1-15 minutes after addition of $ButCh^{+}$.

The results obtained for the incubation experiments show that the incubation time of the paraoxon with the enzyme has a strong effect on its hydrolysing power. Figure 7.9 shows the results obtained for incubation of a 10 ppb concentration of paraoxon for times of 0, 5, 10 and 15 minutes incubation. Also shown is the result for a blank containing only $ButCh^+$. Figure 7.10 shows the cyclic voltammograms obtained for an incubation time of 15 minutes.

The 0, 5, and 10 minute results clearly exhibit exponential behaviour whereas the 15 minute incubation period results in an almost linear response. Not shown on figure 7.9 is the result for a blank in which the cell was left for 30 minutes before adding the substrate. This gave a response similar to that of zero minutes incubation with the paraoxon, indicating that the enzyme does not denature significantly during this period. The difficulties inherent to these experiments precluded any attempt to fit the data with the model used for the sample addition experiments.

7.2.3 Substrate Concentration Variation

These experiments, and those of 7.2.4, were carried out in order to fully characterise the enzymatic reaction, under the experimental conditions stated in 7.2.1. Standards containing different concentrations of $ButCh^+$ (aqueous phase concentration of 50, 140 and 290 μM) and no paraoxon were added to the cell, which contained x = 350 (Udm^{-3}, cell 7.1).

The results obtained for experiments where the substrate cell concentration was varied between 50 and 290 mM are shown in figure 7.11. These results demonstrate the reaction to be slower for higher substrate concentrations,

but also show that, even at approximately six times the substrate concentration used in 7.2.1 and 7.2.2, the reaction can still be treated as being pseudo first-order.

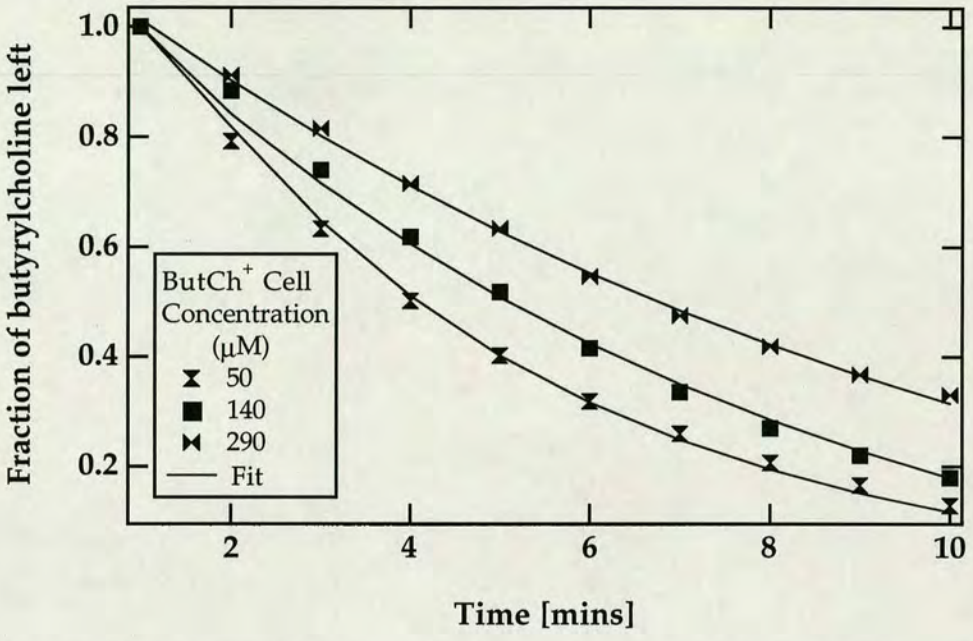

Figure 7.11 - Plots of fraction of substrate left versus time (varying substrate concentration). x = 350 (Udm^{-3}, cell 7.1).

7.2.4 Enzyme Concentration Variation

Enzyme solutions containing 50, 150, 250 and 350 U dm^{-3} were prepared and the relative rates of hydrolysis of $ButCh^+$ observed. The concentration of $ButCh^+$ was the same as in 7.2.1, and the sample contained no paraoxon.

The results shown in figure 7.12 illustrate the effect of varying the enzyme concentration. For a concentration of x = 50 (Udm^{-3}, cell 7.1) the reaction appears to be almost linear, whereas for x = 100, 200 and 350, it is clearly pseudo first-order in [S]. Figure 7.13 shows the cyclic voltammetric responses for x = (a) 50 and (b) 200.

Sections 7.2.3 and 7.2.4 corroborated the idea that under the experimental conditions employed in sections 7.2.1 and 7.2.2 diffusion of the $ButCh^+$ to the active sites of the enzyme, and not enzyme reaction, played the important rate-determining role.

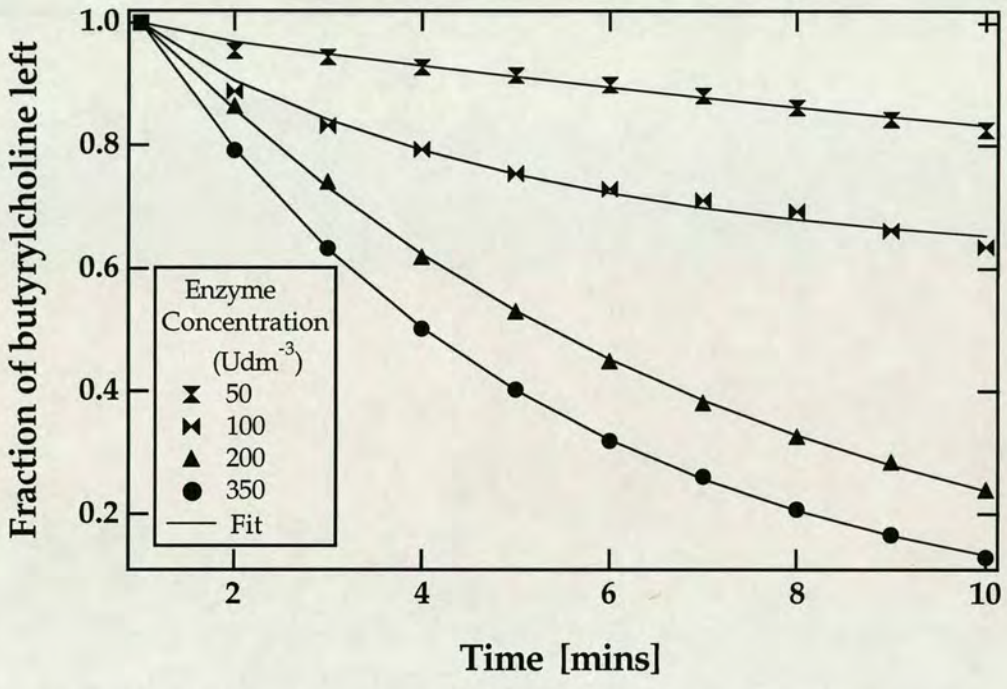

Figure 7.12 - Plots of fraction of substrate left versus time (varying enzyme concentration). $ButCh^+$ concentration = 50 μM (cell 7.1).

7.3 Conclusions

It has been successfully demonstrated that ion transfer across the ITIES can act as an effective transducer upon which sensor design may be based, as realised by Senda and co-workers [60].

The hydrolysis of $ButCh^+$ by the enzyme BChE has been demonstrated for various substrate and enzyme concentrations. The inhibition of the enzyme BChE by paraoxon, without pre-incubation, could be satisfactorily analysed in a quantitative way. The working range of detection was 20-120 ppb of

paraoxon using cyclic voltammetry, although if differential pulse voltammetry were the method used, this range could possibly be improved. The incubation time of the paraoxon with the enzyme was also shown to be a powerful factor in the ability of BChE to function effectively, using a concentration of only 10 ppb of paraoxon. The effect of the 1,2-DCE phase on the stability of the enzyme was also shown to be negligible over the time ranges considered.

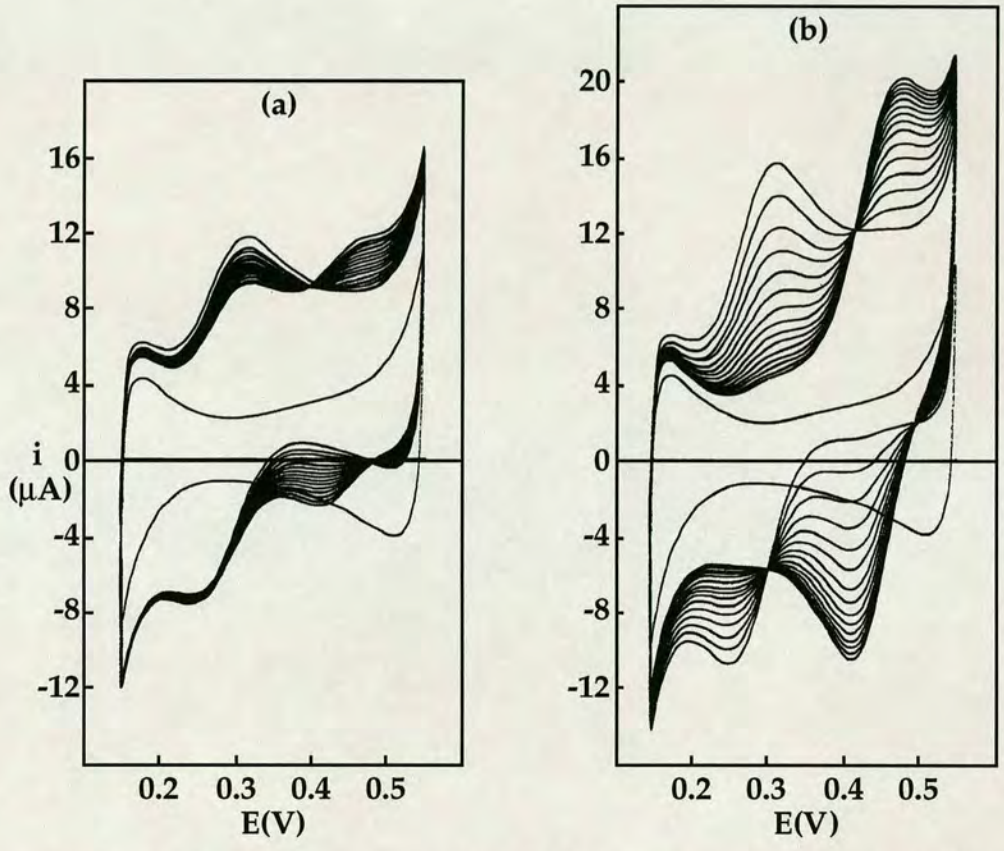

Figure 7.13 - Cyclic voltammograms for cell 7.1. Enzyme concentrations of (a) 50 and (b) 200 Udm^{-3}, ButCh^{+} concentration = 50 μM.

The results obtained compared very favourably with other approaches [165-172] where the best limits of detection tended to be in the low ppb range with the exception of [172] in which a sub-ppb limit was claimed.

Chapter Eight

CONCLUSIONS AND FUTURE WORK

The experimental work presented in chapters four and five, using a.c. impedance and steady-state voltammetry of the micro-ITIES, has conclusively demonstrated that simple ion transfer reactions, and assisted ion transfer processes of the TIC/TID type, are controlled by diffusion of the participating species to the interface. This ends over 15 years of speculation that kinetic parameters for simple ion transfer reactions are accessible by electrochemical means. Only thermodynamic information, such as diffusion coefficients and formal potentials, may be obtained. Further work in this field should be concerned with the evaluation of more complex systems, to establish whether it is possible to obtain kinetic data of any kind concerning charge transfer across an ITIES.

Ion transfer may be considered to be a transport phenomenon as opposed to an electrochemical reaction. The results presented in this thesis indicate that the energy required to transport an ion across the ITIES is of the same order of magnitude, or lower, than the Gibbs free energy of diffusion for an ion in solution.

In chapter six, interfacial electron transfer between the hexacyanoferrate redox couple in the aqueous phase and ferrocene (Fec) and 1,1'-dimethylferrocene (DmFec) respectively, in the organic phase, was found to be complicated by the effects of adsorption of the products of the reactions. In spite of this, it was shown that DmFec is more easily oxidised than Fec -

this was confirmed by independent measurement of the half-wave potentials for oxidation on a solid platinum microdisc electrode.

Similarly, electron transfer between copper (II) ions in the aqueous phase and ferrocene in the organic phase was observed to occur, and the reduction of Cu^{2+} to Cu^{+} was illustrated to be more difficult than the corresponding reduction of $[Fe(CN)_6]^{3-}$ to $[Fe(CN)_6]^{4-}$, in step with the values quoted in the literature.

As indicated in the conclusions to chapter six, the Fec/$[Fe(CN)_6]^{3-/4-}$ system has been shown, by workers at E.P.F.L., to exhibit characteristics of a fully reversible, single charge transfer reaction under the conditions of molar acid in the aqueous phase. Future work in this field should concentrate on the use of the micro-ITIES as a tool to establish whether kinetic parameters for electron transfer reactions may be obtained, or if they too are controlled by diffusion of the relevant species to the interface.

The essence of the work presented in chapter six is that heterogeneous electron transfer reactions at the ITIES do indeed occur and that they relate to the general scheme of standard reduction potentials observed at the metal electrode/electrolyte solution interface.

Chapter seven has illustrated the potential of the ITIES as a transducer to follow enzyme reactions, and also the inhibition of such processes. The rate of hydrolysis of butyrylcholine ($ButCh^{+}$) by the enzyme butyrylcholin-esterase (BChE) was followed by the decrease in the peak current for $ButCh^{+}$ transfer across the ITIES. The rate of this decrease was observed to slow in the presence of the organophosphate compound paraoxon, corresponding to

irreversible inhibition of BChE. The rate constants for the hydrolysis of the substrate and the inhibition of the enzyme could also be obtained. Future work should focus on the incorporation of the enzyme into some form of sensor matrix.

Investigation of the interface between two immiscible electrolyte solutions is still a very fruitful area of research. Work into the solidification of the ITIES, and its incorporation into practical sensor schemes utilising microtechnology, is currently under way at the Laboratoire d'Electrochimie, E.P.F.L. This surely represents one of the most promising ways forward for future applications of the ITIES.

References

[1] W.Nernst and E.H.Riesenfield, Ann.Phys., 8(1902)600

[2] M.Cremer, Z.Biol., 47(1906)562

[3] E.L.W.Verwey and K.F.Niessen, Philos., 28(1939)435

[4] M.Kahlweit and H.Strehlow, Z.Elektrochem., 58(1954)658

[5] C.Gavach, T.Mlodnicka and J.Gustalla, C.R.Acad.Sci., C266(1968)1196

[6] C.Gavach and F.Henry, J.Electroanal.Chem., 54(1974)361

[7] C.Gavach, B.D'Epenoux and F.Henry, J.Electroanal.Chem., 64(1975)107

[8] B.D'Epenoux, P.Seta, G.Amblard and C.Gavach, J.Electroanal.Chem., 99(1979)77

[9] Z.Samec, V.Marecek, J.Koryta and M.W.Khalil, J.Electroanal.Chem., 83(1977)393

[10] Z.Samec, V.Marecek and J.Weber, J.Electroanal.Chem., 100(1979)841

[11] T.Kakutani, T.Osakai and M.Senda, Bull.Chem.Soc.Jpn., 56(1983)991

[12] Z.Samec, V.Marecek, J.Weber and D.Homolka, J.Electroanal.Chem., 99(1979)385

[13] D.Homolka and V.Marecek, J.Electroanal.Chem., 112(1980)91

[14] V.Marecek and Z.Samec, Anal.Chim.Acta., 151(1983)265

[15] B.Hundhammer, T.Solomon and H.Alemu, J.Electroanal.Chem., 149(1983)179

[16] Z.Samec, V.Marecek and D.Homolka, J.Electroanal.Chem., 126(1981)121

[17] G.Taylor and H.H.Girault, J.Electroanal.Chem., 208(1986)179

[18] J.A.Campbell and H.H.Girault, J.Electroanal.Chem., 266(1989)465

[19] D.A.Higgins and R.M.Corn, J.Phys.Chem., 97(1993)489

[20] A.A.Tamburello Luca, P.Hebert, P.F.Brevet and H.H.Girault, Farad.Trans., (submitted for publication)

[21] R.A.Marcus, J.Phys.Chem., 94(1990)1050

[22] I.Benjamin, J.Chem.Phys., 96(1992)577

[23] I.Benjamin, J.Phys.Chem., 95(1991)6675

[24] J.Koryta, Electrochim.Acta., 24(1979)293

[25] Z.Samec, V.Marecek and J.Weber, J.Electroanal.Chem., 96(1979)245

[26] Z.Samec, A.R.Brown, L.J.Yellowlees and H.H.Girault, J.Electroanal. Chem., 288(1990)245

[27] P.Vanysek, 'Electrochemistry on liquid/liquid interfaces', Lecture notes in Chemistry, Vol. 39, Spinger-Verlag, Berlin, 1985

[28] V.S.Markin and A.G.Volkov, Electrochim.Acta., 34(1989)93

[29] Z.Samec, V.Marecek, J.Weber, and D.Homolka, J.Electroanal.Chem., 126(1981)105

[30] Z.Samec, V.Marecek and D.Homolka, J.Electroanal.Chem., 158(1983)25

[31] Z.Samec and V.Marecek, J.Electroanal.Chem., 200(1986)17

[32] T.Wandlowski, V.Marecek and Z.Samec, J.Electroanal.Chem., 242(1988)291

[33] T.Wandlowski, V.Marecek, K.Holub and Z.Samec, J.Phys.Chem., 93(1989)8204

[34] T.Wandlowski, V.Marecek and Z.Samec, J.Electroanal.Chem., 331(1992)765

[35] T.Osakai, T.Kakutani and M.Senda, Bull.Chem.Soc.Jpn., 57(1984)370

[36] T.Kakiuchi, J.Noguchi, M.Kotani and M.Senda, J.Electroanal.Chem., 296(1990)517

[37] T.Kakiuchi, J.Noguchi and M.Senda, J.Electroanal.Chem., 327(1992)63

[38] Y.Shao and H.H.Girault, J.Electroanal.Chem., 282(1990)59

[39] Y.Shao, J.A.Campbell and H.H.Girault, J.Electroanal.Chem., 300(1991)415

[40] Y.Liu and E.Wang, J.Electroanal.Chem., 277(1990)291

[41] T.Osakai, H.Katano, K.Maeda, S.Himeno and A.Saito, Bull.Chem.Soc. Jpn., 66(1993)1111

[42] S.Kihara, M.Suzuki, M.Sugiyama and M.Matsui, J.Electroanal.Chem., 249(1988)109

[43] D.Homolka, L.Q.Hung, A.Hofmanova, M.W.Khalil, J.Koryta, V.Marecek, Z.Samec, S.K.Sen, P.Vanysek, J.Weber, M.Brezina, M.Janda and I.Stibor, Anal.Chem., 52(1980)1606

[44] D.Homolka, V.Marecek, Z.Samec, O.Ryba and J.Petranek, J.Electroanal. Chem., 125(1981)243

[45] P.Vanysek, W.Ruth and J.Koryta, J.Electroanal.Chem., 148(1983)117

[46] J.Koryta, Y.N.Kozlov and M.Skalicky, J.Electroanal.Chem., 234(1987)355

[47] G.Du, J.Koryta, W.Ruth and P.Vanysek, J.Electroanal.Chem., 159(1983)413

[48] A.Sabela, J.Koryta and O.Valent, J.Electroanal.Chem., 204(1986)267

[49] A.Hofmanova, L.Q.Hung and W.Khalil, J.Electroanal.Chem., 135(1982)264

[50] E.Makrlik, L.Q.Hung and A.Hofmanova, Electrochim.Acta., 28(1983)847

[51] Z.Samec and P.Papoff, Anal.Chem., 62(1990)1010

[52] T.Kakutani, Y.Nishiwaki, T.Osakai and M.Senda, Bull.Chem.Soc.Jpn., 59(1986)781

[53] L.Sinru, Z.Zaofan and H.Freiser, J.Electroanal.Chem., 210(1986)137

[54] Z.Sun and E.Wang, Electroanalysis., 1(1989)441

[55] E.Wang, Z.Yu, D.Qi and C.Xu, Electroanalysis., 5(1993)149

[56] Y.Shao, M.D.Osborne and H.H.Girault, J.Electroanal.Chem., 318(1991)101

[57] H.Matsuda, Y.Yamada, K.Kanamori, Y.Kudo and Y.Takeda, Bull.Chem. Soc.Jpn., 64(1991)1497

[58] M.D.Osborne and H.H.Girault, Electroanalysis (in press)

[59]T.Osakai, T.Kakutani and M.Senda, Anal.Sci., 3(1987)521

[60] T.Osakai, T.Kakutani and M.Senda, Anal.Sci., 4(1988)529

[61] E.Makrlik, W.Ruth and P.Vanysek, Electrochim.Acta., 28(1983)575

[62] N.Ogawa and H.Freiser, Anal.Chem., 65(1993)517

[63] E.Wang and Y.Liu, J.Electroanal.Chem., 214(1986)459

[64] E.Wang, Z.Yu and N.Li, Electroanalysis., 4(1992)905

[65] H.Alemu, B.Hundhammer and T.Solomon, J.Electroanal.Chem., 294(1990)165

[66] A.M.Baruzzi and H.Wendt, J.Electroanal.Chem., 279(1990)19

[67] Y.Cheng, D.J.Schiffrin, P.Guerriero and P.A.Vigato, Inorg.Chem., 33(1994)765

[68] S.Matsuno, A.Ohki, M.Tagaki and K.Ueno, Chem.Lett., (1981)1543

[69] M.Guainazzi, G.Silvestri and G.Serraville, J.C.S.Chem.Comm., (1975)200

[70] Z.Samec, V.Marecek and J.Weber, J.Electroanal.Chem., 103(1979)11

[71] A.A.Stewart, J.A.Campbell, H.H.Girault and M.Eddowes, Ber.Bunsenges.Phys.Chem., 94(1990)83

[72] J.Hanzlik, Z.Samec and J.Hovorka, J.Electroanal.Chem., 216(1987)303

[73] J.Hanzlik, J.Hovorka, Z.Samec and S.Toma, Coll.Czech.Chem.Comm., 53(1988)903

[74] G.Geblewicz and D.J.Schiffrin, J.Electroanal.Chem., 244(1988)27

[75] V.J.Cunnane, D.J.Schiffrin, C.Beltran, G.Geblewicz and T.Solomon, J.Electroanal.Chem., 247(1988)203

[76] Y.Cheng and D.J.Schiffrin, J.Electroanal.Chem., 314(1991)153

[77] Y.Cheng and D.J.Schiffrin, J.Chem.Soc.Farad.Trans., 89(1993)199

[78] Q-Z.Chen, K.Iwamoto and M.Seno, Electrochim.Acta, 36(1991)291

[79] S.Kihara, M.Suzuki, K.Maeda, K.Ogura, M.Matsui and Z.Yoshida, J.Electroanal.Chem., 271(1989)107

[80] K.Maeda, S.Kihara, M.Suzuki and M.Matsui J.Electroanal.Chem., 303(1991)171

[81] H.H.Girault, "Charge transfer across liquid/liquid interfaces", in Mod.Asp.Electrochem., 25(1993)1, J.O'M.Bockris, B.Conway, R.White (Eds.), Plenum Press, N.Y.

[82] F.L.Thomson, L.J.Yellowlees and H.H.Girault, J.Chem.Soc.Chem. Commun., (1988)1547

[83] A.R.Brown, L.J.Yellowlees and H.H.Girault, J.Chem.Soc.Farad.Trans., 89(1993)207

[84] V.Marecek, A.H.De Armond and M.K.De Armond, J.Am.Chem.Soc., 111(1989)2561

[85] V.Marecek, A.H.De Armond and M.K.De Armond, J.Electroanal.Chem., 261(1989)287

[86] N.A.Kotov and M.G.Kuzmin, J.Electroanal.Chem., 285(1990)223

[87] Z.Samec, A.R.Brown, L.J.Yellowlees, H.H.Girault, and K.Base, J.Electroanal.Chem., 259(1989)309

[88] J.Guastalla, Proc.2nd Int.Congr.Surf.Act., 3(1957)112

[89] M.Blank, J.Colloid Interf. Sci. 22(1966)51

[90] M.Dupeyrat and E.Nakache, J.Colloid Interf. Sci. 73(1980)332

[91] T.Kakiuchi, T.Usui and M.Senda., Bull.Chem.Soc.Jpn, 63(1990)3264

[92] Z.Yoshida and S.Kihara, J.Electroanal.Chem., 227(1987)171

[93] M.D.Osborne and H.H.Girault, J.Electroanal.Chem., 370(1994)287

[94] H.H.Girault and D.J.Schiffrin., J.Electroanal.Chem, 179(1984)277

[95] H.H.Girault and D.J.Schiffrin in M.J.Allen and P.N.R.Usherwood (Eds), Charge and Field Effects in Biosystems, Abacus Press, England,1984,p.171

[96] T.Kakiuchi, T.Kondo, M.Kotani and M.Senda, Langmuir, 8(1992)169

[97] Y.Cheng, V.J.Cunnane, D.J.Schiffrin, L.Mutomaki and K.Kontturi, J.Chem.Soc.Farad.Trans., 87(1991)107

[98] T.Osakai, T.Kakutani, and M.Senda, Bunseki Kagaku, 33(1984)E371

[99] V.Marecek, H.Janchenova, M.P.Colombini and P.Papoff, J.Electroanal. Chem, 217(1987)213

[100] E.Wang and H.Ji, Electroanalysis, 1(1989)75

[101] B.Hundhammer, S.K.Dhawan, A.Bekele and H.J.Seidlitz, J.Electroanal. Chem, 217(1987)253

[102] P.N.Swan, Ph.D. Thesis, University of Southampton, 1980.

[103] K.B.Oldham, C.G.Zoski, A.M.Bond and D.A.Sweigart, J.Electroanal. Chem., 248(1988)467.

[104] A.J.Bard, G.Denuault, C.Lee, D.Mandler and D.O.Wipf, Acc.Chem.Res., 23(1990)357.

[105] R.M.Wightman, R.T.Kennedy, D.J.Wiedemann, K.T.Kawagoe, J.B.Zimmerman, and D.J.Leszczysyn, "Microelectrodes in Biological Systems", in ref. [107], p.453.

[106] R.M.Wightman and D.O.Wipf, 'Voltammetry at Ultramicroelectrodes', in Electroanal.Chem., 15(1989)267, A.J.Bard (Ed.), Marcel Dekker Inc., N.Y.

[107] M.I.Montenegro, M.Arlete Queiros and J.L.Daschbach (Eds.), "Microelectrodes: Theory and Applications", NATO ASI Series E: Vol. 197 (1991) Kluwer Academic Publishers, Dordrecht, Boston and London.

[108] B.R.Scharifker, "Microelectrode Techniques in Electrochemistry", in Mod.Asp.Electrochem., 22(1992)467, J.O'M.Bockris, B.Conway, R.White (Eds.), Plenum Press, N.Y.

[109] C.Amatore, M.R.Deakin and R.M.Wightman, J.Electroanal.Chem., 220(1987)49.

[110] A.A.Stewart, Y.Shao, C.M.Pereira and H.H.Girault, J.Electroanal. Chem., 305(1991)135.

[111] Y.Shao and H.H.Girault, J.Electroanal.Chem., 334(1992)203.

[112] T.Ohkouchi, T.Kakutani, T.Osakai and M.Senda, Anal.Sci., 7(1991)371.

[113] M.D.Osborne, Y.Shao, C.M.Pereira and H.H.Girault, J.Electroanal. Chem., 364(1994)155.

[114] M.D.Osborne, Ph.D. Thesis, Edinburgh University, 1993.

[115] M.D.Osborne and H.H.Girault, Mikrochim.Acta (in press)

[116] H.H.Girault and D.J.Schiffrin, "Electrochemistry of liquid/liquid interfaces", in Electroanal.Chem., 15(1989)1, A.J.Bard (Ed.), Marcel Dekker Inc., N.Y.

[117] M.Senda, T.Kakiuchi and T.Osakai, Electrochim.Acta, 36(1991)253

[118] E.Grunwald, G.Baughman and G.Kohnstam, J.Am.Chem.Soc., 82(1960)5801

[119] Y.Shao, A.A.Stewart and H.H.Girault, J.Chem.Soc.Farad.Trans., 87(1991)2593

[120] M.C.Couldwell, Cryst.Struct.Commun., 8(1979)469

[121] K.Hoffman and C.Weiss, J.Organomet .Chem., 67(1974)3221

[122] H.H.Girault and D.J.Schiffrin, Electrochim.Acta, 31(1986)1341

[123] C.Gavach, P.Seta, and B.D'Epenoux, J.Electroanal.Chem., 83(1977)225

[124] H.H.Girault and D.J.Schiffrin, J.Electroanal.Chem., 170(1984)127

[125] R.P.Buck, Crit.Rev.Anal.Chem., 5(1975)323

[126] H.H.Girault and D.J.Schiffrin, J.Electroanal.Chem., 195(1985)213

[127] A.E.Stearn and H.Eyring, J.Phys.Chem., 44(1940)955

[128] J.T.Davies, J.Phys.Chem., 54(1950)185

[129] J.A.Campbell, A.A.Stewart and H.H.Girault, J.Chem.Soc.Farad.Trans.1, 85(1989)843

[130] A.Sabela, V.Marecek, J.Koryta and Z.Samec, Coll.Czech.Chem.Comm., 59(1994)1287

[131] Y.Y.Gurevich and Y.I.Kharkats, J.Electroanal.Chem., 200(1986)3

[132] T.Kakiuchi, J.Electroanal.Chem., 322(1992)55

[133] D.E.Goldman, J.Gen.Physiol., 27(1943)37

[134] T.Kakiuchi, J.Noguchi and M.Senda, J.Electroanal.Chem., 336(1992)137

[135] M.Senda, Anal.Sci., 10(1994)649

[136] H.H.Girault and D.J.Schiffrin, J.Electroanal.Chem., 244(1988)15

[137] Y.I.Kharkats and J.Ulstrup, J.Electroanal.Chem., 308(1991)17

[138] R.Greef *et al.* , 'Instrumental Methods in Electrochemistry',* (below)

[139] A.J.Bard and L.R.Faulkner, 'Electrochemical Methods: Fundamentals and Applications', (1980), J.Wiley and Sons, Inc., N.Y.

[140] D.Homolka, K.Holub and V.Marecek, J.Electroanal.Chem., 138(1982)29

[141] Y.Saito, Rev.Polarogr.Jpn., 15(1968)177

[142] A.M.Bond K.B.Oldham and C.G.Zoski, J.Electroanal.Chem., 245(1988)71

[143] K.B.Oldham, J.C.Myland, C.G.Zoski and A.M.Bond, J.Electroanal. Chem., 270(1989)79

[144] C.Gabrielli, 'Identification of Electrochemical Responses by Frequency Response Analysis', (1980), - technical report no. 004/83, Solartron Instruments.

[145] J.E.B.Randles, Trans.Farad.Soc., 44(1948)327

[146] P.G.Bruce, A.Lisowska-Oleksiak, P.Los and C.A.Vincent, J.Electroanal. Chem., 367(1994)279

[147] M.Fleischmann and S.Pons, J.Electroanal.Chem., 250(1988)277

[148] L.M.Abrantes, M.Fleischmann, L.M.Peter, S.Pons and B.J.Scharifker, J.Electroanal.Chem., 256(1988)229

[149] K.T.Brown and D.G.Flaming, in 'Advanced Micropipette Techniques for Cell Physiology', (1992)23, J.Wiley and Sons, Inc., N.Y.

[150] D.W.Thomas, C.Foulkes-Williams, P.T.Rumsby and M.C.Gower, in 'Laser Ablation of Electronic Materials', (1992), E.Fogarassy and S.Lazare (Eds.), Elsevier, Lausanne.

* (1985), Southampton Electrochemistry Group, Halsted Press.

[151] M.C.Gower, in 'Laser Processing in Manufacturing', (1993)189, R.C.Crafer and P.J.Oakley (Eds.), Chapman and Hall, London.

[152] Melinex Product Information - Technical Data Sheet MX TD 120, (1990), Imperial Chemical Industries (UK).

[153] R.C.Weast (Ed.), 'CRC Handbook of Chemistry and Physics - 66th Edition', (1985), CRC Press, Inc., Florida.

[154] J.R.Macdonald, 'Impedance Spectroscopy', (1987)39, J.Wiley and Sons, Inc., N.Y.

[155] C.J.Pedersen, Angew.Chem.Int.Ed.Engl., 27(1988)1021

[156] C.J.Pedersen, J.Am.Chem.Soc., 89(1967)2495,7017

[157] D.Shoup and A.Szabo, J.Electroanal.Chem., 160(1984)27

[158] J.A.Campbell, Ph.D Thesis, Edinburgh University, 1991

[159] A.Sabela, V.Marecek, Z.Samec and R.Fuoco, Electrochim.Acta., 37(1992)231

[160] R.D.Purves, in 'Microelectrode Methods for Intracellular Recording and Ionophoresis', (1981)30, Academic Press, London.

[161] A.Brown, Ph.D Thesis, Edinburgh University, 1992

[162] K.A.Hassall, in 'The Biochemistry and Uses of Pesticides: Structure, Metabolism, Mode of Action and Uses in Crop Protection - Second Edition', (1990), Chapter 4, Macmillan, Basingstoke.

[163] F.Matsumura, in 'Toxicology of Insecticides', (1975), Chapters 3 and 4, Plenum Press, New York.

[164] J.N.Seiber, Q.X.Li, and J.M.Van Emon, in 'Immunochemical Methods for Environmental Analysis', (1990), Chapter 13, American Chemical Society.

[165] L.H.Goodson, W.B.Jacobs and B.R.Cage, Proc.Natl.Conf.Ctrl.Haz.Mat., Apr 11-13, (1978), Food and Drug Administration.

[166] P.Durand, J.Mallevialle and J.M.Nicaud, J.Anal.Toxicol., 8(1984)112

[167] S.Kumaran and C.Tranh-Minh, Electroanalysis, 4(1992)949

[168] V.J.Razumas, J.J.Kulys and A.A.Malinauskas, Env.Sci.Technol., 15(1981)360

[169] L.Campanella, M.Achilli, M.P.Sammartino and M.Tomassetti, Bioelectrochem.Bioenerg., 26(1991)237

[170] M.Bernabei, C.Cremisini, M.Mascini and G.Palleschi, Anal.Lett., 24(1991)1317

[171] J.Kulys and E.J.D'Costa, Biosens.Bioelectron., 6(1991)109

[172] P.Skladal, Anal.Chim.Acta, 269(1992)281

[173] P.Vanysek and M.Behrendt, J.Electroanal.Chem., 130(1981)287

[174] U.Schoknecht and D.Otto, in 'Chemistry of Plant Protection 2', (1989)117, Springer-Verlag, Berlin.

[175] H.Soreq, A.Gnatt, Y.Lowenstein and L.F.Neville, TIBS, Sept.(1992)353

[176] A.Chatonnet and O.Lockridge, Biochem.J., 260(1989)625

[177] H.W.Chambers, in 'Organophosphates: Chemistry, Fate and Effects', (1992), Chapter 1, Academic Press, Inc., San Diego.

[178] K.D.Racke, in 'Organophosphates: Chemistry, Fate and Effects', (1992), Chapter 3, Academic Press, Inc., San Diego.

[179] L.Michaelis and M.Menten, Biochem.Z., 49(1913)333

[180] G.B.Koelle, Fund.Appl.Toxicol., 1(1981)129

[181] A.L.Lehninger, 'Biochemistry - Second Edition' (1981), Chapter 8, Worth Publishers, Inc., N.Y.

[182] R.M.C.Dawson, D.C.Elliott, W.H.Elliott and K.M.Jones (Eds.), 'Data for Biochemical Research', (1969)475, Oxford University Press.

[183] T.Wandlowski, V.Marecek and Z.Samec, Electrochim.Acta, 35(1990)1173

[184] F.Dubois and R.G.Wellington, (unpublished).

Courses and Conferences Attended

R.S.C. Analytical Division (Electroanalytical Group) - "Spring" Informal Meeting, Southampton University, 16-18th September, 1991.

R.S.C. Analytical Division (Electroanalytical Group) - "Analytical Applications of Chemically Modified Electrodes", Bristol University, 7-8th February, 1992.

R.S.C. Analytical Division - "Symposium on Fungicides, Herbicides and Insecticides", London, 27th March, 1992.

EIRELEC, Limerick, Ireland, 11-15th September, 1993.

184th Meeting of The Electrochemical Society, New Orleans, U.S.A., 10-15th October, 1993.

Departmental Colloquia (1991-'92, Edinburgh University).

Departmental Colloquia (1992-'94, E.P.F.L.).

Physical Chemistry Thursday Evening Seminars (1991-'92).

Appendix One

The study of assisted ion transfer reactions has generally been concerned with one of the limiting cases, in which the concentration of either the ion or the ionophore is in large excess with respect to the other. With this state of affairs in mind, it was deemed of interest to investigate a situation where the concentration of both ion and ionophore were equivalent. The assisted ion transfer of potassium by the ionophore Db18C6 across the large interface between water and 1,2-DCE was investigated for the following cell, using cyclic voltammetry:

$$\underset{\text{REFERENCE ELECTRODE}}{\text{Ag|AgCl|10mM TBACl}}\Big|\underset{\text{1mM Db18C6}}{\text{10mM TBATPBCl}}\Big\|\underset{\text{KCl}}{\text{xmM}}\Big|\underset{\text{REF. E.}}{\text{AgCl|Ag}'}$$

$\overleftarrow{\text{REFERENCE ELECTRODE}}$ $\overleftarrow{\text{1,2-DCE}}$ $\overleftarrow{\text{WATER}}$ $\overleftarrow{\text{REF. E.}}$

TBA^+ ion selective electrode

Cell A1 - where x corresponds to a value given in the text.

The value of x in cell A1 was 5, 2, 1 and 0.5 in successive experiments. The voltammograms obtained are shown in figure A1. The values obtained for the peak-to-peak separations, ΔE_p, are given in table A1 together with the experimentally obtained half-wave potentials. On the same table are the formal potentials for the assisted ion transfer reaction relative to the 'TPAsTPB' scale. These were calculated using the following equation:

$$\Delta^{w}_{o}\phi^{o'}_{(Db18C6)K^+} = \Delta^{w}_{o}\phi^{1/2}_{(Db18C6)K^+} - (\Delta^{w}_{o}\phi^{1/2}_{TMA^+} - \Delta^{w}_{o}\phi^{o'}_{TMA^+}) \qquad (A1.1)$$

which is analogous to equation 6.1. The experimental values for the half-wave potential of TMA^+ were obtained through addition of $(TMA)_2SO_4$ to

blank systems containing the relevant concentration of potassium ion and no Db18C6 (x = 0, cell A1).

Table A1 - Half-wave and formal potential values, together with ΔE_p data, for the assisted ion transfer of potassium, K^+, by Db18C6.

K^+ conc. (mM)	ΔE_p ± 4 (mV)	$\Delta^w_o\phi^{1/2}_{(Db18C6)K^+}$ ± 4 (mV)	$\Delta^w_o\phi^{0'}_{(Db18C6)K^+}$ ± 4 (mV)
5	58	328	70
2	58	375	95
1	80	388	---
0.5	60	410	95

The results clearly indicate that the assisted ion transfer reaction deviates from full reversibility only in the instance where the ratio of the potassium ion to the Db18C6 concentration is 1:1. Hopscotch and numerical simulations, performed by Dr. R.G.Wellington and Prof. H.H.Girault of the Institut Chimie Physique (III), E.P.F., Lausanne, Switzerland respectively (see appendix three (3) for details), both predict slightly greater ΔE_p values for ratios of 1:1, 1:2 and 2:1 ion to ligand concentration. As stated previously in chapter five, however, Osborne [114] has shown that the assisted ion transfer of potassium by Db18C6 at the microhole-supported ITIES is fully reversible for a potassium ion to Db18C6 ratio of 2:1. Therefore the results given in table A1 are validated against the possibility of effects due to overcompensation of the iR drop. However, it does not rule out the possibility that weighing errors may have influenced the 1:1 experimental result.

One aspect of the experimental results is that the formal potential values obtained for the 1:2 and 2:1 cases are identical. This is not unexpected since the half-wave potential value (on the TPAsTPB scale) will only be shifted by the potassium ion concentration down to the point at which the ion is still in marginal excess with respect to the Db18C6. After that point the reaction is controlled by diffusion of both the Db18C6 and the potassium to the interface, yielding a peak-to-peak separation which is greater than 60 mV. When the concentration of the ionophore becomes greater than that of the ion, the reaction is controlled by diffusion of the potassium to the interface and a peak-to-peak separation of 60 mV is again observed.

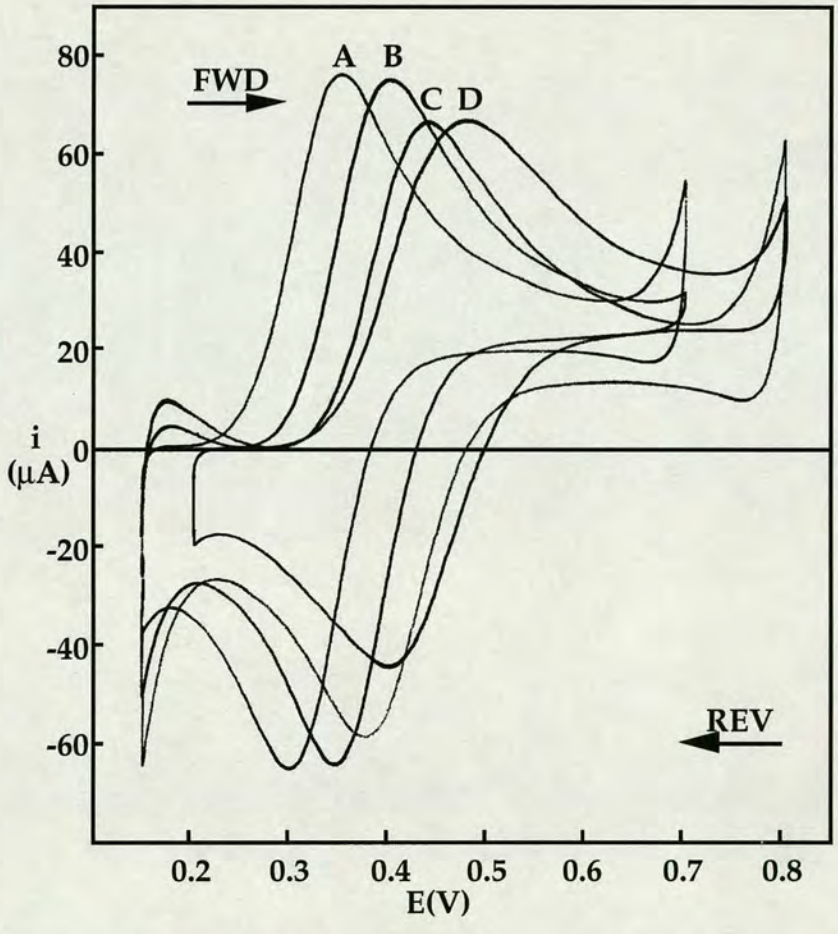

Figure A1 - Cyclic Voltammograms obtained for cell A1, with x values of (A) 5, (B) 2, (C) 0.5, and (D) 1 (mM KCl).

Appendix Two

A simple analytical model for the treatment of irreversible enzyme inhibition - provided by Dr. P.P.Infelta of the Institut de Chimie Physique (II), Ecole Polytechnique Federale de Lausanne, Switzerland.

Consider the simple enzyme reactions:

$$E + S \underset{k_{-1}}{\overset{k_1}{\rightleftharpoons}} ES \xrightarrow{k_2} E + Prod \qquad (A2.1)$$

$$E + P \xrightarrow{k_3} EP \text{ (enzyme consumed)} \qquad (A2.2)$$

where P = Paraoxon.

Assumptions:

(1) The equilibrium between the enzyme, the substrate and the enzyme-substrate complex is very rapid.

(2) The amount of ES present is very small. $K = k_1/k_{-1}$ is small. The time law for the disappearance of the enzyme is derived as follows:

$$d[E] = d[P] \Rightarrow [E] - [P] = [E_0] - [P_0] \qquad (A2.3)$$

$$\frac{dE}{dt} = -k_3[E][P] = -k_3[E]([E] - ([E_0] - [P_0])) = -k_3[E]^2 + k_3([E_0] - [P_0])[E] \qquad (A2.4)$$

using $y = 1/[E]$ as the variable:

$$\frac{dy}{dt} = k_3 - k_3 y([E_0] - [P_0]) \Rightarrow y = \frac{1}{[E_0] - [P_0]} + Ae^{-k_3([E_0] - [P_0])t} \quad \text{(A2.5)}$$

and using the initial condition that at t = 0, [E] = $[E_0]$

$$[E] = [E_0]\frac{[E_0] - [P_0]}{[E_0] - [P_0]e^{-k_3([E_0] - [P_0])t}} \quad \text{(A2.6)}$$

The special case where $[E_0] = [P_0]$, for which a solution can be easily obtained, is ignored.

In the absence of inhibitor, the analytical expression for the substrate disappearance is:

$$\ln\frac{[S]}{[S_0]}\ln = -k_2K[E_0]t \quad \text{(A2.7)}$$

In the presence of inhibitor, the law for the disappearance of S is as follows:

$$\frac{dS}{dt} = -\frac{dProd}{dt} = -k_2[ES] \text{ with } k_1[E][S] = k_{-1}[ES] \quad \text{(A2.8)}$$

$$\frac{dS}{dt} = -k_2K[S][E_0]\frac{[E_0] - [P_0]}{[E_0] - [P_0]e^{-k_3([E_0] - [P_0])t}} \quad \text{(A2.9)}$$

$$\ln\frac{[S]}{[S_0]} = \frac{k_2K}{k_3}\ln\left\{\frac{([E_0] - [P_0])e^{-k_3([E_0] - P_0])t}}{[E_0] - [P_0]e^{-k_3([E_0] - P_0])t}}\right\} \quad \text{(A2.10)}$$

The experimental results are normalized as the fraction of substrate left as a function of time with respect to substrate left at time t = 1 min. Assuming

that the reaction takes place from time t = 0, and applying the above result to time t = 1 min. the following expression is obtained:

$$\ln\frac{[S_1]}{[S_0]} = \frac{k_2K}{k_3}\ln\left\{\frac{([E_0] - [P_0])e^{-k_3([E_0] - [P_0])}}{[E_0] - [P_0]e^{-k_3([E_0] - [P_0])t}}\right\} \qquad \text{(A2.11)}$$

Combining the two preceding equations:

$$\ln\frac{[S]}{[S_1]} = \frac{k_2K}{k_3}\ln\left\{e^{-k_3([E_0] - [P_0])(t-1)}\ \frac{([E_0] - [P_0])e^{-k_3([E_0] - [P_0])}}{[E_0] - [P_0]e^{-k_3([E_0] - [P_0])t}}\right\} \qquad \text{(A2.12)}$$

This is the relation to which an attempt was made to fit the data.

Independent parameters:

The enzyme concentration is expressed in Udm^{-3}, and the concentration of the paraoxon, is expressed in parts per billion (ppb). Calculations have to be carried out with an homogeneous set of concentration units. Therefore, the initial concentrations of BChE and paraoxon are defined as:

$$[E_0]\{moldm^{-3}\} = \boldsymbol{a}\,[E_{init}]\{U\ dm^{-3}\} \qquad \text{(A2.13)}$$

and

$$[P_0]\{moldm^{-3}\} = \boldsymbol{b}\,[P_{init}]\{ppb\} \qquad \text{(A2.14)}$$

Taking M.Wt. = 277g for the paraoxon, 1ppb = $1mgdm^{-3}$ = $(1)10^{-6}/277$ = $(3.6)10^{-9}$ $moldm^{-3}$. Therefore $\boldsymbol{b} = (3.6)10^{-9}$.

Thus, there are three parameters to obtain from a fit:

$k_2K\{mol^{-1}min^{-1}\}$, $k_3\{mol^{-1}min^{-1}\}$, and $\boldsymbol{a}.\{molU^{-1}\}$.

Appendix Three

Published Papers

(1) Determination of Butyrylcholinesterase Inhibition Using Ion Transfer Across the Interface Between Two Immiscible Liquids.
P.D.Beattie, P.P.Infelta and H.H.Girault, Anal.Chem., 66(1994)52

(2) Investigation of the Kinetics of Assisted Potassium Ion Transfer by Dibenzo-18-Crown-6 at the Micro-ITIES by Means of Steady-State Voltammetry.
P.D.Beattie, A.Delay and H.H.Girault, J.Electroanal.Chem., 380(1995)167

(3) Cyclic Voltammetry for Assisted Ion Transfer at an ITIES.
P.D.Beattie, R.G.Wellington and H.H.Girault, J.Electroanal.Chem., (in press)

(4) Investigation of the Kinetics of Ion and Assisted Ion Transfer by the Technique of A.C. Impedance of the Micro-ITIES.
P.D.Beattie, A.Delay and H.H.Girault, Electrochim.Acta., (accepted for publication)

Determination of Butyrylcholinesterase Inhibition Using Ion Transfer across the Interface between Two Immiscible Liquids

P. D. Beattie
Department of Chemistry, University of Edinburgh, West Mains Road, Edinburgh, EH9 3JJ, Scotland, U.K.

P. P. Infelta and H. H. Girault*
Institut de Chimie Physique, Ecole Polytechnique Federale de Lausanne, CH-1015 Lausanne, Switzerland

An investigation was made into the inhibition of the enzyme butyrylcholinesterase by paraoxon (diethyl *p*-nitrophenyl phosphate), using butyrylcholine chloride as the substrate. Experimental measurement was based on the transfer of the butyrylcholine cation across the interface between water and 1,2-dichloroethane using cyclic voltammetry. By this method it was possible to determine the rate constants for both the inhibition of the enzyme and the hydrolysis of butyrylcholine.

The aim of this work is to show that the enzyme butyrylcholinesterase (BCHE) can be studied using the transfer of the butyrylcholine cation (ButCh) across the water/1,2-dichloroethane interface, by means of cyclic voltammetry, and that the inhibition of the enzyme by the organophosphate compound paraoxon can also be demonstrated.

Organophosphate compounds, and related substances, are the most widely used insecticides in the world, having replaced the older, and more persistent, organochlorine compounds. The target of these substances is the central nervous system (CNS) of insects but because the CNS of both vertebrates and invertebrates operates by cholinergic transmission, accidential poisonings due to crop spraying or other uses may severely harm humans.[1]

Nerve transmission ends when the enzyme acetylcholinesterase (ACHE) hydrolyses the neurotransmitter acetylcholine to choline and acetic acid in order to reestablish the initial state of the postsynaptic membrane.[1] Organophosphate compounds imitate the overall molecular shape of acetylcholine and can bind irreversibly to the esteratic active site of the enzyme, rendering it nonfunctional.[2]

Due to the health threat posed by the buildup of pesticide residues in the environment, legislation has made the detection of these compounds at the parts per billion (ppb) and sub–ppb domains a necessity. At the moment, the best techniques are gas chromatography (GC), high-performance liquid chromatography (HPLC), and GC coupled with mass spectrometry (GC/MS).[3] Although such techniques are the best available, they are expensive and they require skilled personnel to operate them efficiently. In the search for less costly alternatives, a lot of effort has been devoted to the development of relatively inexpensive electrochemical techniques, such as enzyme or antibody biosensors, to try and effect the same performance as the conventional methods. Some examples of enzymatic methods developed specifically for the detection of organophosphate compounds are described below. The methods developed generally fall into two broad categories—amperometric and potentiometric.

Potentiometric Methods. A commercial, field-based instrument utilizing replaceable pads with gel-entrapped BCHE as the sensor was developed by Goodson et al.[4] in the 1970s. Pesticide detection was based on the production of electroactive thiocholine from the hydrolysis of butyrylthiocholine. The inhibition of the enzyme produced a change in the measured voltage of the cell.

Durand et al.[5] and Kumaran and Tran-Minh[6] used pH electrodes modified with an enzymic layer to investigate ACHE[5] and BCHE[6] inhibition, using acetylcholine (ACh) and butyrylcholine (ButCh) as the respective substrates. The method of detection was based on the fact that one proton is produced per hydrolyzed substrate molecule.

Amperometric Methods. Razumas et al.[7] studied BCHE inhibition in solution using indoxyl acetate as the substrate, producing indoxyl, which could be measured amperometrically.

Campanella et al.[8] investigated ACHE and BCHE inhibition using a method based on an oxygen electrode covered with a membrane, on which choline oxidase was immobilized. ACHE or BCHE was either free in solution or immobilized with the choline oxidase. The substrates used were ACh and ButCh. Any inhibition of the enzyme led to an increase in the oxygen concentration being measured. Their results showed that BCHE was more sensitive to organophosphate inhibition than ACHE for a given inhibitor.

Bernabei et al.[9] studied ACHE inhibition using the same principles but replaced the oxygen electrode with a hydrogen

(1) Hassall, K. A. *The biochemistry and uses of pesticides: structure, metabolism, mode of action and uses in crop protection*, 2nd ed.; Macmillan: Basingstoke, U.K., 1990; Chapter 4.
(2) Matsumura, F. *Toxicology of insecticides*; Plenum Press: New York, 1975; Chapters 3 and 4.
(3) Seiber, J. N., Li, Q. X., Van Emon, J. M. In *Immunochemical methods for environmental analysis*; Van Emon, J. M., Mummar, R. O., Eds.; ACS Symposium Series 442; American Chemical Society: Washington, DC, 1990; Chapter 13.
(4) Goodson, L. H., Jacobs, W. B., Cage, B. R. *Proc. Natl. Conf. Control Hazard. Mater.* April 11–13, 1978.
(5) Durand, P.; Mallevialle, J.; Nicaud, J. M. *J. Anal. Toxicol.* **1984**, *8*, 112.
(6) Kumaran, S., Tranh-Minh, C. *Electroanalysis* **1992**, *4*, 949.
(7) Razumas, V. J., Kulys, J. J., Malinauskas, A. A. *Environ. Sci. Technol.* **1981**, *15*, 360.
(8) Campanella, L., Achilli, M., Sammartino, M. P., Tomassetti, M. *Bioelectrochem. Bioenerg.* **1991**, *26*, 237.
(9) Bernabei, M., Cremisini, C., Mascini, M., Palleschi, G. *Anal. Lett.* **1991**, *24*, 1317.

0003-2700/94/0366-0052$04.50/0

peroxide sensor and sandwiched the enzyme-loaded membrane between two membranes, one designed to protect the electrode from electrochemical interferences and the other to protect the enzyme from large molecules and bacteria. Their results showed that experiments with the ACHE free in solution were more sensitive than for immobilized case.

Kulys and D'Costa[10] and Skladal[11] studied BCHE inhibition using printed-strip amperometric sensors containing the immobilized enzyme and a redox mediator. The substrate used in each case was butyrylthiocholine.

From the various investigations cited above,[4-11] the general conclusions were that the inhibition of the enzyme is favored by incubation with the pesticide for a certain amount of time and that the longer the incubation time observed the greater the inhibition. It is clear, however, that amperometric methods tend to give much better sensitivity in general than the potentiometric methods.

Vanysek and Behrendt[12] investigated the hydrolysis of ACh by ACHE at the interface between two immiscible electrolyte solutions (ITIES), in their case water and nitrobenzene, in an attempt to demonstrate an alternative assay for enzyme activity. The problem with this method, however, is that the ACh and choline (Ch) peaks are poorly resolved, making it difficult to allow unambiguous determination of enzyme activity. The resolution of ButCh and Ch is much clearer, which makes the enzyme reaction easier to follow, as will be shown.

EXPERIMENTAL SECTION

BCHE (EC 3.1.1.8) from horse serum (500 units mg^{-1}), ButCh chloride, and paraoxon were supplied by Sigma. Acetone, methanol, tris(hydroxymethyl)aminomethane hydrochloride, tris(hydroxymethyl)aminomethane, anhydrous lithium chloride, and tetrabutylammonium chloride ((TBA)Cl) were supplied by Fluka. 1,2-Dichloroethane (1,2-DCE) was supplied by Merck. Tetrabutylammonium tetrakis(4-chlorophenyl) borate ((TBATPB)Cl) was prepared by metathesis of (TBA)Cl and K(TPB)Cl (Lancaster) and recrystallized twice from methanol. All reagents used were analytical grade or better.

The apparatus used was a four-electrode potentiostat, of a design similar to that given in ref 13. It consisted of an ordinary three-electrode potentiostat (Southampton University) and a "homemade" zerostat. The potential was supplied by a waveform generator PPRI (Hi-Tek Instruments), which was coupled to an *X–Y* recorder (Bryans Instruments). The cell used was constructed of glass and was of the design shown in Figure 1. Both the cell and the four-electrode potentiostat were housed in a Faraday cage. The cell was furthermore kept at a temperature of 37 ± 0.5 °C by means of a thermostated water bath (unless otherwise stated).

The paraoxon was dissolved in acetone before being diluted with water to make standard solutions, which also contained (ButCh)Cl. The enzyme and the lithium chloride were diluted with 0.1 M tris-HCl buffer to give a concentration of x units L^{-1}/10 mM LiCl (x is a value specified in the text) and a pH

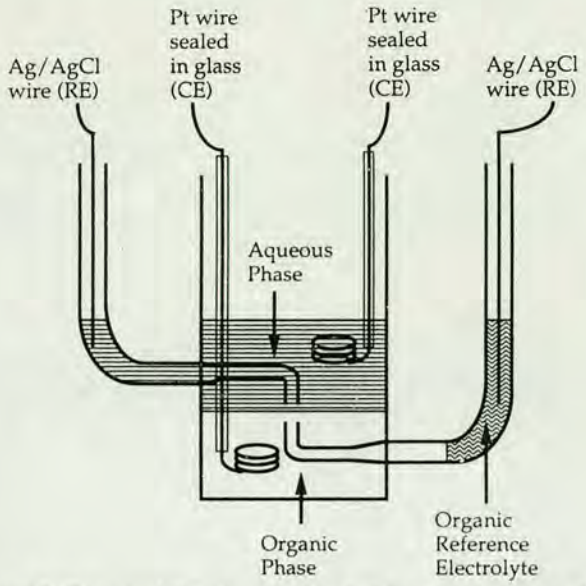

Figure 1. Representation of an ITIES cell: CE, counter electrode; RE, reference electrode.

of 8 ± 0.05 at 37 °C. This solution was used as the aqueous phase of the cell, and the volume added was always 2 mL so that a constant amount of enzyme was maintained. The basic reaction studied was

$$\text{ButCh} \xrightarrow{\text{BCHE}} \text{Ch} + \text{butyric acid}$$

and the system used for the experiments was

$$\underset{\text{REFERENCE ELECTRODE}}{\text{Ag|AgCl|10mM TBACl}} \| \underset{\text{Cell I}}{\begin{matrix}\text{10mM} \\ \text{TBATPBCl}\end{matrix} \| \begin{matrix}\text{10mM LiCl and xUl}^{-1} \\ \text{BCHE in 0.1M tris/HCl}\end{matrix}} \underset{\text{REF. E.}}{\text{|AgCl|Ag'}}$$

The scan rate was 0.1 $V\,s^{-1}$, the aqueous phase was unstirred, and iR drop compensation was not used. The concentration of butyrylcholine chloride being studied was near the limit of detectability for cyclic voltammetry at the liquid/liquid interface. The organic phase reference electrode was a TBA^+ ion-selective electrode comprised of a silver/silver chloride wire immersed in a solution of TBACl.

Four principal types of experiments were performed:

(1) Sample Addition Reactions (x = 350 units L^{-1}). A 100-μL aliquot of the paraoxon standard containing ButCh was injected into the thermostated cell. The decrease in the ButCh cation peak height with time (1-min intervals) was observed using cyclic voltammetry. The emergence of a peak due to the production of Ch was also seen. Experiments were carried out for a cell concentration of 50 μM (ButCh)Cl together with 0, 20, 35, 50, 70, 100, and 120 ppb paraoxon.

(2) Sample Incubation Reactions (x = 350 units L^{-1}). A 10 ppb sample of paraoxon (cell concentration) was incubated with the enzyme for 0, 5, 10, and 15 min prior to addition of the (ButCh)Cl (cell concentration as in (1)).

(3) Substrate Concentration Variation (x = 350 units L^{-1}). Standards containing different concentrations of (ButCh)Cl (cell concentrations of 50, 140, and 290 μM) were added to the cell.

(4) Enzyme Concentration Variation. Enzyme solutions containing 50, 150, 250, and 350 units L^{-1} were prepared and

(10) Kulys, J., D'Costa, E. J. *Biosens. Bioelectron.* **1991**, *6*, 109.
(11) Skladal, P. *Anal. Chim. Acta* **1992**, *269*, 281.
(12) Vanysek, P., Behrendt, M. *J. Electroanal. Chem.* **1981**, *130*, 287.
(13) Samec, Z., Marecek, V., Weber, J. *J. Electroanal. Chem.* **1979**, *100*, 841.

the relative rates of hydrolysis of ButCh observed. The cell concentration of ButCh was in (1).

RESULTS AND DISCUSSION

The equations for enzyme kinetics were first developed by Michaelis and Menten[14] and are based on the mechanism

$$E + S \underset{b}{\overset{a}{\rightleftarrows}} ES \xrightarrow{c} E + Prod$$

where the substrate, S, combines with the enzyme, E, to form an enzyme/substrate complex, ES, which proceeds to form the product, Prod, and the free enzyme. The reaction involving BCHE and ButCh is analogous to this. The enzyme contains two active sites. One is an esteratic site, the function of which is to cleave the ester linkage, and the other is an anionic site, which simply holds the substrate molecule in position, by interaction with the nitrogen group, while cleavage occurs. A simplified equation for the reaction is as follows:

$$E + ButCh \underset{b}{\overset{a}{\rightleftarrows}} EComp \xrightarrow{c} EBut + Ch \xrightarrow{d} E + ButA$$

where the last step is recovery of the enzyme (EComp = enzyme/substrate complex, ButA = butyric acid). It is the last step which the inhibiting molecule interferes with. In the case of the butyrylated enzyme (EBut) this step is very fast, but for a phosphorylated enzyme the step is very slow. Although the inhibition is not completely irreversible, it is still slow enough to render the enzyme effectively nonfunctional.

In the case of reversible inhibition, where the inhibitor is in equilibrium with the enzyme or enzyme/substrate complex, Michaelis–Menten principles may be applied for analysis of the results. Irreversible inhibition, however, cannot be treated in a similar manner.[15] A simplified treatment of the enzyme kinetics for irreversible inhibition is therefore presented, along with the results.

(1) Sample Addition Experiments. Figure 2 shows the enzyme reaction with the blank sample, containing only (ButCh)Cl. The peak of interest here was that of ButCh, at ~0.32 V on the forward scan (left to right, positive current). It should be stressed at this point that the cyclic voltammetric peaks displayed on this figure correspond to a flux of ions across the water/1,2-dichloroethane interface and are in no way redox in nature. Positive current relates to the fact that the potential of water with respect to the organic phase is being made more positive on the forward scan, and this is the convention for all ITIES experiments. The potential scale is completely arbitrary in form and is specific only to be the system under study (cell I). Readers are referred to refs 16 and 17 for a full treatment of the principles and nature of the ITIES. Scans were performed at 1-min intervals after the addition of the substrate. On the same figure is the scan prior to addition, showing the potential window. It should also be mentioned that there was no visible effect on the potential window by the enzyme. Both enzyme-free and enzyme-containing solutions gave exactly the same potential window.

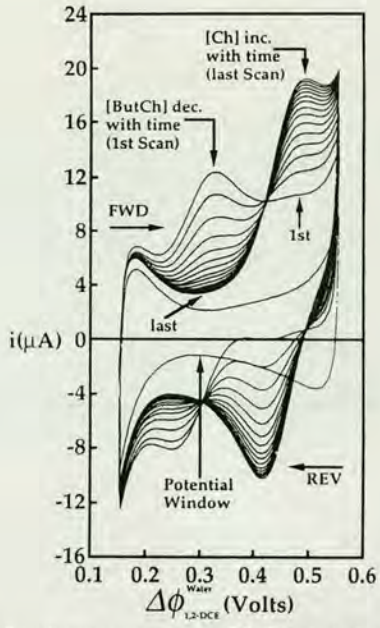

Figure 2. Cyclic voltammogram for the BCHE hydrolysis of butyrylcholine to choline over the time range 1–15 min (potential scale is with respect to cell I). The potential window for the system is also shown. The butyrylcholine peak (~0.32 V) decreases with time while the choline peak (~0.49 V) increases. The scan rate is 0.1 V s^{-1}.

As the experiment progressed, the ButCh peak was observed to decrease with time, and the emergence of a peak due to Ch at ~0.49 V, produced by the enzyme reaction, was also seen. In subsequent experiments with the paraoxon standards, the separation between successive scans was observed to decrease. The results obtained for all reactions were analyzed according to the height of the ButCh peak at 1 min after the addition of the sample. The peaks corresponding to the range 2–10 min were measured and expressed as a fraction of the 1-min peak. The reason for this approach was to mitigate against the intrinsic difficulty of reproducibility at the concentration of ButCh being dealt with (50 μM). The main reasons for peak height inconsistency in the different experiments were the simplicity of sample injection into the aqueous phase and the fact that the aqueous phase was unstirred. Other factors such as bubble formation at the interface during the course of the experiment, due to the elevated cell temperature, may also have contributed. The results obtained are shown in Figure 3.

Simple Analytical Model

$$E + S \underset{k_{-1}}{\overset{k_1}{\rightleftarrows}} ES \xrightarrow{k_2} E + Prod$$

$$E + P \xrightarrow{k_3} EP \text{ (enzyme consumed)}$$

where P = paraoxon. The following assumptions were made: (1) The equilibrium between the enzyme, the substrate, and the enzyme/substrate complex is very rapid. (2) The amount of ES present is very small. $K = k_1/k_{-1}$ is small. The time law for the disappearance of the enzyme is derived as follows:

$$d[E] = d[P] \rightarrow [E] - [P] = [E_0] - [P_0]$$

$$\frac{d[E]}{dt} = -k_3[E][P] = -k_3[E]([E] - ([E_0] - [P_0])) =$$

$$-k_3[E]^2 + k_3([E_0] - [P_0])[E]$$

(14) Michaelis, L., Menten, M. *Biochem. Z.* **1913**, *49*, 333.
(15) Lehninger, A. L. *Biochemistry*, 2nd ed.; Worth Publishers, Inc.: New York, 1981; Chapter 8.
(16) Koryta, J. *Electrochim. Acta* **1979**, *24*, 293.

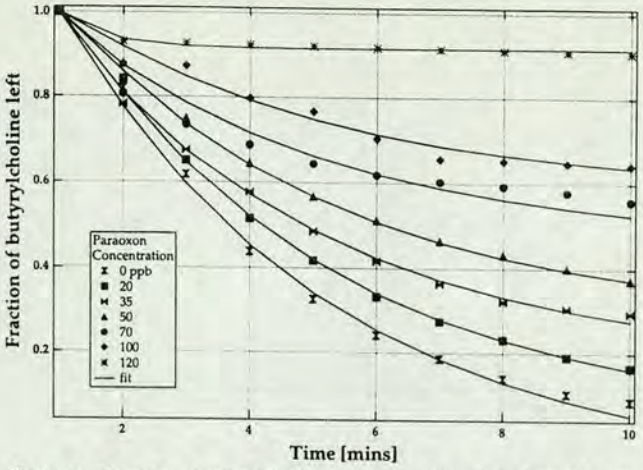

Figure 3. Fraction of butyrylcholine left versus time from initial sample addition (enzyme concentration, 350 units per liter; ButCh concentration, 50 μM), for different concentrations of paraoxon.

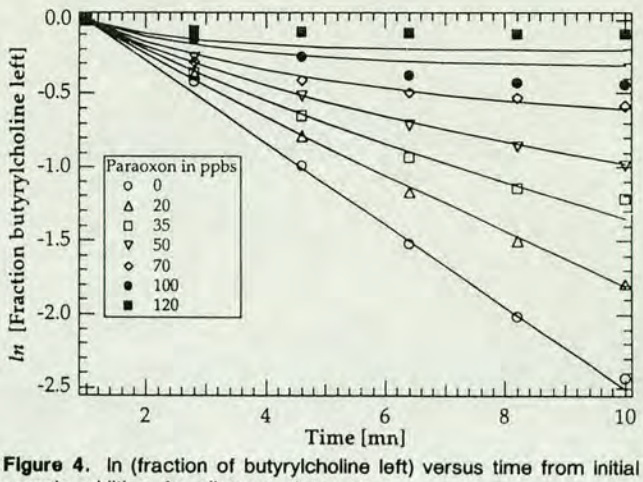

Figure 4. ln (fraction of butyrylcholine left) versus time from initial sample addition, for all seven data sets.

using $y = 1/[E]$ as the variable

$$\frac{dy}{dt} = k_3 - k_3 y([E_0] - [P_0]) \rightarrow y = \frac{1}{[E_0] - [P_0]} + Ae^{-k_3([E_0]-[P_0])t}$$

and using the initial condition that at $t = 0$, $[E] = [E_0]$

$$[E] = [E_0]\frac{[E_0] - [P_0]}{[E_0] - [P_0]e^{-k_3([E_0]-[P_0])t}}$$

The special case where $[E_0] = [P_0]$, for which a solution can be easily obtained, is ignored.

In the absence of inhibitor, the analytical expression for the substrate disappearance is

$$\ln\frac{[S]}{[S_0]} = -k_2K[E_0]t$$

In the presence of inhibitor, the law for the disappearance of S is

$$\frac{d[S]}{dt} = -\frac{d[Prod]}{dt} = k_2[ES] \quad \text{with} \quad k_1[E][S] = k_{-1}[ES]$$

$$\frac{d[S]}{dt} = -k_2K[S][E_0]\frac{[E_0] - [P_0]}{[E_0] - [P_0]e^{-k_3([E0]-[P_0])t}}$$

$$\ln\frac{[S]}{[S_0]} = \frac{k_2K}{k_3}\ln\left\{\frac{([E_0] - [P_0])e^{-k_3([E_0]-[P_0])t}}{[E_0] - [P_0]e^{-k_3([E_0]-[P_0])t}}\right\}$$

The results have been normalized as the fraction of substrate left as a function of time with respect to substrate left at time $t = 1$ min. Assuming that the reaction takes place from time $t = 0$, and applying the above result to time $t = 1$ min, the following expression is obtained:

$$\ln\frac{[S_1]}{[S_0]} = \frac{k_2K}{k_3}\ln\left\{\frac{([E_0] - [P_0])e^{-k_3([E_0]-[P_0])}}{[E_0] - [P_0]e^{-k_3([E_0]-[P_0])}}\right\}$$

Combining the two preceding equations we obtain

$$\ln\frac{[S]}{[S_1]} = \frac{k_2K}{k_3}\ln\left\{e^{-k_3([E_0]-[P_0])(t-1)}\frac{([E_0] - [P_0])e^{-k_3([E_0]-[P_0])}}{[E_0] - [P_0]e^{-k_3([E_0]-[P_0])t}}\right\}$$

This is the relation to which an attempt was made to fit the data.

Independent Parameters. The enzyme concentration is expressed in units per liter, and the concentration of the paraoxon, is expressed in ppb. Calculations have to be carried out with an homogeneous set of concentration units. Therefore, the initial concentrations of BCHE and paraoxon are defined as

$$[E_0]\ (\text{mol L}^{-1}) = \alpha[E_{init}]\ (\text{U L}^{-1})$$

$$[P_0]\ (\text{mol L}^{-1}) = \beta[P_{init}]\ (\text{ppb})$$

Taking MW = 277 for the paraoxon, 1 ppb = 1 μg L^{-1} = 1 $\times$ 10^{-6}/277 = 3.6 $\times$ 10^{-9} mol L^{-1}. Therefore $\beta = 3.6 \times 10^{-9}$. Thus, there are three parameters to obtain from a fit: k_2K (mol^{-1} min^{-1}), k_3 (mol^{-1} min^{-1}), and α.

The fit to the above relation together with the experimental data is shown in Figure 4. At higher concentrations of paraoxon, the data do not fit the model as well as would be expected. This could possibly be attributed to a change in the factors affecting the rate as the activity of the enzyme tends to zero or could, more probably, be a manifestation of the experimental conditions given that individual experimental results are under considerations. Figure 5 shows the result where the best five data sets are used. The fit to the data is very good in each case, and the values obtained for the parameters are not very different going from seven to five data sets. The three parameters each have an error of roughly 10%, and are as follows:

seven data sets

$$k_2K = (1.34 \pm 0.11) \times 10^6\ \text{mol}^{-1}\ \text{min}^{-1}$$

$$k_3 = (2.21 \pm 0.15) \times 10^6\ \text{mol}^{-1}\ \text{min}^{-1}$$

$$\alpha = (5.93 \pm 0.47) \times 10^{-10}\ \text{mol units}^{-1}$$

five data sets

$$k_2K = (1.51 \pm 0.13) \times 10^6\ \text{mol}^{-1}\ \text{min}^{-1}$$

(17) Girault, H. H., Schiffrin, D. J. Electrochemistry of liquid–liquid interfaces. In *Electroanalytical Chemistry*; Bard, A. J., Ed.; Marcel Dekker, Inc.: New York, 1989; Vol. 15.

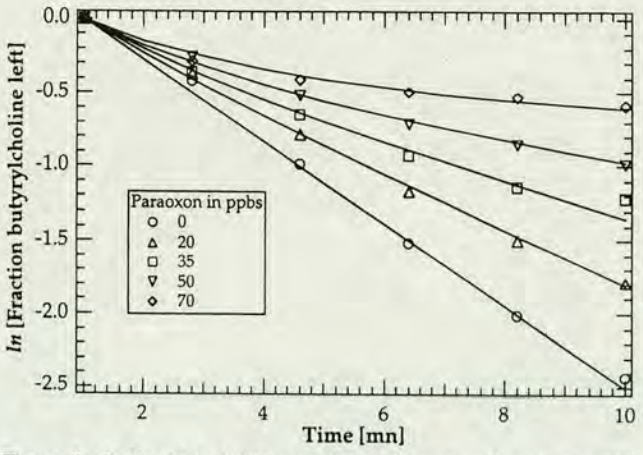

Figure 5. ln (fraction of butyrylcholine left) versus time from initial sample addition, for the best five data sets.

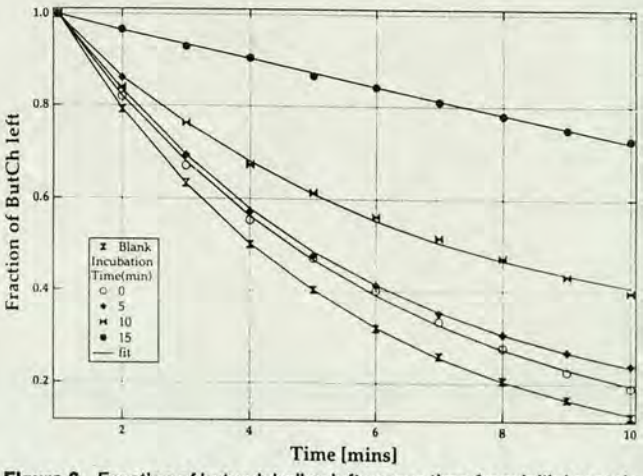

Figure 6. Fraction of butyrylcholine left versus time from initial sample addition, for a paraoxon concentration of 10 ppb and different incubation times.

$$k_3 = (2.00 \pm 0.14) \times 10^6 \text{ mol}^{-1} \text{ min}^{-1}$$

$$\alpha = (5.29 \pm 0.45) \times 10^{-10} \text{ mol units}^{-1}$$

The value obtained for α using a molecular weight for the protein of ~440 000 and a value of 500 units (mg of protein)$^{-1}$ is 4.5×10^{-12} mol units^{-1}, so there would seem to be a discrepancy in that the value obtained for α from the fit predicts either a smaller molecular weight for the protein or much smaller activity. However, this value depends to a great extent on the purity of the supplied protein as well and should not necessarily be viewed as a negative aspect.

According to the supplier's specifications, the activity should have been hydrolysis of 1 μmol of butyrylcholine by 1 unit of enzyme during 1 min, at 37 °C and pH 8.0. Therefore, under ideal conditions it should have taken just over 8 s for the enzyme to hydrolyze the 0.1 μmol of butyrylcholine in the cell. It is clear, however, that under our experimental conditions the activity is roughly 1% of the stated value. The most important point to remember when faced with such a discrepancy is that the cell was unstirred during the course of the experiment. Also, the stated value is presumably for the case where the substrate is in large excess compared with the available active sites of the enzyme and therefore would only be limited by the efficiency of the enzyme. Another contributory factor can be the choice of buffer for the experiments. Tris-HCl was chosen primarily for its ability to buffer in the pH range 7.1–8.9.[18] Other groups[5-11] have tried using phosphate, glycine, and phosphate/glycine buffers in varying concentrations, but always in the stated pH range. Goodson et al.,[4] however, used tris buffer in their commercial system. The high ionic strength of the aqueous phase might also have had an effect on the enzyme, especially considering that one of the active sites plays an electrostatic role. A combination of the above factors was probably the reason for the low activity observed, although an independent test of enzyme activity would be required to bear this out.

Another experiment, which was carried out at room temperature (23 ± 0.5 °C), showed that the BuTCh was hydrolyzed just as quickly as at 37 °C. Although this would suggest that the diffusion of the ButCh is independent of temperature, which is clearly an erroneous conclusion to draw, the effect of temperature on the rate of hydrolysis is clearly minimized, probably because the solution is unstirred.

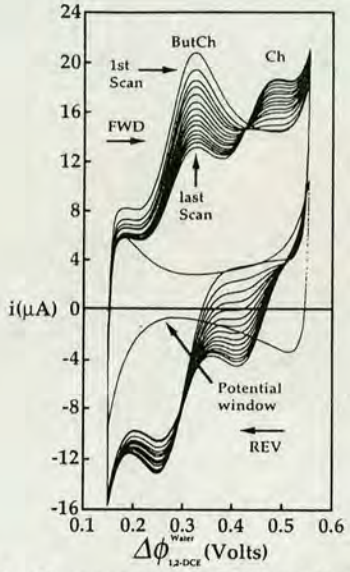

Figure 7. Cyclic voltammogram for the BCHE hydrolysis of butyrylcholine to choline over the time range 1–15 min, for a preincubation time of 15 min with 10 ppb paraoxon (potential scale is with respect to cell I).

(2) Sample Incubation Experiments. The results obtained for the incubation experiments showed that the incubation time of the paraoxon with the enzyme has a strong effect on the hydrolyzing power. Figure 6 shows the results obtained for incubation of a 10 ppb concentration of paraoxon for 0, 5, 10, and 15 min of incubation. Also shown is the result for a blank containing only (ButCh)Cl. The 0-, 5-, and 10-min results clearly show an exponential dependence, whereas the 15-min incubation period results in an almost linear response. Figure 7 shows the voltammograms for the 15-min case. Not shown in Figure 6 is the result for a blank in which the cell was left for 30 min after equilibration before adding the substrate. This result gave a response similar to that of 0-min incubation with the paraoxon, indicating that the enzyme does not denature significantly during this period.

In the Experimental Section, it was explained that the paraoxon was dissolved in a small amount of acetone before

(18) Dawson, R. M. C., Elliott, D. C., Elliott, W. H., Jones, K. M., Eds. *Data for Biochemical Research*; Oxford University Press: Oxford, U.K., 1969; pp 475–508.

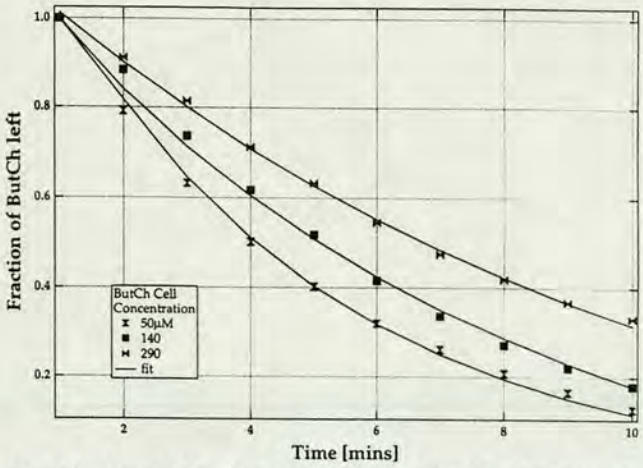

Figure 8. Fraction of butyrylcholine left versus time from initial sample addition, for different substrate concentrations.

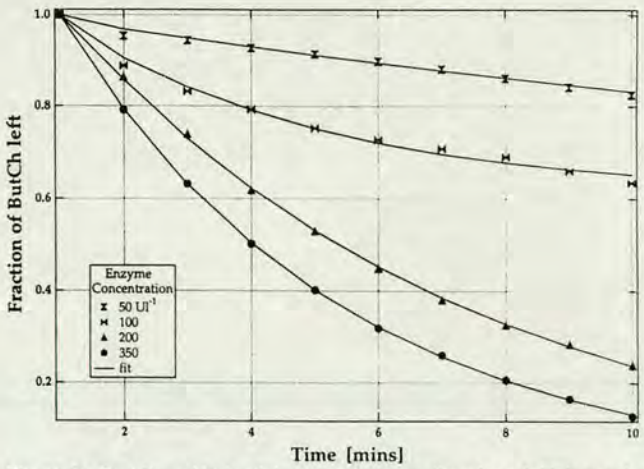

Figure 9. Fraction of butyrylcholine left versus time from initial sample addition, for different enzyme concentrations (ButCh concentration, 50 μM).

being diluted with water to make the necessary experimental standards. The effect of acetone, at the concentrations present in solution, was found to be negligible.

The difficulties inherent to these experiments precluded any attempt to fit our data with the model used for the sample addition experiments.

(3) Substrate Concentration Variation. The results obtained for experiments where the substrate cell concentration was varied between 50 and 290 μM are shown on Figure 8. These results show the reaction to be slower for higher substrate concentrations, but also show that even at ~6 times the substrate concentration used in (1) and (2) the reaction can still be treated as being pseudo first order in [S].

(4) Enzyme Concentration Variation. The results shown on Figure 9 illustrate the effect of varying the enzyme concentration. For concentrations of 50 and 100 units per liter the reaction appeared to be almost linear, whereas for 200 and 350 units per liter it was clearly pseudo first order in [S].

Sections 3 and 4 corroborate the idea that under the experimental conditions observed in sections 1 and 2 diffusion of the ButCh to the active sites of the enzyme, and not enzyme concentration, plays the important rate-determining role.

CONCLUSIONS

It has been shown that ion transfer across the ITIES can act as an effective transducer upon which sensor design may be based, as realized by Senda et al.[19]

The hydrolysis of butyrylcholine by the enzyme butyrylcholinesterase has been demonstrated for various substrate and enzyme concentrations. The inhibition of the enzyme BCHE by paraoxon, without preincubation, could be satisfactorily analyzed in a quantitative way. The working range of detection was 20–120 ppb paraoxon using cyclic voltammetry, although if differential pulse voltammetry were the method used, the detection limits would be improved. The incubation time of the paraoxon with the enzyme was also shown to be a powerful factor in the ability of BCHE to function effectively, using a concentration of only 10 ppb of paraoxon. The effect of the 1,2-dichloroethane phase on the stability of the enzyme was also shown to be negligible over the time ranges considered.

The results obtained compare very favorably with other approaches[4–11] where the best limits of detection tend to be in the low-ppb range with the exception of ref 11 in which a sub-ppb limit is claimed.

ACKNOWLEDGMENT

P.D.B. acknowledges the financial support given to him by the Science and Engineering Research Council (UK) and Medisense (UK) for a CASE award, and also that of the Ecole Polytechnique Fédérale de Lausanne for a visiting fellowship.

Received for review July 8, 1993. Accepted October 6, 1993.*

(19) Osaki, T., Kakutani, T., Senda, M. *Anal. Sci.* **1988**, *4*, 529.

* Abstract published in *Advance ACS Abstracts*, November 15, 1993.

ELSEVIER

Journal of Electroanalytical Chemistry 380 (1995) 167–175

JOURNAL OF ELECTROANALYTICAL CHEMISTRY

Investigation of the kinetics of assisted potassium ion transfer by dibenzo-18-crown-6 at the micro-ITIES by means of steady-state voltammetry

P.D. Beattie [a], A. Delay [b], H.H. Girault [b]

[a] *Department of Chemistry, University of Edinburgh, West Mains Road, Edinburgh, EH9 3JJ, UK*
[b] *Laboratoire d'Electrochimie, Institut de Chimie Physique 3, Ecole Polytechnique Federale de Lausanne, CH-1015 Lausanne, Switzerland*

Received 15 March 1994; in revised form 3 May 1994

Abstract

Micropipettes, with internal tip diameters ranging from 1.2 to 38 μm, were fabricated using borosilicate glass capillaries. These were then used to support a micro-interface between two immiscible electrolyte solutions (micro-ITIES). The assisted ion transfer of potassium from water to 1,2-dichloroethane by the neutral ionophore dibenzo-18-crown-6 was followed using both cyclic voltammetry and chronoamperometry. Supplementary investigations included variation of potassium ion and dibenzo-18-crown-6 concentration and an ac impedance study of the micropipette tip resistance. These investigations showed that the assisted ion transfer process is not limited by charge transfer, but only by diffusion of the participating species. The lower limit of the standard rate constant, k°, for the charge-transfer step was estimated to be 3 cm s^{-1}.

Keywords: Potassium ion transfer; Dibenzo-18-crown-6; Micro-ITIES; Voltammetry

1. Introduction

The aim of the experimental work undertaken was to establish whether the micro-interface between two immiscible electrolyte solutions (micro-ITIES) can be used to obtain kinetic information concerning assisted ion transfer reactions. To that end, this paper focuses on the assisted ion transfer of potassium across the interface between water and 1,2-dichloroethane (1,2-DCE) by the neutral ionophore dibenzo-18-crown-6 (DB18C6).

Ever since the late 1970s when Fleischmann and co-workers popularized microelectrodes [1], the field has been continually developing and expanding. Major research applications include the study of reaction kinetics, characterization and modification of surfaces and in vivo sensing [2–4].

The properties of micro- and ultramicroelectrodes have been extensively reviewed elsewhere [5–7] but one of the main advantages, critical to so many applications, is the decreased effect of solution resistance. This criterion opened the way to studies in highly resistive media which were previously inaccessible by conventional means [8].

The analogous nature of the ITIES with the ideally polarizable electrode has been thoroughly documented [9–11]. In 1986, Taylor and Girault [12] miniaturized the ITIES by supporting it at the tip of a micropipette. In liquid liquid electrochemistry, the solution resistance of the organic phase must be compensated for when working at centimetre-scale interfaces, owing to the use of organic solvents with low permittivity, such as 1,2-DCE. Miniaturization sought to bypass this requirement altogether, and initial results were very promising, showing that it was relatively easy to study reversible ion transfer reactions at the micropipette tip-supported ITIES [12].

Further work by Stewart et al. [13] focused on the use of the micropipette as a tool for the determination of the ionic species limiting the potential window. Shao et al. [14] have investigated the assisted (or facilitated) ion transfer of alkali metal cations, such as potassium, from the aqueous to the organic phase using micropipettes. This type of transfer reaction was first studied by Koryta [10] in 1979. Assisted ion transfer from aqueous electrolyte solutions to low supporting electrolyte organic phase solutions has also been investigated [15]. Most of the above work suffered, however

SSDI 0022-0728(94)03541-A

from drawbacks associated with poor reproducibility of the tip geometry. Tips were produced on a trial and error basis by breaking the end of the pulled pipette, which meant that they were seldom regular in shape, and this led to a decrease in the mechanical stability of the liquid liquid interface. In this work, the problem of reproducible tip geometry has been effectively eliminated by the use of a more sophisticated puller and much thinner glass, yielding pipettes which have a wide range of diameters. In addition, thick glass capillaries were used to produce micropipettes having internal tip diameters of less than 2 μm.

In 1991 Ohkouchi et al. [16] investigated the analytical applicability of micropipettes, when they used a micropipette containing the organic phase to study the transfer of the acetylcholine cation from water to nitrobenzene. Their studies showed that it was possible to carry out stripping voltammetry of acetylcholine, at micromolar levels, by preconcentration of the acetylcholine in the nitrobenzene phase.

In assisted ion transfer reactions, aqueous phase cations, such as lithium, sodium and potassium, which would normally transfer at the water-positive end of the polarization range, can be made to transfer at significantly less positive potentials by complexation with neutral ionophore molecules (for example, DB18C6). The ionophore, in effect, lowers the apparent Gibbs energy of transfer for the cation. Provided that these ionophores are suitably hydrophobic, remaining in the organic phase solvent, transfer from the aqueous to the organic phase occurs by a process called transfer by interfacial complexation (TIC) and the reverse is termed transfer by interfacial dissociation (TID) (see Fig. 1). This terminology was first coined by Shao et al. [14]. This transfer mechanism is directly analogous to electron transfer at the electrode |solution interface. The organic phase is usually outside the pipette, with the exception of the work in Ref. [16], and the current arises from diffusion to and from the tip-supported interface by the ion–ionophore complex. As this diffusion is intrinsically of a spherical nature, a steady-state current response is observed.

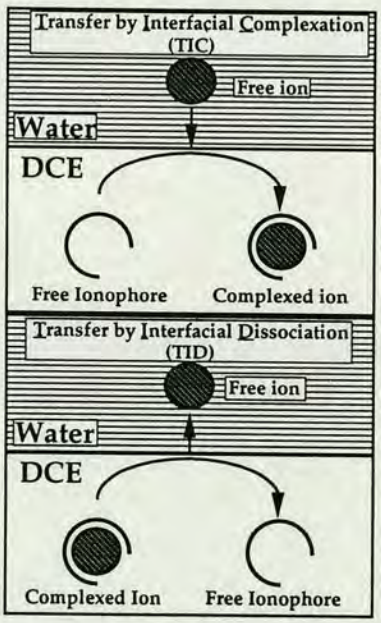

Fig. 1. Representation of the TIC/TID mechanism for assisted ion transfer by a neutral ionophore.

In contrast, simple ion transfer reactions at the micropipette are characterized by an asymmetric diffusion regime. The transfer of ions out of the pipette (egress) is controlled by linear diffusion, whereas transfer into the pipette (ingress) is controlled by diffusion of a spherical type. The two processes are easily distinguished during cyclic voltammetry, as the egress transfer leads to a peak-shaped current response, whereas ingress transfer produces a steady-state wave [13].

Another method of creating micro-ITIES is to support it in a microhole, formed by UV excimer laser photoablation of a thin polyester film, as realized in 1989 by Campbell and Girault [17]. Unlike the micropipette, the diffusion regime at a microhole-supported ITIES is approximately symmetrical. Thus, both ion transfer and assisted ion transfer reactions produce current responses of a steady-state type [17,18]. The exact position of the interface within the hole has not been fully established, although the observed currents are the same as those for an inlaid microdisc electrode [18].

This paper deals with the aforementioned assisted ion transfer reaction at the micropipette tip-supported ITIES. It first reports a study of the internal tip radius as a function of current, together with separate investigations into the effect of potassium ion and DB18C6 concentration variations. This is complemented by an ac impedance evaluation of the tip resistance of the micropipettes.

2. Experimental

The aqueous and organic phase solvents were deionized water from a Milli-Q system (Millipore) and 1,2-DCE (Merck) respectively. DB18C6, potassium chloride and tetrabutylammonium chloride (TBACl) were supplied by Fluka. Tetrabutylammonium tetrakis(4-chlorophenyl) borate (TBATPBCl) was prepared by metathesis of TBACl with potassium tetrakis(4-chlorophenyl)borate (KTPBCl), obtained from Lancaster Synthesis. The purity of the DB18C6 was > 98%. All other reagents used were of analytical grade or better.

Micropipettes were made from borosilicate glass capillaries (length 10 cm, outer diameter (o.d.) 1.5 mm, inner diameter (i.d.) 1.7 mm (thin glass), and o.d. 1.5 mm, i.d. 0.86 mm (thick glass), from Science Products,

Germany), and were pulled with a 'Flaming–Brown' type puller (Model P87, Sutter Instrument, USA). The pulling sequence was computer controlled, with the glass being clamped horizontally between two pulleys, and heated in the middle by means of a 3 mm cubic element open on two opposing sides (through which the glass was inserted). Once the melting glass reached a certain velocity, monitored by the computer, the heating was stopped and the glass was cooled automatically using an air pressure unit to prevent further melting. A series of such steps was required to form a micropipette, beginning with an element temperature equal to that at which the glass first melts (this was determined independently with a heat ramp test on a separate glass capillary). In each subsequent step the temperature was reduced by a fixed amount (20°C for thin glass, 10 or 20°C for thick glass). In this way it was possible to fabricate pipettes having internal tip diameters of between 5 and 38 μm (thin glass) and 2 μm or less (thick glass), which had very flat tips. Fig. 2 shows a scanning electron micrograph of a pipette (thin glass) with an i.d. of 6 μm taken using a JEOL JSM-6300F scanning electron microscope. The advantage of this microscope is that it does not require gold coating of the sample to be examined. Tip diameters were first established using an Olympus IMT-2 microscope, fitted with a measuring graticule. The error on these measurements was estimated to be ± 0.5 μm, using scanning electron microscopy (SEM). Owing to the large number of micropipettes being used it was not deemed practical, nor indeed was it possible, to analyse each one by SEM.

The borosilicate capillaries had a very thin filament, running the entire length of the glass, on the inside. This meant that pipettes could be filled by back-filling with a syringe and a very fine needle, the point of the pipette filling by capillary action.

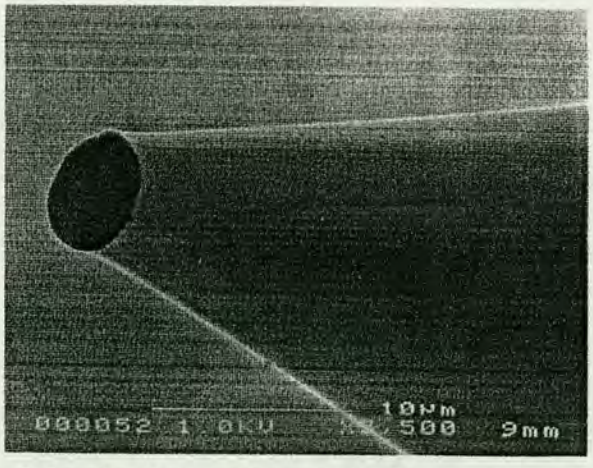

Fig. 2. Scanning electron micrograph of a pipette with an internal diameter of 6 μm (thin-walled glass). The picture was taken using a JEOL-JSM 6300F scanning electron microscope.

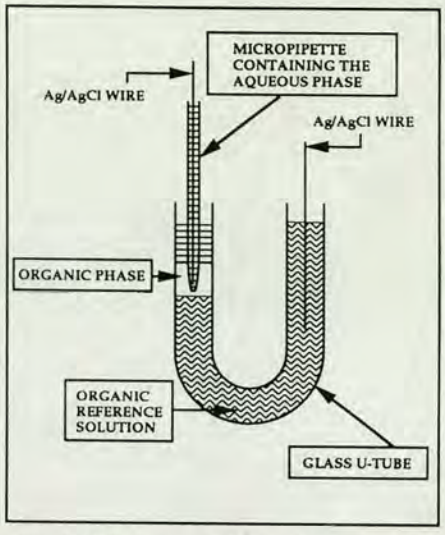

Fig. 3. Cell diagram of micropipette assembly.

The cell used for micropipette experiments was composed of a glass U-tube containing a small volume of the organic phase, supported by the organic reference solution. This was in turn covered with aqueous KCl to prevent release of harmful 1,2-DCE vapour. The micropipette, containing the same concentration of aqueous KCl, was immersed in the organic phase, and the distance between its tip and the organic reference solution was made as small as possible to minimize any effect due to *IR* drop. A two-electrode electrochemical cell was configured by means of two silver/silver chloride wires acting as reference/counter electrodes. One wire was placed inside the micropipette, while the other was placed in the organic reference solution, thereby forming an organic cation-selective electrode (see Fig. 3). All of the micropipette-assisted ion transfer experiments were carried out at a room temperature of 23 ± 1°C.

In the cyclic voltammetric and chronoamperometric experiments the voltage ramp and pulse, respectively, were provided by means of a PPR1 waveform generator (HiTek Instruments, UK). The resulting current was measured with a current follower based on a high-input impedance FET operational amplifier (Burr Brown OAP 104). Voltammograms and chronoamperomograms were recorded on an analog X–Y recorder (Series 60000, Advanced Bryans Instruments, UK).

For the ac impedance experiments on the micropipette, the glass U-tube was filled with aqueous KCl solution only, as inside the micropipette. The micropipette was simply inserted into one arm of the U-tube for measurement of the tip resistance. The dc potential was supplied by means of a Schlumberger Solartron 1286 electrochemical interface, while the ac signal was provided by a Schlumberger Solartron 1250 frequency response analyser. These experiments were carried out at a room temperature of 25 ± 1°C.

All micropipette experiments were conducted in an earthed faraday cage.

3. Results and discussion

The system under study was the following:

$$\underset{\text{Reference electrode}\atop\text{TBA}^+\text{ ion-selective electrode}}{\text{Ag}\,|\,\text{AgCl}\,|\,\text{10 mM TBACl}} \Big| \underset{\text{and } x \text{ mM DB18C6}}{\text{10 mM TBATPBCl}} \Big| \underset{\text{KCl}}{y \text{ mM}} \Big| \underset{\text{Ref. E}}{\text{AgCl}\,|\,\text{Ag}}$$

1,2-DCE | Water

Electrochemical cell 1: where x and y correspond to values given in the text. Generally, in the case where $x \gg y$, the observed limiting current is proportional to the KCl concentration. If $x \ll y$, however, the limiting current is proportional to the DB18C6 concentration.

The reaction under study was

$$K^+(\text{aq.}) + \text{DB18C6(org.)} \underset{k_b}{\overset{k_f}{\rightleftharpoons}} K^+\text{DB18C6(org.)} \quad (1)$$

3.1. Internal tip radius dependence study

3.1.1. Cyclic voltammetry

In the first set of experiments, the steady-state current was investigated with respect to the internal tip radius of the micropipettes. Micropipettes having internal tip radii of 16, 8, 6, 5, 3.5 and 2.5 μm were used to support the micro-interface between the aqueous KCl phase inside the pipette (cell 1, $y = 10$ mM) and the organic phase outside it, containing the DB18C6 (cell 1, $x = 0.6$ mM DB18C6). The assisted ion transfer of potassium by DB18C6 was studied by means of cyclic voltammetry. The scan rate in all cases was 0.1 V s^{-1}. Many experimenters might consider this excessive when attempting steady-state voltammetry; however, the response was shown to be independent of the scan rate between 0.1 and 0.02 V s^{-1}. Thus, since the pipette can suffer adversely from vibrations, leading to erratic responses over lengthy sweeps, a scan rate of 0.1 V s^{-1} was considered optimal.

Fig. 4(a) shows the cyclic voltammogram recorded for the 16 μm radius tip. The potential scale is completely arbitrary and corresponds only to electrochemical cell 1. The direction of the forward scan is from left to right, with the potential of the aqueous phase becoming more positive with respect to the organic phase as the potential is increased. Fig. 4(b) is the semi-logarithmic plot of $\ln(I/(I_{ss} - I))$ versus potential, which yielded a straight line with a slope of 39.9 V^{-1}. From the forward wave of the cyclic voltammogram, the Tomes' criterion ($E_{3/4} - E_{1/4}$) was found to be 55 mV. For a fully reversible charge-transfer process, the semi-logarithmic plot should yield a slope of 39.2 V^{-1} and the Tomes' criterion should be equal to 55.5 mV at 23°C. Thus, the assisted ion transfer of potassium by

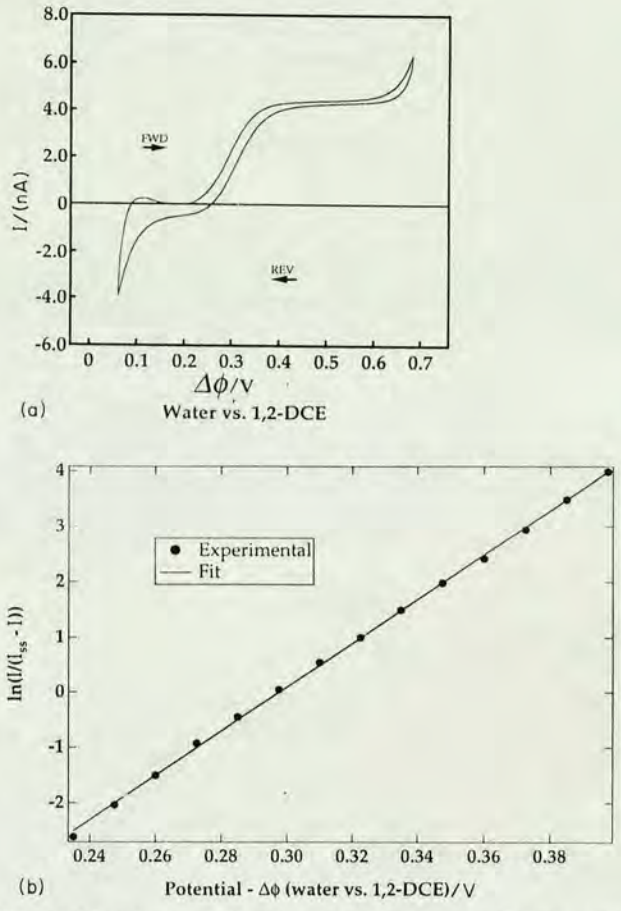

Fig. 4. (a) Steady-state voltammogram for an internal tip radius of 16 μm (thin-walled glass). K^+ concentration = 10 mM; DB18C6 concentration = 0.6 mM. (b) Plot of $\ln(I/I_{ss} - I)$ versus potential for the 16 μm radius pipette.

DB18C6 can be said to be effectively reversible under the experimental conditions. Therefore, the effect of *IR* drop in the organic phase seems to have been eliminated at this tip size.

The diffusion coefficient of the DB18C6 was calculated from experiments conducted at the large ITIES (experimental set-up described elsewhere [19]) under the same experimental conditions as above. These gave a value of 4.55 ± 0.25 cm^2 s^{-1} (average of two results).

Fig. 5(a) and (b) show the cyclic voltammetric responses obtained for internal tip radii of 8, 6, 5, 3.5 and 2.5 μm. These waves were analysed in the same way as that for the 16 μm radius tip, and the results are presented in Table 1(a), together with values for the half-wave potential. Clearly there is a significant change in behaviour between a tip radius of 16 μm and that of 8 μm. The transfer process would appear to be reversible at 16 μm, whereas for tip radii of 8 μm or less the transfer process deviates from this to become quasi-reversible in nature. At the same time, however, the slope of the $\ln(I/(I_{ss} - I))$ versus potential plots and the Tomes' criteria appear to remain relatively

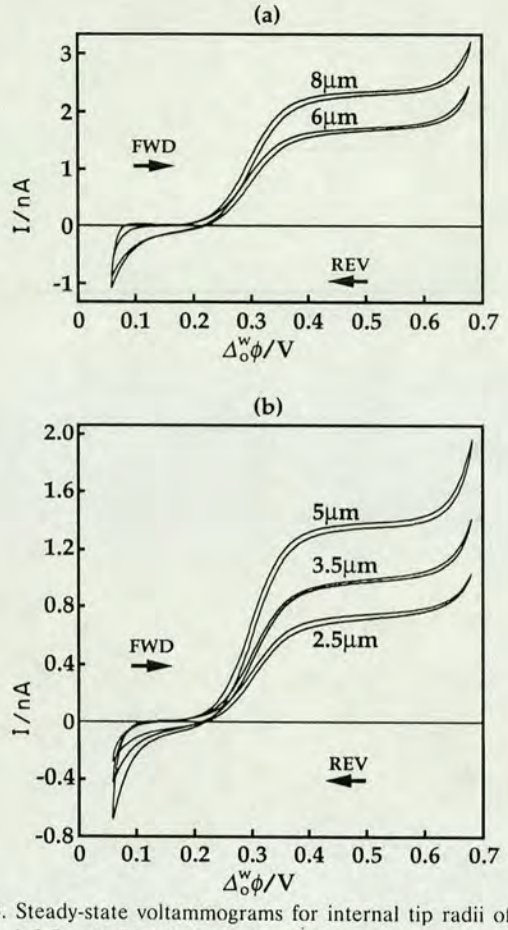

Fig. 5. Steady-state voltammograms for internal tip radii of 8, 6, 5, 3.5 and 2.5 μm (thin-walled glass). K^+ concentration = 10 mM; DB18C6 concentration = 0.6 mM.

constant over this range of tip radii, suggesting that the change in behaviour must occur below a certain size of tip. Initially it was thought that this phenomenon was a consequence of increased tip resistance when working with smaller micropipettes. However, this notion was ruled out when, as will be shown later, experimental evidence was obtained which showed that if the tip resistance was the controlling factor, then the expected *IR* drop for the 16 μm radius tip would be greater than

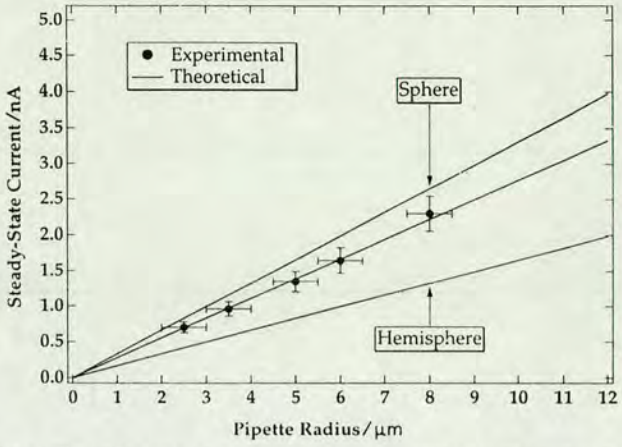

Fig. 6. Plot of steady-state current versus internal pipette radius for tip radii of 8, 6, 5, 3.5 and 2.5 μm.

that of the rest. Clearly this is in conflict with the result in Fig. 4(a), which shows the transfer process to be reversible. Another aspect of the experimental results would seem to be a change in the half-wave potential for the transfer process with decreasing tip size. However, this is misleading since results obtained using thick glass pipettes, listed in Table 1(b), show the half-wave potential to be effectively constant over the radii range from 8 to 0.6 μm. This then rules out the possibility that the reaction is controlled by charge-transfer kinetics, having already ruled out *IR* drop.

The steady-state current versus tip radius for the 8, 6, 5, 3.5 and 2.5 μm radii tips in Table 1(a) was plotted as shown in Fig. 6. Additional lines on this figure, showing the theoretical response for a shrouded hemisphere in an infinite insulating plane, and for an isolated sphere, were calculated using the diffusion coefficient value stated previously. The results demonstrate that the micropipette tip-supported ITIES exhibits behaviour between that of a hemisphere and a sphere:

Microhemisphere $I_{ss} = 2\pi nFD_I c_I^b r_0$ (2)

Micropipette $I_{ss} = 3.35\pi nFD_I c_I^b r_0$ (3)

Microsphere $I_{ss} = 4\pi nFD_I c_I^b r_0$ (4)

Table 1
Data from tip radius dependence study

	Pipette radius/μm	Steady-state current nA	Slope/V^{-1}	Tomes' criterion $(E_{3/4} - E_{1/4})$/mV	Half-wave potential/V
(a)	16	4.4	39.9	55	0.295
	8	2.3	34.6	62	0.296
	6	1.65	35.7	63	0.297
	5	1.35	35.6	64	0.301
	3.5	0.96	33.4	65	0.302
	2.5	0.7	34.7	63	0.304
(b)	0.84 [a]	0.16	34.1	65	0.300
	0.6 [b]	0.1	35.0	64	0.302

Potassium ion concentration = 10 mM; DB18C6 concentration = 0.6 mM.
[a] Thick-walled glass, pulling protocol with −10°C between heating steps.
[b] Thick-walled glass, pulling protocol as for thin-walled glass.

where I_{ss} = steady-state current, D_1 = diffusion coefficient of the ionophore, n = charge number, F = Faraday constant, c_1^b = bulk concentration of ionophore and r_0 = radius) The reasons for this are not explicitly clear, yet there are two possibilities:

(i) the interface is a partial sphere, with the aqueous phase bulging out of the pipette, thereby leading to an increased steady-state current by virtue of the greater interfacial area;

(ii) the interface is hemispherical in shape and the difference in current arises through DB18C6 diffusing to the tip from above the imaginary insulating plane. The interface is, of course, not in an infinite insulating plane, and the glass wall at the tip of the micropipette is very thin (Fig. 2). Shoup and Szabo [20] showed that for a microdisc embedded on the top of a cylinder, the radius of the surrounding insulating material should be at least twice the radius of the disc for the behaviour of the electrode to be similar to that of a microdisc in an infinite insulating plane. In the case where the insulating material is of negligible thickness, they predicted an increased current of 40%. Obviously, for a hemisphere the increase would be different.

Stewart et al. [21] showed the behaviour of their thick-walled micropipettes to be between that of a microdisc and a microhemisphere in an infinite insulating plane, for ingress transfer of the tetraethylammonium ion. As explained earlier, however, the crudity of their pipette manufacture may have influenced this outcome. Another factor, however, may be the fact that the micropipette profiles are very different for thick- and thin-walled glass. In general, the profile for the thick glass is much more cylindrical than that of the thin glass, for the same pulling protocol. This might have an effect on the shape of the interface from pressure related considerations.

3.1.2. Chronoamperometry

The current–time response, under the same experimental conditions as in Section 3.1.1, was followed by means of chronoamperometry for micropipettes having tip radii of 5 and 2.5 μm. The potential was pulsed from a point where there was effectively zero assisted ion transfer (0.160 V on Fig. 5) to a point on the limiting current plateau (0.460 V on Fig. 5) and back,

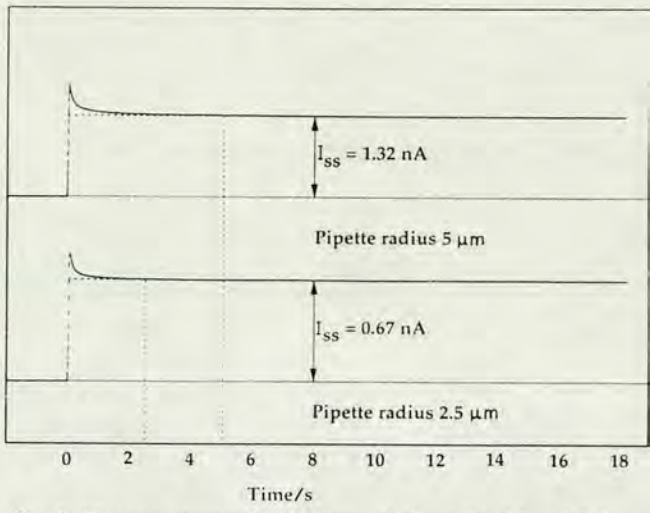

Fig. 7. Chronoamperograms for internal tip radii of 5 and 2.5 μm. K^+ concentration = 10 mM; DB18C6 concentration = 0.6 mM.

thereby producing the observed current–time responses shown in Fig. 7. These experiments were carried out in order to have independent steady-state current values for comparison with those obtained using cyclic voltammetry. The data shown in Fig. 7 and Table 1(a) demonstrate that the two techniques are in good agreement. The times taken to reach a steady state (the point at which there is no further decrease in current with respect to the baseline) were 2.5 and 5 s (approximately) for the 2.5 and 5 μm radius pipettes, respectively.

3.2. Variation of the potassium ion concentration

In this investigation, the concentration of aqueous KCl (y in cell 1) was varied, and a series of 3.5 μm radius pipettes were used to conduct the experiments. Potassium ion concentrations of y = 5, 50 and 100 mM were studied, with x = 0.6 mM DB18C6.

The cyclic voltammograms obtained are shown in Fig. 8, together with the result obtained for y = 10 mM KCl from Section 3.1.1. The relevant wave information is presented in Table 2. From the results it is evident that there is a good correlation between the different micropipettes and the steady-state current values. This

Table 2
Data from potassium ion concentration variation study

Potassium ion concentration/mM	Steady-state current/nA	Slope/V^{-1}	Tomes' criterion $(E_{3/4} - E_{1/4})$/mV	Half-wave potential/V
100	1.00	38.9	57.5	0.186
50	0.98	35.9	60	0.210
10	0.96	33.4	65	0.302
5	0.96	31.1	70	0.340

Radii of pipettes = 3.5 μm; DB18C6 concentration = 0.6 mM.

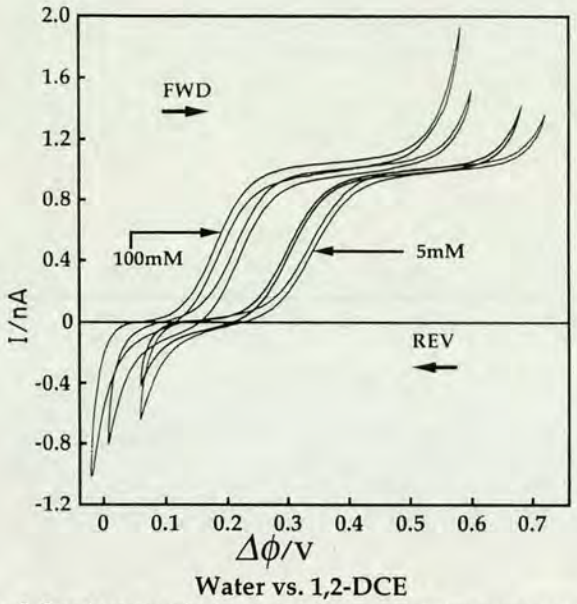

Fig. 8. Steady-state voltammograms for potassium ion concentrations of 100, 50, 10 and 5 mM. DB18C6 concentration = 0.6 mM; radius of micropipettes = 3.5 μm.

also illustrates that the observed current is proportional to the DB18C6 concentration when $x \ll y$ (cell 1).

In the case where $x \ll y$ (cell 1), the reversible half-wave potential for the transfer reaction is given by

$$\Delta_o^w\phi^{1/2}_{(DB18C6)K^+} = \Delta_o^w\phi^{0\prime}_{K^+} + \frac{RT}{2F}\ln\left(\frac{D_I}{D_{IM}}\right) - \frac{RT}{nF}\ln(K_a c_{K^+}) \quad (5)$$

where K_a is the association constant for the assisted ion transfer reaction (normally expressed in the form log K_a) and c_{K^+} is the metal ion concentration. D_I and D_{IM} are the diffusion coefficients of the ionophore and the ion–ionophore complex, respectively, where normally $D_I \approx D_{IM}$. Indeed, Osborne [22] showed that for the assisted transfer of the ammonium ion by DB18C6, at the large ITIES, the diffusion coefficients are effectively equivalent. Hence this explains the shift in half-wave potential with concentration, although clearly the reaction at the micropipette is only in the reversible region for 100 mM KCl.

The data in Table 2 demonstrate that as the potassium ion concentration is increased the reversibility of the assisted ion transfer reaction is improved. This then shows the change in reversibility for the 10 mM K^+ case to be an artifact created by the asymmetry of the diffusion regime at the micropipette. Essentially, on the rising portion of the wave, the assisted ion transfer reaction is dependent on both the diffusion of the potassium ion (linear) and DB18C6 (spherical). At high rates of mass transfer, however, the reaction becomes limited only by the diffusion of DB18C6 to the interface.

Using a 10 μm radius hole, Osborne [22] showed that the assisted ion transfer of potassium by DB18C6 at the microhole-supported ITIES was fully reversible, even when the concentration of potassium was 1 mM and that of the DB18C6 was 0.5 mM. This result confirms the conclusion for the micropipette that the change in reversibility is an artifact of the diffusion regime, and not of the reaction itself.

3.3. Variation of the DB18C6 concentration

In these experiments the steady-state current as a function of DB18C6 concentration was studied using values of x = 0.25, 0.5 and 1 mM (cell 1) and a series of 3 μm radius pipettes. The concentration of the potassium ion was 10 mM (y, cell 1). The observed current responses are illustrated in Fig. 9, along with the result for a DB18C6 concentration of x = 0.6 mM (cell 1). The waves were analysed as before and the data are displayed in Table 3. In this case, the reversibility of the assisted ion transfer reaction is favoured by a decrease in the DB18C6 concentration.

Fig. 10 shows a plot of the steady-state current versus DB18C6 concentration. On the same plot is the line calculated using Eq. 3, showing good agreement between the experimental and the expected current.

3.4. Evaluation of the micropipette tip resistance by ac impedance

In this investigation the total impedance of a cell consisting of a micropipette filled with aqueous KCl and inserted into one arm of a glass U-tube, also

Table 3
Data from DB18C6 concentration variation study

DB18C6 concentration/mM	Steady-state Current/nA	Slope/V^{-1}	Tomes' criterion $(E_{3/4} - E_{1/4})$/mV	Half-wave potential/V
1	1.40	31.0	71	0.310
0.6	0.81	34.6	65.5	0.301
0.5	0.67	36.0	63.5	0.303
0.25	0.38	36.3	61	0.304

Radii of pipettes = 3 μm; potassium ion concentration = 10 mM.

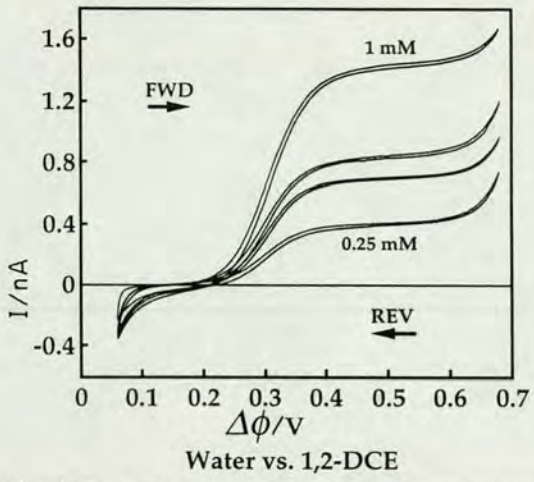

Fig. 9. Steady-state voltammograms for DB18C6 concentrations of 1, 0.6, 0.5 and 0.25 mM. K^+ concentration = 10 mM; radius of micropipettes = 3 μm.

containing aqueous KCl (concentration identical with that in the micropipette), was determined by ac impedance. The total impedance is taken to be the sum of the resistance of (i) the micropipette tip cone (the end of the first Ag AgCl wire was placed adjacent to this) and (ii) that of the remaining distance between the end of the tip and the other Ag AgCl wire. Experiments were carried out at a room temperature of 25 ± 1°C. From a plot of the imaginary impedance, Z_{imag}, versus the real impedance, Z_{real}, as a function of the frequency, ω, it was possible to evaluate the total impedance of the cell. This was achieved by extrapolation of the linear portion of the plot, at low frequencies, to $Z_{imag} = 0$ on the Z_{real} axis.

Data from the experiments was acquired by computer, which then dealt with the information handling and the extrapolation sequence to give the required impedance value.

In the first part of this study, a series of 3.5 μm radius pipettes were filled with various concentrations

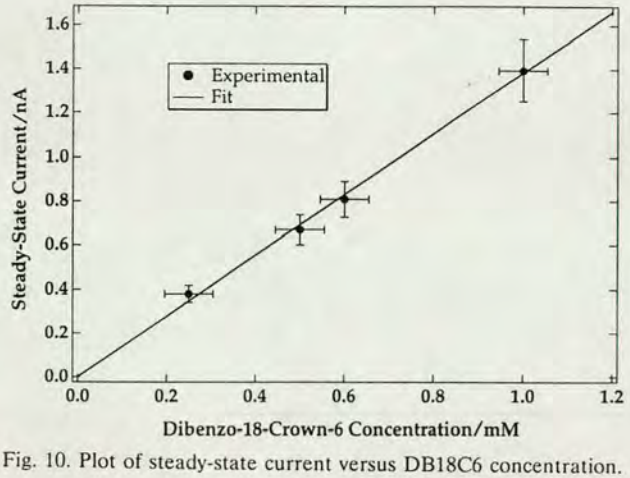

Fig. 10. Plot of steady-state current versus DB18C6 concentration.

Table 4
Data from ac impedance analysis of pipettes: K^+ concentration dependence using 3.5 μm radius pipettes

Potassium ion concentration/M	Total impedance $\times 10^{-4}/\Omega$
1	4.75
0.1	46.3
0.01	497

of KCl (0.01, 0.1 and 1 M) and the impedance was evaluated as described above. Table 4 lists the data obtained for all the experiments. Each result is an average of two determinations using the same pipette. As the concentration of KCl was increased by a factor of 10, the total impedance decreased by a factor of 10, approximately.

In the second part of the investigation, the effect of pipette radius on the tip resistance was evaluated using a KCl concentration of 1 M. These results were then used to predict an *IR* drop value for the 10 mM KCl case, based on the expected steady-state current for the respective pipettes, using the above approximation. In this way the error on the impedance evaluation was minimized. These results are shown in Table 5 and are again based on an average of two determinations using the same pipette. In one of these experiments the end of the pipette was broken off and the resistance of the system re-evaluated. The value obtained, for the cell minus the micropipette tip, was of the order of 0.5 kΩ, and was therefore judged to be relatively insignificant in comparison with the total impedance.

The calculated *IR* drop value for the 13 and 19 μm radii pipettes is higher than those of the other pipettes. Thus, as mentioned in Section 3.1, the change in wave behaviour from reversible to quasi-reversible on going from a tip size of 16 μm to one of 8 μm cannot be attributed to tip resistance. It must, therefore, be a characteristic of micropipettes which are below a certain size.

It is clear that, below a certain tip size, the asymmetry of the diffusion regime at the micropipette, and the

Table 5
Data from ac impedance analysis of pipettes: (Internal tip radius dependence)

Pipette radius/ μm	Total impedance $\times 10^{-4}/\Omega$	Estimated IR drop/ mV [a]
19	1.50	7.9
13	1.92	6.9
10	2.24	6.2
6.5	3.02	5.4
3.5	4.75	4.5
2.5	7.20	5
~ 0.6	76.8	8

Potassium ion concentration = 1 M.
[a] Potassium ion concentration = 10 mM.

fact that the interface is not in an insulating plane, begin to affect the assisted ion transfer reaction by leading to a shortage of potassium ions near the interface. This idea is strengthened by the results from Sections 3.2 and 3.3, which establish the trends in reversibility as being related to the potassium ion and DB18C6 concentrations, respectively. Indeed, in Section 3.2, the reaction is fully reversible for a potassium ion concentration of 100 mM.

Although the experimental technique has been shown to be inadequate in quantitatively determining the kinetics of the charge-transfer process, the lower limit for $k°$, the standard rate constant, can be set. The results shown in Tables 1 and 2 illustrate that a 0.6 μm pipette is not small enough to create a kinetic shift when the potassium ion concentration is in excess with respect to the DB18C6. Oldham et al. [23] stated that for an effectively reversible steady-state voltammogram, a dimensionless parameter, $\kappa°$, (which is equal to $r_0 k°/D_I$ for spherical geometries) should be greater than 40. Hence this sets the lower limit of $k°$ for the charge-transfer step of the assisted transfer of the potassium ion from the aqueous phase to the organic phase at 3 cm s^{-1}. For this evaluation the assumption is made that the micropipette tip-supported ITIES takes the form of a hemisphere, with an increased current contribution because it does not lie in an infinite insulating plane.

4. Conclusions

By using the micro-ITIES it has been shown that the assisted ion transfer of potassium, by the neutral ionophore DB18C6 is not controlled by charge transfer, but instead only by the diffusion of the species involved in the reaction. This suggests that the charge-transfer process must be significantly faster than diffusion, and in fact the lower limit of the standard rate constant, $k°$, for this step was estimated to be 3 cm s^{-1}.

The problems with the micropipette are its short lifetime and the fact that it cannot be re-used owing to accumulation of debris in the tip. In this respect the microhole has much greater potential. Since the technology to produce smaller microholes has been acquired recently it will surely be this path which will be taken towards future fundamental studies of ion transfer at the ITIES.

Acknowledgements

The authors thank Dr. Horst Vogel for the use of his pipette puller and Brian Senior, of the I^2M service at the Ecole Polytechnique Fédérale de Lausanne (EPFL), for carrying out the SEM work on the micropipettes. P.D.B. acknowledges the joint financial support given to him by the Science and Engineering Research Council (UK) and Medisense (UK), in the form of a CASE award, and also that of the EPFL for a visiting fellowship.

References

[1] P.N. Swan, Ph.D. Thesis, University of Southampton, 1980.
[2] K.B. Oldham, C.G. Zoski, A.M. Bond and D.A. Sweigart, J. Electroanal. Chem., 248 (1988) 467.
[3] A.J. Bard, G. Denuault, C. Lee, D. Mandler and D.O. Wipf, Acc. Chem. Res., 23 (1990) 357.
[4] R.M. Wightman, R.T. Kennedy, D.J. Wiedemann, K.T. Kawagoe, J.B. Zimmerman, and D.J. Leszczysyn, Microelectrodes in biological systems, in M.I. Montenegro, M. Arlete Queiros and J.L. Daschbach (Eds.), Microelectrodes: Theory and Applications, NATO ASI Series E. Vol. 197, Kluwer, Dordrecht, 1991, p. 453.
[5] R.M. Wightman and D.O. Wipf, Voltammetry at Ultramicroelectrodes, in A.J. Bard (Ed.), Electroanalytical Chemistry, Vol. 15, Marcel Dekker, New York, 1989, p. 267.
[6] M.I. Montenegro, M. Arlete Queiros and J.L. Daschbach (Eds.), Microelectrodes: Theory and Applications, NATO ASI Series E, Vol. 197, Kluwer, Dordrecht, 1991.
[7] B.R. Scharifker, Microelectrode techniques in electrochemistry, in J.O'M. Bockris, B. Conway and R. White (Eds.), Modern Aspects of Electrochemistry, Vol. 22, Plenum, New York, 1992, 467.
[8] C. Amatore, M.R. Deakin and R.M. Wightman, J. Electroanal. Chem., 220 (1987) 49.
[9] C. Gavach and F. Henry, J. Electroanal. Chem., 54 (1974) 361.
[10] J. Koryta, Electrochim. Acta, 24 (1979) 293.
[11] H.H. Girault and D.J. Schiffrin, Electrochemistry of liquid–liquid interfaces, in A.J. Bard (Ed.), in Electroanalytical Chemistry, Vol. 15, Marcel Dekker, New York, 1989, p. 1.
[12] G. Taylor and H.H. Girault, J. Electroanal. Chem., 208 (1986) 179.
[13] A.A. Stewart, Y. Shao, C.M. Pereira and H.H. Girault, J. Electroanal. Chem., 305 (1991) 135.
[14] Y. Shao, M.D. Osborne and H.H. Girault, J. Electroanal. Chem., 318 (1991) 101.
[15] Y. Shao and H.H. Girault, J. Electroanal. Chem., 334 (1992) 203.
[16] T. Ohkouchi, T. Kakutani, T. Osakai and M. Senda, Anal. Sci., 7 (1991) 371.
[17] J.A. Campbell and H.H. Girault, J. Electroanal. Chem., 266 (1989) 465.
[18] M.D. Osborne, Y. Shao, C.M. Pereira and H.H. Girault, J. Electroanal. Chem., 364 (1994) 155.
[19] P.D. Beattie, P.P. Infelta and H.H. Girault, Anal. Chem., 66 (1994) 52.
[20] D. Shoup and A. Szabo, J. Electroanal. Chem., 160 (1984) 27.
[21] A.A. Stewart, G. Taylor, H.H Girault and J. McAleer, J. Electroanal. Chem., 296 (1990) 491.
[22] M.D. Osborne, Ph.D. Thesis, Edinburgh University, 1993.
[23] K.B. Oldham, J.C. Myland, C.G. Zoski and A.M. Bond, J. Electroanal. Chem., 270 (1989) 79.